Construction of Isostructural Hydrogen-Bonded Organic Frameworks through Stacking of Nonplanar π-Conjugated Molecules

YUTO SUZUKI

MARCH 2023

Construction of Isostructural Hydrogen-Bonded Organic Frameworks through Stacking of Nonplanar π-Conjugated Molecules

A dissertation submitted to

THE GRADUATE SCHOOL OF ENGINEERING SCIENCE

OSAKA UNIVERSITY

in partial fulfillment of the requirements for the degree of

DOCTOR OF PHILOSOPHY IN ENGINIEERING

BY

YUTO SUZUKI

MARCH 2023

Abstract

Porous materials (PMs) are structures with numerous spaces (voids) in solid materials, represented by activated carbon and zeolite. By adjusting the size, surface area, and surface functionality of the pores, various unique functions are promising. The systematical construction of these pores will lead to the development of superior functions. In storage, separation, sensing, and catalytic reactions, the porous chemical environment is related directly to selectivity and functionality. Therefore, the research of adjustable porous materials has been progressing.

In addition to activated carbon and zeolite, which are porous materials also obtained from nature, metal–organic frameworks (MOFs), covalent organic frameworks (COFs), and hydrogen-bonded organic frameworks (HOFs) were discovered and developed. These porous materials are classified as crystalline and amorphous. Crystalline PMs, such as zeolites and MOFs, exhibit high porosity and a small pore distribution due to their regularly aligned structure. These materials can be engineered by selecting appropriate constituents through “crystal engineering” approaches to understand the structure-function correlation of high crystalline structures.

MOFs, COFs, and HOFs are representative porous frameworks composed of organic molecules and have been actively researched for the last 30 years. This is because a tailorable porous structure with a specific pore and function can be constructed based on a diverse organic molecule. In pioneering frameworks such as MOFs and COFs, structural design has been developed based on “reticular chemistry” and further systematic approaches. Based on previously synthesized structures, desired similar frameworks, so-called "isostructural frameworks" are obtained from bottom-up construction by designing or modifying the constituent molecules.

Contrary, HOFs are assembled with non-covalent bond (π-π stacking, hydrogen bonding, and others) rather than strong covalent or coordination bonds. They are designed and constructed by crystal engineering approaches to control intermolecular interactions and arrangements through hydrogen-bonding (H-bonding). Due to reversibility of the bonding, HOFs can be obtained as a single-crystalline material with large domain by facile recrystallization. Solution processes *via* re-solubilization allows for re-use and re-generation. However, HOFs tend to lose its porosity due to the weakness of the bonds compared to other porous frameworks, but this is an advantage in constructing flexible porous materials. Furthermore, the frameworks same as the originally designed are not always formed, and unexpected structure sometimes forms, in other words, diverse structures can be constructed. Although recent studies have reported HOFs that exhibit permanent porosity or are capable of construction of desired similar structures, there is still a need for design principles for the systematic construction of high crystalline, regeneratable HOFs compatible with stability and designability.

Recently, these shortcomings of stability have been overcome by networking through charge-assisted H-bonding and assembling *via* π–π stacking to give stable HOFs. The former can form the same network due to the electrostatic forces to form strong bonds. In the latter, π-π stacking of molecules limits the

possible molecular assemblies. In the system of π-stacking, isostructural construction is also reported. The construction of isostructural HOFs has been conducted by designing a planar π-conjugated molecule (core) and peripheral functional groups (spacers and H-bonding sites). However, systematical construction of a series of isostructural HOFs is challenging and several isostructural HOFs were constructed successfully because the individual interactions are relatively weak and more sensitive to the constituted molecules.

HOFs require the systematic construction of isostructural frameworks based on their design/structure and design/function correlations. Of particular note is the highly stable HOF based on carboxylic acid derivatives with hexaazatriphenylene, a nonplanar π-conjugated core. This HOF is achieved by uniformly stacking to inhibit layer slippage, so-called "shape-fitted docking." The nonplanar nature of the hexaazatriphenylene (HAT) can provide a platform for designing spacers of isostructural construction.

In this thesis, the author explored the core structures that can form shape-fitted docking, and also found a correlation between structure and function built by spacer design, and explored the limitations and possibilities of the design.

In Chapter 1, general introductions about tailorable porous materials and these systematic constructions are described. The author mentioned about classification and properties of amorphous or crystalline porous materials, IUPAC definitions of pore shape and size, and definitions of isostructural or isoreticular. Porous organic frameworks have been actively developed for the construction and application of a wide variety of structures. In this chapter, the author discusses design guidelines for MOFs, COFs, and HOFs with systematic examples of isostructural frameworks, and current issues. Subsequently, the author described the motivation and purpose of this thesis.

In Chapter 2, the author described the isostructural construction by spacer-designed analogs with HAT as core and carboxylic acid as bonding motif. The building blocks are **BPHAT** and **TPHAT** with biphenyl and terphenyl groups as spacer, respectively, which are extended by phenylene groups from **CPHAT**. In addition, **TolHAT** and **ThiaHAT** were designed to replace the terphenyl moiety to tolane and 4,7-diphenylbenzo-2,1,3-thiadiazol to reduce and increase the steric hindrance of the double-terminated Ph group, respectively. Except for low crystalline precipitates of **TPHAT**, other derivatives **BPHAT**, **TolHAT**, and **ThiaHAT** constructed isostructural HOFs by shape-fitted docking of ***pcu*** network. Only **TolHAT** was fragile, but **BPHAT** and **ThiaHAT** showed excellent stability against heat (over 300 °C), solvent immersion, and removal. A fluctuation of the peripheral groups from molecular dynamics simulation can precisely evaluate this stability. The spacer design enabled the systematic construction of rigid isostructural HOFs with extended pores.

In Chapter 3, the author attempted to construct isostructural HOFs with a core of dibenzo[*g*,*p*]chrysene (DBC), a nonplanar π-conjugated molecule, because DBC is also expected to be accumulated through shape-fitted docking. The tetrakis(4-carboxyphenyl) derivative **CPDBC**, gave **CPDBC-1** with eclipsed stacking. In addition, an unexpected structure with staggered stacking, **CPDBC-2**, was obtained. **CPDBC-2** has a structure stacked in a 90° rotation and was a "*disappeared crystal*". Bulk crystalline **CPDBC-1** showed excellent thermal stability and porosity. As a comparison, HOF construction was performed with non-annulated analog **CBPE**, which forms a triaxial woven structure. These results indicate the importance

of nonplanar π-conjugated cores.

In Chapter 4, the author attempted to design a spacer in the system of DBC core. The derivative **CBPDBC** with carboxybiphenyl groups yields poor crystalline precipitates due to solubility and aggregation problems. However, the DBC derivatives with 1,4-, 1,5-, and 2,6-substituted naphthyl groups yielded isostructural HOFs (**C1N4DBC-1**, **C1N5DBC-1**, and **C2N6DBC-1**, respectively), comparable to **CPDBC-1**. Importantly, these isostructures possessed different properties ranging from stable to flexible to fragile toward guest removal. These differences are attributed to the pore geometry and H-bonding style due to the isomeric effect. The results implied that the DBC core is fundamental to isostructural constructed HOFs and that the isomeric effect at spacers significantly affected structural properties.

Abbreviations

2-c	2-connected
3-c	3-connected
4-c	4-connected
6-c	6-connected
BET	Brunauer–Emmett–Teller
BSSE	basis set superposition error
BTQ	benzotriquinoxaline
C_3PI	C_3-symmetric π-conjugated molecules
CMPs	conjugated microporous polymers
COFs	covalent organic frameworks
CPE	tetrakis(4-carboxyphenyl)ethene
CSP	crystal structure prediction
CT	charge transfer
CTFs	covalent triazine frameworks
DAT	2,6-diamino-1,3,5-triazine
DBC	dibenzo[*g*,*p*]chrysene
DC	tri(dithiolylidene)cyclohexanetrione
DEAni	*N*,*N*-diethylaniline
DFT	density functional theory
DMA	*N*,*N*-dimethylacetamide
DMF	*N*,*N*-dimethylformamide
DMSO	dimethyl sulfoxide
d-POSs	diamondoid porous organic salts
ECL	electrochemiluminescence
ED	electron diffraction
ESF	energy-structure-function
FP-TRMC	flash-photolysis time-resolved microwave conductivity
GAFF	general AMBER force field
GFP	green fluorescent protein
GPC	gel permeation chromatography
H_3TATB	1,3,5-tris(4-carboxyphenyl)benzene: H_3BTB
HAT	1,4,5,8,9,12-hexaazatriphenylene
HATN	diquinoxalino[*2*,*3-a*:*2'*,*3'-c*]phenazine
HCPs	hyper-crosslinked polymers
HexNet	hexagonal network

HOFs	hydrogen-bonded organic frameworks
HOMO	highest occupied molecular orbital
IRF	instrument response function
IRMOF	isoreticular metal–organic framework
IUCr	international union of crystallography
IUPAC	international union of pure and applied chemistry
LA-HexNet	layered assemble hexagonal networks
LJ	Lennard-Jones
LUMO	lowest unoccupied molecular orbital
MD	molecular dynamics
MeBz	methyl benzoate
MOFs	metal–organic frameworks
nCOFs	non-covalent organic frameworks
NLDFT	nonlocal density functional theory
PAFs	porous aromatic frameworks
PCPs	porous coordination polymers
PhT	phenylene triangle
PIMs	polymers of intrinsic microporosity
PMCs	porous molecular crystals
PMs	porous materials
PME	particle-mesh Ewald
POCs	porous organic cages
POFs	porous organic frameworks
POSs	porous organic salts
POPs	porous organic polymers
PT	proton transfer
PXRD	powder X-ray diffraction analysis
RCSR	Reticular Chemistry Structure Resource
RESP	restrained electrostatic potential
RMSD	root mean square deviation
RV	replace vacuum
SCXRD	single-crystalline X-ray diffraction
SEM	scanning electron microscope
SBU	secondary building unit
SMC	Suzuki-Miyaura cross coupling
SOFs	supramolecular organic frameworks
STP	standard pressure
TBU	tertiary building unit

tBuXy	5-*tert*-butyl-*m*-xylene
TCB	1,2,4-trichlorobenzene
TMB	1,2,4-trimethylbenzene
TCPA	tris(4-carboxyphenyl)amine
TCBP	1,3,5-tris(4-carboxyphenyl)benzene
TCSPC	time-correlated single photon counting
TG	thermal gravimetric
TGA	thermogravimetric analysis
TMSA	trimethylsilylacetylene
Tp	triphenylene
TPE	1,1,2,2-tetraphenylethene
TPMA	triphenylmethylamine
TV	thermal vacuum
Tz	2,1,3-benzothiadiazole
VT-PXRD	variable-temperature powder X-ray diffraction

Contents

Chapter 1. General introduction

1.1 Tailorable porous materials 1
1.2 Pore shape and size 3
1.3 Crystal engineering 4
1.3.1 Hydrogen bond 5
1.3.2 π Interaction 6
1.4 Type of porous materials 7
1.5 Metal-organic frameworks (MOFs) / porous coordination polymers (PCPs) 8
1.6 Covalent organic frameworks (COFs) 10
1.7 Hydrogen-bonded organic frameworks (HOFs) 12
1.7.1 Carboxylic acid 14
1.7.2 2,6-Diamino-1,3,5-triazine (DAT) 14
1.7.3 Pyrazole 15
1.7.4 Urea 15
1.7.5 G-quadruplex 15
1.7.6 Hydroxy group 15
1.7.7 Cyano group 16
1.7.8 Pyridine 16
1.7.9 Ammonium carboxylate 16
1.7.10 Ammonium sulfonate 16
1.7.11 Amidinium carboxylate 17
1.7.12 Guanidium sulfonate 17
1.7.13 Pyridinium carboxylate 17
1.7.14 Other H-bondings 18
1.7.15 Other charge-assisted H-bondings 18
1.8 Systematic construction of isostructural crystalline POFs 19
1.8.1 Topological network 21
1.8.2 MOFs 21
1.8.3 COFs 22
1.8.4 HOFs 23
A. Carboxylic acid 24

A-1. Tricarboxylic acid 24
A-2. Tetracarboxylic acid 28
A-3. Hexacarboxylic acid 35
A-4. Other Hexacarboxylic acid 39
B. Diaminotriazine (DAT) 40
C. Pyrazole 42
D. Urea 44
E. Amidinium carboxylate 46
F. Ammonium carboxylate 48
G. Ammonium sulfonate 49
H. Pyridinium carboxylate 51
1.9 Purpose of this thesis 52
1.10 References 54

Chapter 2. Isostructural construction of HOFs with extended spacer based on shape-fitted docking of hexaazatriphenylene core

2.1 Introduction 69
2.2 Synthesis and crystallization 71
2.3 Crystallography 73
2.4 Thermal analysis and activation 79
2.5 Evaluation of the chemical durability 84
2.6 Evaluation of the porosity 85
2.7 Computational evaluation of stability 87
2.8 UV-vis steady state properties 88
2.9 Conclusion 98
2.10 Experimental section 100
2.10.1 Synthesis of building blocks 100
2.10.2 Single crystal X-ray measurement and analysis 112
2.10.3 Variable temperature PXRD (VT-PXRD) measurement 113
2.10.4 Sorption/desorption experiments 114
2.10.5 Theoretical calculations 114
2.10.6 Molecular dynamics simulations 114

2.10.7 Time-resolved spectroscopy 115
2.10.8 Microscopic fluorescence spectroscopy 115
2.11 References 117

Chapter 3. HOFs constructed through different assemblies: shape-fitted docking of nonplanar π-conjugated cores and triaxially-woven of non-annulated planar cores

3.1 Introduction 120
3.2 Synthesis and crystallization 122
3.3 Crystallography 123
3.4 Thermal behaviors and durability 130
3.5 Solid state fluorescence behaviors 134
3.6 Photo-conductivity of **CPDBC-1** 136
3.7 Evaluation of porosity 136
3.8 Conclusion 138
3.9 Experimental section 139
3.9.1 Synthesis of **CPDBC** 139
3.9.2 X-ray diffraction measurements 140
3.9.3 VT-PXRD measurement 141
3.9.4 Flash-photolysis time-resolved microwave conductivity (FP-TRMC) 142
3.9.5 Solid state fluorescence behaviors 142
3.9.6 Sorption/desorption experiments 142
3.10 References 145

Chapter 4. Isomeric effect of naphthyl spacers on structures and properties of isostructural HOFs

4.1 Introduction 147
4.2 Synthesis and crystallization 149
4.3 Crystallography 150

4.4 Thermogravimetric analysis of as-formed HOFs 155
4.5 VT-PXRD measurements 157
4.6 Activation condition 157
4.7 Structure of activated framework of **C1N4DBC-1** 160
4.8 Gas sorption measurements 161
4.9 *In situ* PXRD measurements with loaded molecules 162
4.10 Proposed lattice change in **C1N4DBC-1** 164
4.11 Computational evaluation of stability 167
4.12 Conclusion 168
4.13 Experimental section 169
4.13.1 Synthesis of building blocks 170
4.13.2 Single crystal X-ray or electron diffraction measurement and analysis 177
4.13.3 Powder X-ray diffraction measurement 178
4.13.4 VT-PXRD measurement 179
4.13.5 *In situ* sorption-PXRD measurements 179
4.13.6 Powder X-ray diffraction analysis of **C1N4DBC-1a** 179
4.13.7 Sorption/desorption experiments 180
4.13.8 Theoretical calculations 180
4.14 References 182

General conclusion 186

List of publication 188

Acknowledgement 189

Chapter 1. General introduction

1.1 Tailorable porous materials

Porous solid is defined in IUPAC recommendations[1] as "*a solid with pores, i.e. cavities, channels or interstices, which are deeper than they are wide*". The high internal surface area serves as an adsorption site for atoms and molecules, making it an ideal adsorbent material for gas storage, separation, and contaminant removal. The absorption process and selectivity are important properties, which are engineered by adjusting size, shape, surface area, and surface functionality.

These porosities hold significant potential such as storage[2,3] and separation[2,4] materials, heterogeneous catalysts or catalyst supports[5–7], as well as in new areas such as sensing[8,9], energy storage[10,11], energy conversion[12,13], and biomedical[14,15] materials. Especially for sensing and catalytic applications, the selectivity or catalytic activity need to be specific to the target compound or reaction, so the precise design of the chemical porous environment is very important. For this reason, the search and construction of porous materials with freely adjustable unique property is now ongoing.

Various porous materials (PMs), both crystalline and amorphous, have been developed (for details, see section 1.4). For instance, activated carbon[16,17], zeolite, porous organic polymers (POPs)[18–23], porous molecular crystals (PMCs)[24–31], and porous organic frameworks (POFs): metal–organic frameworks (MOFs)[32–39], covalent organic frameworks (COFs)[40–45], and hydrogen-bonded organic frameworks (HOFs)[46–52].

Representative examples of amorphous PMs are activated carbons and POPs, which have a sufficiently high surface area (over 3000 $m^2\,g^{-1}$ for activated carbon), but they show a wide pore distribution due to their disordered structure[53]. Specimen of crystalline PMs are zeolites, PMCs, and POFs, whose porosities are engineerable opposite to amorphous PMs. They exhibit both high porosity and narrow pore distribution due to the regularly ordered structure. The highly crystalline structure allows an approach based on structure–function correlation to select appropriate components and control their function. This approach is called crystal engineering[54–59] or reticular chemistry[32–39].

POFs (MOFs, COFs, and HOFs), which are composed of organic molecules, have been actively researched for the last 30 years. This is because a tailorable porous structure with a specific pore/function can be constructed by the crystal engineering approach based on a diverse organic molecule (Figure 1a,b). Tailorability is achieved through the systematic construction of diverse and isostructural structures. For example, molecular modification has been conducted for functional tuning, optimizing the structure and chemical environment of the pores (Figure 1b, top). Elongated or substituted organic molecules are also used to construct POFs with optimized pores for gases, organic molecules, or even proteins (Figure 1b, bottom). In representative and pioneering frameworks such as MOFs and COFs, structural design has been developed based on reticular chemistry and further systematic approaches (*de novo*[60], reconstruction[61]). Based on previously synthesized structures, the desired similar framework, the so-called "isostructural framework", is obtained through bottom-up construction by designing or modifying the constituent molecules.

Contrary, HOFs, which are subclass of porous molecular crystals (POMs), are assembled with non-covalent bonds (hydrogen bonding, π-π stacking, and others) rather than strong covalent or coordination bonds[33] (Figure 1c). They are designed and constructed by crystal engineering approaches to control intermolecular interactions and arrangements through hydrogen bonding (H-bonding). Due to reversibility of the bonding, HOFs can be obtained as a single-crystalline material with large domain by facile recrystallization or as a crystalline powder by mechanochemical methods. Solution processes *via* re-solubilization allows for re-use and re-generation. However, HOFs tend to lose its porosity due to the weakness of the bonds compared to other porous frameworks, but this is an advantage in constructing flexible porous materials. Furthermore, the frameworks same as the originally designed were not always formed, and unexpected structure sometimes forms, in other words, diverse structures can be constructed. Although recent studies have reported HOFs that exhibit permanent porosity or are capable of constructing desired similar structures, there is still a need for design principles for the systematic construction of high-crystalline, regeneratable HOFs compatible with stability and designability.

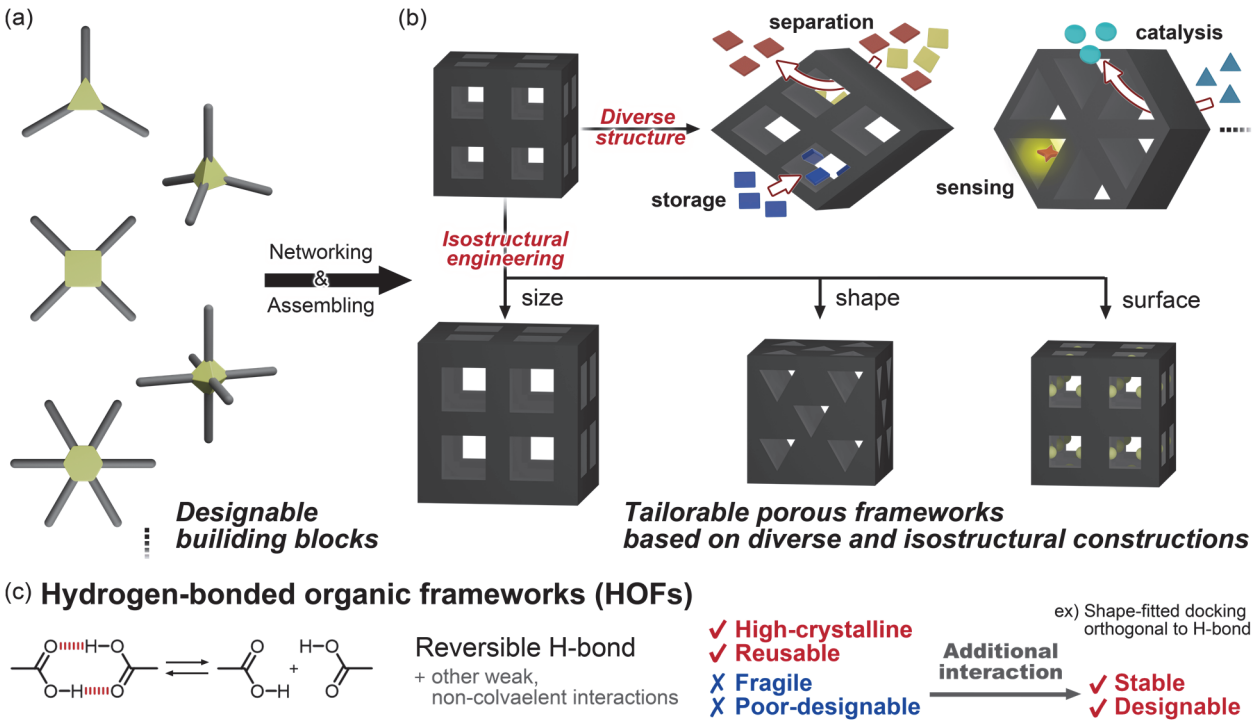

Figure 1. Construction of porous materials. (a) Designable building block composed porous materials. (b) Tailorable porous frameworks for applications such as storage, separation, catalysis, and sensing. Isostructural engineering of diverse porous structures is conducted to yield frameworks with different size, shape, and surface of the pores. (c) Features of hydrogen-bonded organic frameworks (HOFs), which is constructed through reversible bond such as dimer of carboxylic acids. In order to construct stable and designable HOFs, it is necessary to overcome the shortcomings through an additional interaction, such as a shape-fitted docking orthogonal to H-bond.

1.2 Pore shape and size

Porous materials exhibit different properties depending on the size and shape of pores. IUPAC recommendation of size[1,62,63] and shape[1] are described below. Pore width is defined as the diameter of the pore or the interlayer distance (space between two layers) of slit pores. According to the IUPAC recommendation in 1985, pores are classified into three categories according to pore size (Figure 2 bottom)[48], macropore: over 50 nm, mesopore: 2–50 nm, and micropore: < 2 nm. Following the development of nanoporous materials, IUPAC refined the classification in 2015 and introduced three new types of pores [49], nanopore: <100 nm, supermicropore: 0.7–2 nm, and ultramicropore：< 0.7 nm. New definitions indicate that nanopores include micropores, mesopores, and macropores, but the upper limit is 100 nm. Supermicropores and ultramicropores are two subtypes of micropores. Micropore improves the specific surface area and void. Since the pore size is close to small molecules, ultramicropores can strongly adsorb gas molecules such as helium, nitrogen, and carbon dioxide, while supermicropores can adsorb other gas molecules, ions (Li^+, etc.), and small organic molecules. Mesopores can hold common organic molecules and provide sufficient space for sensing and use in catalytic reaction. Macropores are larger than the previous two and are used to improve access to micro/mesopores through hierarchical pore construction because of their superior diffusion of materials[64–66].

The pore can be classified into two main types[63]: accessible or inaccessible to external liquid. One is closed pores, also called “0D pore”, which is inaccessible and completely isolated from external environments. They influence only macroscopic properties but are inactive in porous processes. Other pores are open pores, which are accessible to the external environments. They are further classified into “blind pores” and “through pores”. Through pores, also called channel, are described as a pore that pierces from one point to a different point on the surface. Blind pores, also called as dead-end or saccate pores, are pores that has not been pierced. It is important to note that a blind pore is conventionally defined as one whose depth is greater than the aperture, based on the IUPAC definition of a porous solid.

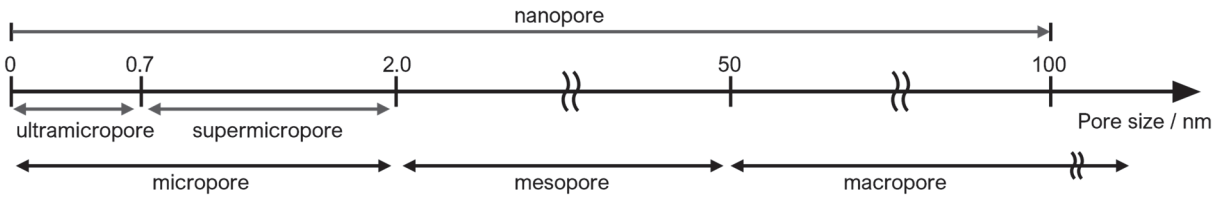

Figure 2. Definition of pore size.

1.3 Crystal engineering

The physical and chemical properties of crystals are determined by the nature of the constituent molecules and their structures[59]. Systematical understanding and control of intermolecular interactions in crystals, and optimization of molecular design for new crystals is defined as "crystal engineering"[54–58,67]. This engineering can be understood as *"retro-construction"* approach, as in retrosynthesis in organic synthesis.

In order to simplify the supramolecular interactions and to control crystal structures systematically, "supramolecular synthon" and "tecton" were proposed by Desiraju in 1995[55], and Wuest *et al.* in 1991[68], respectively. The "supramolecular synthon" is defined as *"structural units within supermolecules, which can be formed and/or assembled by known or conceivable synthetic operations involving intermolecular interactions"*[54]. Thus, supramolecular synthons are a spatial arrangement of intermolecular interactions. The "tecton" was proposed for *"any molecule whose interactions are dominated by particular associative forces that induce the self-assembly of an organized network with specific architectural or functional features"*.

For pre-designed construction, supramolecular synthon is used to determine the orientation and multiplicity of networks and its assemblies, and tectons are used to determine shape, size, rigidity, and functionality. H-bonds are representative of directional non-covalent bonds[69,70] (Scheme1a–d). Other interactions as supramolecular synthons are halogen bond, π-interaction (π-π, CH-π, cation/anion-π, and others), and van der Waals force (dipole-dipole, dispersion force, and others) (Scheme 1e,f). The following sections describe representative supramolecular synthons, H-bond, and π-interaction.

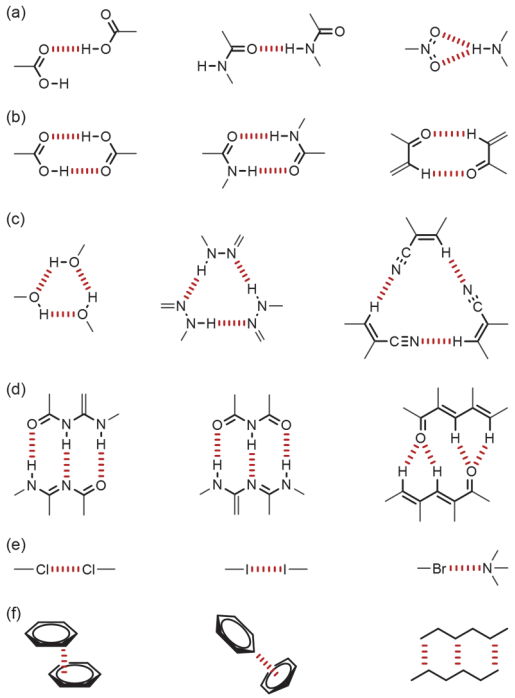

Scheme 1. Chemical structure of representative supramolecular synthons. (a) Monomeric H-bonding dimers, (b) complementary H-bonding dimers, (c) cyclic H-bonding trimers, (d) dimer with multiple H-bonding, (e) dimers of halogen bonding, and (f) π-interaction and dispersion force.

1.3.1 Hydrogen bond

There are many H-bonding motifs as a supramolecular synthon, such as the complementary dimer of carboxylic acids, 1D networking of amides, and guanine-cytosine bonding shown in Scheme1a–d.

The definition of H-bond, according to the IUPAC recommendation at 2011[71] is "*The hydrogen bond is an attractive interaction between a hydrogen atom from a molecule or a molecular fragment X–H in which X is more electronegative than H, and an atom or a group of atoms in the same or a different molecule, in which there is evidence of bond formation.*" H-bond is described as X-H···Y, where H is named a H-bond donor and Y is a H-bond acceptor. The H-bonding energy depends on the constituent species and geometric structure. That is, it depends on the electrostatic environment of the constituent molecules and a length and an angle of the resulting bond (Table 1). The strengths are typically 10–40 kJ mol^{-1}, and range from 1 to 170 kJ mol^{-1} including all examples[33,72] such as charge-assisted H-bonding[73,74] (Figure 3). Compared with coordination bonds (90–350 kJ mol^{-1}) and covalent bonds (300–600 kJ mol^{-1})[33], the rigidity and directionality of H-bonds are lower but more diverse. H-bonding interactions were proposed to be classified as weak, moderate, and strong H-bond according to the binding geometry and energy. Strong H-bonds are highly directional due to their short bonding distance and narrow angular range. Weak H-bonds have long bonding distances and poor directionality.

The representative, highly directional, and strong H-bonds are mainly intermolecular O/N–H···O/N interactions, which are often dominant and widely exist in many supramolecular systems. This has been observed in the dimer of carboxylic acid, the amido H-bonding interaction in α-helix and β-sheet, and Watson-Crick base pairs.

Table 1. Criteria for H-bonds adapted from Steiner and Jeffrey[405]. (Reproduced permission from ref. 72, copyright 2019 The Royal Society of Chemistry.)

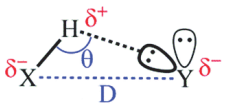	**Strong**	**Moderate**	**Weak**
D / Å	2.2–2.5	2.5–3.2	>3.2
H···Y / Å	1.2–1.5	1.5–2.2	>2.2
θ / °	170–180	>130	>90
X–H *vs.* H···Y	X–H ~ H···Y	X–H > H···Y	X–H >> H···Y
Bond energy / kJ mol^{-1}	63–167	17–63	<17

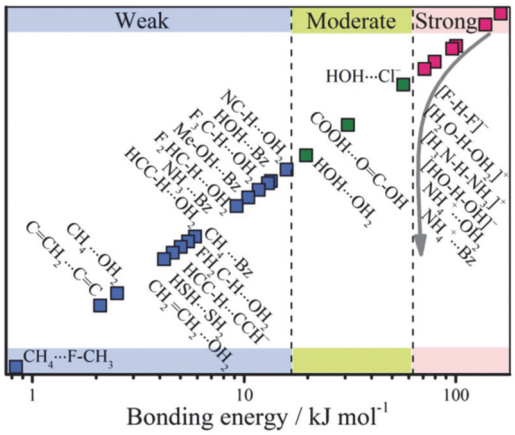

Figure 3. Various types of H-bonds. This sketch is not exactly quantitative but the coloring attempts to give a visual scale of bonding energies. Data from Steiner's paper[405]. (Reproduced permission from ref. 72, copyright 2019 The Royal Society of Chemistry.)

1.3.2 π Interaction

Interactions by π electron include a homotypic interaction between π-electrons and a hetero-interaction between π-electron and other charge species (Scheme 2)[75,76]. The interaction by organic molecules can be classified into four types: π-π, CH-π, π-anion, π-cation interaction[75]. Neutral interactions include the π-π and CH-π interactions, which act between an aromatic hydrogen atom and π-electrons. The face-to-face π-π interaction become more stable in large π system, while the edge-to-edge CH-π interaction is the most stable in small π systems such as benzene[77]. In 1989, G. R. Desiraju, *et al*. stated that the crystal structures of simple PAHs were divided into four types: herringbone, sandwich, γ, and β[78]. To date, the accumulation of π-conjugated molecules with functional groups was classified as follows: herringbone stacking, brick layer stacking, slipped stacking, and cofacial stacking (Figure 4)[79]. In the normal π system, cofacial stacking is unfavorable due to the repulsion between hydrogens or π-electrons, resulting in the construction of displacement stacking. However, in the case of electron-deficient aromatic interactions, the repulsion changes to interaction, which leads to an advantage in cofacial stacking. There are also interactions between ion and π system, cation-π interactions[75,80–85] and anion-π interactions[85–89].

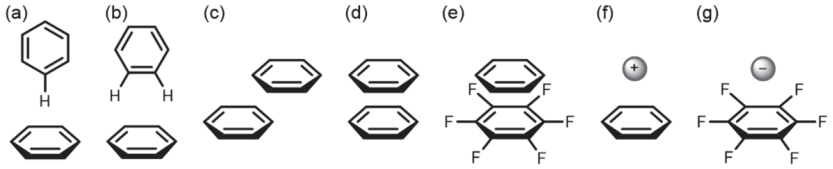

Scheme 2. Chemical structure of π interaction. (a) T-shaped and (b) Y-shaped CH-π interaction. (c) Parallel displaced and (d) cofacial parallel stacked π-π interaction. (e) π-π Interaction with electron-deficient aromatics. (f) Cation-π interaction and (g) anion-π interaction with electron-deficient aromatics.

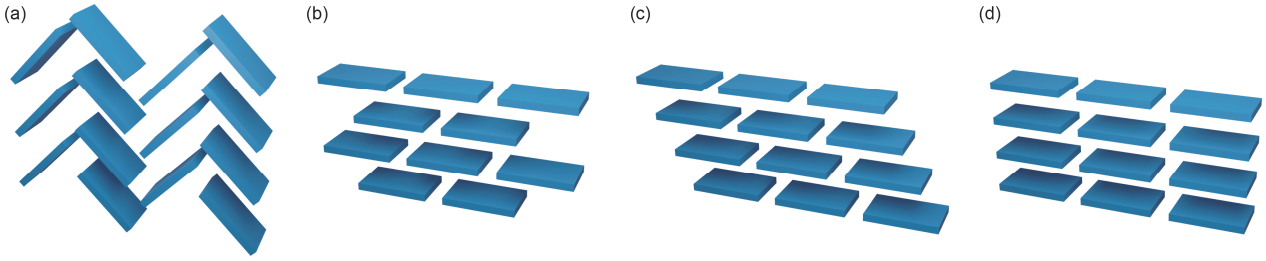

Figure 4. Four typical stacking type of π-conjugated molecules in crystals: (a) herringbone stacking, (b) brick layer stacking, (c) slipped stacking, and (d) cofacial stacking.

1.4 Type of porous materials

Active researches have led to the creation of diverse porous materials: nanoporous carbons[90–95], mesoporous silicates, zeolites, porous organic polymers (POPs)[18–23], porous molecular crystals (PMCs)[24–31], porous organic cages (POCs)[18–23], metal–organic frameworks (MOFs) [32–39], covalent organic frameworks (COFs)[40–44], and hydrogen-bonded organic frameworks (HOFs)[46–52]. These materials are classified as amorphous and crystalline states (Figure 5).

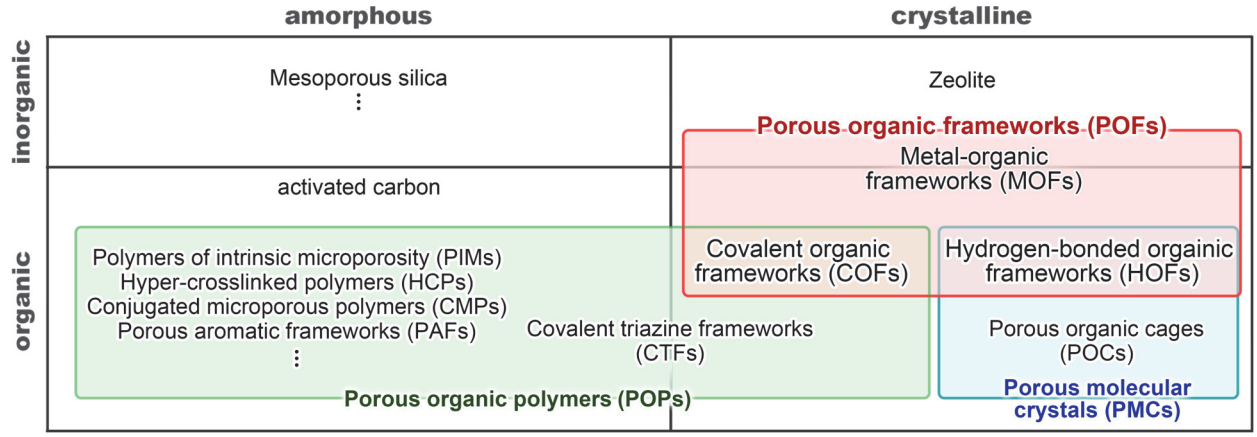

Figure 5. Classification of porous materials.

The amorphous PMs are activated carbon, nanoporous carbons, mesoporous silica, and most porous organic polymers (POPs). POPs are the polymer networked by organic molecules that exhibit porosity derived from the constituent molecular backbone and/or the network structure. These porous polymer networks are usually amorphous and disordered structures. COFs are the subset of POPs possessing crystalline networks. Polymers of intrinsic microporosity (PIMs)[96–100] are 1D polymers, which are achieved through inefficient packing of the twisted polymer backbone. Hyper-crosslinked polymers (HCPs)[101–105], covalent triazine frameworks (CTFs)[106–110], porous aromatic frameworks (PAFs)[111–113], and conjugated microporous polymer (CMPs)[114–118] are covalently bonded 2D or 3D structures. Each subclass of materials is structurally different, but they are united by their high microporosity, lightweight, and permanent bondings.

The crystalline PMs are zeolite, POCs, PMCs, MOFs, COFs, and HOFs. In terms of porosity, they are engineering materials that exhibit both of high porosity and narrow pore distribution due to the regularly ordered structure. PMCs are crystalline materials with pores. Inclusion crystals[68,118–142] are the predominant materials in which the main component encapsulates solvent molecules or guest molecules. This enables selective inclusion and separation during recrystallization by recognizing size, shape, functional group, or chirality. PMCs have structures maintaining porosity after guest removal, namely a system with permanent porosity. The pores are classified as intrinsic and extrinsic. Porous organic cages (POCs) are structures with intrinsic pore, which is derived from the internal space of the molecule, such as macrocyclic molecules (pillararenes)[144,145] or cage molecules. Therefore, after removing molecules in the pores, stable POCs remaining porosity are rarely obtained[122], although there are examples in imine-linked cages[146]. In contrast,

there are crystalline frameworks with extrinsic pore, which is a void formed by the alignment of molecules during crystallization. HOFs is a subclass of them.

In this thesis, “frameworks” refers to ordered networks comprising strong and directional intermolecular bonds (coordination, covalent, and hydrogen), and “porous organic frameworks (POFs)” refers to crystalline porous materials with porosity constructed by frameworks, such as MOFs, COFs, and HOFs, unless specified. Tailorable POFs based on organic molecules have been actively studied in the last 30 years, and have realized a various structures and functions. In sections 1.5 to 1.7, The author would like to describe about MOFs, COFs, and HOFs, respectively.

1.5 Metal-organic frameworks (MOFs) / porous coordination polymers (PCPs)

Metal-organic frameworks (MOFs)[147] / porous coordination polymers (PCPs)[148,149] are porous frameworks constructed by self-assembly of metal ions and organic ligands. MOFs/PCPs (referred to MOFs for simplicity unless otherwise noted) are subsets of coordination polymers with porosity. The definition of IUPAC is below[150].

Coordination polymer: “*A coordination compound with repeating coordination entities extending in 1, 2, or 3 dimensions.*”

Coordination network: “*A coordination compound extending, through repeating coordination entities, in 1 dimension, but with cross-links between two or more individual chains, loops, or spiro-links, or a coordination compound extending through repeating coordination entities in 2 or 3 dimensions.*”

Metal-organic framework (MOF): “*metal–organic framework, abbreviated to MOF, is a coordination network with organic ligands containing potential voids.*”

IUPAC recommendations do not include crystallinity as a requirement, and a growing number of non-crystalline MOFs (amorphous MOFs[151–154], MOF liquids[155,156], and MOF glasses[155,157–159]) are starting to construct and challenge their crystalline equivalents[160–162]. Most research in the field of MOFs is placed on the crystalline structure.

In 1997, S. Kitagawa *et al.* reported a 3D framework constructed by coordination bond between Co^{2+} and 4,4'-bipyridine as PCP. It exhibited porous properties, maintaining a stable framework structure after the guest removal and adsorb gas molecules[148]. In 1999, O. M. Yaghi *et al.* reported MOF-5, a structure composed of a three-dimensional network of zinc ions and dicarboxylate ligands, which also exhibited porosity based on gas adsorption measurements[147]. MOFs are synthesized by solvothermal, micro-wave, mechanochemical, and other methods[163–165]. In response to the combined metal clusters with organic ligands, numerous MOFs have been reported[166]. The specific topology can be designed by a secondary building unit (SBU)[167,168] whose components are deduced from the molecular shape and number of bonds in design (Figure 6).

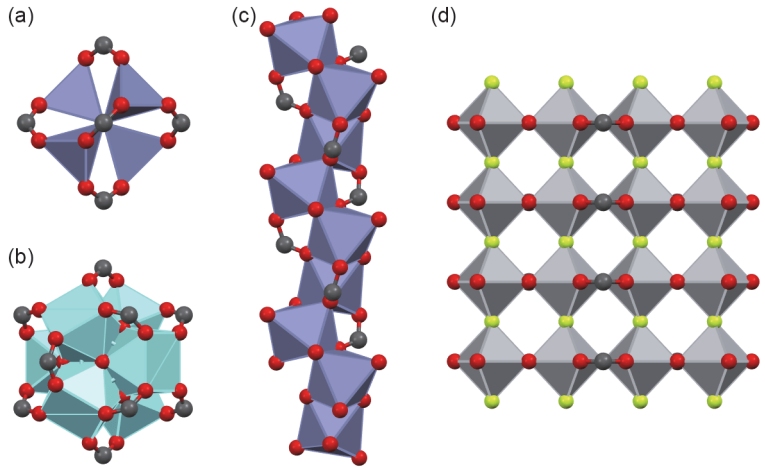

Figure 6. Structures of SBUs. (a) 0D Zn node, (b) 0D Zr node, (c) 1D Zn node, and (d) 2D V node. Dark gray, red, green, purple, cyan, and light gray represent C, O, F, Zn, Zr, and V atoms, respectively.

This crystal engineering approach is proposed as "reticular chemistry"[169]. There are differences in the accuracy of the induced network construction and the avoidance of dense packing due to the strong coordination bond.

The chemical environment in the pore was modified by post- and pre-synthesis construction. There have been active attempts to introduce interaction points with guest molecules, which improves the function as not only storage and separation but also applied properties such as catalytic activity and photophysical properties.

MOFs have a problem with ligand exchange. It is known that MOF-5 transforms to a different form by metal clusters reacting with water[170–172], and that it rapidly progresses and loses its porosity at humidity over 50% at rt[173]. Although this problem depends on the metal species, the design of ligands and metal species makes it possible to maintain porosity under heating conditions in water, strong acids, and bases.

The resulting MOFs have been developed into functional materials. Excellent photoreduction efficiency and activity were achieved by forming appropriately shaped TiO_2 clusters in the vacancies of MIL-101[174]. The novel nitrogen/methane selectivity and nitrogen permanence/flux balance were achieved in Zr-MOFs based on mixed linkers of fumaric acid and mesaconic acid with a pore aperture shape asymmetry[175]. JNU-3a exhibited a novel dynamic molecular sieving with orthogonal arrays, 1D channels with embedded molecular pockets opening to propylene and propane substantially. This MOF can realize high-purity propylene (≥99.5%) in a single adsorption–desorption cycle from an equimolar propylene and propane mixture over a broad range of flow rates[176]. As described above, specific functions are successfully demonstrated by tailorable MOFs.

1.6 Covalent organic frameworks (COFs)

Porous solids without inorganic molecules, such as POPs, have been actively developed. Covalent organic frameworks (COFs) are crystalline POPs composed of 2D or 3D networks of mainly light elements (C, Si, B, O, N, and others). Diverse organic molecules are applied to construct COFs with lightweight and high thermal and chemical stability. That is, COFs are a subset of POPs with crystallinity, porous stability, structural pre-designability, synthetical controllability, and functional manageability.

In 2005, O. M. Yaghi *et al.* reported porous frameworks[177], COF-1 with boroxine moieties obtained by condensation of 1,4-phenyldiboronic acid, and COF-5 with boronic ester synthesized from boronic acid and catechol moiety. To date, it has been reported that COFs are constructed by diverse covalent bonds[178,179]: linear linkages (imine[180], hydrazone, azine[181], vinylene[182,183], ester[184], urea[185], and some others[186–190]), cyclic linkages (boronic ester[177], boroxine[177], dioxine[191], phenazine[192], imide[193], borazine[194], and some others[195–203]), and ionic linkages (spiroborate[204], viologen[205], silicate[206], and some others[207,208]) (Scheme 3).

As with MOFs, the approach of reticular chemistry can be applied to design COFs. It is possible to design constituent molecules possessing a suitable shape, symmetry, and linkage to form COFs with specific topology *via* polymerization. Multiple components permit more diverse and asymmetric topological design[209–211]. Generally, covalent networking often leads to the formation of instinctive polymers, resulting in amorphous solids. Actually, COFs tend to have lower crystallinity than other POFs and have been studied to solve the crystalline problem.

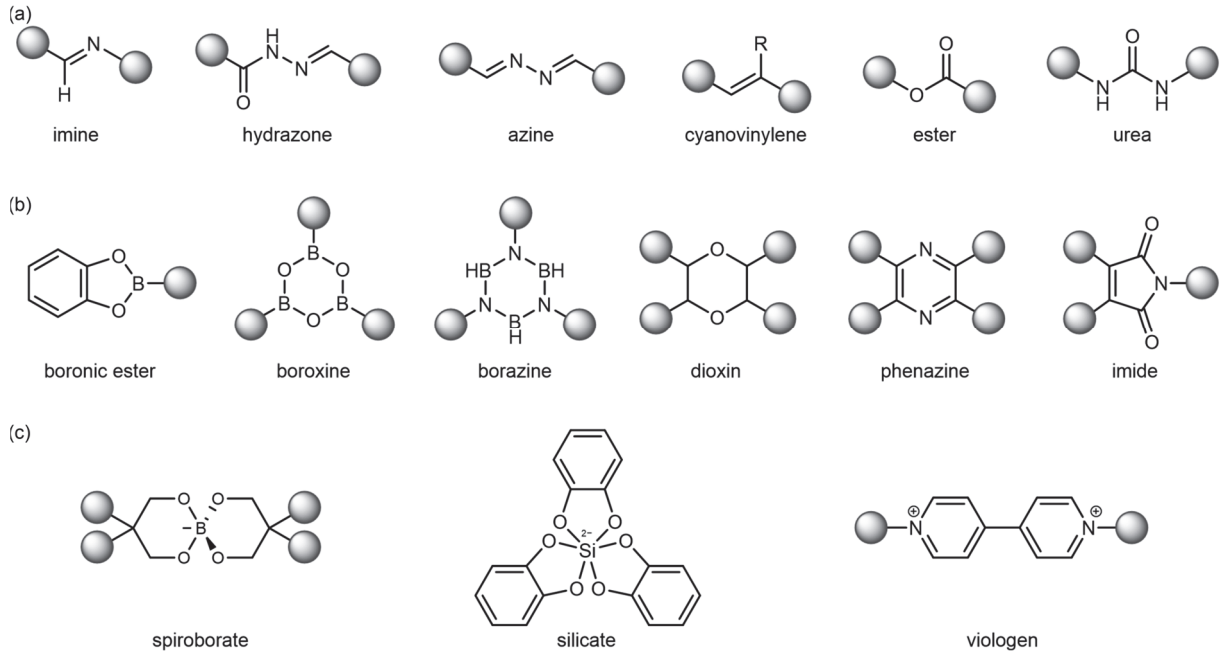

Scheme 3. Representative covalent bonds for COFs. (a) Linear linkages, (b) cyclic linkages, and (c) ionic linkages.

COFs are classified into COFs with reversible bonds and those with irreversible bonds. Reversible bonding provides self-correction (correct-error) during the synthesis process to enhance crystallinity, which is an important factor in minimizing defects and determining optimal porosity. However, COFs based on reversible bond have water-induced cleavage, which makes them unstable under harsh conditions (hot water, acidic, or basic media). This limitation of practical applications has been solved by following strategies. (1) Protection or stabilization of the reaction site by steric hindrance[212,213], additive[214,215], intramolecular H-bonding interaction[216–218], and intermolecular interaction around linkage among layers[219,220], (2) utilization of ionic covalent bonds[204], and (3) tautomerization[221–224]. Post-transformation of linkage from a reversible COF to an irreversible COF has also been conducted to improve the stability[188–202, 224].

On the other hand, irreversible COFs are stable but have problems in crystallinity. In addition to the post-synthesis from reversible COFs mentioned above, there are several strategies to improve crystallinity: (1) highly rigid molecules with few conformational degrees of freedom[226–228], (2) slow reaction[229–233] and addition[234–237] of monomers, and (3) annealing the synthesized COFs[238,239].

Furthermore, the synthesis of single-crystalline COFs has also been reported in several examples: (1) single-crystalline 2D COF with aniline as a modulator to control the crystal growth rate through control of reversible reaction by competing with COF bond formation[230–232], (2) single crystalline 3D COFs crystallized by adding ionic liquids as additive[233], and (3) single-crystalline 2D COFs synthesized by ultra-fast polymerization in supercritical fluid CO_2[240]. As described, COFs that overcome the disadvantages have been achieved.

The resulting COFs have been developed into functional materials. Asymmetric michael reactions were optimized by engineering the amount of catalytically active ligands in COFs through introduction of chiral pyrrolidines *via* click reaction[219]. Highly π-electron delocalized COFs by 8-connected pentiptycene-based D_{2h} building block and 2D conjugated molecules are demonstrated to be lithium-sulfur batteries with good capacities, rate capabilities, and cycling stability[241]. As described above, specific functions are successfully demonstrated by tailorable COFs.

1.7 Hydrogen-bonded organic frameworks (HOFs)

Crystalline porous materials made of constituent molecules networking through H-bonding are termed hydrogen-bonded organic frameworks (HOFs) in analogy to MOFs and COFs[242]. Highly reversible bond results in higher crystallinity than other POFs. HOFs are a subset of PMCs[24–31] focused on H-bonding and permanent porosity. Its structural design is based on a supramolecular synthon, which is directional and facilely predict molecular assembly styles. The framework assembled by H-bonding is named supramolecular organic frameworks (SOFs)[243–245], non-covalent organic frameworks (nCOFs)[246], and porous organic salts (POSs)[247–253], as well as HOFs.

In 1969, Duchampe *et al.* reported the first crystal structure of H-bonded networks, waved honeycomb networks through complementary dimers of 1,3,5-benzenetricarboxylic acid (trimesic acid)[254]. The H-bonding diamondoid network of adamantane-1,3,5,7-tetracarboxylic acid was reported by O. Ermer *et al.* in 1988[255]. It is noted that these structures are nonporous due to interpenetration but pioneering studies of supramolecular networking. H-bonded networks encapsulating guest molecules have been actively reported since the 1990s as inclusion crystals with supramolecular synthons of pyridone[68,130,137,138], resorcinol[139–143], carboxylic acid[120,121], diaminotriazine (DAT) derivatives[122–128], and others[129,131–136]. In 1997, J. D. Wuest *et al.* reported the structure of a tetraphenylmethane derivative with DAT synthons[122] and B. Chen *et al.* reinvestigated its porosity and reported it as **HOF-1** in 2011[242]. **HOF-1** is the first example of permanent porosity and showed adsorption of CO_2 and C_2H_2/C_2H_4 selectivity.

Various HOFs have been constructed to date through H-bonds such as DAT, carboxylic acid, and others. Details are described in the following sections (1.7.1 to 15). Features of HOFs are described as follows, which are similar to PMCs[29].

(1) High crystallinity. We can yield the crystals with large domain *via* facile solvent-process as recrystallization, and crystalline balks *via* mechanochemical process.
(2) Re-usability. We can re-use and re-generate HOFs *via* solvent process as re-dissolution.
(3) Structural flexibility. It is realized by weak and reversible non-covalent bonds.
(4) Structural diversity. Since H-bond is not dominant in structure formation, we expect to build porous structures not realized with other POFs.

On the other hand, structural flexibility and diversity are also disadvantages with respect to structural stability and designability. H-bonds are weak bonds compared to coordination bonds and covalent bonds[33]. Therefore, unlike frameworks based on reticular chemistry (COFs and MOFs), the stability of the porous structure is low because the removal of the inclusion molecule frequently causes structural transition and consequent collapsing of its structure to lose porosity. The weakness of H-bonding sometimes causes the formation of an unexpected H-bond and the penetration of solvent molecules, resulting in the formation of a diverse porous structure. Furthermore, the same frameworks as the initially designed do not always form, and unexpected structure sometimes forms. This unpredictability makes the designability of HOFs poor.

However, some designs have been developed to overcome the issues. One uses an electrostatic force, and the other uses an orthogonal interaction to H-bonding by rigid core skeletons[256] (Figure 7). These designs stabilized the structure by existing bonds and additional bonds, respectively. Former HOFs were

networked by charge-assisted H-bonding, which is stronger than neutral H-bond and found in various salt: ammonium sulfonate, guanidinium sulfonate, amidinium carboxylate, and others. Latter HOFs were assembled by π-π stacking, which is predictable and constructed by biphenyl, pyrene, C_3-symmetric π-conjugated molecules (C_3PI) such as hexaazatriphenylene (HAT), and others. They exhibited persistent porosity and stability against heat, solvent removal, and solvent soaking. While there are still challenges, the construction to overcome the shortcomings is undergoing.

There are functional HOFs in different fields, including separation[257–262], adsorption, proton conductivity, electron conductivity[263,264], sensing and fluorescence detection[265–267], catalyst, electrocatalyst, photocatalyst[268,269], energy storage[270,271], optical material[272], and biomedical materials[273–275].

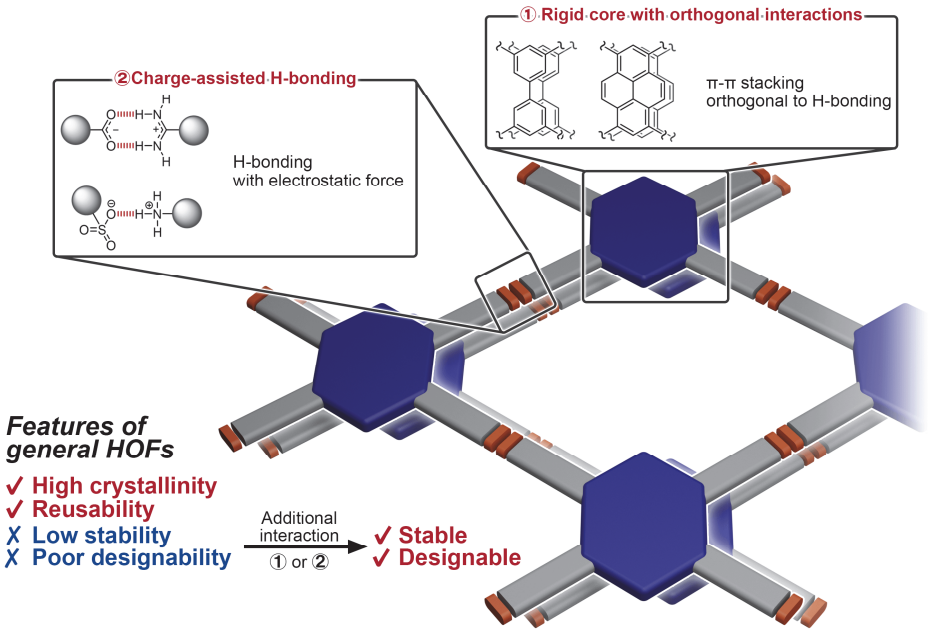

Figure 7. Design of stable and designable HOFs, which is constructed through orthogonal interactions of rigid core and charge-assisted H-bonding.

1.7.1 Carboxylic acid

Carboxylic acid possesses the carbonyl group (H-bond acceptor) and the hydroxy group (H-bond donor). This group forms some supramolecular synthons (Scheme 4a–c). It can be easily synthesized by hydrolyzing the precursor possessing carboxylic acid esters or cyano groups into the backbone. Due to its high directivity (linearity) of H-bonding (Scheme 4a), there has been numerous HOF construction. In general, the design of HOFs is based on forming a complementary dimer (Scheme 4a) because of the high probability[276,277]. For example, planar tricarboxylic acid derivatives form honeycomb networks, and planar tetracarboxylic acid derivatives form chicken wire networks (Scheme 4d,e). Naturally, open H-bonding or truncated H-bonding (Scheme 4b,c) and solvent penetration also occur depending on the molecular and crystallization conditions.

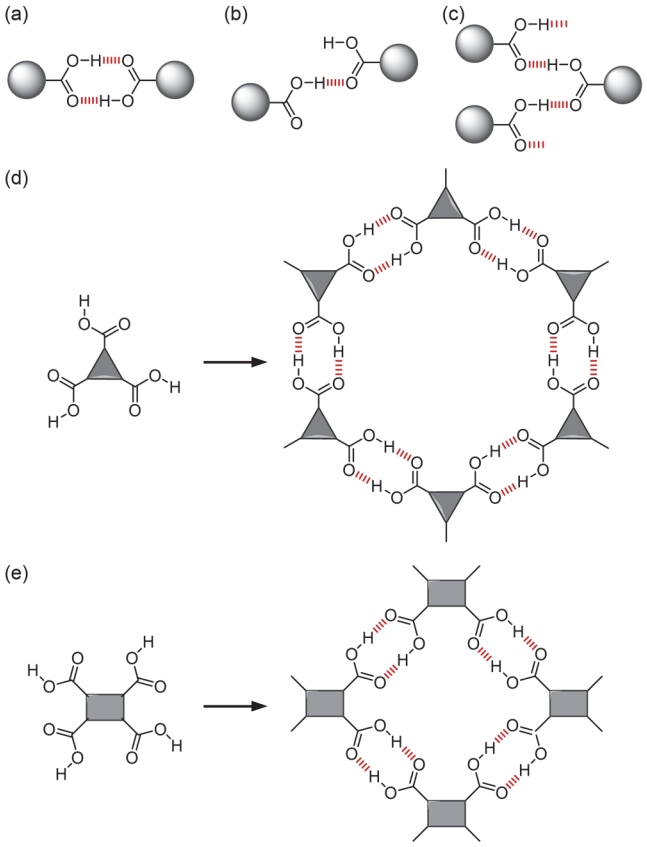

Scheme 4. Three types of H-bonding motif. (a) Complementary dimer, (b) truncated dimer, and (c) ladder-like chain bonding of carboxylic acids. (d) Honeycomb network based on complementary dimers of planar tricarboxylic acid. (e) Chicken-wire network based on complementary dimers of planar tetracarboxylic acid.

1.7.2 2,6-Diamino-1,3,5-triazine (DAT)

2,6-Diamino-1,3,5-triazine (DAT) has two amino groups, whose H-N_{amine} atoms act as H-bond donors, and three N atoms in triazine as H-bond acceptors. Since a DAT group has multiple donors and acceptors, they can form various types of H-bonding. Three examples of H-bonding dimers, “front-front”, “edge-edge”, and “front-edge” are shown in Scheme 5. These supramolecular synthons are combined to form chain H-bonds (Scheme 5d) and other H-bonding styles[122–128]. This system indicates lower directivity than carboxylic acids and is suitable for constructing diverse structures.

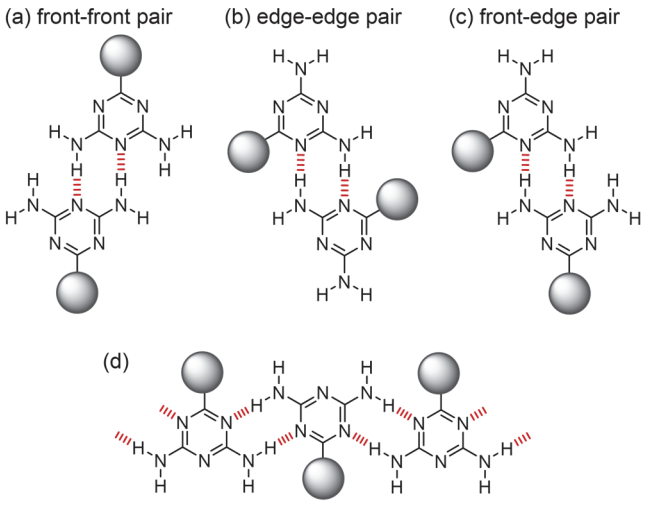

Scheme 5. Three possible H-bonding motifs of DAT: (a) front-front, (b) edge-edge, and (c) front-edge pair. (d) 1D Chain H-bonding of edge-edge type motif in HOF-5.

1.7.3 Pyrazole

Pyrazoles have N atoms as H-bond acceptors and H-$N_{pyrazole}$ as H-bond donors adjacent to each other. The triangular motif is applied to constructing porous HOF, and the others: a C_{2h} symmetric dimer and C_{4h} symmetric tetramer (Scheme 6a,c) were shown in nonporous structures[246,278–280].

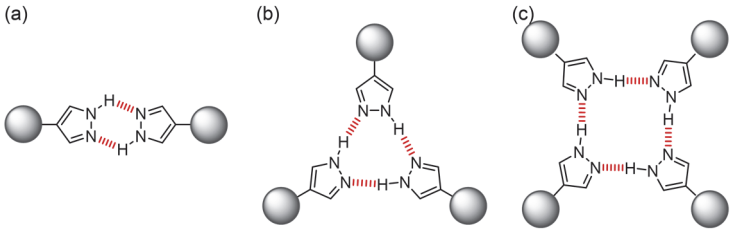

Scheme 6. Chemical structures of H-bonding motif. (a) Dimer, (b) trimer, and (c) tetramer.

1.7.4 Urea

Urea has one carbonyl group as H-bond acceptor and two N_{amide} hydrogen atoms as H-bond donor. Because the $O_{carbonyl}$ atom has two lone pairs, it interacts with two hydrogens to form a one-dimensional chain H-bond as shown in Scheme 7.

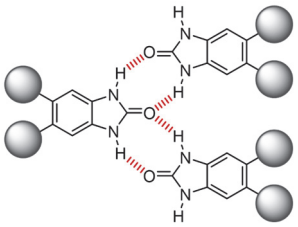

Scheme 7. Chemical structures of H-bonding motif, 1D chain of urea.

1.7.5 G-quadruplex

This is a bio-inspired supramolecular synthon, G-quartets (Scheme 8a), which is square planar tetramer formed by four guanines association through Hoogsteen H-bonding[281]. Rod-like aromatic molecules (Scheme 8b) with two guanines introduced at each end assemble to form a porous HOF with stacked chicken wire networks. Similar structures have been obtained with modified aromatic moieties, and these HOFs are used for applications such as charge transfer and photocatalysis.

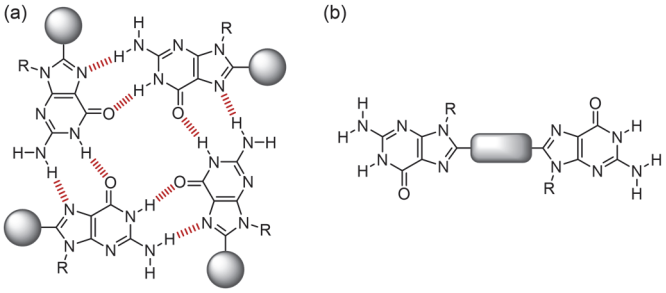

Scheme 8. Chemical structures of (a) H-bonding motif of four guanines to form G-quadraplex and (b) rod-like tecton with two guanines.

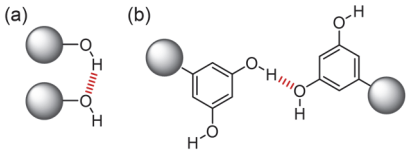

Scheme 9. Chemical structures of H-bonding motif between (a) hydroxyl groups and (b) resorcinols.

1.7.6 Hydroxy group

H-bonding between hydroxyl groups is common interaction. This bond is not highly directional, but is used with multiple or other interactions. This simple moiety was introduced into the skeleton such as resorcinol (Scheme 9b), and several networks had been reported over the years[139–143,282].

1.7.7 Cyano group

This has an N atom as H-bond acceptor, which interacts with other H-bond donors. The supramolecular synthon (Scheme 10) has no directionality to construct flexible HOFs with other weak non-covalent interactions.

Scheme 10. Chemical structures of H-bonding motif between H-C_{Ar} and cyano group.

1.7.8 Pyridine

An N atom as H-bond acceptor interact with H-bond donor of other molecules. (Scheme 11a) HOF construction *via* H-C_{Ar}[272], and H-N_{amide}[283] has been reported. The structure based on H-C_{Ar} is a flexible porous structure due to particularly fragile H-C_{Ar} interactions. On the other hand, the structure based on H-N_{amide} is a stable HOF, whose tetramer (Scheme 11b) maintains the original structure of the HOF up to 350 °C.

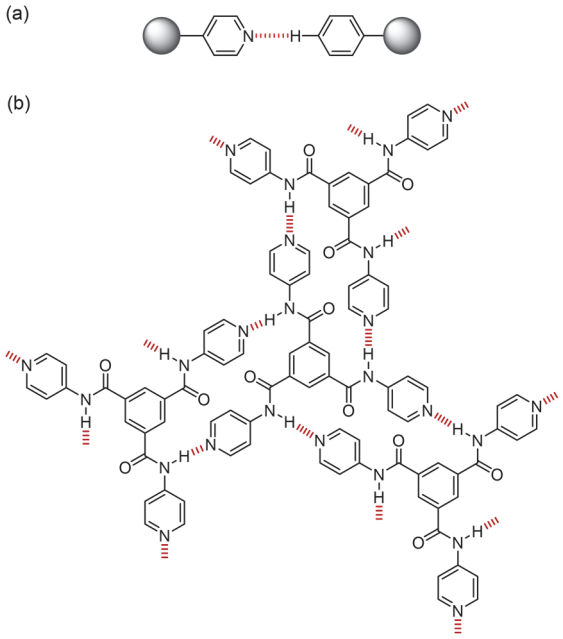

Scheme 11. Chemical structures of (a) H-bonding motif between H-C_{Ar} and pyridine and (b) tetramer of H-N_{amide} and pyridine.

1.7.9 Ammonium carboxylate

This is a salt possessing one $O_{carboxylate}$ as H-bond acceptor and three $H_{ammonium}$ as H-bond donors (Scheme 12). Considering H-bonding by one pair, it is not highly directional since it can interact from various directions. Neutral H-bonds sometimes are formed depending on the combination of carboxylic acid and amine.

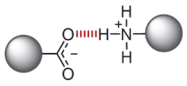

Scheme 12. Chemical structures of H-bonding motif of ammonium carboxylate.

1.7.10 Ammonium sulfonate

This is a charge-assisted H-bonding between $O_{sulfonate}$ as acceptor and H-$N_{ammonium}$ as donor. (Scheme 13a) The sulfonates interact with an amine in multiple directions, resulting this bond is generally less directional. When a sterically hindered primary amine such as a tritylamine are applied, [4+4] tetrahedral-shaped clusters are formed (Scheme 13b). The

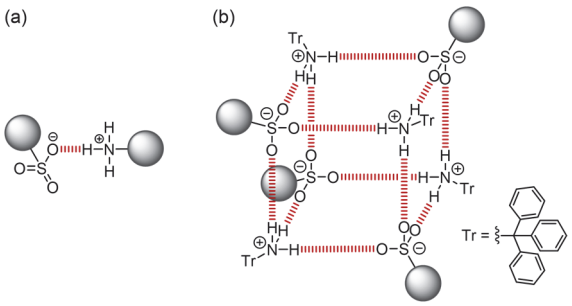

Scheme 13. Chemical structures of H-bonding motif of ammonium sulfonate between (a) two molecules and (b) four sulfonates and four ammoniums with bulky substitution as trityl group to form a [4+4] tetrahedral-shaped supramolecular cluster.

diamondoid networks resulting from this cluster are designable and systematically constructed as *d*-POSs[247–253].

1.7.11 Amidinium carboxylate

Amidinium carboxylate forms several H-bonding motifs (Scheme 14). The carboxylate acts as H-bond acceptor, and the amidinium cation acts as H-bond donor. This can form rigid charge-assisted H-bonding *via* complementary dimer (Scheme 14a), and also form a truncated dimer (Scheme 14b). Both bonding motifs are linear and highly directional, and can yield a pre-designed network. Various diamondoid networks are constructed by combining tetrahedral and linear tectons[284].

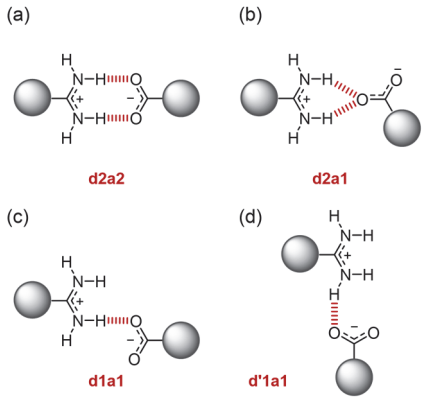

Scheme 14. Chemical structures of amidinium carboxylate H-bonding motif. (a) Complementary dimer and (b–d) truncated dimer.

1.7.12 Guanidium sulfonate

This salt forms several H-bonds between H-$N_{guanidinium}$ as H-bond donor and $O_{sulfonate}$ as H-bond acceptor. This pair can form a complementary dimer shown in Scheme 15a. This enables the formation of [3+3] hexagonal clusters and [2+2] square clusters (Scheme 15b,c). The pore is constructed by polysulfonate derivatives[285–293]; for example, sandwich-types pore have been constructed by disulfonate derivatives[285,288].

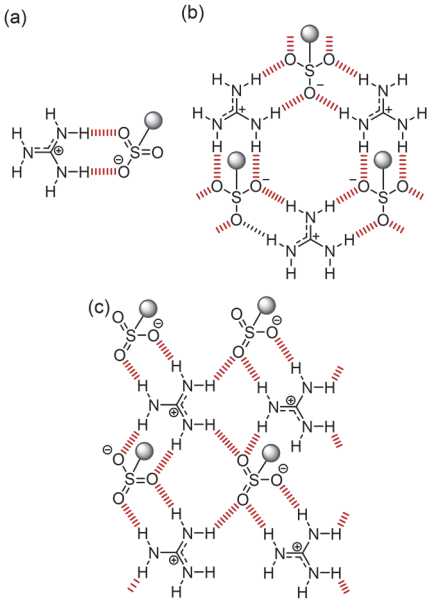

Scheme 15. Chemical structures of H-bonding motif between (a) two molecules. (b) [3+3] Cluster to form a hexagonal cycle and (c) [2+2] Cluster to form a square cycle.

1.7.13 Pyridinium carboxylate

This is a salt of pyridine and carboxylic acid (Scheme 16). It formed H-bonding between $O_{carboxylate}$ and H-$N_{pyridinium}$. In some cases of compounds, no salt forms and interactions occur between H-$O_{carboxylic\ acid}$ and $N_{pyridine}$.

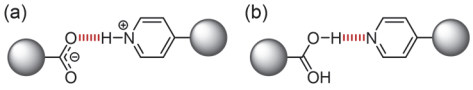

Scheme 16. Chemical structures of H-bonding motifs between (a) pyridinium and carboxylate and (b) pyridine and carboxylic acid.

1.7.14 Other H-bondings

Other neutral H-bonding motifs are shown in Scheme 17. Phosphonate derivatives[294] form H-bonding with themselves. This is not charge-assisted H-bonding because it is an anion-anion rather than an anion/cation pair. In crystals, it forms three types of H-bonds (Scheme 17a–c). As neutral molecules, 2-amino-1,3,5-triazine[295], 3-amino-1,2,4-triazole[270], acetyl groups[296] are reported. 2-Amino-1,3,5-triazine has two N_{Ar} atoms in triazine as H-bond acceptors and two H-N_{amino} atoms as H-bond donors. It forms a 1D chain-like bonding (Scheme 17b) similar to Urea (section 1.7.4).

3-Amino-1,2,4-triazole has two N_{Ar} as acceptor and two H-N_{amino} and one H-N_{Ar} as donor (Scheme 17c). This forms a complex network with carbonyl groups of tecton moieties. Acetyl groups exhibit the weak and less directional H-bonding between $O_{carbonyl}$ and H-C_{α} (Scheme 17d). Weak H-bonds are generally used with other interactions such as π-π stacking.

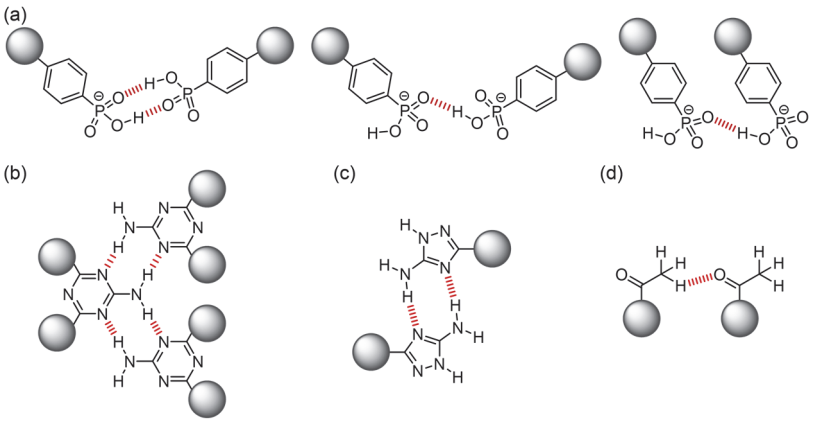

Scheme 17. Chemical structures of H-bonding motifs. (a) Dimeric, and (b,c) monomeric H-bonding between phosphonate salts. (d) 2-Anino-1,3,5-triazine, (e) 3,5-diamino-1,2,4-triazole, and (f) acetyl group.

1.7.15 Other charge-assisted H-bondings

Other supramolecular synthons of charge-assisted H-bonding motif, pyridinium carboxylate[297–300], pyridinium dihydrogenphosphonate[266], pyridinium sulfonate[301], amidinium sulfonate[302], and diaminotriadinium sulfonate[266] are reported (Scheme 18). Imidazolium carboxylate and imidazolium sulfonate (Scheme 18a,b) formed the 2D[303] and 3D[304] network, respectively. These acid anions were connected by imidazolium. Amidinium sulfonate, and diaminotriazinium sulfonate formed dimers (Scheme 18c,f) similar to amidinium sulfonate (section 1.7.11). Pyridinium dihydrogenphosphonate[266], pyridinium sulfonate[301] had the same interaction as pyridinium carboxylate (section 1.7.13) between O and H-$N_{pyridine}$. There is an unexpected interaction between two dihydrogenphosphonates in the former crystal.

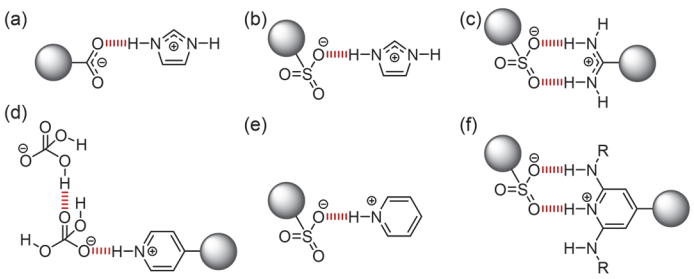

Scheme 18. Chemical structures of H-bonding motifs. (a) Imidazolium carboxylate, (b) imidazolium sulfonate, (c) amidinium sulfonate, (d) pyridinium dihydrogenphosphate, (e) pyridinium sulfonate, and (f) diaminotriazinium sulfonate.

1.8 Systematic construction of isostructural crystalline POFs

The crystalline POFs (MOFs, COFs, and HOFs) are the focus of much attention to systematically constructing a wide variety of structures through crystal engineering and reticular chemistry approaches. Based on the various topological structures modified by molecular design, their isostructures are constructed, allowing a wide variety of porous structures to be realized. The construction principle for the systematic construction of diverse and isostructural porous structures is shown in Figure 8. The constituent molecules are theoretically innumerable. There are also a huge number of topological networks formed by combining components, and then many whole porous structures are obtained by assembling them through interactions. Each component is defined as follows.

(1) A constituent unit consists of a molecular skeleton and bonding motifs, which lead to supramolecular synthon and tecton, respectively. They are classified as shape and connecting numbers: 2-connected (2-*c*) units; liner, bent, zigzag, twisted. 3-*c* units; various triangles, 4-*c* units; square, rectangle, tetrahedron, and 6-*c* units; regular hexagon, distorted hexagon, octahedron.

(2) A topological network consists of networking of constituent units through each bonding: coordination, covalent, hydrogen, halogen, and other bonds.

(3) A whole porous structure consists of assembling of the topological network through interpenetration, stacking, non-assembling, interwoven, and other accumulations.

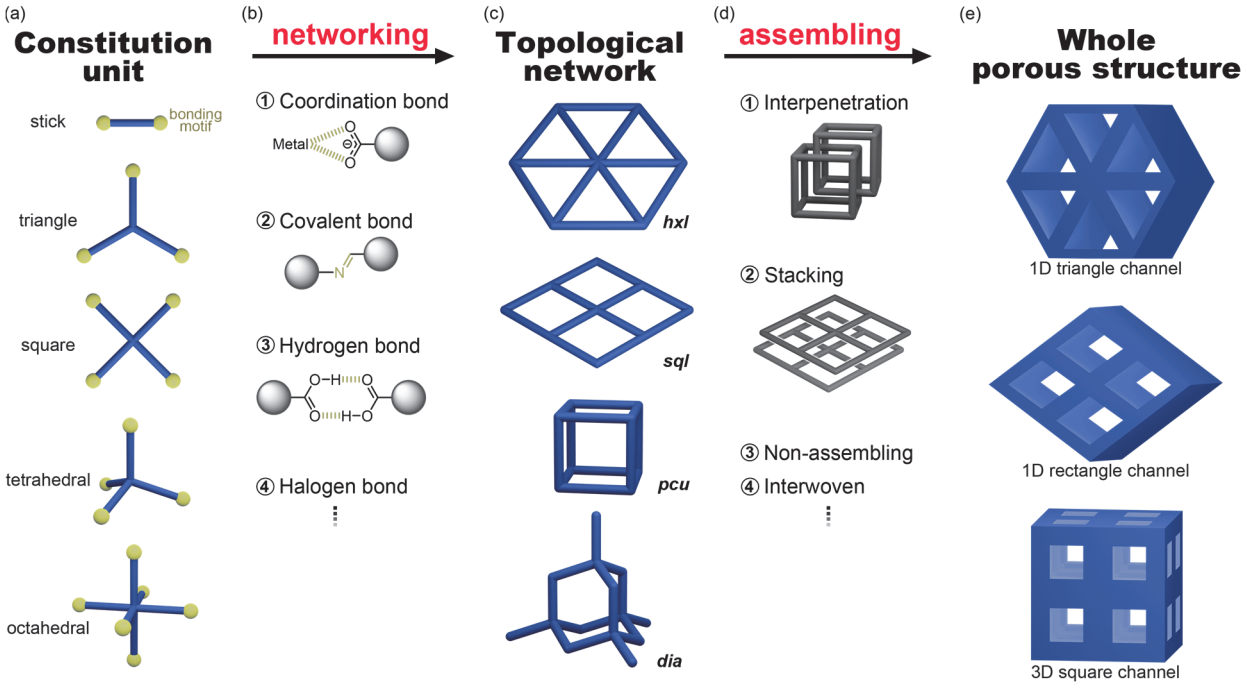

Figure 8. Design principle of systematically hierarchical constructing porous organic frameworks. (a) Shapes of constitution unit, (b) networking through each bonding, (c) representative topological networks: ***hxl***, ***sql***, ***pcu***, and ***dia***, (d) assembling manners, and (e) models of whole porous structures.

Networking and assembling are determined by the constitution unit and external factors (crystallization solvent, speed, temperature, and other conditions). The design of the constituent molecules is derived from the supramolecular synthon, while the external factors are determined by the chaotic conditions of the entire system (stable or metastable, and thermodynamic or kinetic process depending on a respective system). Therefore, it is often observed that different networking by analogs and assembly by homotypic networks through specific networking result in different whole structures. It is essential to explore the correlation among molecular design, construction conditions, and the resulting overall structure. Systematic construction based on appropriate design principles is necessary to freely construct porous materials with desired structures and functions. Especially there is a systematic construction method to develop structures with the same structural framework or topology from organic molecules with similar skeletons (or ligands with the same topology). In other words, different porous structures can be formed while maintaining the topology/connection or structure of the original porous structure. These frameworks are called ”isostructural” or ”Isoreticular”.

In online dictionary of crystallography of IUCr[305], it defined as “*Two crystals are said to be isostructural if they have the same structure, but not necessarily the same cell dimensions nor the same chemical composition, and with a 'comparable' variability in the atomic coordinates to that of the cell dimensions and chemical composition. For instance, calcite $CaCO_3$, sodium nitrate $NaNO_3$ and iron borate $FeBO_3$ are isostructural. One also speaks of* isostructural series*, or of isostructural polymorphs or isostructural phase transitions. The term* ***isotypic*** *is synonymous with isostructural.*”

In section 3.3.8.6. of “twinning of isostructural crystals of international tables for crystallography”, volume D[306], It defined as ”The crystals in each series have the same (or closely related) structure, space group, lattice type and lattice coincidences.” and the following examples are given. (1) Quartz (SiO_2), quartz-homotypic gallium phosphate ($GaPO_4$) and benzil [$(C_6H_5CO)_2$, so-called ‘organic quartz’] crystallize under normal conditions. (2) Iron borate $FeBO_3$, calcite $CaCO_3$, and sodium nitrate $NaNO_3$ crystallize under normal conditions. (3) series of crystals with the sodium chloride structure (AgCl, AgBr, PbS, NaCl, and LiF).

A term of “isoreticular” was proposed by O. M. Yaghi *et al.*[307] for “having the same network topology” and coined from "iso" + "reticular”.

Isostructural means the same arrangement and includes no topology, while isoreticular is defined by topology and includes no arrangement, but these terms are applied in roughly the same sense.

It is important in reticular chemistry to construct isostructural frameworks as it leads to the systematically constructing not one-of-a-kind but tailorable POFs. The following sections (1.8.2 to 1.8.4) describes designs and examples of isostructural construction undertaken in MOFs, COFs, and HOFs.

1.8.1 Topological network

The constructed porous frameworks are classified by topology, which is described according to the naming rules. Originally described by Wells, it is now mainly denoted by vertex, point, or face symbol notation[308]. The definition of this topology or structure type is based on the concept of node and edge, where molecules (nodes) are connected by chemical bonds (edges), producing periodic and infinite graphs. In particular, Yaghi *et al.* developed a topological symbol consisting of three letters in the early 2000s that is widely used in current reticular chemistry. A simple network is exemplified by a hexagonal network: ***hxl***, a chicken wire network: ***sql***, a cubic network: ***pcu***, and a diamondoid network: ***dia*** (Figure 8c). Databases have been developed to classify these networks [Reticular Chemistry Structure Resource (RCSR)[309,310] and ToposPro database[311–314]].

The rational design of POFs structures in light of the specific topology is conducted through the following procedure. First, the vertex and edge types are identified based on the desired topology. Then the geometry of the building units derives the chemical equivalents, which are appropriately selected to be networked into isostructural POFs. This is a systematic concept aimed at achieving the construction of the desired structure by rational structural design with an arrangement of a symmetrical topology.

1.8.2 MOFs

MOFs are composed of metal clusters and organic ligands, which are connected by coordination bond. Frameworks with the desired topology are systematically obtained by designing the connecting number and shape of node. The suitable reaction conditions[315] and pre-synthesized SBUs[167] allowed combinations of metal clusters and ligands that were impossible to obtain by conventional synthetic methods. Further diverse isostructural MOFs were realized and actively constructed into applications[316]. Ligands are designed by shape in Figure 8, and metal clusters are designed by tertiary building unit (TBU)[317] in addition to SBU, which are 0D[147], 1D[318], 2D[319], and 3D[320].

In 2005, O. M. Yaghi *et al.* first reported that isostructural construction in ***pcu***-topological MOFs. These MOFs with zinc carboxylate clusters were named isoreticular MOFs (IRMOFs), which were systematically constructed with different dicarboxylate ligands[307]. In a series of isostructural MOFs with 1D SBU units linked by disalicylate derivatives, the ligands with eleven phenylene length yielded hugest pore to the author's best knowledge with apertures of 85 × 98 Å, which can include even a green fluorescent protein (GFP)[321]. Moreover, isostructural MOFs not previously available were constructed through engineering the pre-synthesized SBU units[322,323].

A series of switchable MOFs were constructed by ligands, bis(9H-carbazole-3,6-dicarboxylate)aryl moieties, which is elongated from phenylene to quaterphenylene. One of these MOFs, **DUT-49**, is reported to show negative gas absorption to methane[324]. Different metal cations (Cu^{2+} and Zn^{2+}) and counter anions (SiF_6^{2-}, GeF_6^{2-}, and NbF_6^{2-}) were used to construct isostructural MOFs with fine pore difference to improve

CO_2/C_2H_2 separation selectivity[325]. Isostructural phosphate chiral MOFs with 16 different metal clusters were constructed to tune chemical durability and Lewis acidity. They provide a versatile family of heterogeneous catalysts for asymmetric reaction with good enantioselectivity[326]. The isostructural construction and associated functional tuning have been actively conducted, followed by further systematic construction (defect, *de novo* synthesis) to construct diverse MOFs.

1.8.3 COFs

COFs are composed of organic molecules, which are connected by a covalent bond. COFs with desired topology are systematically obtained by designing the connecting number and shape of constituents[40,327,328]. There are fewer topologies than MOFs, because there are fewer possible shapes for organic molecules than those for metal and SBU nodes. Systematic constructions of isostructural COFs are achieved by pre-synthetic and post-synthetic methods.

Specifically, isostructural COFs with different molecular length[329–331], substitution[332,333], and arrangement[334–336] are constructed. At the same time, functional optimization based on isostructural COFs had also been performed. As example of molecular length, isostructural COFs with pores ranging from 4 nm up to 10 nm have been reported by optimizing interlayer interactions in imine-linkage COFs[329,330]. This huge pore encapsulated proteins. As example of molecular substitutions, isostructural COFs were synthesized by pre-synthesized organic molecules with various chiral amines. They acted as chiral heterogenous catalysts with excellent enantioselectivity and yield[332]. Electrochemiluminescence (ECL) luminophores with various wavelengths was constructed by controlling conjugation and donor-acceptor interactions to adjust HOMO-LUMO levels[333]. In optimized isostructural photoactive COFs, the redox reaction of poly(vinylcyclopropanes) by radical ring-opening polymerization showed excellent efficiency with controlled molecular weight, low dispersity, and high linear/cycle selectivity[331]. The isostructural construction of COFs as well as MOFs and the resulting functional tuning is actively progressing.

1.8.4 HOFs

The molecular shape and the number of the H-bonding roughly determine the network topology of the HOF. The diversity of H-bonds often results in different assembly patterns as designed, so the topology is more difficult to predict than other POFs. Highly directional binding motifs facilitate the design. However, there are a few examples of isomorphic construction due to the significant influence of structural modification.

The HOF components can be divided into three parts (Figure 9). The core structure, which is the main

moiety of tecton and specifies the shape and assembling style, and the H-bonding motif are connected by the spacer, which is classified as tecton. Although crystal engineering approaches realize the homotypic networks by modifying the core, it is still challenging to construct isostructural HOFs with the same assembling because the assembly of these networks is largely dependent on the molecules. For example, in the system of 2D-HOFs of C_3-symmetric π-conjugated molecules (C_3PI) as cores, homotypic hexagonal networks (HexNet) were obtained by networking with carboxylic acid dimers. However, the stacking of HexNet had different layer offsets and patterns (AB or ABC stacking). There are many examples of constructing homotypic networks, but their networks are assembled by different stacking or interpenetrations to form isomeric HOFs. It is also difficult to design spacers, resulting in a few examples of homotypic networks and isostructural HOFs. The reason is that additional efforts are needed to stabilize the expanded porous structure. The homotypic or isomeric networks and their assembling results obtained by analogs are shown following subsections for each molecular shape and supramolecular synthon; **A.** Carboxylic acid, **B.** Diaminotriazine (DAT), **C.** Pyrazole, **D.** Urea, **E.** Amidinium carboxylate, **F.** Ammonium carboxylate, **G.** Ammonium sulfonate, and **H.** Pyridinium carboxylate.

A. Carboxylic acid

Numerous HOFs have been reported due to the formation of highly directional complementary dimers. The examples of HOF constructions by analogs, divided by the number of tritopic, tetratopic, hexatopic carboxylic acids, and some others are presented in the following: **A-1** to **A-4**.

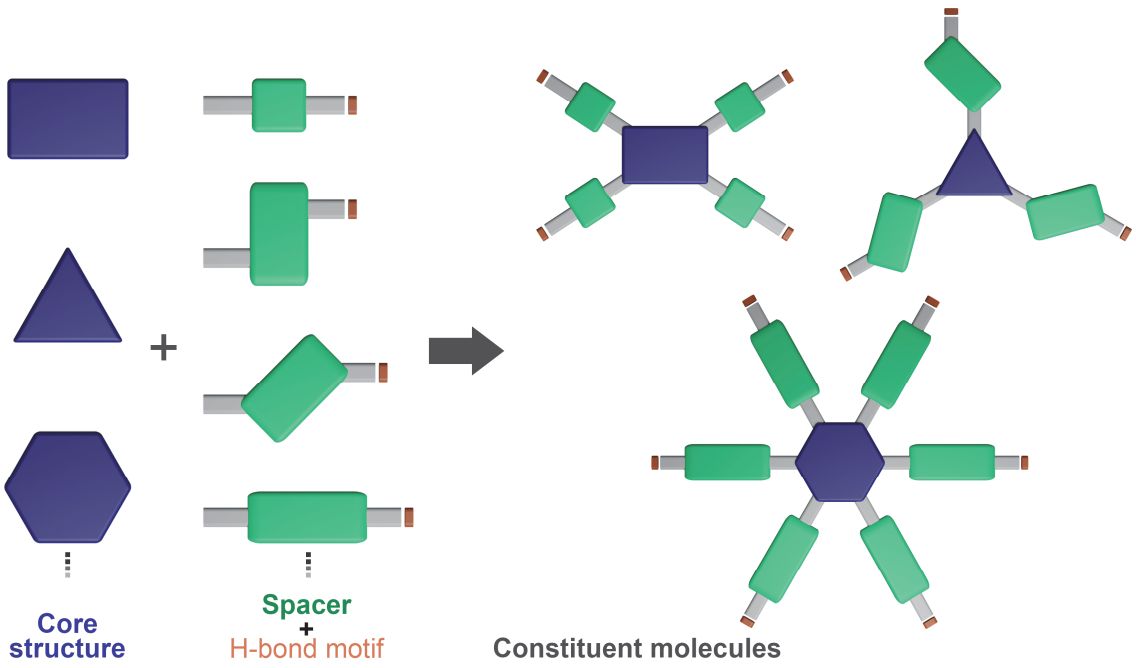

Figure 9. Design of HOFs. Three building parts – core structures (left), spacers, and H-bond motifs (middle) – combine to form the constituent molecules (right).

A-1. Tricarboxylic acid

As tritopic carboxylic acid tecton, trimesic acid[337,338], tris(4-carboxyphenyl)amine[258,339,340], 2,4,6-tris(4-carboxyphenyl)-1,3,5-triazine[341], 2,5,8-tris(4-carboxyphenyl)heptazine[342], and 1,3,5-tris(4-carboxyphenyl)benzene analogues[343–347] are reported (Scheme 19). These C_3-symmetric planar molecules form ***hcb*** network, assembled by π-interaction to construct non-interpenetrated or interpenetrated structure. Some cores can control the assembling, but examples were limited.

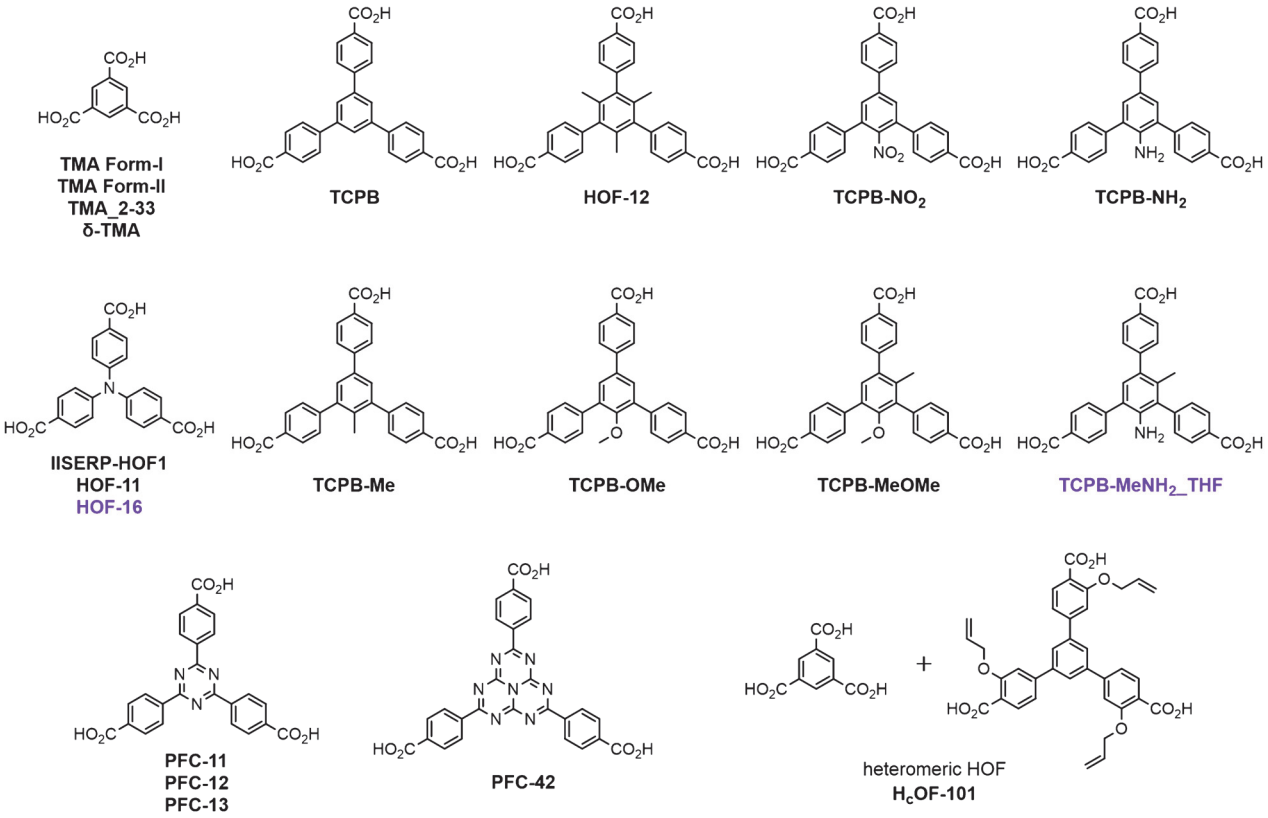

Scheme 19. Chemical structures of tricarboxylic acid tecton and obtained HOFs. HOFs in black denotes the complementary dimer motif, and the purple one denotes H-bonding with solvent.

A non-porous structure of trimesic acid was well known to consist of interpenetrated hexagonal networks connected through dimerization of carboxy groups. By screening the recrystallization conditions, a porous structure with a 1D channel assembled by AB stacking, **TMA Form II**, has been constructed (Figure 10a)[338]. G. M. Day, A. I. Cooper, *et al.* have discovered a new 'hidden' porous polymorph through crystal structure prediction (CSP) with a robotic crystallization screen[337]. One of the polymorphs, **TMA_2-33** are non-interpenetrated ABC stacking structure, which is the same as **TMA Form II** with only a slight difference in the lattice. Its activated form, **δ-TMA** are tilted stacking structure (Figure 10b). Both are different from **TMA Form II.**

Two HOFs formed by the carboxylic acid dimer of tris(4-carboxyphenyl)amine (TCPA) structures have been reported, **IISERP-HOF1**[339] and **HOF-11**[340], which are the same structure (Figure 11). The lattice is slightly different depending on the crystallization conditions (acetic acid at 150 °C and THF at r.t., respectively). Both are porous structures with 1D channels by 11-folded interpenetrated **(10,3)-b** topological networks. Meanwhile, a structure with a free carboxylic acid, **HOF-16**, has also been reported[258]. This pseudo-polymorph is an example of functionalization that takes advantage of the weakness of H-bonds and is simultaneously an example of the difficulty of isostructural construction.

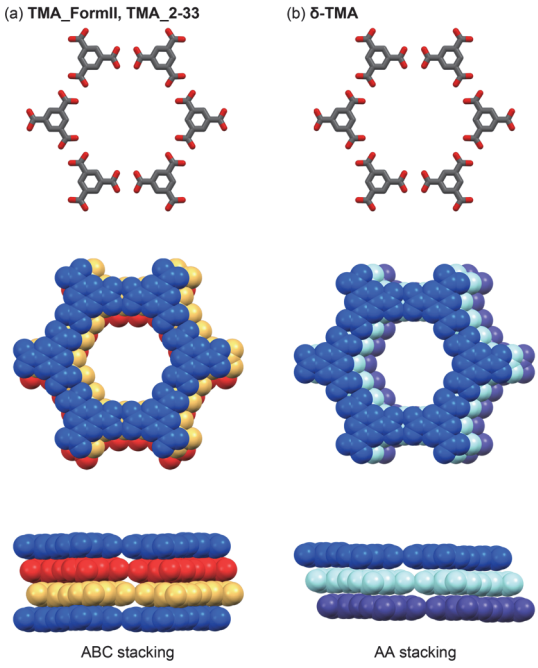

Figure 10. Crystal structures of (a) **TMA FormII** and **TMA_2-33**, and (b) **δ-TMA**. (Top) Hexagonal network, assembling viewed (middle) down, and (bottom) side.

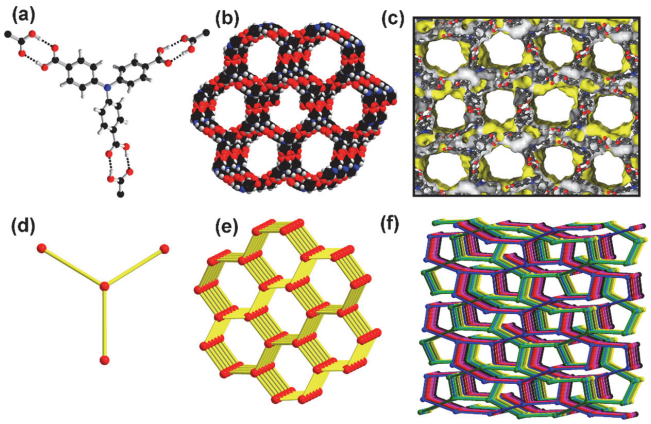

Figure 11. Crystal structures of **HOF-11** showing (a) a constituent and H-bonding interactions between neighboring carboxylate groups from different modules (carbon: black; hydrogen: white; nitrogen: blue); (b) a three-dimensional (3D) H-bonded supramolecular network; (c) packing diagrams of **HOF-11** along the [010] direction; (d) a constituent was regarded as a 3-connected node; (e) a (10,3)-b topology; and (f) a 3D interpenetrated topological networks along the [010] direction (different colors represent different networks). (Reproduced permission from ref. 340, copyright 2017 American Chemical Society.)

Many HOFs have been reported for tris(4-carboxyphenyl)benzene and its analogs (Figures 12 and 14). Homotypic ***hcb*** networks through H-bonding dimer were obtained from the cores: methyl-, trimethyl-, methoxy-, methoxy- and methyl-, amino-, and nitro-substituted benzene derivatives except for the solvent penetration ***hcb*** network of **TCPB-MeNH$_2$_THF** (Figure 12e top). However, the assembling manner is different depending on the functional group. They were categorized into four distinct assemblies: simple stacking, single-layer offset interpenetration, double-layer offset interpenetration, and rotated-layer interpenetration. Only **TCPB-OMe** formed simple stacking, non-interpenetrated assembly (Figure 12a). **TCPB-Me**, **HOF-12**, **TCPB-MeOMe**, and **TCPB-MeNH$_2$_THF** belong to single-layer offset interpenetration, which is the most common assembling among the tritopic carboxylic acid tecton (Figure 12c–e). The parallel layers are slipped along each other, leading to a gap where one layer can interpenetrate. **TCPB-NO$_2$** forms double-layer offset interpenetration, which has a gap where two layers can interpenetrate (Figure 12f). **TCPB** and **TCPB-NH$_2$** form rotated-layer interpenetration. This assembling is a two-axis interpenetration of specific layer-stacked networks, which are classified into two distinct layers (A and B layers of simple stacking hexagonal sheet). The B layer is a rotated layer of simple stacking hexagonal sheet. The B layer is rotated by 60° toward the A layer. The number of layers varies depending on the constituent molecules (**TCBP**: three and four layers, **TCBP-NH$_2$**: three and three layers) (Figure 13).

In HOFs with complementary dimers, **H$_c$OF-101** obtained by co-crystallization of trimesic acid and *o*-alkoxycarboxylic acid derivatives is the only example of heteromeric HOFs[347]. There are also examples where carboxylic acid dimers are formed but do not construct plane ***hcb*** sheets. In the case of 1,3,5-triazine core structure, networks are undulated and parallel polycatenated, resulting in intricate crisscrossed 3D porous structure (Figure 14)[341]. Other examples were reported in the polymorphism of the interpenetrated structure of trimesic acid[338] described above. As a further example, 2,5,8-tris(4-carboxyphenyl)heptazine did not construct a ***hcb*** network[342].

Of course, the above molecules may construct isostructural HOFs by CSP or crystallization screening. However, H-bonds are not strong enough to dominate the system compared to π-interactions and dispersion forces, resulting in a wide variety of accumulation. The layered assembly system has stability issues, such as a high tendency to structural transition and decay, while the interpenetration system is subject to void size and ratio reduction.

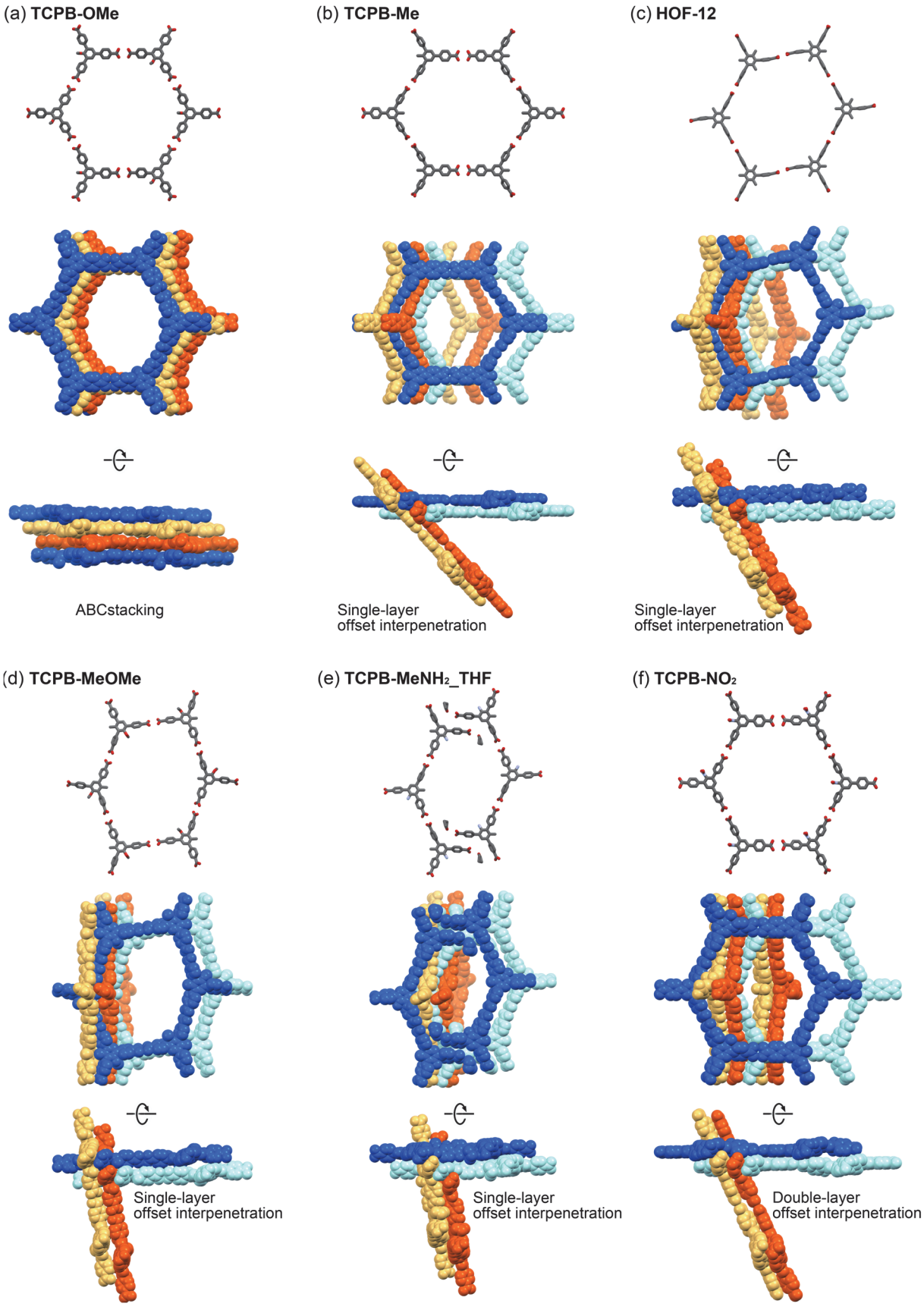

Figure 12. Crystal structures of (a) **TCPB-OMe**, (b) **TCPB-Me**, (c) **HOF-12**, (d) **TCPB-MeOMe**, (e) **TCPB-MeNH$_2$_THF**, and (f) **TCPB-NO$_2$**. (Top) Hexagonal network, assembling viewed (middle) down, and (bottom) side. Disordered moieties are omitted for clarity.

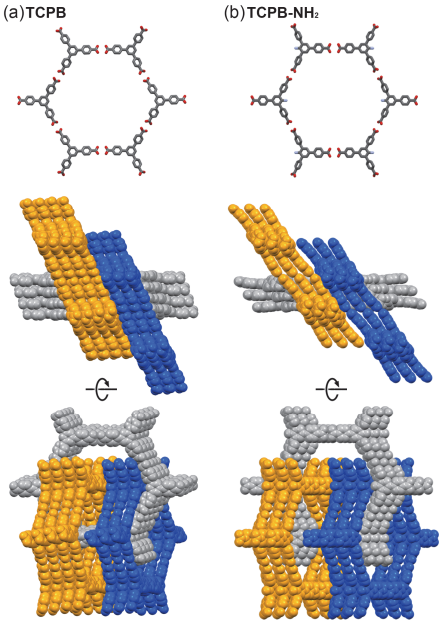

Figure 13. Crystal structures of (a) **TCPB**, and (b) **TCPB-NH₂**. (Top) Hexagonal networks, assembling of rotated-layer interpenetration viewed (middle) down, and (bottom) side. Disordered moieties are omitted for clarity.

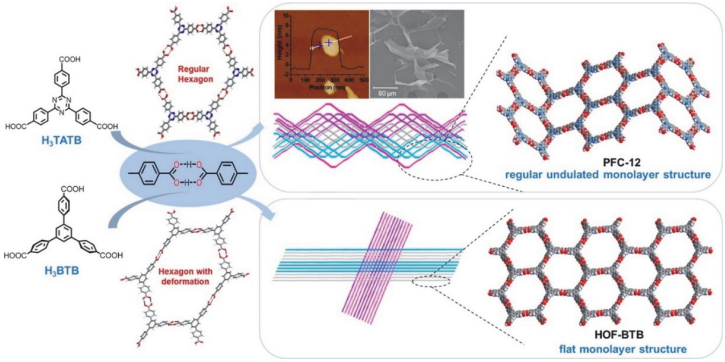

Figure 14. Representation of the chemical structure, the obtained hexagonal honeycomb motifs, and the resulting monolayer and polycatenated networks constructed by 2,4,6-tris(4-carboxyphenyl)-1,3,5-triazine (upper panel) and 1,3,5-tris(4-carboxyphenyl)benzene (lower panel). Atomic force microscope (AFM) and scanning electron microscope (SEM) images of the solute in supernatant during the crystallization process (fifth and third days, respectively) of **PFC-12** (inset). (Reproduced permission from ref. 341, copyright 2020 American Chemical Society.)

A-2. Tetracarboxylic acid

4-Connected tectons have been reported in Schemes 20 and 21. These core structures are as follows: benzene[284,348], C_2-symmetric *N*-containing polycyclic derivatives[284,348–350], tetrathiafulvalene[348], tetraphenylethene[351], pyrene[269,352–355], 1,2,3,6,7,8-hexahydropyrene[352], porphyrin and metalloporphyrin [268,275], terphenyl analogues[356–358], biphenyl derivatives[257,259,284,359], *p*-phenylenediamine[261], 5'-phenyl-*m*-terphenyl[360], tetra[2,3]thienylene[361], methane[362], silane[362], and adamantane[337,362]. These molecules are classified into planar or nonplanar molecules with π-conjugated skeletons, or other three-dimensional molecules.

The π-conjugated planar tectons (Scheme 20) form chicken wire networks with ***sql*** topology. These homotypic networks are assembled by stacking through π-interactions (π-π or CH-π) to form layered frameworks. Interpenetrated structures are not common in the case of planar tetracarboxylic acids because the molecules are large and prefer to be stabilized by stacking. Compounds listed in Scheme 20 construct 2D-layer assembled porous structures. Their stacking styles, namely stacking order (AA stacking, AB stacking, and others) and correlation offsets, are variable depending on their cores. The nonplanar tectons (Scheme 21) form diamondoid networks denoted by ***dia*** topology. During the construction of 3D HOFs, molecular assembly through non-covalent bonding can also proceed in parallel with the networking growth through H-bonding. When the size of the resulting pores is larger than that of the components, an additional

network is formed in parallel from molecules that interact with the existing network, leading to a dense porous structure with interpenetration. Homotypic networks are easily obtained by complementary dimers, while entire structures are not always isostructural because interactions between the networks depend on the molecular structure.

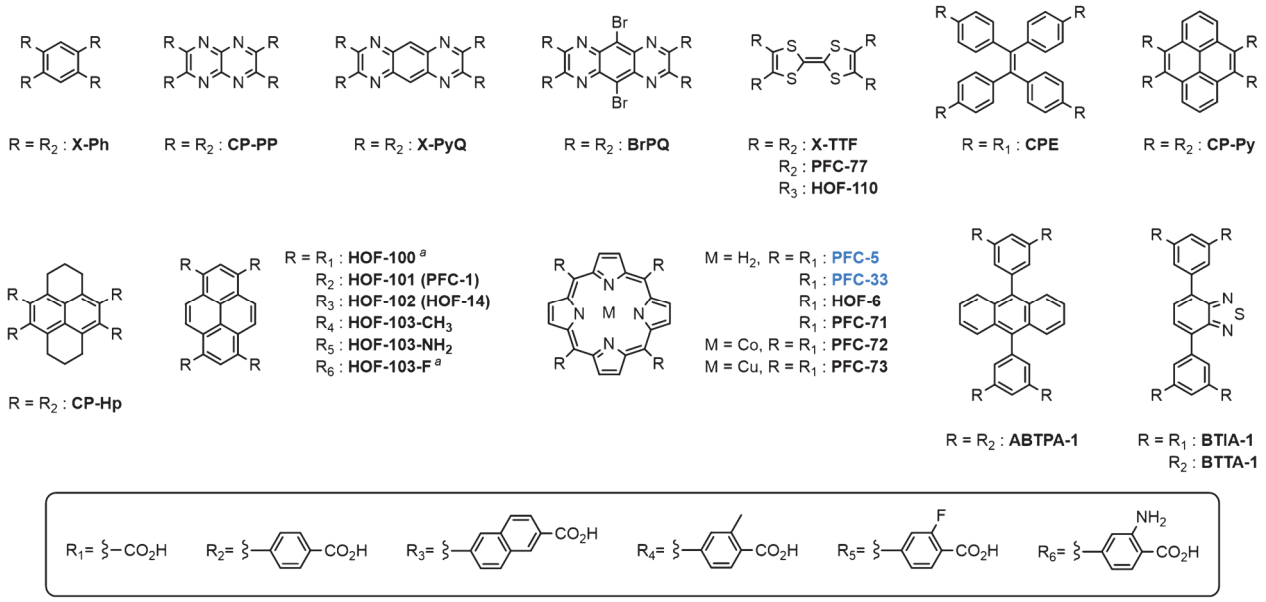

Scheme 20. Chemical structures of two-dimensional tecton of tetracarboxylic acids, and HOF names. HOFs in black denote the complementary dimer motif, and the blue ones denote the other H-bonding motif. [a] Construction of homotypic network is determined by only PXRD patters and crystal structure is not obtained.

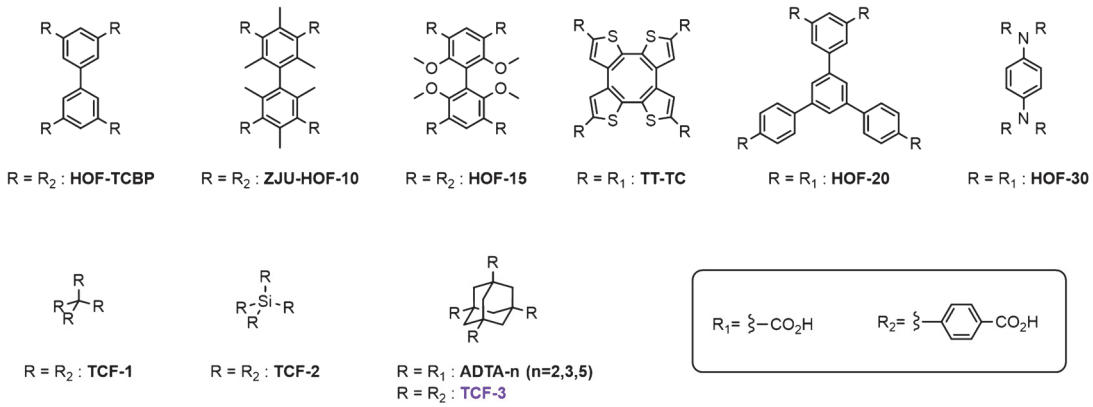

Scheme 21. Chemical structures of three-dimensional tecton of tetracarboxylic acids, and HOF names. HOFs in black denote the complementary dimer motif, and the purple one denotes H-bonding with solvent.

As shown in Figures 15–19, the planar tectons with π-conjugated skeleton tend to form homotypic networks, while they are often stack with different manners such as AA or AB stacking, resulting in non-isostructural HOFs consequently (Figure 15a,e). Derivatives with similar cores (**X-PyQ** and **BrPQ**, and **BITA-1** and **BTTA-1**) yielded isostructural HOFs with similar AA-stacking deviation of homotypic networks. **CP-Py** and **CP-Hp** yield isostructural HOFs with almost identical lattices (Figure 15l,j). This similarity led to a non-stoichiometric co-crystalline framework, whose components are not distributed as uniformly as the ideal solid solution but gradationally or inhomogeneously[352]. These isostructural HOFs are identified with the guest included and are different structures after guest removal.

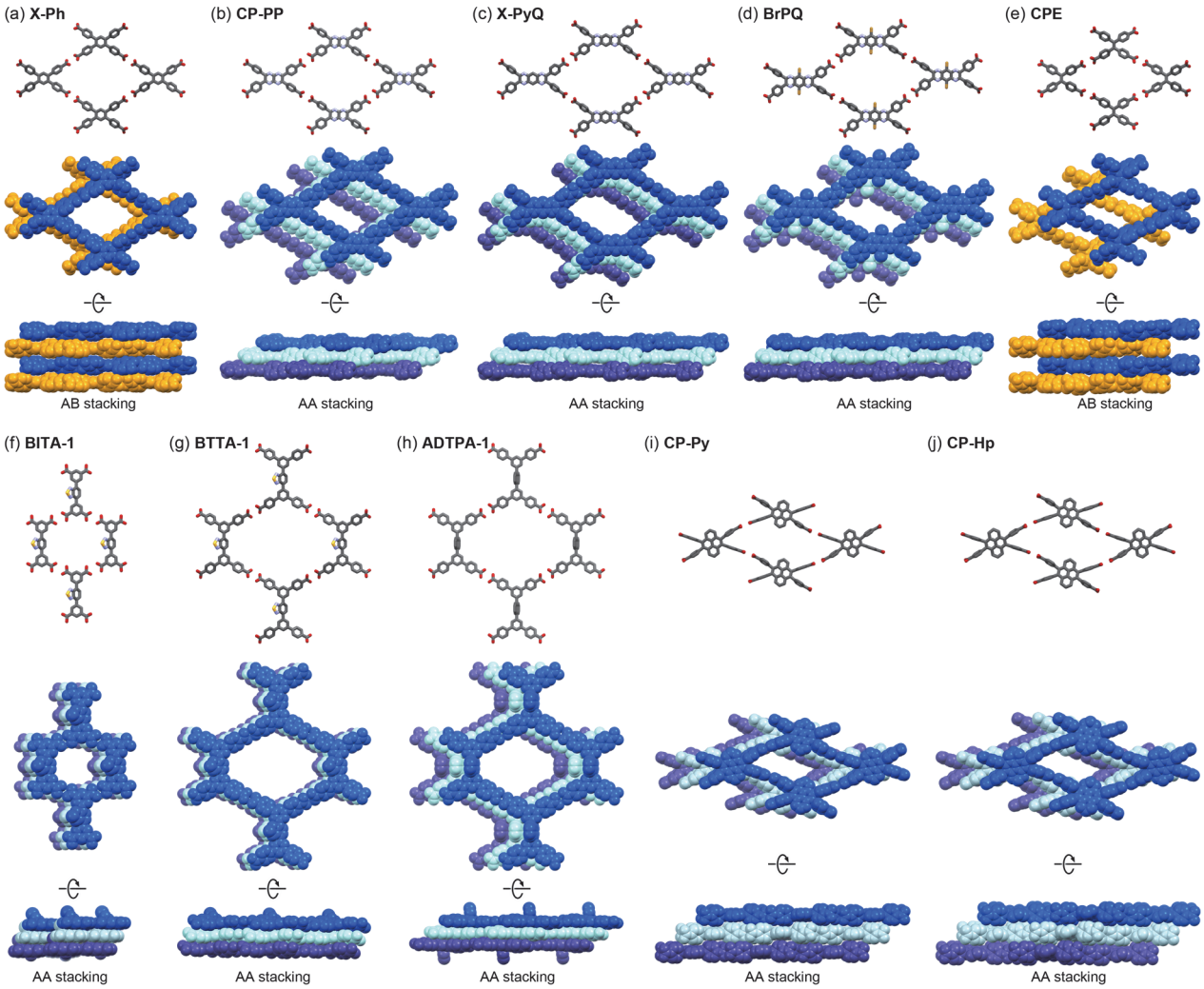

Figure 15. Crystal structures of (a) **X-Ph**, (b) **CP-PP**, (c) **X-PyQ**, (d) **BrPQ**, (e) **CPE**, (f) **BTIA-1**, (g) **BTTA-1**, (h) **ADTPA-1**, (i) **CP-Py**, and (j) **CP-Hp**. (Top) Square-lattice networks and assembled structures (middle) viewed down and (bottom) viewed side. Disordered moieties are omitted for clarity. These structures were obtained from SCXRD experiment excepted for **BTIA-1**, which was analyzed from PXRD experiment.

In addition to a 2D layered-assembling structure of porphyrin-based tectons (Figure 16a), a 3D porous structure of interpenetrated ***sql*** network (Figure 16d), and a layered porous structure with a 1D channel through non-complementary dimers (Figure 17) were obtained. 2D Assembled HOFs based on metalloporphyrin were reported, and their offsets of ***sql*** network were modulated depending on the metal species (Figure 16a–c). Diverse structures have been obtained for porphyrins and similar structures with different layer displacements of homotypic networks for metalloporphyrins.

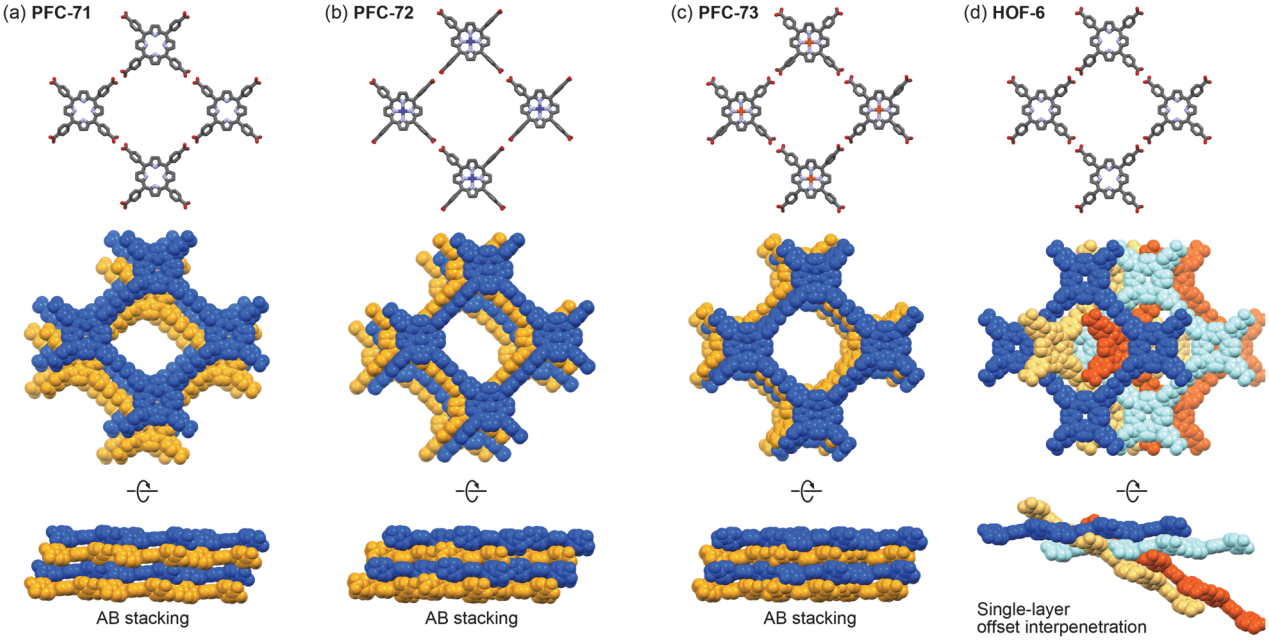

Figure 16. Crystal structures of (a) **PFC-71**, (b) **PFC-72**, (c) **PFC-73**, and (d) **HOF-6**. (Top) Square-lattice networks and assembling structures (middle) viewed down and (bottom) viewed side. Disordered moieties are omitted for clarity.

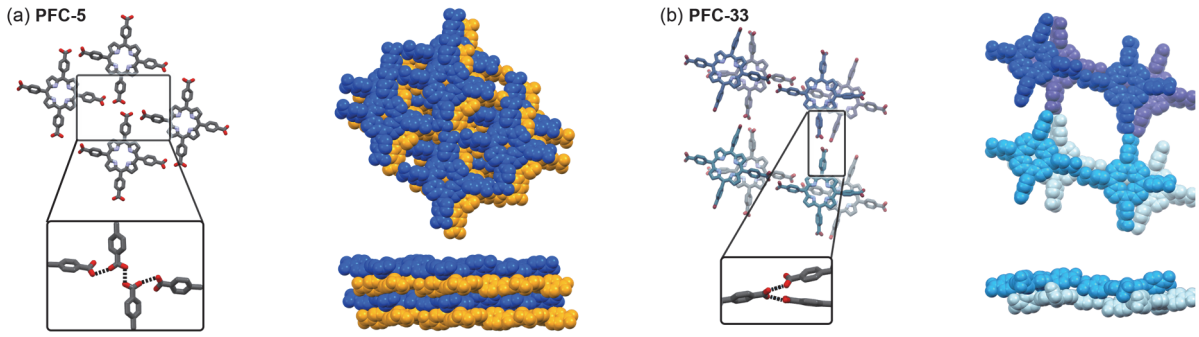

Figure 17. Crystal structures of (a) **PFC-5** and (b) **PFC-33**. (Left) H-bonding network and motif and assembling structure (Top right) viewed down and (bottom right) viewed side.

Only in the tetrathiafulvalene (TTF) core and pyrene core[269,353–355] systems, isostructural HOF construction with spacer modification were accomplished (Figures 18 and 19). A TTF derivative with 2-carboxynaphth-6-yl groups formed a homotypic network as that with 4-carboxyphenyl groups. This structure **HOF-110** had similar stacking and offset to one of the polymorphs of 4-carboxyphenyl derivatives

and is isostructural HOFs (**PFC-77-acetone**, Figure 18c). In the pyrene system, homotypic networks were obtained with the six analogs. 4-Carboxyphenyl, 2-carboxynaphthyl, 3-methyl-4-carboxyphenyl, and 3-animo-4-carboxyphenyl substituted pyrene derivatives yielded single-crystalline isostructural HOFs (Figure 19) and carboxy and 4-carboxy-3-fluorophenyl substituted derivatives also gave isostructural crystalline precipitates whose structures were estimated from PXRD experiments. The crystal structures indicated that the networks are assembled by slipped staking. **HOF-103-CH_3**, and **-NH_2**, have slightly larger interlayer distances and offsets due to their steric hindrance (former: 3.42 Å and 1.71 Å, latter: 3.46 and 1.73 Å), and those lengths of **PFC-1** and **HOF-14** are similar (former: 3.39 Å and 1.65 Å, latter: 3.40 and 1.67 Å). Therefore, these four derivatives gave isostructural HOFs.

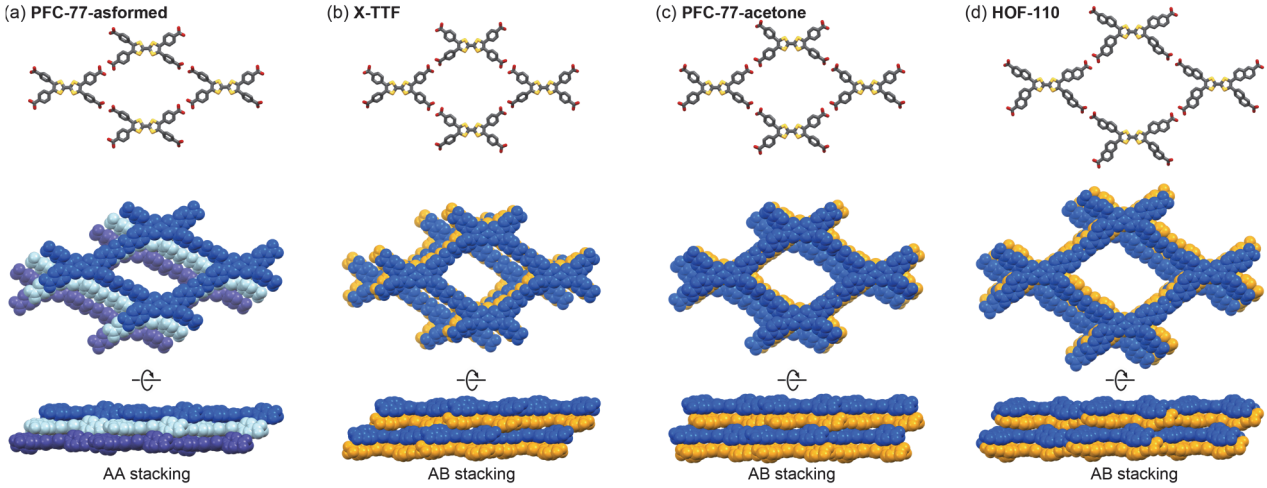

Figure 18. Crystal structures of (a) **PFC-77-asformed**, (b) **X-TFF**, (c) **PFC-77-acetone**, and (d) **HOF-110**. (Top) Square-lattice networks and assembling structures (middle) viewed down and (bottom) viewed side. Disordered moieties are omitted for clarity.

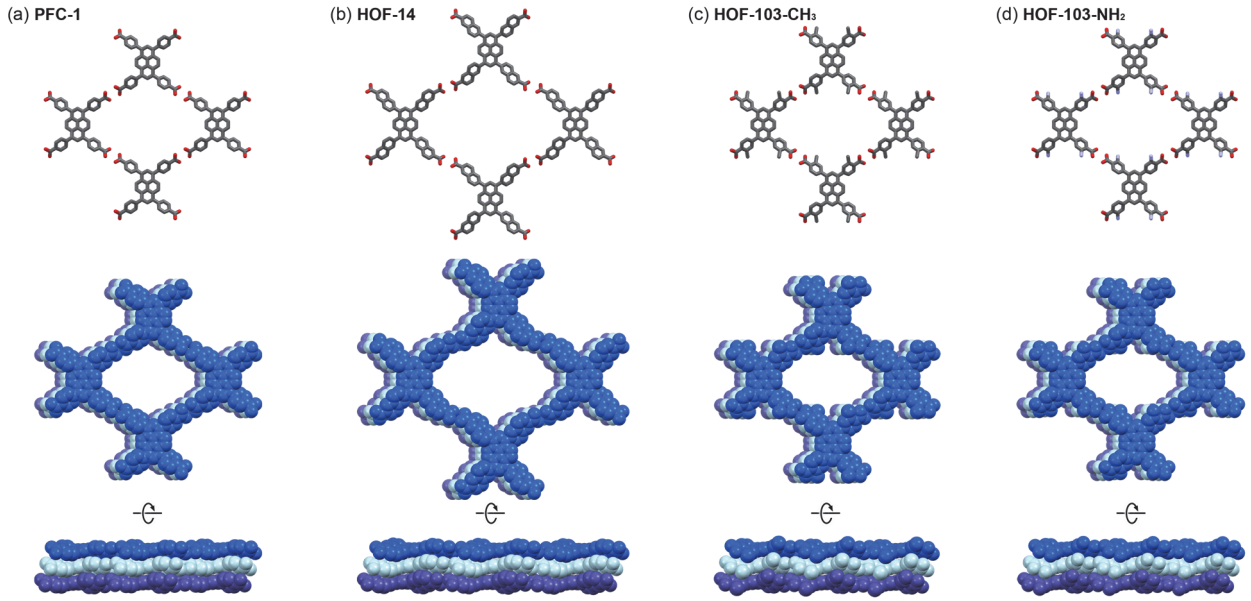

Figure 19. Crystal structures of (a) **HOF-101** (**PFC-1**), (b) **HOF-102** (**HOF-14**), (c) **HOF-103-CH_3**, and (d) **HOF-103-NH_2**. (Top) Square-lattice networks and assembling structures (middle) viewed down and (bottom) viewed side. Disordered moieties are omitted for clarity.

The biphenyl core acts as a 3D tecton because two phenylenes cannot be co-planar. **HOF-TCBP**, **ZJU-HOF-10**, and **HOF-15** have interpenetrated ***dia*** network structures. The biphenyl substituents differ in the shape and assembly of ***dia*** networks. In **HOF-TCBP**, non-substituted biphenyl tecton accumulates by π-π stacking (Figure 20a). In **ZJU-HOF-10** and **HOF-15**, methyl- or methoxy-substituted tectons inhibit the accumulation and assemble by CH-π interaction (Figure 20b,c), whose directions are the same as, and different to **HOF-TCBP**, respectively. **HOF-20** is a hetero biphenyl tecton with carboxy and 4-carboxyphenyl groups. This HOF has a ***ThSi2*** [**(10^3)-b** as described in point symbol] topological network, which has a similar shape to ***dia*** network (Figure 20e). Tetra[2,3]thienylene-based HOF **TT-TC** has a porous structure, in which ***dia*** network structures are assembled by π-π stacking (Figure 20d). Its stacking is the same as that of **HOF-TCBP**, so it is an isostructural HOFs. **HOF-30** possesses *p*-phenylenediamine moieties with the perpendicular orientation of phenylene core to the amine moieties, so its ***dia*** network interpenetrates through an accumulation of less overlapping molecules (Figure 20f). From the above, the ***dia*** network has the potential to be integrated as pre-designed by the appropriate π-conjugated core.

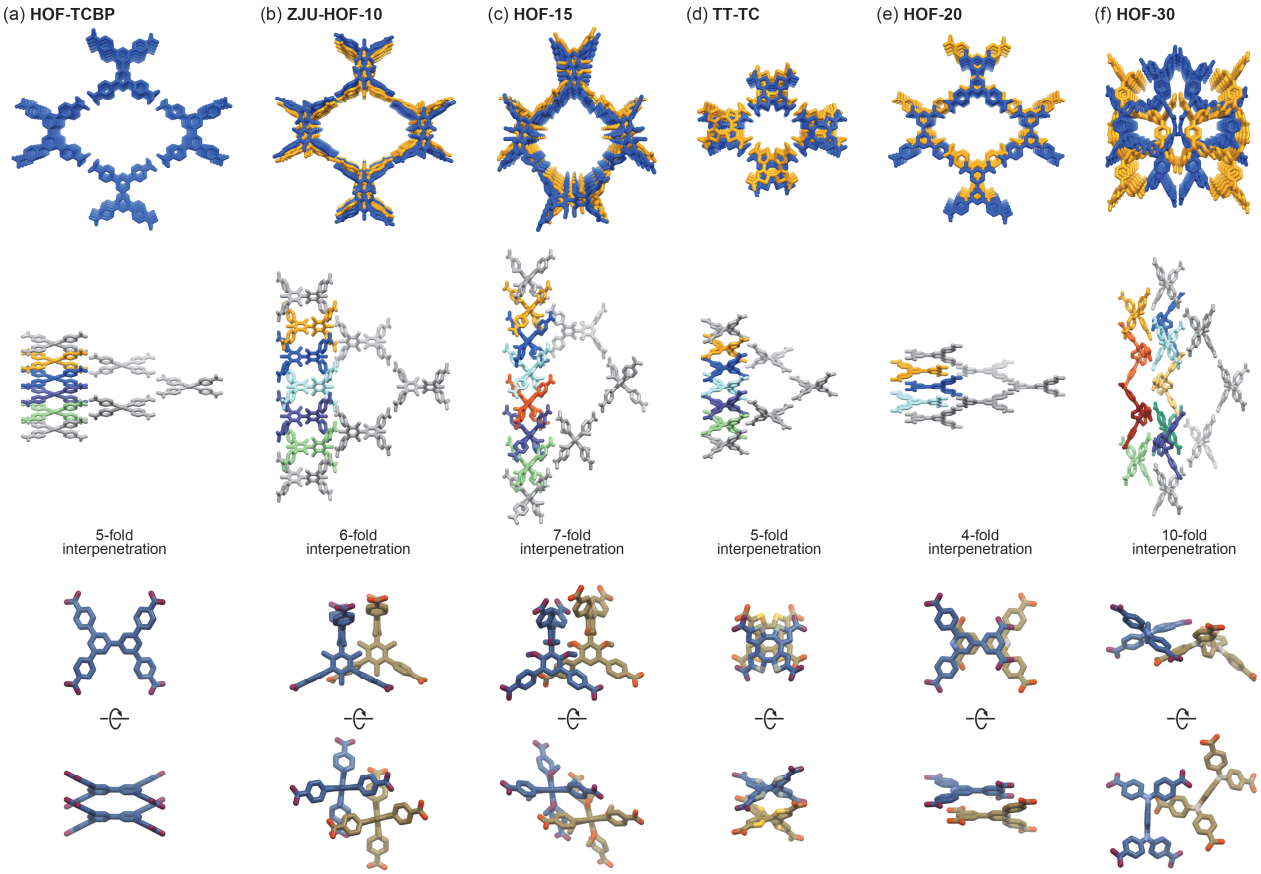

Figure 20. Crystal structures of (a) **HOF-TCBP**, (b) **ZJU-HOF-10**, (c) **HOF-15**, (d) **TT-TF**, (e) **HOF-20**, and (f) **HOF-30**. (Top) Assembling porous structures, (middle) single ***dia***-networks (colored grey) and 1D assembled columnar structures, for which the number of colors in the stacked molecules correspond to the number of the frameworks interpenetrated, and (bottom) stacking diagrams of adjacent molecules. The guest molecules and disordered moieties are omitted for clarity.

T_4-symmetric core (methane, silane, and adamantane) provide ***dia*** topological networks, which interpenetrate by dispersion forces (Figure 21). The CSP with screening has been successfully applied to construct porous structure **ADTA** with 2- and 3-fold interpenetration. **TCF-1** and **-2** were porous structures based on interpenetrated ***dia*** networks of 4-carboxyphenyl substituted methane and silane, respectively. The patterns of 6-fold interpenetration are different: **TCF-1** has a one-dimensional channel, and **TCF-2** has a three-dimensional channel. Adamantane tetracarboxylic acid did not form carboxy dimers and non-porous structure, **TCF-3**. The presence of the THF molecules disrupts the formation of dimers and promotes a side-to-side interaction between the peripheral spacers.

Since there is no directional interaction in the network of non π-conjugated molecules, the assembling is easily variable depending on the molecular structure and crystallization conditions, resulting in a wide variety of porous structures. Even if they exhibit persistent porosity, they often undergo structural transition upon guest removal.

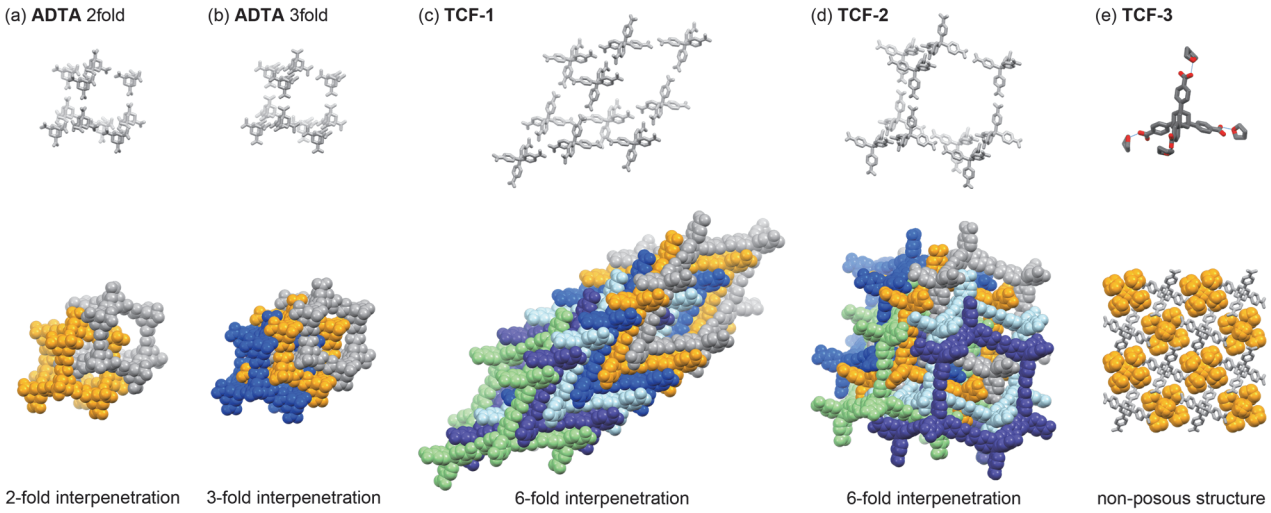

Figure 21. Crystal structures of (a) **ADTA** (2-fold interpenetration), (b) **ADTA** (3-fold interpenetration), (c) **TCF-1**, and (d) **TCF-2**. (top) Diamond networks and (bottom) assembling structures. (e) Non-porous structure of **TCF-3**. (top) A solvent penetrated structure and (bottom) a whole structure with solvents in orange. The guest molecules in ***dia*** networks and disordered moieties are omitted for clarity.

A-3. Hexacarboxylic acid

As 6-c tecton, benzene[363,364], series of C_3PI molecules (Tp[365], TpMe[366], TpF[366], T12[365], T12F[367], TQ12[368], T18[365,369], and Ex[365].), hexaazatriphenylene (HAT)[370], hexaazatrinaphthylene (HATN)[371], benzotriquinoxaline (BTQ)[372], tri(dithiolylidene)cyclohexanetrione (DC)[373], are reported (Scheme 22). 2,4,6-Trimethylbenzene-1,3,5-triylisophthalate (TMBTI)[262] are also reported as 3D tecton. Except for **HOF-76**, **CPHAT**, and **CPDC**, planar C_3PI molecules (Figure 22c) form a phenylene triangle (PhT) to yield a hexagonal network(HexNet). These homotypic networks form non-isostructural HOFs by diverse layered assembly of π-π stacking.

The substructure with carboxyphenyl groups (Figure 22a) is known as a dicarboxy-*o*-terphenyl motif. This motif forms a phenylene triangle (PhT) and a ***hxl*** topological (hexagonal) network through complementary H-bonded dimers. The carboxylic acid networked by the complementary dimer forms a *cis* conformer (O=C-O-H dihedral ~0°), in which the carboxylic acid and benzene ring are co-planar[374]. In the PhT system with the Ph spacer, not all dimers are in ideal conformation because steric hindrance limits

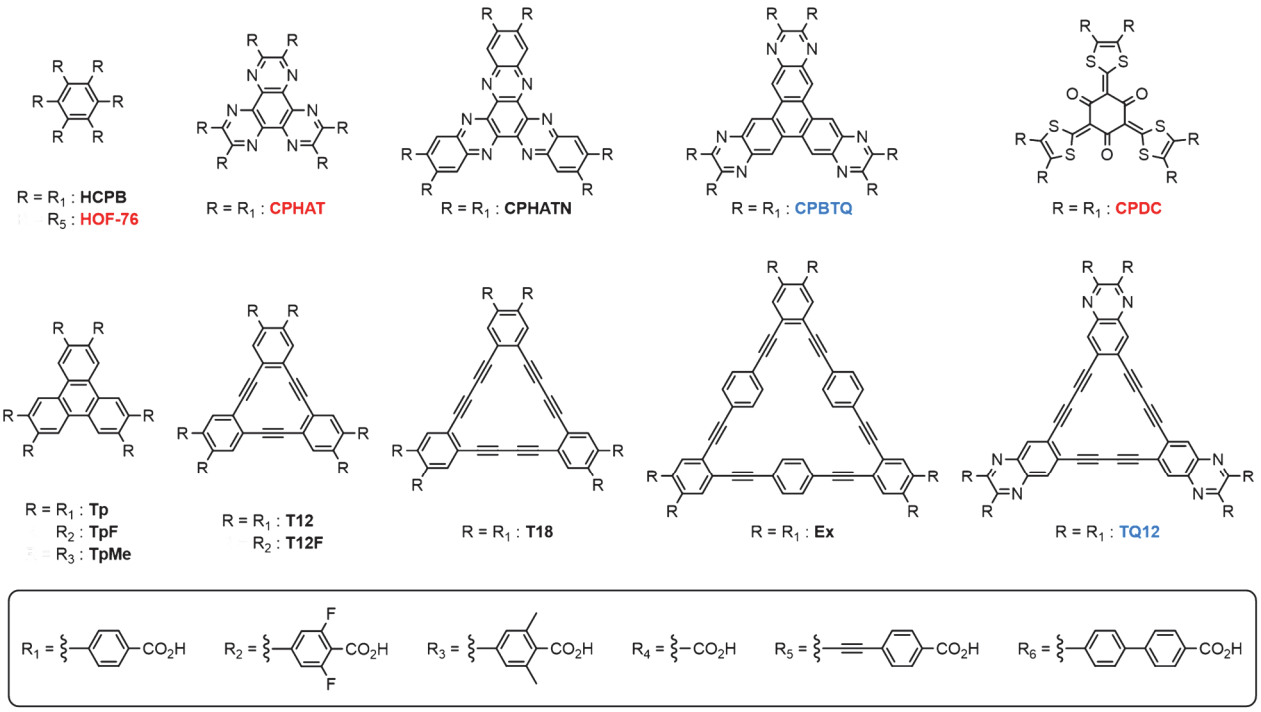

Scheme 22. Chemical structures of haxatopic carboxylic acid tecton and obtained HOF. HOFs in black denote the complementary dimer motif, and the blue ones denote the other H-bonding motif, and the red ones denote that three-dimensional structure based on the complementary dimer motif.

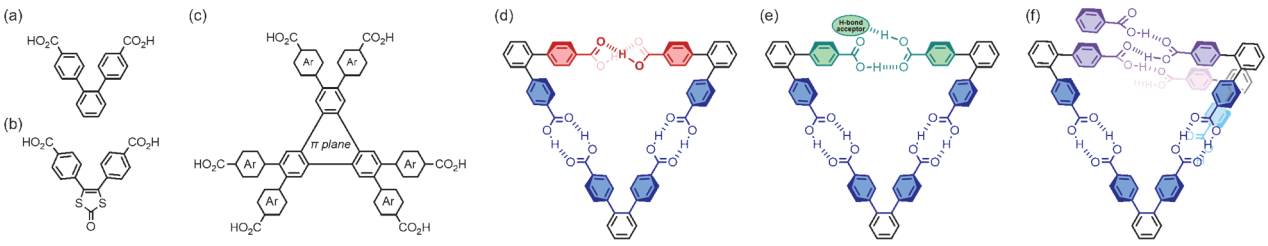

Figure 22. Chemical structure of (a) dicarboxy-o-terphenyl motif, (b) bis(4-carboxyphenyl)-1,3-dithiole motif, and (c) C_3-symmetrical π-conjugated molecules with each core structure. Phenylene-triangle (PhT) with (d) one frustrated H-bonding, (e) one fractured H-bonding, and (f) one truncated H-bondings.

the conformation of *ortho*-substituted phenylene groups. Thus, one of three dimers is frustrated (Figure 22d), fractured (Figure 22e), or truncated (Figure 22f) H-bond, which are the steric H-bond, H-bond with other solvents, or H-bond with other tectons, respectively. C_3PI tecton with 2,6-substituted benzoic acids such as R_2 and R_3 (Scheme 22) formed non-frustrated PhT due to the nonplanarity between carboxylic acid and benzene.

HCPB, **CPHATN**, and C_3PIs (**Tp**, **TpF**, **TpMe**, **T12**, **T12F**, **T18**, and **Ex**) formed homotypic HexNet and

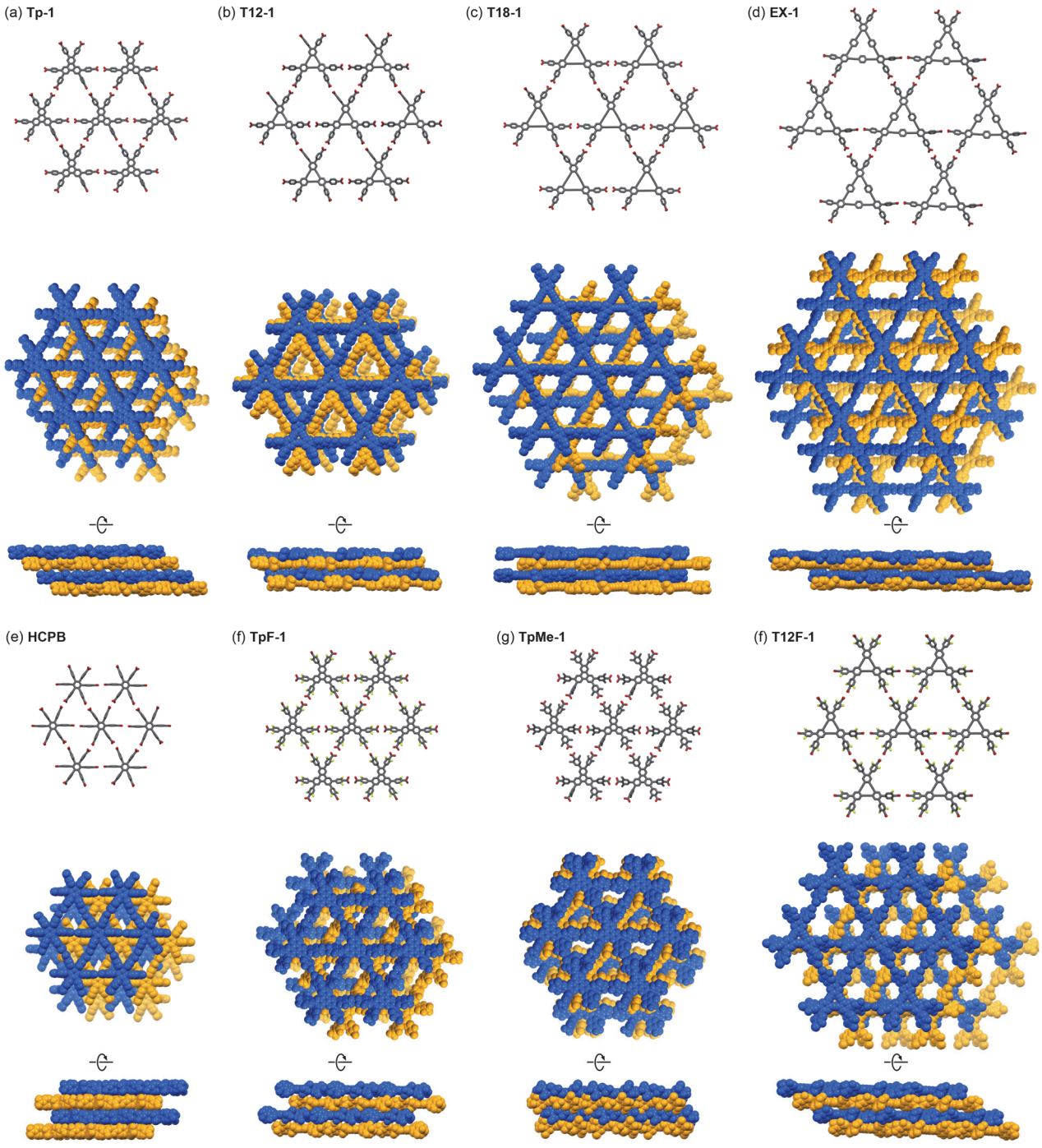

Figure 23. Crystal structures of (a) **Tp**, (b) **T12**, (c) **T18**, (d) **Ex**, (e) **HCPB**, (f) **TpF**, (g) **TpMe**, and (h) **T12F**. Hexagonal network (top) and assembling structure of AB stacking (middle) viewed down and (bottom) viewed side. Guest molecules are omitted for clarity.

constructed layered assemble HexNet (LA-HexNet) through assembling of π-π and CH-π interaction (Figures 23 and 24a). These stackings are determined by a constituent environment (structure and crystallization conditions). The resulting offsets of AB stacking are different from each other. Tp formed some polymorphic porous structures with different H-bonding, frustrated or fractured, and different offsets.

CPBTQ and **TQ12** formed 3D networks with truncated H-bonding motifs, which are tetramer and tetramer with water, respectively (Figure 24c,e). These structures were 2-fold interpenetrated structures, but if the tetramer motif was ignored, they belonged to the LA-HexNet. Therefore, they were defined as quasi-LA-HexNet. **CPBTQ** forms an ABCD stacking of quasi-LA-HexNet, and **TQ12** forms an AB stacking of quasi-LA-HexNet (Figure 24b,d).

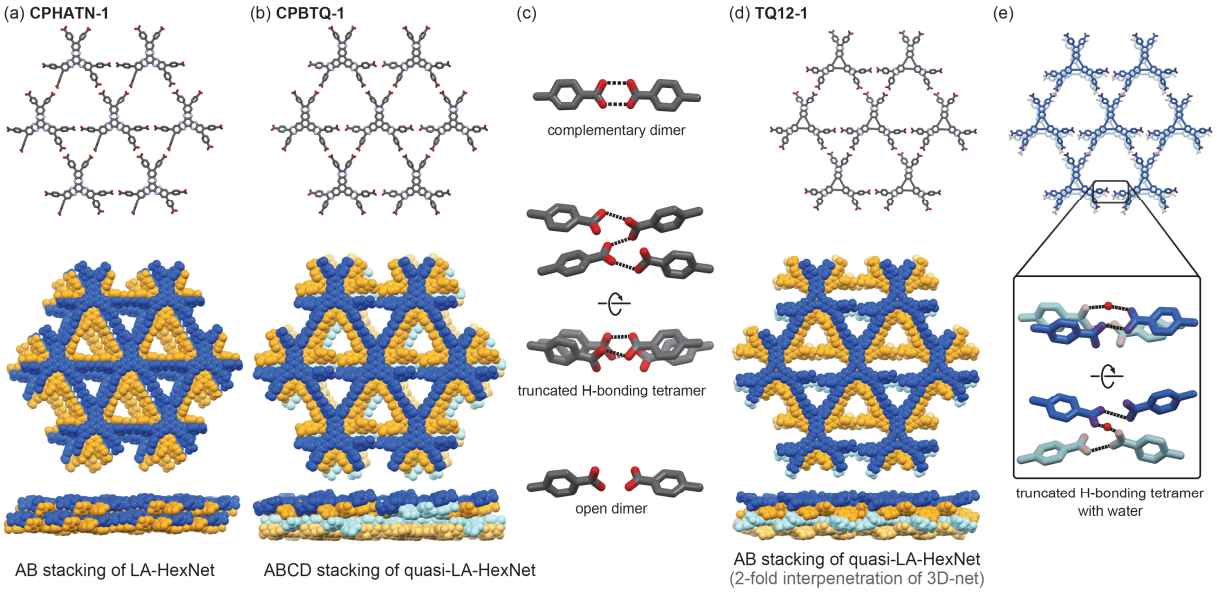

Figure 24. Crystal structures of (a) **CPHATN**, (b) **CPBTQ**, and (d) **TQ12**. (top) Hexagonal networks and assembling structure (middle) viewed down and (bottom) viewed side. (c) Three types of H-bonding motif in **CPBTQ**. (e) Three-dimensional network of **TQ12** and its truncated H-bonding motif. Guest molecules and disordered moieties are omitted for clarity.

CPHAT has a hexaazatriphenylene core, a nitrogen atom introduced into the triphenylene. While HAT was well known as rigid planar molecules, it formed nonplanar structure by π-interaction in HOF structure. **CPHAT** formed not ***hxl*** network but ***pcu*** network through helical H-bonding. These three-dimensional networks are assembled uniformly by π-stacking to form a 4-fold interpenetrated porous structure (Figure 25a). **HOF-76** is a similar steric structure, which possesses ***pcu*** network without interpenetration (Figure 25b). **CPDC** was constructed by a hexacarboxylic acid derivative whose substructure is bis(4-carboxyphenyl)dithiol. The angle between two 4-carboxyphenyl groups is *ca.* 73°, which is smaller than that of the dicarboxy-*o*-terphenyl group, so it is impossible to form the same networking as that of PhT. The ***pcu*** topological network also cannot be formed and an anomalistic helical network, namely $\{8^2.10\}$ network as point symbol, was constructed. This network without interpenetration gave a porous structure with a 1D

channel (Figure 25c). These nonplanar structures are characterized by permanent porosity (maintaining original structures even after heat over 300 °C and guest removal.)

LA-HexNet exhibit different styles and stability of stacking depending on the constituent environment. On the other hand, nonplanar networks are stable structures such as **CPHAT-1**, **HOF-76**, and **CPDC-1** due to the inhibition of transition of the 3D network by π-stacking.

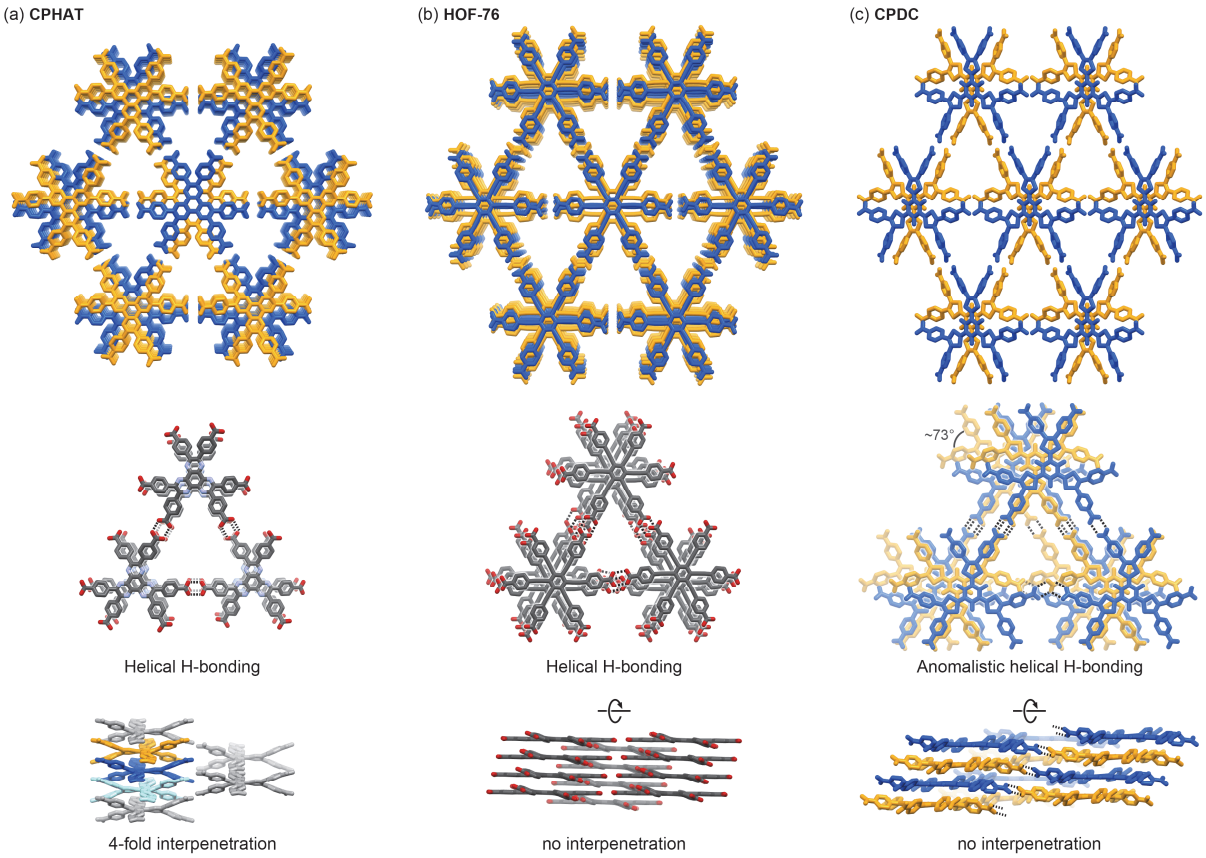

Figure 25. Crystal structures of (a) **CPHAT**, (b) **HOF-76**, and (c) **CPDC**. (top) Whole hexagonal structures and H-bonding networks (middle) viewed down and (bottom) viewed side. Guest molecules are omitted for clarity.

A-4. Other hexacarboxylic acid

This example is a diverse construction rather than an isostructural one by derivatives of triptycene-based hexacarboxylic acids[375,376] (Scheme 23). Hexakis(4-carboxyphenyl)derivatives formed **PETHOF-1** and **PETHOF-2** (Figure 26). In both superstructures, constituent molecules acted as trigonal prismatic hexatopic linkers, which were connected by the dimer of carboxylic acids to form hexagonal topology, ***acs***. They had the same topology but were interpenetration isomers with two- and five-fold interpenetration. On the other hand, the spacer-extended HOFs **PETHOF-3** yielded a different topological network (Figure 27). To understand topological network simplicity, the tris-molecular cluster was described as a 12-connected supramolecular polyknot. Carboxyl dimers connected the cuboctahedral knots to form an ***hcp*** topological network. **PETHOF-3** had tetrahedral and octahedral pore cages with effectively accessible diameters of 1.6 and 3.0 nm, respectively.

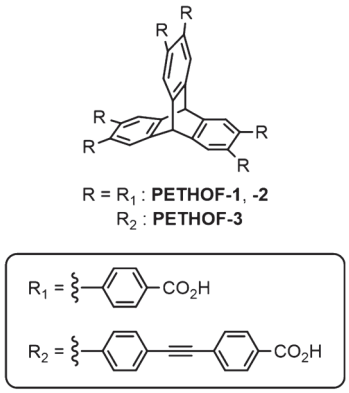

Scheme 23. Chemical structures of hexacarboxylic acid tecton.

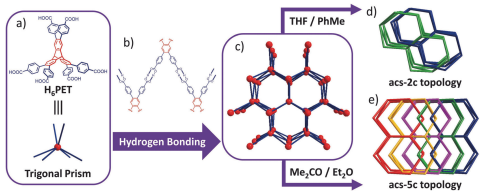

Figure 26. The assembly of a pair of "interpenetration isomers". (a) The trigonal prismatic building block. (b) The hydrogen-bonding pattern involved in crystal superstructures. (c) The ***acs*** topology. (d,e) The two- and five-fold interpenetrated superstructures, **PETHOF-1** and **PETHOF-2**. (Reproduced permission from ref. 375, copyright 2019 Wiley-VCH.)

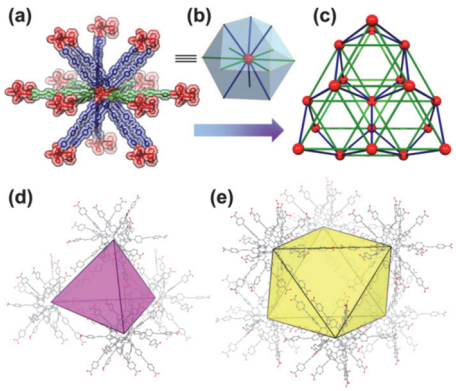

Figure 27. (a–b) The tris-molecular cluster viewed as a 12-connected node in a cuboctahedral geometry. The triptycene cores are shown in red. The connecting bridges composed of a single and two paralleled carboxyl dimers are shown in green and blue, respectively. Irrelevant molecular components are omitted for the sake of clarity. (c) The ***hcp*** topology (the red spheres, as the vertices, correspond to the tristriptycene cores; the green and blue sticks, as the edges, correspond to the single and two paralleled carboxyl dimer linkages, respectively). (d–e) Depictions of the tetrahedral (with magenta faces) and the octahedral (with yellow faces) cages with the tris-molecular clusters as the vertices. (Reproduced permission from ref. 376, copyright 2019 American Chemical Society.)

B. Diaminotriazine (DAT)

Many frameworks have been reported in systems with DAT as the synthon, both with[241,376–385] and without[122–128] porosity evaluation. HOFs with homotypic molecular skeletons and permanent porosity are listed in Scheme 24. **HOF-1** and **HOF-4** are analogs elongated with phenylene. **HOF-3**, **HOF-9**, **and UPC-HOF-6** are the 3-connected triangle motifs, and the distortion angle of peripheral phenylene groups differ depending on the core (mesitylene, benzene, nitrogen, respectively). The H-bond network and whole porous structure are shown below. The H-bonding link is different in each crystal, which was attributed to the H-bonded diversity of DAT. **HOF-1** had a 1D chain-like H-bonding network (Figure 28), while **HOF-4** had a closed H-bonding motif with four DATs (Figure 30a). Hence, the network topology is also different, with **HOF-1** being ***bcu*** (Figure 29) and **HOF-4** being ***PtS***, a binodal four-connected network (Figure 30b).

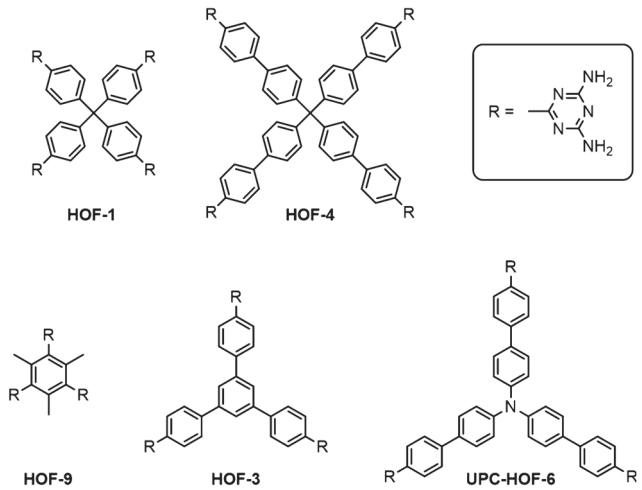

Scheme 24. Chemical structures of homotypic 4- and 3-connected DAT derivatives.

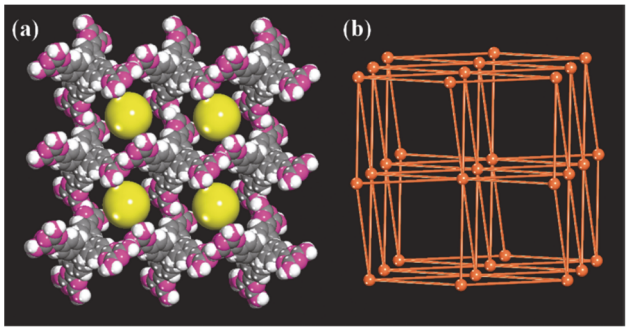

Figure 29. X-ray crystal structure of **HOF-1** featuring (a) one-dimensional channels along the *c* axis with a size of ~8.2 Å (yellow spheres) and (b) three-dimensional body-centered cubic **bcu** $\{4^{24}6^4\}$ network topology. (Reproduced permission from ref. 242, copyright 2011 American Chemical Society.)

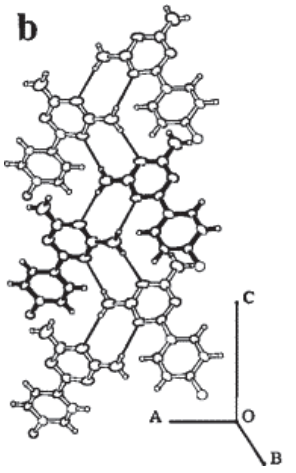

Figure 28. ORTEP views of the three-dimensional hydrogen-bonded network present in crystals of inclusion compound 1·1HCOOH· 4dioxane. In each view, non-hydrogen atoms are represented by ellipsoids corresponding to 40% probability, hydrogen atoms are shown as spheres of arbitrary size, and hydrogen bonds are represented by narrow lines. (b) This view (along *b*) is perpendicular to the channels and shows how their walls are constructed. The arms of two tectons (represented by broad filled lines) are joined by hydrogen bonds to form one side of a cyclic quartet. These tectons are linked by hydrogen bonds in the c direction to tectons in adjoining quartets (open lines). (Reproduced permission from ref. 122, copyright 1997 American Chemical Society.)

Tritopic DAT derivatives also constructed HOFs with different H-bonding and topological networks. In **HOF-9**, the DAT moiety was oriented perpendicular to the core (Figure 31a) and the H-bonding motif is a front-edge pair (Figure 31e), yielding a ***pcu*** topological network (Figure 31d). **HOF-3** had a DAT moiety oriented perpendicular to the core (Figure 32a) and H-bonds (Figure 32b) to form 1D H-bonding chain, resulting to form ***srs*** topological network (Figure 32c). In **UPC-HOF-6**, the DTA moiety is approximately parallel to the molecular plane (Figure 33a, *ca.* 17° tilted). The 3D H-bonding networks and accumulation (Figure 33b,c) resulted in a complex topological network[384].

From HOF construction by DAT analogs, the less directional nature of the synthon makes them unsuitable for the systematic construction of isostructural HOFs but advantageous for the formation of diverse topological networks.

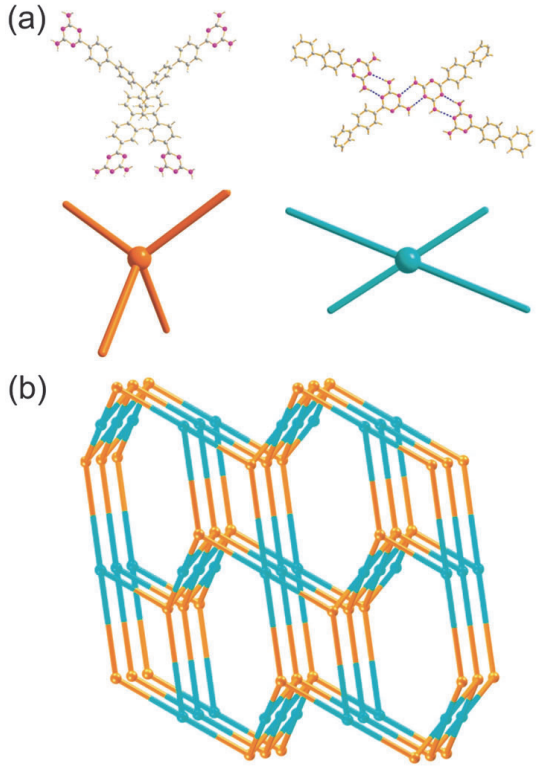

Figure 30. X-ray structure of **HOF-4** featuring (a) the basic organic building block in which the central carbon atoms act as tetrahedral nodes (brown balls) and centers of multiple hydrogen bonding motifs act as square planar nodes (cyan balls). (b) A simplified binodal four-connected ***PtS*** ($4^2 8^4$) topology. (Reproduced permission from ref. 379, copyright 2014 The Royal Society of Chemistry.)

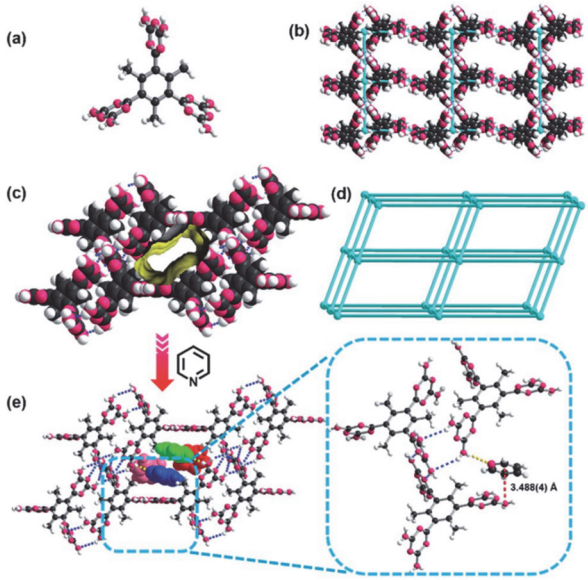

Figure 31. Crystal structure of **HOF-9** exhibiting (a) the building block and (b) a supramolecular quadrangle grid with the dimer acting as a 6-*c* node (cyan ball). (c) Packing diagram of **HOF-9** along the *a* axis showing the pore surfaces of 1D channels highlighted as yellow/grey (inner/outer) curved planes. (d) An uninodal 6-*c* ***a-Po*** net. (e) The crystal structure of **HOF-9** Py indicating the hydrogen-bonding interactions between Py and the **HOF-9** framework (yellow dashed line), the π–π interaction between the DAT group and Py molecule (red dashed line) and packed Py molecules residing in the channel of the framework along the *a* axis (C: black, N: pink, and H: white). (Reproduced permission from ref. 384, copyright 2017 The Royal Society of Chemistry.)

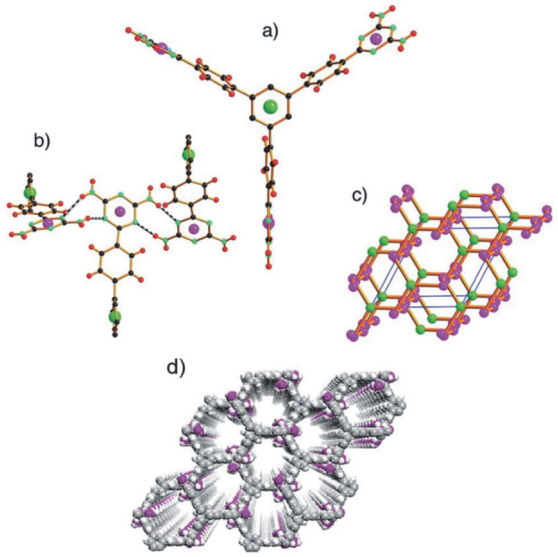

Figure 32. X-ray crystal structure of **HOF-3** featuring (a) the basic organic building block in which the centers of central benzene ring (green balls) and centers of three 1,3,5-triazine rings (magenta balls) act as nodes. (b) The H-bonded link between DAT groups showing that each is joined to two other DAT groups. (c) The net of 3-*c* branch points as it occurs in the crystal structure; and d) three-dimensional packing showing the 1D hexagonal channels of about 7.0 Å in diameter along the *c* axis (C gray, H white, N pink). (Reproduced permission from ref. 380, copyright 2015 Wiley-VCH.)

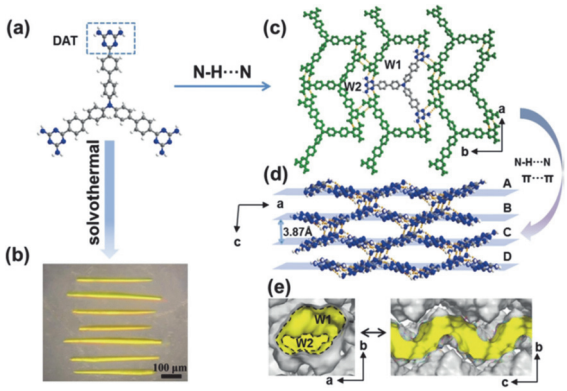

Figure 33. (a) Organic building block, (b) digital photograph, (c) 2D supramolecular layers, and (d) 3D structure of **UPC-HOF-6** (C gray, H white, N blue; the dotted yellow line represents the hydrogen bonds) (e) the wave-shaped interlaced channels of **UPC-HOF-6** along the c axis (the yellow part is the channel, and the gray is the channel wall). (Reproduced permission from ref. 378, copyright 2020 Wiley-VCH.)

C. Pyrazole

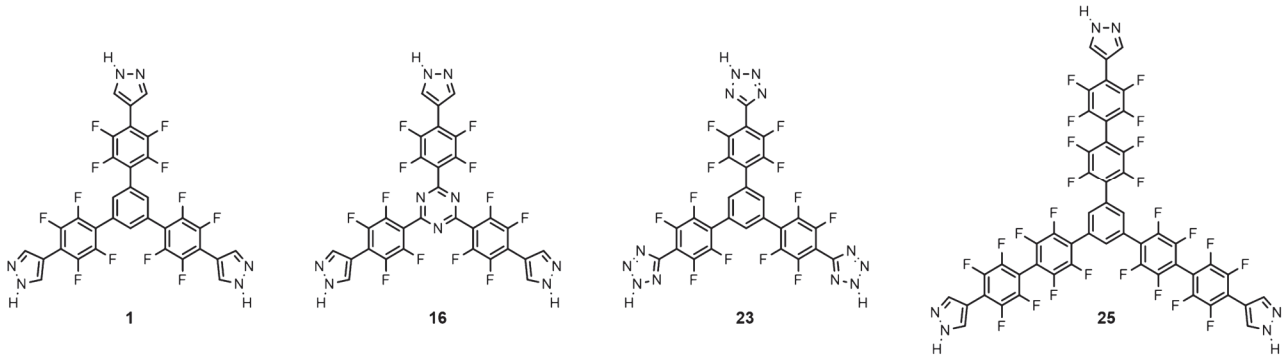

Scheme 25. Chemical structure of fluorinated trispyrazole derivatives **1**, **16**, and **25**, and a tristetrazole derivative **23**.

In pyrrole (and tetrazole) synthon system, crystal structures have been reported for the four analogs **1, 16, 23,** and **25** in Scheme 25 [246,279,280]. Pyrroles formed triangle H-bonding motif (Scheme 26a). Compound **16** is a derivative with the central benzene changed to triazine, whose twist angle of the peripheral tetrafluorobenzene is reduced. Compound **23** is a derivative with the 1,2,3,4-tetrazole as a

synthon. Compound **25** is a derivative with a simple elongation of the spacer from compound **1**. The obtained HOFs are shown in Figures 34–36.

The 1,2,3,4-tetrazole derivative **23** did not form a triangular H-bond motif (Scheme 26b) but formed a 1D chain bond (Scheme 26d) vertical to the molecular plane. The nature of the terminal H-bonding group can be switched between a 1H-tetrazole and a 2H-tetrazole in Scheme 26c, effectively morphing into an infinite chain of H-bonds rather than triangle bonding. The HOF **23** is porous but different structure from others (Figure 35). Compounds **16** and **25** form the trimeric H-bond motif and construct isostructural and quasi-isostructural HOFs, respectively. The isostructural HOFs, **1** and **16**, have differences in pore size (16.5 and 18.0 Å), stacking distance (3.47 and 3.38 Å), and torsion angle between a central aryl moiety and a peripheral tetrafluorobenzene (36.8–49.5°, and 32.3–46.0°), but other respects are relatively similar (Figure 34). The extended quasi-isostructural HOF **25** forms a homotypic 2D network connected *via* trimeric H-bonding motif (Figure 36). There is a difference in assembling. Compound **1** forms AB stacking, but compound **25** forms AABB stacking. Although the order is different, the stacking direction is the same, resulting in the same hexagonal pores. Hence, **25** is described as *pseudo-isostructure*. The diameter of hexagonal pores and BET specific surface areas ($S_{A(BET)}$) calculated from gas absorption experiment increased to 26.4 Å and 1821 $m^2 g^{-1}$ from 16.5 Å and 1159 $m^2 g^{-1}$, respectively.

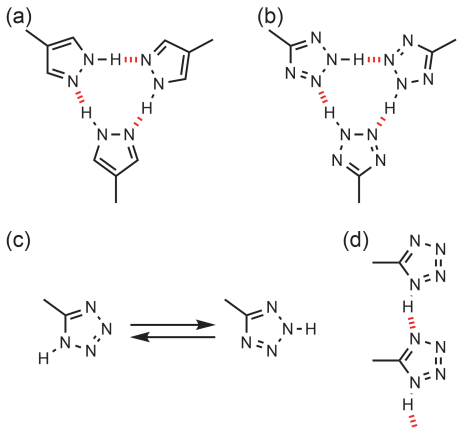

Scheme 26. Chemical structure of triangle H-bonding motif of (a) pyrrole and (b) tetrazole. (c) Tautomerization of (left) 1H-tetrazole and (right) 2H-tetrazole. (d) 1D Chain H-bonding motif of 1H-tetrazole.

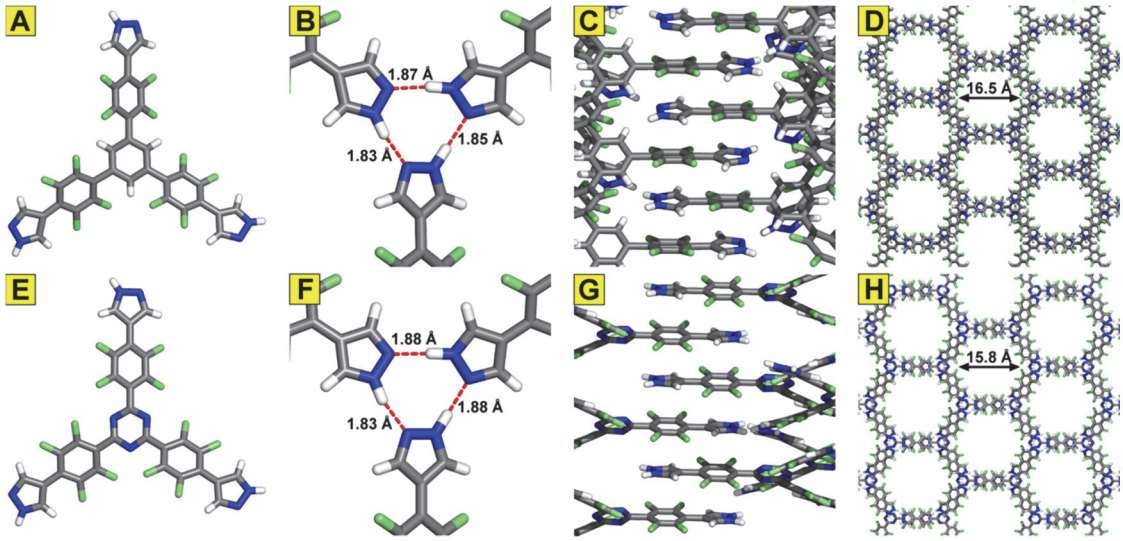

Figure 34. Crystal structures of trigonal precursors **1** (A) and **16** (E) are remarkably similar. They both form triplets of N−H···N hydrogen bonds between pyrazoles (B,F), and establish π-π stacking interactions between electron-rich pyrazoles and electron-poor tetrafluorobenzenes (C,G). Ultimately, both organize into porous networks with hexagonal pores (D,H). (Reproduced permission from ref. 280, copyright 2018 American Chemical Society.)

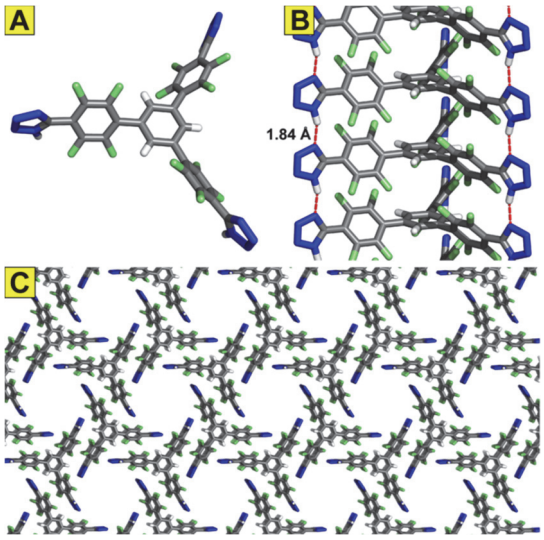

Figure 35. Crystal structure of trigonal compound **23** (A) shows twisting of tetrafluorobenzene rings relative to the plane of the central benzene ring. Molecules of **23** organize into vertical stacks (B) which are stabilized by hydrogen bonds between tetrazoles, as well as by offset π-π stacking of tetrafluorobenzene rings. Overall structure positions these vertical stacks parallel to each other, leaving hexagonal voids which are filled with MeOH in the as-synthesized structure (C, MeOH molecules removed for clarity). (Reproduced permission from ref. 280, copyright 2018 American Chemical Society.)

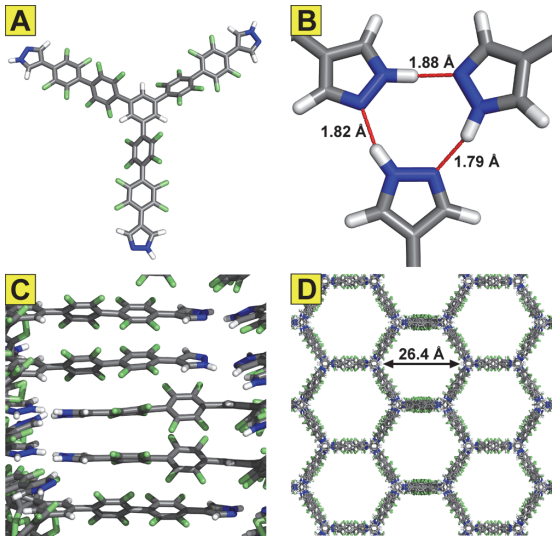

Figure 36. Crystal structure of trigonal **25** (A) reveals significant twisting between the central benzene ring and tetrafluorobenzenes. Triplet of [NH-N] hydrogen bonds (B) and unusual pairwise π-π stacking (C) hold together the overall structure with large hexagonal channels (D), viewed along the crystallographic *a* axis. (Reproduced permission from ref. 280, copyright 2018 American Chemical Society.)

D. Urea

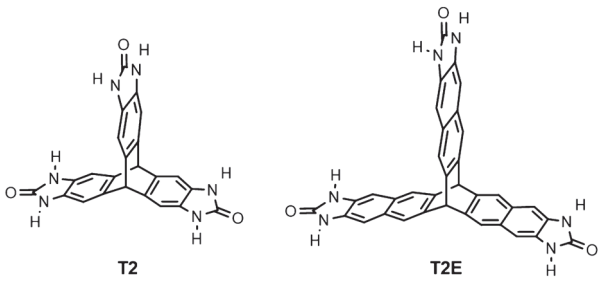

Scheme 27. Chemical structure of triptycene based derivatives with urea as H-bonding motif.

In the system of urea tectons, some HOFs with triptycene were reported (Scheme 27)[387,388]. The energy-structure-function (ESF) map obtained from crystal structure prediction (CSP) methods[389,390] has been analyzed. It is possible to discover structures with the lowest energy possible at stable porous molecular

frameworks from the lower edge of the energy–density representation[391,392]. As shown in the ESF mapping in Figure 37, **T2** has the potential to build a variety of porous polymorphic structures. Based on solvent content calculations and MD dynamics, it was found that crystallization readily produced the porous structures that exhibit no lattice contraction in MD simulation and are stable with respect to the CSP global minimum. The above CSP-based crystallization led to the construction of isostructural HOFs (**T2-γ** and **T2E-α**) with hexagonal pores by **T2** and its benzene-fused analog, **T2E**, respectively (Figures 37 and 38). Note that a single crystal structure has been obtained for **T2-γ**, but the structure of **T2E-α** was speculated based on PXRD analysis. **T2E-α** has a very brittle structure due to its huge voids.

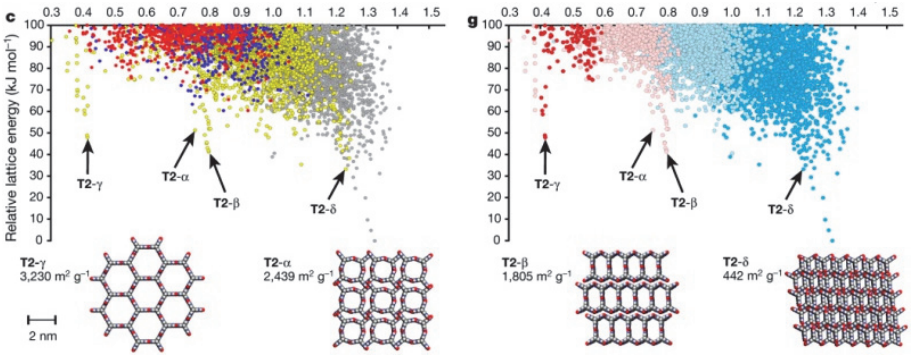

Figure 37. (c) Crystal structure prediction (CSP) energy–density plot for **T2**, with each point corresponding to a computed crystal structure. The symbols are color coded by the dimensionality of the pore channels, assessed using a CH_4 probe radius, 1.7 Å. (g) ESF maps showing the calculated methane deliverable capacities for **T2**, projected onto the energy–density plot. The symbols are color coded by deliverable capacity (in units of v STP/v; 65–5.8 bar, 298). **T2** structures selected from the leading edge of the distributions are also shown. Grey, white, blue and red atoms represent carbon, hydrogen, nitrogen and oxygen, respectively. (Reproduced permission from ref. 388, copyright 2017 Springer Nature.)

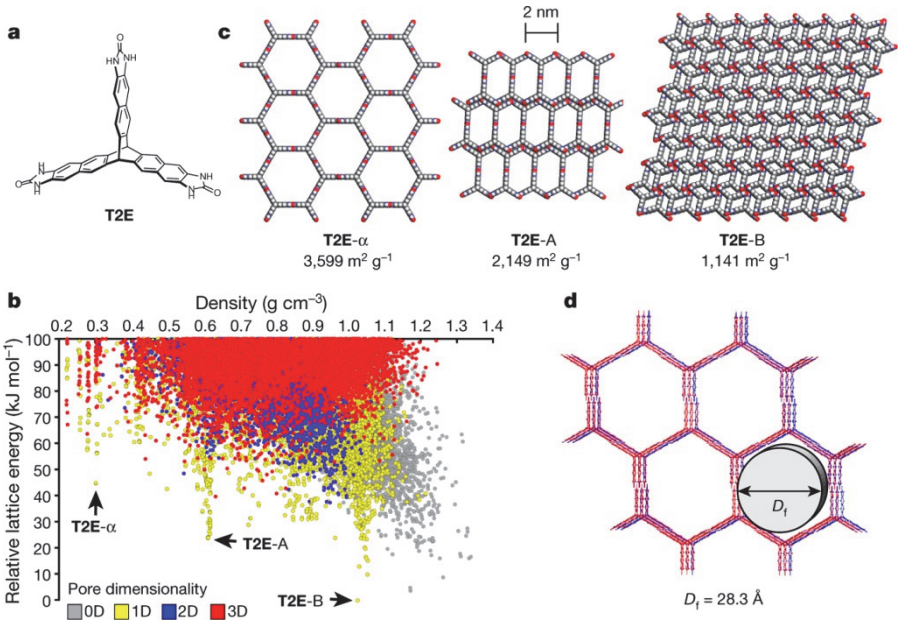

Figure 38. (a) Extended benzimidazolone analogue of **T2**, and **T2E**. (b) CSP energy–density plot. (c) Selected structures for **T2E**, drawn from the leading edge of the energy–density landscape: **T2E-α**, **T2E-A** and the global-minimum structure, **T2E-B**. (d) Overlay of (red) predicted and (blue) experimental structures for **T2E-α**. (Reproduced permission from ref. 388, copyright 2017 Springer Nature.)

E. Amidinium carboxylate

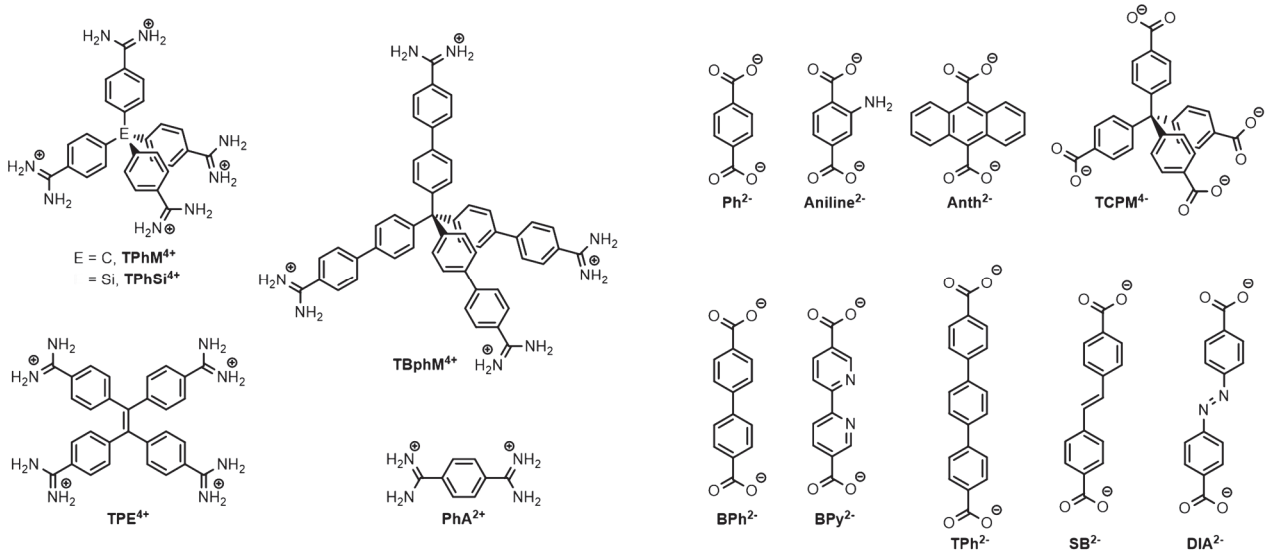

Scheme 28. Chemical structure of amidinium and carboxylate tectons. Tetramidinium derivatives: **TPhM^{4+}**, **TPhSi^{4+}**, **TBPhM^{4+}**, and **TPE^{4+}**, a diamidinium derivative: **PhA^{2+}**, dicarboxylate derivatives: **Ph^{2-}**, **Aniline^{2-}**, **Anth^{2-}**, **BPh^{2-}**, **BPy^{2-}**, **TPh^{2-}**, **SB^{2-}**, **DIA^{2-}**, and a tetracarboxylate derivative: **TCPM^{4-}**.

Amidinium carboxylate forms a complementary dimer (d2a2) and other bonds (Scheme 13b). Systematic structural design is possible to assume d2a2 motif formation. The amidinium and carboxylate in Scheme 28 are used to construct porous HOFs, whose details are described below[393–399].

In the system of **TPE^{4+}**, **TPE^{4+}·2Ph^{2-}**, **TPE^{4+}·2BPh^{2-}**, **TPE^{4+}·2Bpy^{2-}**, **TPE^{4+}·2TPh^{2-}** are reported as porous structures, in which there are water-penetrated H-bonds. Both networking and assembling are different, and they are isomeric HOFs. On the contrary, homotypic ***dia*** networks are obtained by salts with tetrahedral tectons (Figures 39–43) except for a non-***dia*** network through open dimers, **TBPhM^{4+}·2aniline^{2-}**. Only **TBPhM^{4+}·2Anth^{2-}** are constructed with the open dimer, and others are networked through complementary dimers. The networks in Figures 39 and 40 stacks in the same style to form square channels, so these HOFs are isostructural. However, not all homotypic networks yield isostructural HOFs. The structures shown in Figure 41a–e are isomeric microporous structures with the different assembling of networks.

Charge-assisted H-bonding leads to the construction of many homotypic networks but cannot control their accumulation to form isostructural whole structures. They are often fragile to solvent removal and immersion, and even those that have been evaluated for porosity have low gas uptakes[394].

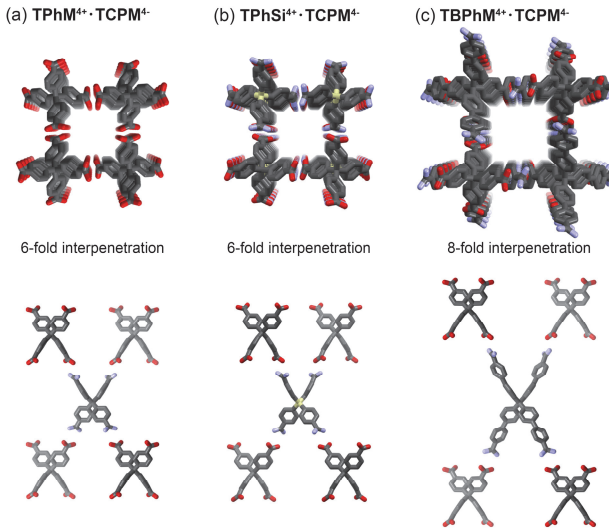

Figure 39. (top) Assembling structures and (bottom) H-bonding networks of amidinium carboxylate derivatives. Disordered moieties and guest molecules are omitted for clarity.

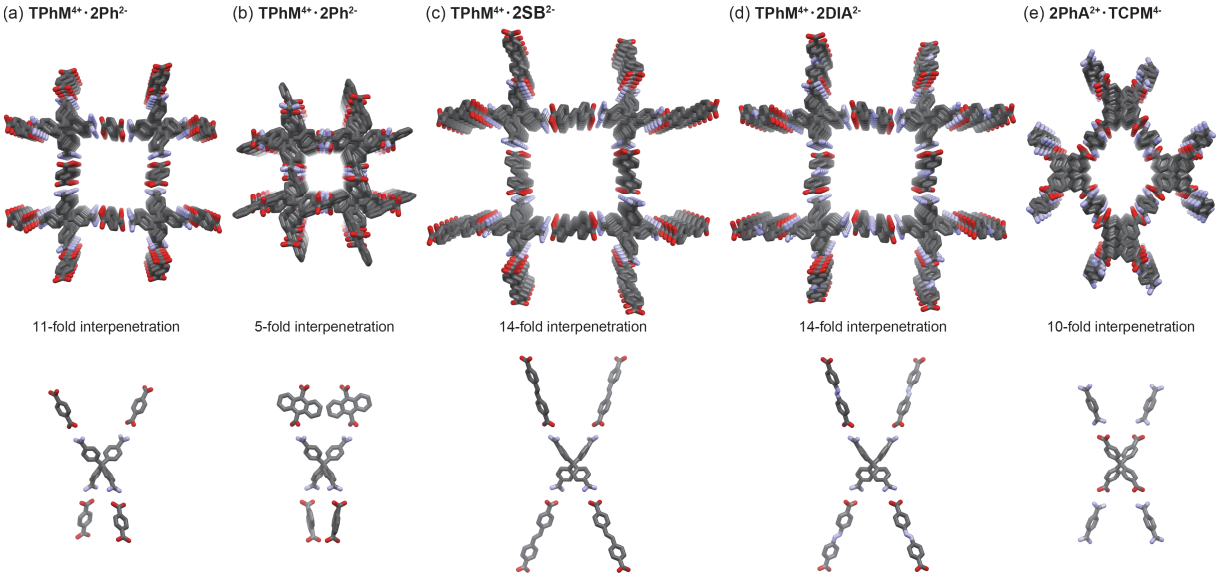

Figure 40. (top) Assembling structures and (bottom) H-bonding networks of amidinium carboxylate derivatives. Disordered moieties and guest molecules are omitted for clarity.

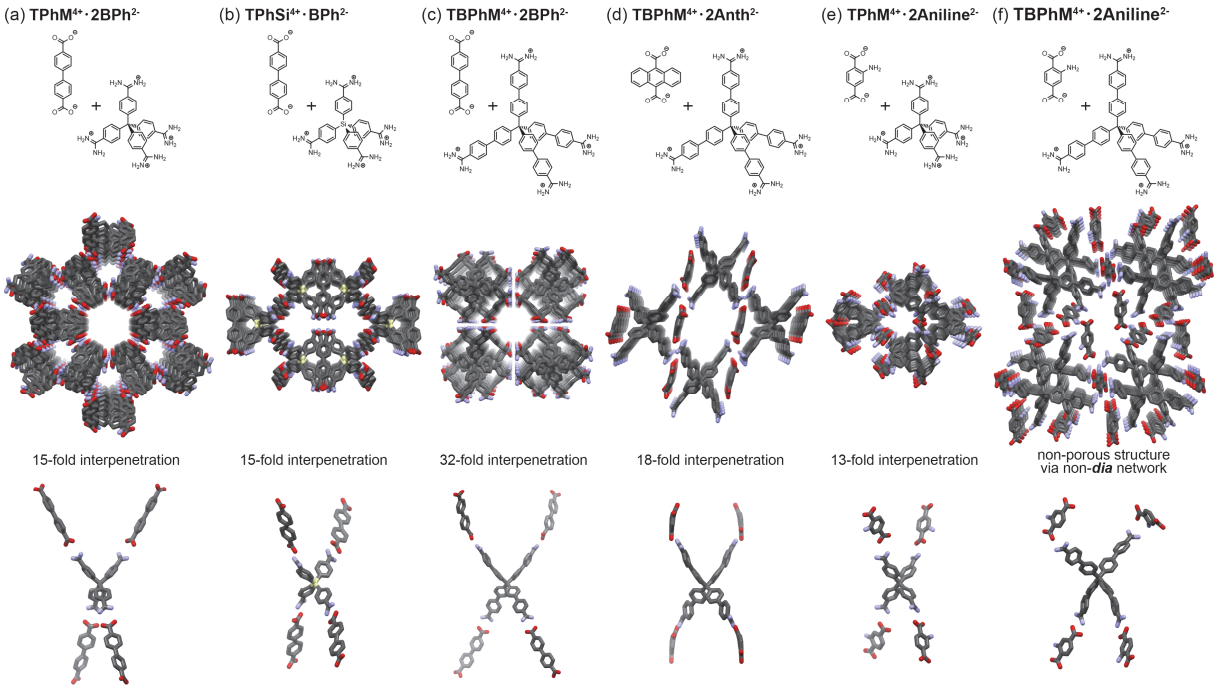

Figure 41. (top) Chemical structures**,** (middle) assembling structures, and (bottom) H-bonding networks of amidinium carboxylate derivatives. Disordered moieties and guest molecules are omitted for clarity.

F. Ammonium carboxylate

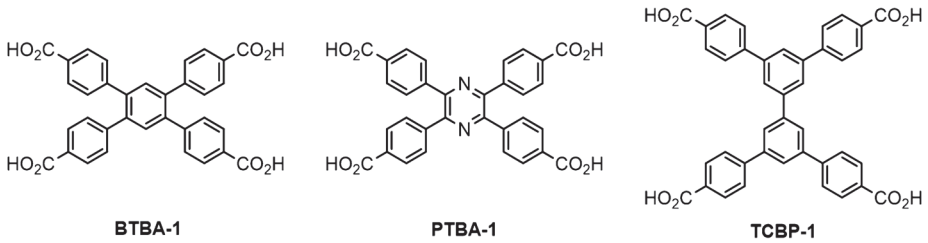

Scheme 29. Chemical structure of planar tetratopic carboxylic acid tectons, **BTBA**, **PTBA**, and **TCBP.**

As salts of ammonium carboxylate, planar tetratopic tectons (Scheme 29)[284] and tetrakis(4-carboxyphenyl)methane[400] were reported. 1:2 Co-crystals of planar tectons and dimethylamine in situ generated from DMF were networked through two types of H-bonding. One tetratopic tecton had two carboxylates and two carboxylic acids, whose H-bonding yielded ***sql*** networks (Figure 42). **BTBA-1** and **PTBA-1** had very similar skeletons and were isostructural HOFs. **TCBP-1** is a quasi-isostructural HOF because the concept of interlayer H-bonding was identical, while its style was different.

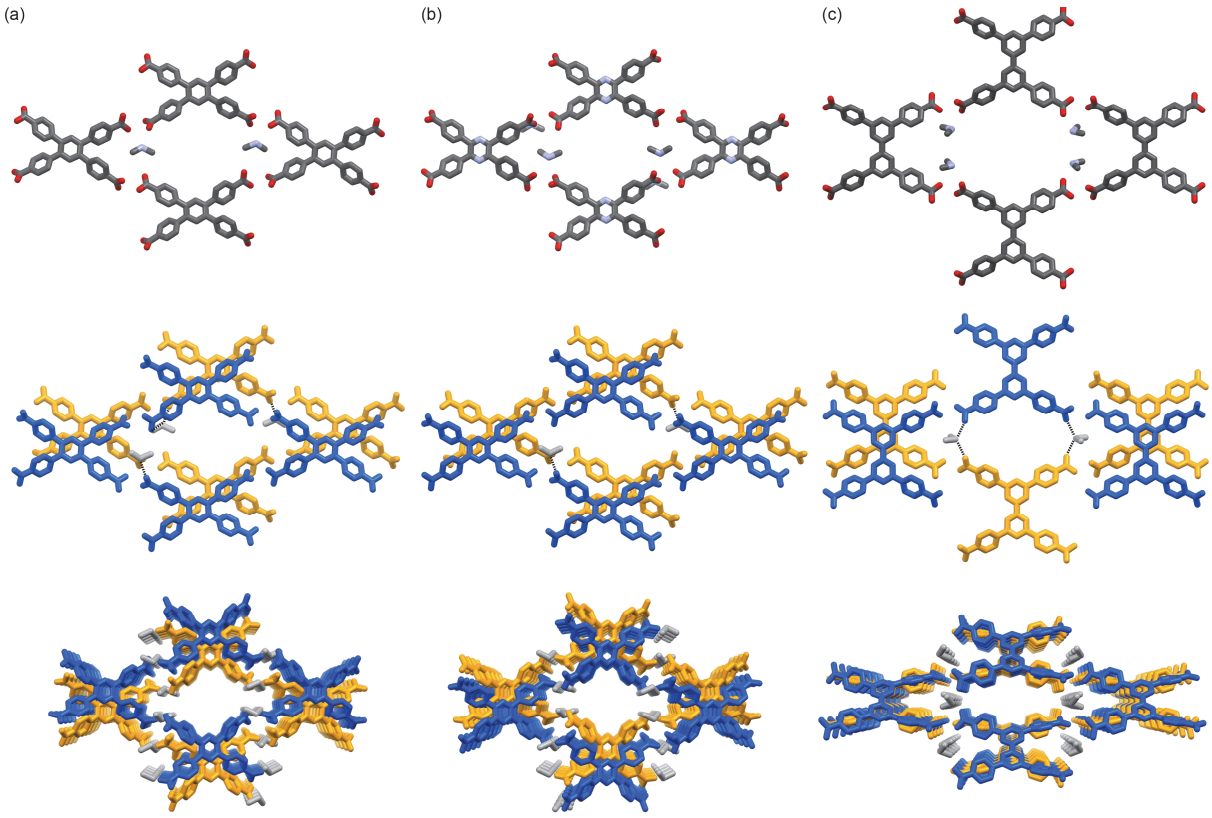

Figure 42. Crystal structures of complexes of dimethylamine and tetratopic carboxylic acid derivative: (a) **BTBA-1**, (b) **PTBA-1**, and (c) **TCBP-1**. (top) Rhombic networks, (middle) H-bonding between layers, and (bottom) assembling structures. Disordered moieties and guest molecules are omitted for clarity.

G. Ammonium sulfonate

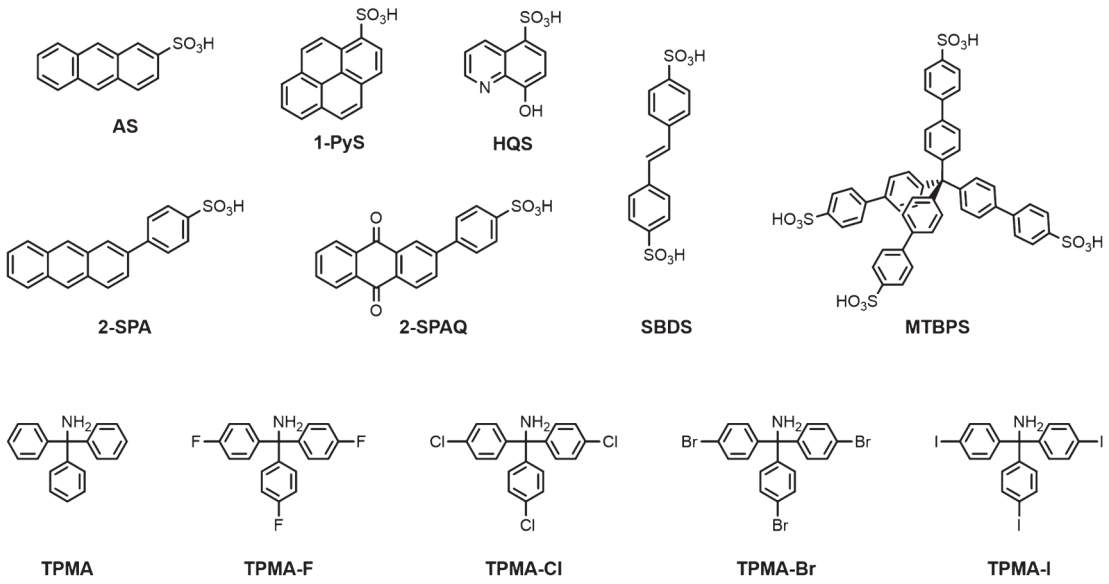

Scheme 30. Chemical structure of sulfonic acids and sterically hindered primary amines, **2-AS**, **1-PyS**, **HQS**, **2-SPA**, **2-SPAQ**, **SBDS**, **MTBPS**, **TPMA**, and **TPMA-X** (X = F, Cl, Br, and I).

Porous structures had also been reported from ammonium sulfonates[247–253,400–404], but there were limited examples of isostructural HOFs. For example, salts of tetrakis(4-sulfophenyl)methane with various diamine derivatives (*trans*-1,4-diaminocyclohexane, *p*-phenylenediamine, and benzidine) show different H-bonds and whole structures[400]. In contrast, salts with a sterically hindered primary amine such as trityl formed a tetrahedral-shaped [4+4] supramolecular cluster (Scheme 13b) through charge-assisted H-bonding. This unique cluster was linked with sulfonic acid derivatives to construct homotypic ***dia*** networks systematically[247–253]. The style and number of interpenetrations depended on constituents and crystalized conditions. Salts of mono-, di-, and tetrasulfonic acids in Scheme 30 and **TPMA** are used. Two monosulfonic acids behaved as a supramolecular disulfonic acid aggregated by H-bonding in **HQS** and π-π stacking in others (Figure 43). In the system of **MTBPS**, the homotypic networks of salts with halogen-substituted **TPMA** (**TPMA-F**, **-Cl**, **-Br**, and **-I**) were reported (Figure 44). Only **MTBPS-TPMA** salt shows anti-parallel interpenetration, whereas the others are isostructural HOFs with parallel interpenetration.

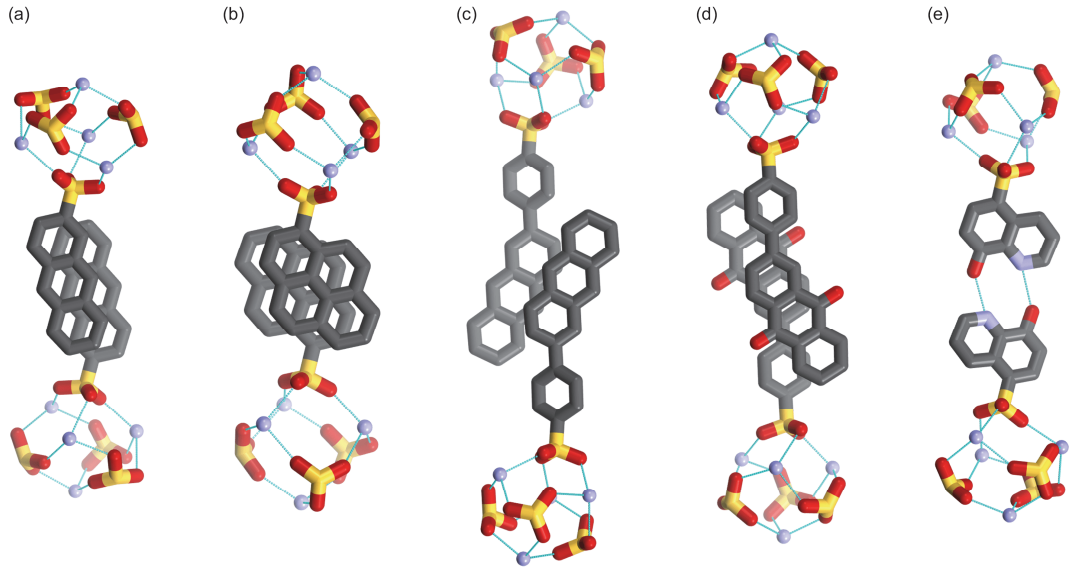

Figure 43. Crystal structures of [4+4] supramolecular cluster and supramolecular disulfonic acids, whose two monosulfonic acids aggregated by hydrogen bonding in **HQS** and π-π stacking in others.

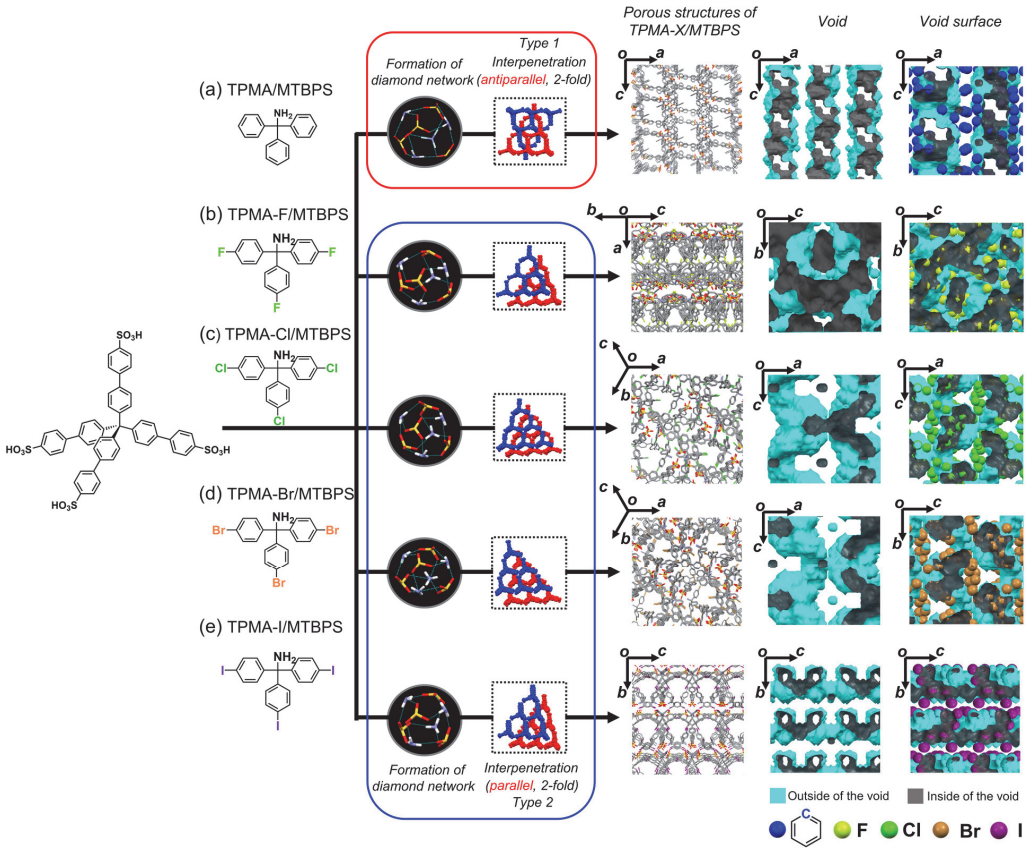

Figure 44. Diversification of void structures and environments in diamondoid porous organic salts (*d*-POSs) using tetrahedral-structured tetrasulfonic acid (**MTBPS**) and triphenylmethylamine derivatives (**TPMA-X**). Schematic images of the construction and the resultant porous and void structures of (a) **TPMA/MTBPS**, (b) **TPMA-F/MTBPS**, (c) **TPMA-Cl/MTBPS**, (d) **TPMA-Br/MTBPS**, (e) **TPMA-I/MTBPS**. (Reproduced permission from ref. 251, copyright 2022 Wiley-VCH.)

H. Pyridinium carboxylate

There are some examples of constructing porous structures by analogous compounds (Scheme 31) but not isostructural HOFs (Figure 45)[244,245]. Only co-crystals **1-3** possessed three-dimensional ***cds*** networks with 4-fold interpenetration, and other co-crystals, **2-3**, **2-4**, and **2-5** formed homotypic ***sql*** networks with different assemblies. In **2-3**, the planar network stacked with offset to form a whole structure with 1D channel *via* AB simple stacking, while **2-4** and **2-5** did not assemble in the same way. In **2-4**, planar networks assembled and formed a single-layer offset interpenetration to yield a high-density porous structure. In **2-5**, undulated ***sql*** networks also formed a single-layer offset interpenetration. As described above, isomeric structures were given by the networks and assemblies, and systematic construction has not yet been completed.

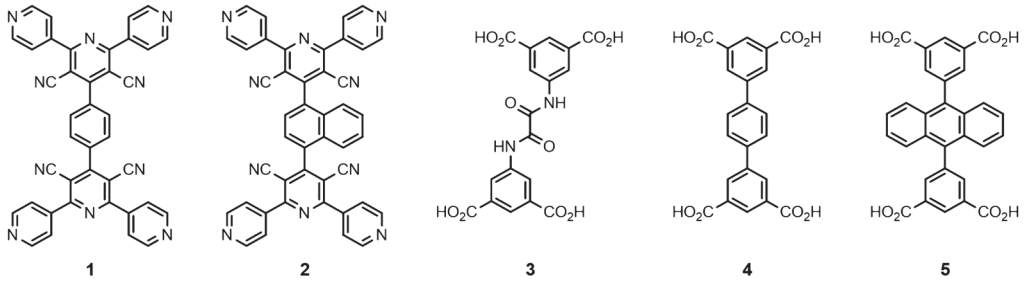

Scheme 31. Chemical structure of tetratopic pyridine and carboxylic acid tectons, **1**, **2**, **3**, **4**, and **5**.

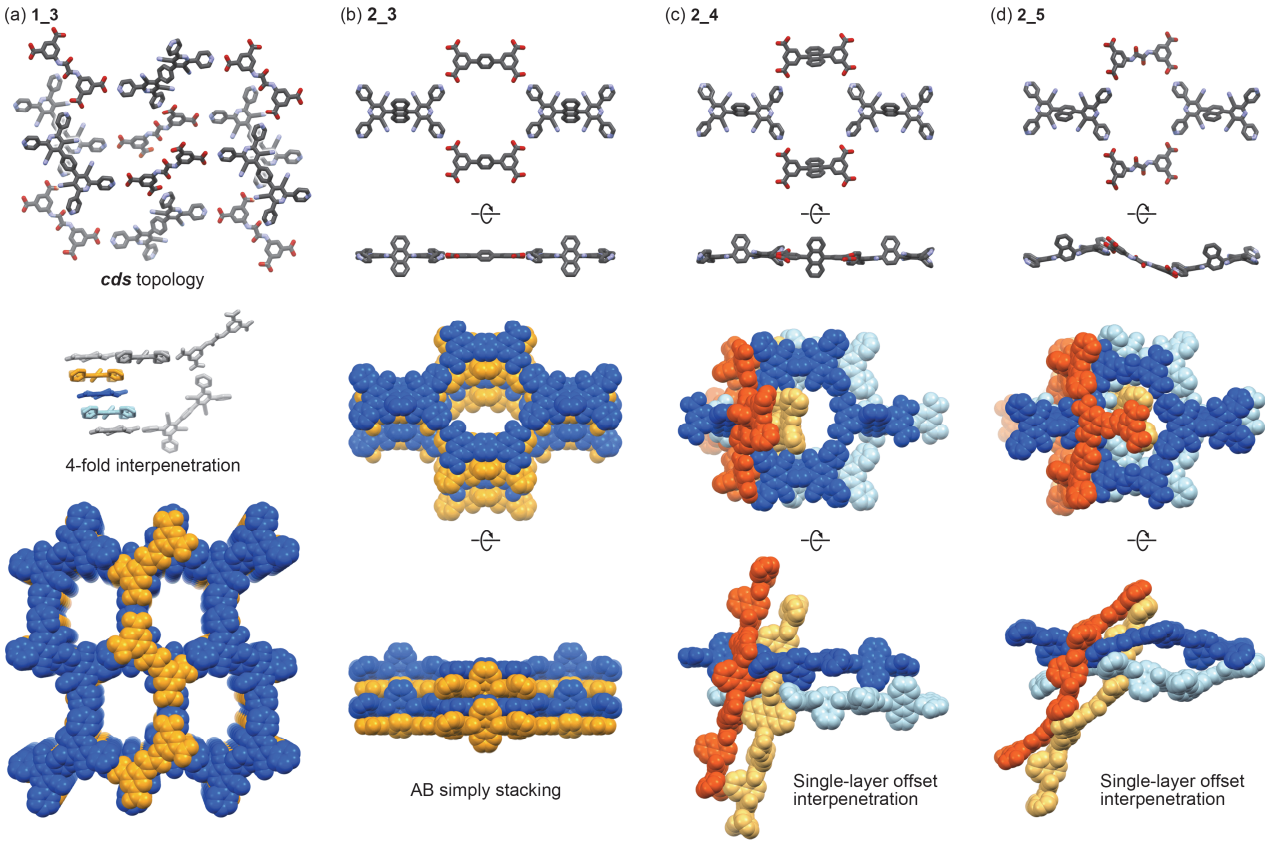

Figure 45. (a) Crystal structure of **1-3**: (top) H-bonding ***cds*** network**,** (middle) interpenetrated network, and (bottom) assembling structure. Crystal structures of (b) **2-3**, (c) **2-4**, and (d) **2-5**: (top) H-bonding ***sql*** networks and (bottom) their assemblies. Disordered moieties and guest molecules are omitted for clarity.

1.9 Purpose of this thesis

POFs can be constructed using a variety of organic molecules, resulting in the systematic construction of diverse and isostructural porous structures. Therefore, POFs have a library of numerous ordered pores compared to other porous materials. In particular, HOFs have attracted much attention in recent years due to high crystallinity, reusability, and structural diversity, but the systematic construction of the entire porous structure is limited and still in progress.

As shown in section 1.8.4, the systematic construction of homotypic networks has been actively developed by controlling the supramolecular synthon and the molecular arrangement based on crystal engineering approaches. However, there are some problems with controlling of network assemblies. Several possible supramolecular synthons for one H-bonding motif lead to various structures. Multiple stable states depending on the molecular structure and construction conditions also result in a variety of structures. As a result, obtained unique structure is also one-of-a-kind, and the construction of isostructural HOFs is still under development. From another perspective, it is also progressing that the systematic construction of highly stable frameworks, such as HOFs with persistent porosity. Developing a systematic design principle that achieves designability and stability in a compatible manner is necessary.

In terms of designability, networking through a complementary dimer of carboxylic acids is an excellent motif due to its high directionality. Planar structures, which are often used as molecular shapes, are challenging to control the assembling because the constituent environments determine the accumulation, and structural transitions due to layer slippage often occur in response to stimuli. There are not many examples of isostructural HOF construction (*i.e.*, carboxylic acid derivatives with pyrene core in Figure 19, and pyrazole derivatives in Figures 34–36). The same problems of assembly exist in three-dimensional networks, but derivatives with π-conjugated core can obtain an interpenetrated porous structure through π-interaction controllably (Figures 20 and 25). Significantly, the interpenetrated structure by π-π stacking of biphenyl (Figure 20a), HAT, benzene, and DC (Figure 25) cores shows excellent stability. To summarize, stacking non-planar π-conjugated molecules results in the stability and controllable assembly.

Given the above, the author focused on the construction method by stacking π-conjugated skeletons with distorted cores, such as HAT. The distorted core skeleton is expected to stack uniformly, even after modifying peripheral spacer groups. This stacking is named "shape-fitted docking," which is uniformly stacking orthogonal to H-bond. The author hypothesized that this docking is a base for isostructural, stable HOFs by spacer design (Figure 46).

In Chapter 2, the author described the isostructural construction by spacer-designed analogs with hexaazatriphenylene as core and carboxylic acid as bonding motif. The building blocks are **BPHAT** and **TPHAT** with biphenyl and terphenyl as spacer, respectively, which are extended from **CPHAT**. In addition, **TolHAT** and **ThiaHAT** were designed to replace the central benzene of the terphenyl moiety was replaced by acetylene and benzo-2,1,3-thiadiazol to reduce and increase the steric hindrance of the double-terminated Ph group, respectively. Except for low crystalline precipitates of **TPHAT**, three analogs: **BPHAT**, **TolHAT**, and **ThiaHAT** constructed isostructural HOFs by shape-fitted docking of ***pcu*** network. Only **TolHAT** was fragile, but **BPHAT** and **ThiaHAT** showed excellent stability against heat (300 °C), solvent

immersion, and removal. A fluctuation of the peripheral groups from molecular dynamics simulation can precisely evaluate this stability. The spacer design enabled the systematic construction of rigid isostructural HOFs with extended pores.

In Chapter 3, the author attempted to construct isostructural HOFs with a core of dibenzo[*g*,*p*]chrysene (DBC), a nonplanar π-conjugated molecule, because DBC is also expected to be accumulated in shape-fitted docking. The tetrakis(4-carboxyphenyl) derivative **CPDBC** gave **CPDBC-1** with eclipsed stacking. In addition, an unexpected structure with staggered stacking, **CPDBC-2**, was obtained. **CPDBC-2** was a structure stacked in a 90° rotation and "disappeared crystal". Bulk crystalline **CPDBC-1** showed excellent thermal stability and porosity. As a comparison, HOF construction was performed with non-annulated analog **CBPE**, which forms not a shape-fitted docking structure but a triaxial woven structure. These results indicate the importance of nonplanar π-conjugated cores.

In Chapter4, the author attempted to design a spacer in DBC derivatives. The derivative **CBPDBC** with carboxybiphenyl groups yields poor crystalline precipitates due to solubility and aggregation problems. It is an example of the limitations of simple phenylene elongation of the spacer. However, the DBC derivatives with 1,4-, 1,5-, and 2,6-substituted naphthyl groups yielded isostructural HOFs (**C1N4DBC-1**, **C1N5DBC-1**, and **C2N6DBC-1**, respectively), comparable to **CPDBC-1**. Importantly, these isostructures possessed different properties ranging from stable to flexible to fragile toward guest removal. These differences are attributed to the pore geometry and H-bonding style due to the isomeric effect. The results implied that the DBC core is fundamental to isostructural construction of HOFs and that the isomeric effect at spacers significantly affected structural properties.

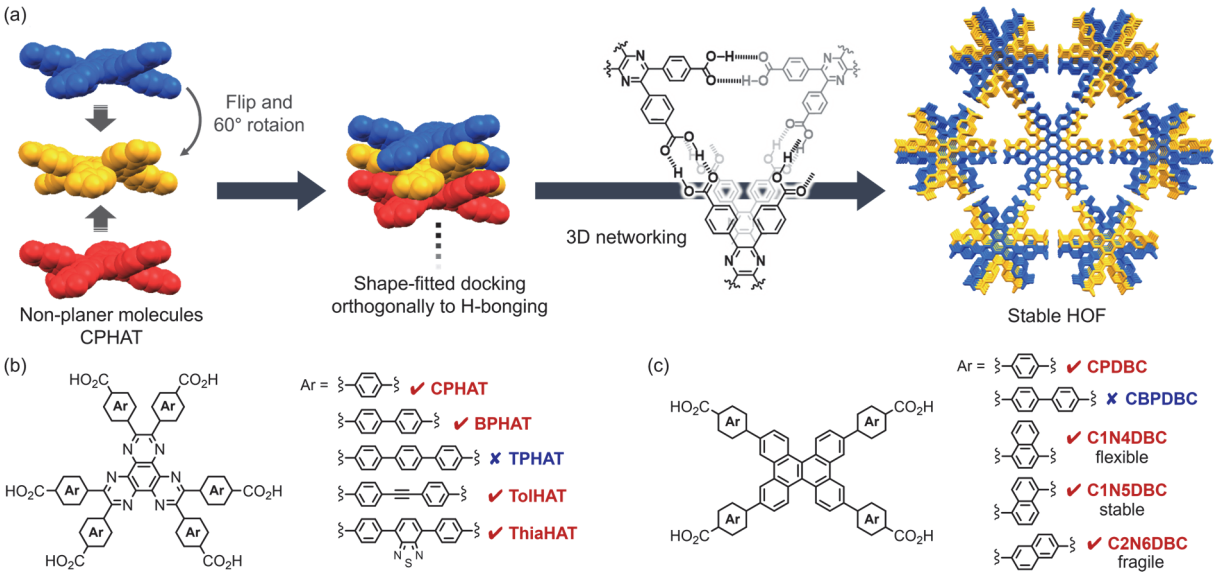

Figure 46. Design principle of assembling nonplanar π-conjugated molecules though orthogonally shape-fitted docking. (a) Hierarchical construction of **CPHAT** through the shape-fitted docking and the 3D H-bonding network of carboxylic acid. Chemical structures of (b) HAT derivatives and (c) DBC derivatives to construct isostructural HOFs. HOFs in red are successful in isostructural construction, while the blue ones are failed.

1.10 References

1 J. Rouquerol, D. Avnir, C. W. Fairbridge, D. H. Everett, J. M. Haynes, N. Pernicone, J. D. F. Ramsay, K. S. W. Sing and K. K. Unger, *Pure Appl. Chem.*, 1994, **66**, 1739–1758.

2 H. Li, K. Wang, Y. Sun, C. T. Lollar, J. Li and H. C. Zhou, *Mater. Today*, 2018, **21**, 108–121.

3 L. Zhu and Y.-B. Zhang, *Molecules*, 2017, **22**, 1149.

4 Z. Wang, S. Zhang, Y. Chen, Z. Zhang and S. Ma, *Chem. Soc. Rev.*, 2020, **49**, 708–735.

5 Y. S. Wei, M. Zhang, R. Zou and Q. Xu, *Chem. Rev.*, 2020, **120**, 12089–12174.

6 Y. N. Gong, X. Guan and H. L. Jiang, *Coord. Chem. Rev.*, 2023, **475**, 214889.

7 Q. Guan, L. Le Zhou and Y. Bin Dong, *Chem. Soc. Rev.*, 2022, **51**, 6307–6416.

8 W.-T. Koo, J.-S. Jang and I.-D. Kim, *Chem*, 2019, **5**, 1938–1963.

9 P. She, Y. Qin, X. Wang and Q. Zhang, *Adv. Mater.*, 2022, **34**, 1–27.

10 X. F. Lu, Y. Fang, D. Luan and X. W. D. Lou, *Nano Lett.*, 2021, **21**, 1555–1565.

11 C. Xia, K. O. Kirlikovali, T. H. C. Nguyen, X. C. Nguyen, Q. B. Tran, M. K. Duong, M. T. Nguyen Dinh, D. L. T. Nguyen, P. Singh, P. Raizada, V. H. Nguyen, S. Y. Kim, L. Singh, C. C. Nguyen, M. Shokouhimehr and Q. Van Le, *Coord. Chem. Rev.*, 2021, **446**, 214117.

12 D. W. Kang, M. Kang and C. S. Hong, *J. Mater. Chem. A*, 2020, **8**, 7474–7494.

13 X. Zhao, P. Pachfule and A. Thomas, *Chem. Soc. Rev.*, 2021, **50**, 6871–6913.

14 E. Linnane, S. Haddad, F. Melle, Z. Mei and D. Fairen-Jimenez, *Chem. Soc. Rev.*, 2022, **51**, 6065–6086.

15 C. Liao and S. Liu, *J. Mater. Chem. B*, 2021, **9**, 6116–6128.

16 G. Crini, *Bioresour. Technol.*, 2006, **97**, 1061–1085.

17 M. T. Yagub, T. K. Sen, S. Afroze and H. M. Ang, *Adv. Colloid Interface Sci.*, 2014, **209**, 172–184.

18 R. L. Albright, *React. Polym. Ion Exch. Sorbents*, 1986, **4**, 155–174.

19 Y. Zhang and S. N. Riduan, *Chem. Soc. Rev.*, 2012, **41**, 2083–2094.

20 D. Wu, F. Xu, B. Sun, R. Fu, H. He and K. Matyjaszewski, *Chem. Rev.*, 2012, **112**, 3959–4015.

21 S. Zhang, Q. Yang, C. Wang, X. Luo, J. Kim, Z. Wang and Y. Yamauchi, *Adv. Sci.*, 2018, **5**, 1801116.

22 T. Zhang, G. Xing, W. Chen and L. Chen, *Mater. Chem. Front.*, 2020, **4**, 332–353.

23 M. G. Mohamed, A. F. M. El-Mahdy, M. G. Kotp and S. W. Kuo, *Mater. Adv.*, 2022, **3**, 707–733.

24 P. Sozzani, S. Bracco, A. Comotti, L. Ferretti and R. Simonutti, *Angew. Chem. Int. Ed.*, 2005, **44**, 1816–1820.

25 C. G. Bezzu, L. A. Burt, C. J. McMonagle, S. A. Moggach, B. M. Kariuki, D. R. Allan, M. Warren and N. B. McKeown, *Nat. Mater.*, 2019, **18**, 740–745.

26 L. J. Barbour, *Chem. Commun.*, 2006, 1163–1168.

27 M. Mastalerz, *Chem. Eur. J.*, 2012, **18**, 10082–10091.

28 M. I. Hashim, C. W. Hsu, H. T. M. Le and O. S. Miljanić, *Synlett*, 2016, **27**, 1907–1918.

29 A. I. Cooper, *ACS Cent. Sci.*, 2017, **3**, 544–553.

30 M. A. Little and A. I. Cooper, *Adv. Funct. Mater.*, 2020, **30**, 1–30.

31 H. Yamagishi, *Chem. Commun.*, 2022, **58**, 11887–11897.

32 O. M. Yaghi, M. O'Keeffe, N. W. Ockwig, H. K. Chae, M. Eddaoudi and J. Kim, *Nature*, 2003, **423**, 705–714.

33 J. Jiang, Y. Zhao and O. M. Yaghi, *J. Am. Chem. Soc.*, 2016, **138**, 3255–3265.

34 O. M. Yaghi, *J. Am. Chem. Soc.*, 2016, **138**, 15507–15509.

35 O. M. Yaghi, *ACS Cent. Sci.*, 2019, **5**, 1295–1300.

36 Z. Chen, S. L. Hanna, L. R. Redfern, D. Alezi, T. Islamoglu and O. K. Farha, *Coord. Chem. Rev.*, 2019, **386**, 32–49.

37 W. Xu, B. Tu, Q. Liu, Y. Shu, C. C. Liang, C. S. Diercks, O. M. Yaghi, Y. B. Zhang, H. Deng and Q. Li, *Nat. Rev. Mater.*, 2020, **5**, 764–779.

38 P. M. Bhatt, V. Guillerm, S. J. Datta, A. Shkurenko and M. Eddaoudi, *Chem*, 2020, **6**, 1613–1633.

39 R. Freund, S. Canossa, S. M. Cohen, W. Yan, H. Deng, V. Guillerm, M. Eddaoudi, D. G. Madden, D. Fairen-Jimenez, H. Lyu, L. K. Macreadie, Z. Ji, Y. Zhang, B. Wang, F. Haase, C. Wöll, O. Zaremba, J. Andreo, S. Wuttke and C. S. Diercks, *Angew. Chem. Int. Ed.*, 2021, **60**, 23946–23974.

40 S. Y. Ding and W. Wang, *Chem. Soc. Rev.*, 2013, **42**, 548–568.

41 P. J. Waller, F. Gándara and O. M. Yaghi, *Acc. Chem. Res.*, 2015, **48**, 3053–3063.

42 S. Kandambeth, K. Dey and R. Banerjee, *J. Am. Chem. Soc.*, 2019, **141**, 1807–1822.

43 K. Geng, T. He, R. Liu, S. Dalapati, K. T. Tan, Z. Li, S. Tao, Y. Gong, Q. Jiang and D. Jiang, *Chem. Rev.*, 2020, **120**, 8814–8933.

44 X. Guan, Q. Fang, Y. Yan and S. Qiu, *Acc. Chem. Res.*, 2022, **55**, 1912–1927.

45 F. Haase and B. V. Lotsch, *Chem. Soc. Rev.*, 2020, **49**, 8469–8500.

46 Y. F. Han, Y. X. Yuan and H. B. Wang, *Porous hydrogen-bonded organic frameworks*, 2017, vol. 22.

47 J. Luo, J. W. Wang, J. H. Zhang, S. Lai and D. C. Zhong, *CrystEngComm*, 2018, **20**, 5884–5898.

48 I. Hisaki, C. Xin, K. Takahashi and T. Nakamura, *Angew. Chem. Int. Ed.*, 2019, **58**, 11160–11170.

49 I. Hisaki, *J. Incl. Phenom. Macrocycl. Chem.*, 2020, **96**, 215–231.

50 P. Li, M. R. Ryder and J. F. Stoddart, *Acc. Mater. Res.*, 2020, **1**, 77–87.

51 L. Chen, B. Zhang, L. Chen, H. Liu, Y. Hu and S. Qiao, *Mater. Adv.*, 2022, **3**, 3680–3708.

52 X. Song, Y. Wang, C. Wang, D. Wang, G. Zhuang, K. O. Kirlikovali, P. Li and O. K. Farha, *J. Am. Chem. Soc.*, 2022, **144**, 10663–10687.

53 G. Kupgan, T. P. Liyana-Arachchi and C. M. Colina, *Langmuir*, 2017, **33**, 11138–11145.

54 G. R. Desiraju, *Crystal Engineering. The Design of Organic Solids*, Elsevier, Amsterdam, 1989.

55 G. R. Desiraju, *Angew. Chem. Int. Ed. Engl.*, 1995, **34**, 2311–2327.

56 B. Moulton and M. J. Zaworotko, *Chem. Rev.*, 2001, **101**, 1629–1658.

57 G. R. Desiraju, *Angew. Chem. Int. Ed.*, 2007, **46**, 8342–8356.

58 G. R. Desiraju, *J. Am. Chem. Soc.*, 2013, **135**, 9952–9967.

59 M. D. Hollingsworth, *Science*, 2002, **295**, 2410–2413.

60 O. K. Farha, A. Ö. Yazaydin, I. Eryazici, C. D. Malliakas, B. G. Hauser, M. G. Kanatzidis, S. T. Nguyen, R. Q. Snurr and J. T. Hupp, *Nat. Chem.*, 2010, **2**, 944–948.

61 W. Zhang, L. Chen, S. Dai, C. Zhao, C. Ma, L. Wei, M. Zhu, S. Y. Chong, H. Yang, L. Liu, Y. Bai, M. Yu, Y. Xu, X. W. Zhu, Q. Zhu, S. An, R. S. Sprick, M. A. Little, X. Wu, S. Jiang, Y. Wu, Y. B. Zhang, H. Tian, W. H. Zhu and A. I. Cooper, *Nature*, 2022, **604**, 72–79.

62 K. S. W. Sing, *Pure Appl. Chem.*, 1985, **57**, 603–619.

63 M. Thommes, K. Kaneko, A. V. Neimark, J. P. Olivier, F. Rodriguez-Reinoso, J. Rouquerol and K. S. W. Sing, *Pure*

Appl. Chem., 2015, **87**, 1051–1069.

64 S. Yuan, L. Zou, J. S. Qin, J. Li, L. Huang, L. Feng, X. Wang, M. Bosch, A. Alsalme, T. Cagin and H. C. Zhou, *Nat. Commun.*, 2017, **8**, 15356.

65 L. Feng, K. Y. Wang, X. L. Lv, T. H. Yan and H. C. Zhou, *Natl. Sci. Rev.*, 2020, **7**, 1743–1758.

66 G. Cai, P. Yan, L. Zhang, H. C. Zhou and H. L. Jiang, *Chem. Rev.*, 2021, **121**, 12278–12326.

67 D. Braga, G. R. Desiraju, J. S. Miller, A. G. Orpen and S. L. Price, *CrystEngComm*, 2002, **4**, 500–509.

68 M. Simard, D. Su and J. D. Wuest, *J. Am. Chem. Soc.*, 1991, **113**, 4696–4698.

69 D. Braga, F. Grepioni and G. R. Desiraju, *Chem. Rev.*, 1998, **98**, 1375–1405.

70 G. R. Desiraju, *Acc. Chem. Res.*, 2002, **35**, 565–573.

71 E. Arunan, G. R. Desiraju, R. A. Klein, J. Sadlej, S. Scheiner, I. Alkorta, D. C. Clary, R. H. Crabtree, J. J. Dannenberg, P. Hobza, H. G. Kjaergaard, A. C. Legon, B. Mennucci and D. J. Nesbitt, *Pure Appl. Chem.*, 2011, **83**, 1619–1636.

72 R. B. Lin, Y. He, P. Li, H. Wang, W. Zhou and B. Chen, *Chem. Soc. Rev.*, 2019, **48**, 1362–1389.

73 A. J. L. Jesus and J. S. Redinha, *J. Phys. Chem. A*, 2011, **115**, 14069–14077.

74 S. E. Kochanek, T. M. Clymer, V. S. Pakkala, S. P. Hebert, K. Reeping, S. M. Firestine and J. D. Evanseck, *J. Phys. Chem. B*, 2015, **119**, 1184–1191.

75 N. J. Singh, S. K. Min, D. Y. Kim and K. S. Kim, *J. Chem. Theory Comput.*, 2009, **5**, 515–529.

76 C. R. Martinez and B. L. Iverson, *Chem. Sci.*, 2012, **3**, 2191–2201.

77 C. Zhang, *J. Comput. Chem.*, 2011, **32**, 152–160.

78 G. R. Desiraju and A. Gavezzotti, *Acta Crystallogr. Sect. B*, 1989, **45**, 473–482.

79 Z. F. Yao, J. Y. Wang and J. Pei, *Cryst. Growth Des.*, 2018, **18**, 7–15.

80 D. A. Dougherty, *Acc. Chem. Res.*, 2013, **46**, 885–893.

81 D. A. Dougherty, *J. Nutr.*, 2007, **137**, 1504–1508.

82 A. S. Mahadevi and G. N. Sastry, *Chem. Rev.*, 2013, **113**, 2100–2138.

83 J. A. Carrazana-García, J. Rodríguez-Otero and E. M. Cabaleiro-Lago, *J. Phys. Chem. B*, 2011, **115**, 2774–2782.

84 C. D. Sherrill, *Acc. Chem. Res.*, 2013, **46**, 1020–1028.

85 A. Frontera, D. Quiñonero and P. M. Deyà, *Wiley Interdiscip. Rev. Comput. Mol. Sci.*, 2011, **1**, 440–459.

86 D. Kim, P. Tarakeshwar and K. S. Kim, *J. Phys. Chem. A*, 2004, **108**, 1250–1258.

87 B. L. Schottel, H. T. Chifotides and K. R. Dunbar, *Chem. Soc. Rev.*, 2008, **37**, 68–83.

88 P. García-Novo, A. Campo-Cacharrón, E. M. Cabaleiro-Lago and J. Rodríguez-Otero, *Phys. Chem. Chem. Phys.*, 2012, **14**, 104–112.

89 A. Campo-Cacharrõn, E. M. Cabaleiro-Lago and J. Rodríguez-Otero, *J. Comput. Chem.*, 2014, **35**, 1533–1544.

90 J. Lee, J. Kim and T. Hyeon, *Adv. Mater.*, 2006, **18**, 2073–2094.

91 W. Chaikittisilp, K. Ariga and Y. Yamauchi, *J. Mater. Chem. A*, 2013, **1**, 14–19.

92 S. Dutta, A. Bhaumik and K. C. W. Wu, *Energy Environ. Sci.*, 2014, **7**, 3574–3592.

93 J. Liu, N. P. Wickramaratne, S. Z. Qiao and M. Jaroniec, *Nat. Mater.*, 2015, **14**, 763–774.

94 M. R. Benzigar, S. N. Talapaneni, S. Joseph, K. Ramadass, G. Singh, J. Scaranto, U. Ravon, K. Al-Bahily and A. Vinu, *Chem. Soc. Rev.*, 2018, **47**, 2680–2721.

95 C. Wang, Y. Yao, J. Li and Y. Yamauchi, *Acc. Mater. Res.*, 2022, **3**, 426–438.

96 N. B. McKeown, B. Gahnem, K. J. Msayib, P. M. Budd, C. E. Tattershall, K. Mahmood, S. Tan, D. Book, H. W. Langmi and A. Walton, *Angew. Chem. Int. Ed.*, 2006, **45**, 1804–1807.

97 M. Carta, R. Malpass-Evans, M. Croad, Y. Rogan, J. C. Jansen, P. Bernardo, F. Bazzarelli and N. B. McKeown, *Science*, 2013, **339**, 303–307.

98 N. B. McKeown, *Polymer (Guildf).*, 2020, **202**, 122736.

99 N. B. Mc Keown and P. M. Budd, *Chem. Soc. Rev.*, 2006, **35**, 675–683.

100 Y. Wang, B. S. Ghanem, Z. Ali, K. Hazazi, Y. Han and I. Pinnau, *Small Struct.*, 2021, **2**, 2100049.

101 J. Y. Lee, C. D. Wood, D. Bradshaw, M. J. Rosseinsky and A. I. Cooper, *Chem. Commun.*, 2006, 2670–2672.

102 C. D. Wood, T. Bien, A. Trewin, N. Hongjun, D. Bradshaw, M. J. Rosseinsky, Y. Z. Khimyak, N. L. Campbell, R. Kirk, E. Stöckel and A. I. Cooper, *Chem. Mater.*, 2007, **19**, 2034–2048.

103 M. P. Tsyurupa and V. A. Davankov, *React. Funct. Polym.*, 2006, **66**, 768–779.

104 N. Fontanals, R. M. Marcé, F. Borrull and P. A. G. Cormack, *Polym. Chem.*, 2015, **6**, 7231–7244.

105 L. Tan and B. Tan, *Chem. Soc. Rev.*, 2017, **46**, 3322–3356.

106 P. Kuhn, M. Antonietti and A. Thomas, *Angew. Chem. Int. Ed.*, 2008, **47**, 3450–3453.

107 P. Katekomol, J. Roeser, M. Bojdys, J. Weber and A. Thomas, *Chem. Mater.*, 2013, **25**, 1542–1548.

108 M. Liu, L. Guo, S. Jin and B. Tan, *J. Mater. Chem. A*, 2019, **7**, 5153–5172.

109 Z. Qian, Z. J. Wang and K. A. I. Zhang, *Chem. Mater.*, 2021, **33**, 1909–1926.

110 H. Chen, X. Suo, Z. Yang and S. Dai, *Adv. Mater.*, 2022, **34**, 2107947.

111 T. Ben, H. Ren, M. Shengqian, D. Cao, J. Lan, X. Jing, W. Wang, J. Xu, F. Deng, J. M. Simmons, S. Qiu and G. Zhu, *Angew. Chem. Int. Ed.*, 2009, **48**, 9457–9460.

112 T. Ben and S. Qiu, *CrystEngComm*, 2013, **15**, 17–26.

113 Y. Yuan and G. Zhu, *ACS Cent. Sci.*, 2019, **5**, 409–418.

114 A. I. Cooper, *Adv. Mater.*, 2009, **21**, 1291–1295.

115 Y. Xu, S. Jin, H. Xu, A. Nagai and D. Jiang, *Chem. Soc. Rev.*, 2013, **42**, 8012–8031.

116 J. S. M. Lee and A. I. Cooper, *Chem. Rev.*, 2020, **120**, 2171–2214.

117 S. Luo, Z. Zeng, H. Wang, W. Xiong, B. Song, C. Zhou, A. Duan, X. Tan, Q. He, G. Zeng, Z. Liu and R. Xiao, *Prog. Polym. Sci.*, 2021, **115**, 101374.

118 W. Zhang, H. Zuo, Z. Cheng, Y. Shi, Z. Guo, N. Meng, A. Thomas and Y. Liao, *Adv. Mater.*, 2022, **34**, 2104952.

119 D. D. M. J. L. Atwood, J. E. D. Davies, *Inclusion Compounds, Vol. 1–3 (Eds.: J. L. Atwood, J. E. D. Davies, D. D. MacNicol), Academic Press, London, 1984*, 1984.

120 F. H. Herbstein, M. Kapon and G. M. Reisner, *J. Incl. Phenom.*, 1987, **5**, 211–214.

121 S. V. Kolotuchin, E. E. Fenlon, S. R. Wilson, C. J. Loweth and S. C. Zimmerman, *Angew. Chem. Int. Ed. Engl.*, 1996, **34**, 2654–2657.

122 P. Brunet, M. Simard and J. D. Wuest, *J. Am. Chem. Soc.*, 1997, **119**, 2737–2738.

123 P. Brunet, E. Demers, T. Maris, G. D. Enright and J. D. Wuest, *Angew. Chem. Int. Ed.*, 2003, **42**, 5303–5306.

124 H. Sauriat-Dorizon, T. Maris, J. D. Wuest and G. D. Enright, *J. Org. Chem.*, 2003, **68**, 240–246.

125 N. Malek, T. Maris, M. Simard and J. D. Wuest, *J. Am. Chem. Soc.*, 2005, **127**, 5910–5916.

126 J.-H. Fournier, T. Maris and J. D. Wuest, *J. Org. Chem.*, 2004, **69**, 1762–1775.

127 D. Laliberté, T. Maris and J. D. Wuest, *J. Org. Chem.*, 2004, **69**, 1776–1787.

128 E. Demers, T. Maris and J. D. Wuest, *Cryst. Growth Des.*, 2005, **5**, 1227–1235.

129 M. D. Hollingsworth, B. D. Santarsiero and K. D. M. Harris, *Angew. Chem. Int. Ed. Engl.*, 1994, **33**, 649–652.

130 X. Wang, M. Simard and J. D. Wuest, *J. Am. Chem. Soc.*, 1994, **116**, 12119–12120.

131 D. Venkataraman, S. Lee, J. Zhang and J. S. Moore, *Nature*, 1994, **371**, 591–593.

132 K. Kobayashi, T. Shirasaka, A. Sato, E. Horn and N. Furukawa, *Angew. Chem. Int. Ed.*, 1999, **38**, 3483–3486.

133 C. J. Davis, P. T. Lewis, D. R. Billodeaux, F. R. Fronczek, J. O. Escobedo and R. M. Strongin, *Org. Lett.*, 2001, **3**, 2443–2445.

134 J. H. Fournier, T. Maris, J. D. Wuest, W. Guo and E. Galoppini, *J. Am. Chem. Soc.*, 2003, **125**, 1002–1006.

135 K. Kobayashi, A. Sato, S. Sakamoto and K. Yamaguchi, *J. Am. Chem. Soc.*, 2003, **125**, 3035–3045.

136 C. H. Görbitz, M. Nilsen, K. Szeto and L. W. Tangen, *Chem. Commun.*, 2005, 4288–4290.

137 M.-Č. Perron, F. Monchamp, H. Duval, D. Boils-Boissier and J. D. Wuest, *Pure Appl. Chem.*, 2004, **76**, 1345–1351.

138 N. Malek, T. Maris, M. È. Perron and J. D. Wuest, *Angew. Chem. Int. Ed.*, 2005, **44**, 4021–4025.

139 K. Endo, T. Sawaki, M. Koyanagi, K. Kobayashi, H. Masuda and Y. Aoyama, *J. Am. Chem. Soc.*, 1995, **117**, 8341–8352.

140 Y. Aoyama, K. Endo, T. Anzai, Y. Yamaguchi, T. Sawaki, K. Kobayashi, N. Kanehisa, H. Hashimoto, Y. Kai and H. Masuda, *J. Am. Chem. Soc.*, 1996, **118**, 5562–5571.

141 P. Bhyrappa, S. R. Wilson and K. S. Suslick, *J. Am. Chem. Soc.*, 1997, **119**, 8492–8502.

142 O. Saied, T. Maris, X. Wang, M. Simard and J. D. Wuest, *J. Am. Chem. Soc.*, 2005, **127**, 10008–10009.

143 T. Sawaki, K. Endo, K. Kobayashi, O. Hayashida and Y. Aoyama, *Bull. Chem. Soc. Jpn.*, 1997, 70, 3075–3079.

144 N. Song, T. Kakuta, T. aki Yamagishi, Y. W. Yang and T. Ogoshi, *Chem*, 2018, **4**, 2029–2053.

145 K. Jie, Y. Zhou, E. Li and F. Huang, *Acc. Chem. Res.*, 2018, **51**, 2064–2072.

146 K. Acharyya and P. S. Mukherjee, *Angew. Chem. Int. Ed.*, 2019, **58**, 8640–8653.

147 H. Li, M. Eddaoudi, M. O'Keeffe and O. M. Yaghi, *Nature*, 1999, **402**, 276–279.

148 M. Kondo, T. Yoshitomi, H. Matsuzaka, S. Kitagawa and K. Seki, *Angew. Chem. Int. Ed. Engl.*, 1997, **36**, 1725–1727.

149 S. Kitagawa, R. Kitaura and S. I. Noro, *Angew. Chem. Int. Ed.*, 2004, **43**, 2334–2375.

150 S. R. Batten, N. R. Champness, X.-M. Chen, J. Garcia-Martinez, S. Kitagawa, L. Öhrström, M. O'Keeffe, M. Paik Suh and J. Reedijk, *Pure Appl. Chem.*, 2013, **85**, 1715–1724.

151 T. Stolar, A. Prašnikar, V. Martinez, B. Karadeniz, A. Bjelić, G. Mali, T. Friščić, B. Likozar and K. Užarević, *ACS Appl. Mater. Interfaces*, 2021, **13**, 3070–3077.

152 T. D. Bennett and A. K. Cheetham, *Acc. Chem. Res.*, 2014, **47**, 1555–1562.

153 L. Zou, C. C. Hou, Z. Liu, H. Pang and Q. Xu, *J. Am. Chem. Soc.*, 2018, **140**, 15393–15401.

154 C. Liu, J. Wang, J. Wan, Y. Cheng, R. Huang, C. Zhang, W. Hu, G. Wei and C. Yu, *Angew. Chem. Int. Ed.*, 2020, **59**, 3630–3637.

155 D. Umeyama, N. P. Funnell, M. J. Cliffe, J. A. Hill, A. L. Goodwin, Y. Hijikata, T. Itakura, T. Okubo, S. Horike and S. Kitagawa, *Chem. Commun.*, 2015, **51**, 12728–12731.

156 R. Gaillac, P. Pullumbi, K. A. Beyer, K. Chapman, D. A. Keen, T. D. Bennett and F. X. Coudert, *Nat. Mater.*, 2017, **16**, 1149–1155.

157 N. Ma and S. Horike, *Chem. Rev.*, 2022, **122**, 4163–4203.

158 J. Hou, C. W. Ashling, S. M. Collins, A. Krajnc, C. Zhou, L. Longley, D. N. Johnstone, P. A. Chater, S. Li, M. V. Coulet, P. L. Llewellyn, F. X. Coudert, D. A. Keen, P. A. Midgley, G. Mali, V. Chen and T. D. Bennett, *Nat. Commun.*, 2019, **10**, 2580.

159 L. Longley, C. Calahoo, R. Limbach, Y. Xia, J. M. Tuffnell, A. F. Sapnik, M. F. Thorne, D. S. Keeble, D. A. Keen, L. Wondraczek and T. D. Bennett, *Nat. Commun.*, 2020, **11**, 5800.

160 T. D. Bennett and S. Horike, *Nat. Rev. Mater.*, 2018, **3**, 431–440.

161 S. Horike, S. S. Nagarkar, T. Ogawa and S. Kitagawa, *Angew. Chem. Int. Ed.*, 2020, **59**, 6652–6664.

162 J. Fonseca, T. Gong, L. Jiao and H. L. Jiang, *J. Mater. Chem. A*, 2021, **9**, 10562–10611.

163 N. Stock and S. Biswas, *Chem. Rev.*, 2012, **112**, 933–969.

164 A. G. Zavyalova, D. V. Kladko, I. Y. Chernyshov and V. V. Vinogradov, *J. Mater. Chem. A*, 2021, **9**, 25258–25271.

165 O. S. Bull, I. Bull, G. K. Amadi, C. Obaalologhi Odu and E. O. Okpa, *Orient. J. Chem.*, 2022, **38**, 490–516.

166 Y. Li, M. Karimi, Y. N. Gong, N. Dai, V. Safarifard and H. L. Jiang, *Matter*, 2021, **4**, 2230–2265.

167 A. Ejsmont, J. Andreo, A. Lanza, A. Galarda, L. Macreadie, S. Wuttke, S. Canossa, E. Ploetz and J. Goscianska, *Coord. Chem. Rev.*, 2021, **430**, 213655.

168 M. Eddaoudi, D. B. Moler, H. Li, B. Chen, T. M. Reineke, M. O'Keeffe and O. M. Yaghi, *Acc. Chem. Res.*, 2001, **34**, 319–330.

169 O. M. Yaghi, M. O'Keeffe, N. W. Ockwig, H. K. Chae, M. Eddaoudi and J. Kim, *Nature*, 2003, **423**, 705–714.

170 L. Huang, H. Wang, J. Chen, Z. Wang, J. Sun, D. Zhao and Y. Yan, *Microporous Mesoporous Mater.*, 2003, **58**, 105–114.

171 S. S. Kaye, A. Dailly, O. M. Yaghi and J. R. Long, *J. Am. Chem. Soc.*, 2007, **129**, 14176–14177.

172 Y. Ming, N. Kumar and D. J. Siegel, *ACS Omega*, 2017, **2**, 4921–4928.

173 Y. Ming, J. Purewal, J. Yang, C. Xu, R. Soltis, J. Warner, M. Veenstra, M. Gaab, U. Müller and D. J. Siegel, *Langmuir*, 2015, **31**, 4988–4995.

174 Z. Jiang, X. Xu, Y. Ma, H. S. Cho, D. Ding, C. Wang, J. Wu, P. Oleynikov, M. Jia, J. Cheng, Y. Zhou, O. Terasaki, T. Peng, L. Zan and H. Deng, *Nature*, 2020, **586**, 549–554.

175 S. Zhou, O. Shekhah, A. Ramírez, P. Lyu, E. Abou-Hamad, J. Jia, J. Li, P. M. Bhatt, Z. Huang, H. Jiang, T. Jin, G. Maurin, J. Gascon and M. Eddaoudi, *Nature*, 2022, **606**, 706–712.

176 H. Zeng, M. Xie, T. Wang, R. J. Wei, X. J. Xie, Y. Zhao, W. Lu and D. Li, *Nature*, 2021, **595**, 542–548.

177 A. P. Coˆté, A. I. Benin, N. W. Ockwig, M. O'Keeffe, A. J. Matzger and O. M. Yaghi, *Science*, 2005, **310**, 1166–1170.

178 F. Zhao, H. Liu, S. D. R. Mathe, A. Dong and J. Zhang, *Covalent organic frameworks: From materials design to biomedical application*, 2018, vol. 8.

179 X. Liang, Y. Tian, Y. Yuan and Y. Kim, *Adv. Mater.*, 2021, **33**, 1–31.

180 F. J. Uribe-Romo, J. R. Hunt, H. Furukawa, C. Klöck, M. O'Keeffe and O. M. Yaghi, *J. Am. Chem. Soc.*, 2009, **131**, 4570–4571.

181 S. Dalapati, S. Jin, J. Gao, Y. Xu, A. Nagai and D. Jiang, *J. Am. Chem. Soc.*, 2013, **135**, 17310–17313.

182 H. Lyu, C. S. Diercks, C. Zhu and O. M. Yaghi, *J. Am. Chem. Soc.*, 2019, **141**, 6848–6852.

183 E. Jin, M. Asada, Q. Xu, S. Dalapati, M. A. Addicoat, M. A. Brady, H. Xu, T. Nakamura, T. Heine, Q. Chen and D. Jiang,

Science, 2017, **357**, 673–676.

184 C. Zhao, H. Lyu, Z. Ji, C. Zhu and O. M. Yaghi, *J. Am. Chem. Soc.*, 2020, **142**, 14450–14454.

185 C. Zhao, C. S. Diercks, C. Zhu, N. Hanikel, X. Pei and O. M. Yaghi, *J. Am. Chem. Soc.*, 2018, **140**, 16438–16441.

186 A. Nagai, X. Chen, X. Feng, X. Ding, Z. Guo and D. Jiang, *Angew. Chem. Int. Ed.*, 2013, **52**, 3770–3774.

187 Z.-B. Zhou, P.-J. Tian, J. Yao, Y. Lu, Q.-Y. Qi and X. Zhao, *Nat. Commun.*, 2022, **13**, 2180.

188 H. L. Nguyen, C. Gropp, N. Hanikel, A. Möckel, A. Lund and O. M. Yaghi, *ACS Cent. Sci.*, 2022, **8**, 926–932.

189 P. J. Waller, S. J. Lyle, T. M. Osborn Popp, C. S. Diercks, J. A. Reimer and O. M. Yaghi, *J. Am. Chem. Soc.*, 2016, **138**, 15519–15522.

190 H. Liu, J. Chu, Z. Yin, X. Cai, L. Zhuang and H. Deng, *Chem*, 2018, **4**, 1696–1709.

191 B. Zhang, M. Wei, H. Mao, X. Pei, S. A. Alshmimri, J. A. Reimer and O. M. Yaghi, *J. Am. Chem. Soc.*, 2018, **140**, 12715–12719.

192 J. Guo, Y. Xu, S. Jin, L. Chen, T. Kaji, Y. Honsho, M. A. Addicoat, J. Kim, A. Saeki, H. Ihee, S. Seki, S. Irle, M. Hiramoto, J. Gao and D. Jiang, *Nat. Commun.*, 2013, **4**, 2736.

193 Q. Fang, Z. Zhuang, S. Gu, R. B. Kaspar, J. Zheng, J. Wang, S. Qiu and Y. Yan, *Nat. Commun.*, 2014, **5**, 4503.

194 K. T. Jackson, T. E. Reich and H. M. El-Kaderi, *Chem. Commun.*, 2012, **48**, 8823–8825.

195 C. Li, Y. Ma, H. Liu, L. Tao, Y. Ren, X. Chen, H. Li and Q. Yang, *Chinese J. Catal.*, 2020, **41**, 1288–1297.

196 J. Feng, Y. J. Zhang, S. H. Ma, C. Yang, Z. P. Wang, S. Y. Ding, Y. Li and W. Wang, *J. Am. Chem. Soc.*, 2022, **144**, 6594–6603.

197 S. Yang, C. Yang, C. Dun, H. Mao, R. S. H. Khoo, L. M. Klivansky, J. A. Reimer, J. J. Urban, J. Zhang and Y. Liu, *J. Am. Chem. Soc.*, 2022, **144**, 9827–9835.

198 Y. Yang, L. Yu, T. Chu, H. Niu, J. Wang and Y. Cai, *Nat. Commun.*, 2022, **13**, 2615.

199 P. J. Waller, Y. S. Alfaraj, C. S. Diercks, N. N. Jarenwattananon and O. M. Yaghi, *J. Am. Chem. Soc.*, 2018, **140**, 9099–9103.

200 X. Li, C. Zhang, S. Cai, X. Lei, V. Altoe, F. Hong, J. J. Urban, J. Ciston, E. M. Chan and Y. Liu, *Nat. Commun.*, 2018, **9**, 2998.

201 F. Haase, E. Troschke, G. Savasci, T. Banerjee, V. Duppel, S. Dörfler, M. M. J. Grundei, A. M. Burow, C. Ochsenfeld, S. Kaskel and B. V. Lotsch, *Nat. Commun.*, 2018, **9**, 2600.

202 S. J. Lyle, T. M. Osborn Popp, P. J. Waller, X. Pei, J. A. Reimer and O. M. Yaghi, *J. Am. Chem. Soc.*, 2019, **141**, 11253–11258.

203 Y. Wang, H. Liu, Q. Pan, C. Wu, W. Hao, J. Xu, R. Chen, J. Liu, Z. Li and Y. Zhao, *J. Am. Chem. Soc.*, 2020, **142**, 5958–5963.

204 Y. Du, H. Yang, J. M. Whiteley, S. Wan, Y. Jin, S. H. Lee and W. Zhang, *Angew. Chem. Int. Ed.*, 2016, **55**, 1737–1741.

205 G. Das, T. Skorjanc, S. K. Sharma, F. Gándara, M. Lusi, D. S. Shankar Rao, S. Vimala, S. Krishna Prasad, J. Raya, D. S. Han, R. Jagannathan, J. C. Olsen and A. Trabolsi, *J. Am. Chem. Soc.*, 2017, **139**, 9558–9565.

206 J. Roeser, D. Prill, M. J. Bojdys, P. Fayon, A. Trewin, A. N. Fitch, M. U. Schmidt and A. Thomas, *Nat. Chem.*, 2017, **9**, 977–982.

207 H. Chen, H. Tu, C. Hu, Y. Liu, D. Dong, Y. Sun, Y. Dai, S. Wang, H. Qian, Z. Lin and L. Chen, *J. Am. Chem. Soc.*, 2018, **140**, 896–899.

208 Z. Li, Z. W. Liu, Z. J. Mu, C. Cao, Z. Li, T. X. Wang, Y. Li, X. Ding, B. H. Han and W. Feng, *Mater. Chem. Front.*, 2020, **4**, 1164–1173.

209 Y. Zeng, R. Zou, Z. Luo, H. Zhang, X. Yao, X. Ma, R. Zou and Y. Zhao, *J. Am. Chem. Soc.*, 2015, **137**, 1020–1023.

210 N. Huang, L. Zhai, D. E. Coupry, M. A. Addicoat, K. Okushita, K. Nishimura, T. Heine and D. Jiang, *Nat. Commun.*, 2016, **7**, 12325.

211 X. Zhao, R. R. Liang, S. Y. Jiang and A. Ru-Han, *Chem. Soc. Rev.*, 2020, **49**, 3920–3951.

212 L. M. Lanni, R. W. Tilford, M. Bharathy and J. J. Lavigne, *J. Am. Chem. Soc.*, 2011, **133**, 13975–13983.

213 X. Wu, X. Han, Y. Liu, Y. Liu and Y. Cui, *J. Am. Chem. Soc.*, 2018, **140**, 16124–16133.

214 Y. Du, D. Calabro, B. Wooler, P. Kortunov, Q. Li, S. Cundy and K. Mao, *Chem. Mater.*, 2015, **27**, 1445–1447.

215 Y. Du, K. Mao, P. Kamakoti, P. Ravikovitch, C. Paur, S. Cundy, Q. Li and D. Calabro, *Chem. Commun.*, 2012, **48**, 4606–4608.

216 S. Kandambeth, V. Venkatesh, D. B. Shinde, S. Kumari, A. Halder, S. Verma and R. Banerjee, *Nat. Commun.*, 2015, **6**, 6786.

217 S. Kandambeth, D. B. Shinde, M. K. Panda, B. Lukose, T. Heine and R. Banerjee, *Angew. Chem. Int. Ed.*, 2013, **52**, 13052–13056.

218 S. Kandambeth, D. B. Shinde, M. K. Panda, B. Lukose, T. Heine and R. Banerjee, *Angew. Chem. Int. Ed.*, 2013, **52**, 13052–13056.

219 H. Xu, J. Gao and D. Jiang, *Nat. Chem.*, 2015, **7**, 905–912.

220 A. Halder, S. Karak, M. Addicoat, S. Bera, A. Chakraborty, S. H. Kunjattu, P. Pachfule, T. Heine and R. Banerjee, *Angew. Chem. Int. Ed.*, 2018, **57**, 5797–5802.

221 L. Ai, W. Li, Q. Wang, F. Cui and G. Jiang, *ChemCatChem*, 2022, **14**, e202200935.

222 M. Hussain, N. Maile, K. Tahir, A. A. Ghani, B. Kim, J. Jang and D. S. Lee, *Chem. Eng. J.*, 2022, **446**, 1–21.

223 X. Liu, X. S. Luo, H. X. Fu, W. Fan, S. L. Chen and M. H. Huang, *Chem. Commun.*, 2020, **56**, 2103–2106.

224 S. Kandambeth, A. Mallick, B. Lukose, M. V. Mane, T. Heine and R. Banerjee, *J. Am. Chem. Soc.*, 2012, **134**, 19524–19527.

225 Y. Wang, H. Liu, Q. Pan, C. Wu, W. Hao, J. Xu, R. Chen, J. Liu, Z. Li and Y. Zhao, *J. Am. Chem. Soc.*, 2020, **142**, 5958–5963.

226 W. Liu, M. Ulaganathan, I. Abdelwahab, X. Luo, Z. Chen, S. J. Rong Tan, X. Wang, Y. Liu, D. Geng, Y. Bao, J. Chen and K. P. Loh, *ACS Nano*, 2018, **12**, 852–860.

227 S. Thomas, H. Li, R. R. Dasari, A. M. Evans, I. Castano, T. G. Allen, O. G. Reid, G. Rumbles, W. R. Dichtel, N. C. Gianneschi, S. R. Marder, V. Coropceanu and J. L. Brédas, *Mater. Horizons*, 2019, **6**, 1868–1876.

228 K. Baek, I. Hwang, I. Roy, D. Shetty and K. Kim, *Acc. Chem. Res.*, 2015, **48**, 2221–2229.

229 M. Liu, Q. Huang, S. Wang, Z. Li, B. Li, S. Jin and B. Tan, *Angew. Chem. Int. Ed.*, 2018, **57**, 11968–11972.

230 L. Liang, Y. Qiu, W. D. Wang, J. Han, Y. Luo, W. Yu, G. L. Yin, Z. P. Wang, L. Zhang, J. Ni, J. Niu, J. Sun, T. Ma and W. Wang, *Angew. Chem. Int. Ed.*, 2020, **59**, 17991–17995.

231 C. Kang, K. Yang, Z. Zhang, A. K. Usadi, D. C. Calabro, L. S. Baugh, Y. Wang, J. Jiang, X. Zou, Z. Huang and D. Zhao, *Nat. Commun.*, 2022, **13**, 1370.

232 T. Ma, E. A. Kapustin, S. X. Yin, L. Liang, Z. Zhou, J. Niu, L.-H. Li, Y. Wang, J. Su, J. Li, X. Wang, W. D. Wang, W.

Wang, J. Sun and O. M. Yaghi, *Science*, 2018, **361**, 48–52.

233 X. Wang, R. Enomoto and Y. Murakami, *Chem. Commun.*, 2021, **57**, 6656–6659.

234 R. L. Li, N. C. Flanders, A. M. Evans, W. Ji, I. Castano, L. X. Chen, N. C. Gianneschi and W. R. Dichtel, *Chem. Sci.*, 2019, **10**, 3796–3801.

235 B. J. Smith, L. R. Parent, A. C. Overholts, P. A. Beaucage, R. P. Bisbey, A. D. Chavez, N. Hwang, C. Park, A. M. Evans, N. C. Gianneschi and W. R. Dichtel, *ACS Cent. Sci.*, 2017, **3**, 58–65.

236 C. R. Deblase, K. Hernández-Burgos, K. E. Silberstein, G. G. Rodríguez-Calero, R. P. Bisbey, H. D. Abruña and W. R. Dichtel, *ACS Nano*, 2015, **9**, 3178–3183.

237 M. Liu, K. Jiang, X. Ding, S. Wang, C. Zhang, J. Liu, Z. Zhan, G. Cheng, B. Li, H. Chen, S. Jin and B. Tan, *Adv. Mater.*, 2019, **31**, 1807865.

238 R. Shi, L. Liu, Y. Lu, C. Wang, Y. Li, L. Li, Z. Yan and J. Chen, *Nat. Commun.*, 2020, **11**, 178.

239 Y. Li, X. Gao, M. Wang, Y. Gao and D. Jiang, *Small*, 2022, **18**, 2205400.

240 L. Peng, Q. Guo, C. Song, S. Ghosh, H. Xu, L. Wang, D. Hu, L. Shi, L. Zhao, Q. Li, T. Sakurai, H. Yan, S. Seki, Y. Liu and D. Wei, *Nat. Commun.*, 2021, **12**, 5077.

241 W. Liu, L. Gong, Z. Liu, Y. Jin, H. Pan, X. Yang, B. Yu, N. Li, D. Qi, K. Wang, H. Wang and J. Jiang, *J. Am. Chem. Soc.*, 2022, **144**, 17209–17218.

242 Y. He, S. Xiang and B. Chen, *J. Am. Chem. Soc.*, 2011, **133**, 14570–14573.

243 W. Yang, A. Greenaway, X. Lin, R. Matsuda, A. J. Blake, C. Wilson, W. Lewis, P. Hubberstey, S. Kitagawa, N. R. Champness and M. Schröder, *J. Am. Chem. Soc.*, 2010, **132**, 14457–14469.

244 J. Lü, C. Perez-Krap, M. Suyetin, N. H. Alsmail, Y. Yan, S. Yang, W. Lewis, E. Bichoutskaia, C. C. Tang, A. J. Blake, R. Cao and M. Schröder, *J. Am. Chem. Soc.*, 2014, **136**, 12828–12831.

245 J. Lü, C. Perez-Krap, F. Trousselet, Y. Yan, N. H. Alsmail, B. Karadeniz, N. M. Jacques, W. Lewis, A. J. Blake, F. X. Coudert, R. Cao and M. Schröder, *Cryst. Growth Des.*, 2018, **18**, 2555–2562.

246 T.-H. Chen, I. Popov, W. Kaveevivitchai, Y.-C. Chuang, Y.-S. Chen, O. Daugulis, A. J. Jacobson and O. Š. Miljanić, *Nat. Commun.*, 2014, **5**, 5131.

247 A. Yamamoto, T. Hamada, I. Hisaki, M. Miyata and N. Tohnai, *Angew. Chem. Int. Ed.*, 2013, **52**, 1709–1712.

248 A. Yamamoto, T. Hasegawa, T. Hamada, T. Hirukawa, I. Hisaki, M. Miyata and N. Tohnai, *Chem. Eur. J.*, 2013, **19**, 3006–3016.

249 A. Yamamoto, T. Hirukawa, I. Hisaki, M. Miyata and N. Tohnai, *Tetrahedron Lett.*, 2013, **54**, 1268–1273.

250 T. Miyano, N. Okada, R. Nishida, A. Yamamoto, I. Hisaki and N. Tohnai, *Chem. Eur. J.*, 2016, **22**, 15430–15436.

251 T. Ami, K. Oka, K. Tsuchiya and N. Tohnai, *Angew. Chem. Int. Ed.*, 2022, **61**, e202202597.

252 T. Miyano, I. Hisaki and N. Tohnai, *Chem. Lett.*, 2017, **46**, 225–227.

253 A. Yamamoto, S. Uehara, T. Hamada, M. Miyata, I. Hisaki and N. Tohnai, *Cryst. Growth Des.*, 2012, **12**, 4600–4606.

254 D. J. Duchamp and R. E. Marsh, *Acta Crystallogr. Sect. B Struct. Crystallogr. Cryst. Chem.*, 1969, **25**, 5–19.

255 O. Ermer, *J. Am. Chem. Soc.*, 1988, **110**, 3747–3754.

256 S. Yu, G. Xing, L. Chen, T. Ben and B. Su, *Adv. Mater.*, 2020, **32**, 2003270.

257 J. X. Wang, X. W. Gu, Y. X. Lin, B. Li and G. Qian, *ACS Mater. Lett.*, 2021, **3**, 497–503.

258 J. Gao, Y. Cai, X. Qian, P. Liu, H. Wu, W. Zhou, D. X. Liu, L. Li, R. B. Lin and B. Chen, *Angew. Chem. Int. Ed.*, 2021,

60, 20400–20406.

259 W. Yang, J. X. Wang, B. Yu, B. Li, H. Wang and J. Jiang, *Cryst. Growth Des.*, 2022, **22**, 1817–1823.

260 X. Ding, Z. Liu, Y. Zhang, G. Ye, J. Jia and J. Chen, *Angew. Chem. Int. Ed.*, 2022, **134**, e202116483.

261 B. Yu, S. Geng, H. Wang, W. Zhou, Z. Zhang, B. Chen and J. Jiang, *Angew. Chem. Int. Ed.*, 2021, **60**, 25942–25948.

262 X. Zhang, J. X. Wang, L. Li, J. Pei, R. Krishna, H. Wu, W. Zhou, G. Qian, B. Chen and B. Li, *Angew. Chem. Int. Ed.*, 2021, **60**, 10304–10310.

263 K. O. Kirlikovali, S. Goswami, M. R. Mian, M. D. Krzyaniak, M. R. Wasielewski, J. T. Hupp, P. Li and O. K. Farha, *ACS Mater. Lett.*, 2022, **4**, 128–135.

264 S. Goswami, K. Ma, J. Duan, K. O. Kirlikovali, J. Bai, J. T. Hupp, P. Li and O. K. Farha, *Langmuir*, 2022, **38**, 1533–1539.

265 R. Liang, J. Samanta, B. Shao, M. Zhang, R. J. Staples, A. D. Chen, M. Tang, Y. Wu, I. Aprahamian and C. Ke, *Angew. Chem. Int. Ed.*, 2021, **60**, 23176–23181.

266 T. Chen, H. B. Jiang, K. Bin Jiang, D. L. Hu, L. Z. Cai, M. S. Wang and G. C. Guo, *ACS Appl. Mater. Interfaces*, 2022, **14**, 11619–11625.

267 H. Xiao, H. Ma, M. Han, N. Wu, Z. Guo, Z. An and H. Zhan, *Cryst. Growth Des.*, 2021, **21**, 3420–3427.

268 Q. Yin, E. V. Alexandrov, D. Si, Q. Huang, Z. Fang, Y. Zhang, A. Zhang, W. Qin, Y. Li, T. Liu and D. M. Proserpio, *Angew. Chem. Int. Ed. Engl.*, 2022, **61**, e202115854.

269 Y. Wang, K. Ma, J. Bai, T. Xu, W. Han, C. Wang, Z. Chen, K. O. Kirlikovali, P. Li, J. Xiao and O. K. Farha, *Angew. Chem. Int. Ed. Engl.*, 2022, **61**, e202115956.

270 Y. Wu, X. Mao, M. Zhang, X. Zhao, R. Xue, S. Di, W. Huang, L. Wang, Y. Li and Y. Li, *Adv. Mater.*, 2021, **33**, 2106079.

271 X. Liu, X. Yang, H. Wang, I. Hisaki, K. Wang and J. Jiang, *J. Mater. Chem. A*, 2022, **10**, 1808–1814.

272 Y. Lv, Z. Xiong, Y. Li, D. Li, J. Liang, Y. Yang, F. Xiang, S. Xiang, Y. S. Zhao and Z. Zhang, *J. Phys. Chem. Lett.*, 2022, **13**, 130–135.

273 Z. Tang, X. Li, L. Tong, H. Yang, J. Wu, X. Zhang, T. Song, S. Huang, F. Zhu, G. Chen and G. Ouyang, *Angew. Chem. Int. Ed.*, 2021, **60**, 23608–23613.

274 P. Wied, F. Carraro, J. M. Bolivar, C. J. Doonan, P. Falcaro and B. Nidetzky, *Angew. Chem. Int. Ed.*, 2022, **61**, e202117345.

275 H. Zhang, D. Yu, S. Liu, C. Liu, Z. Liu, J. Ren and X. Qu, *Angew. Chem. Int. Ed.*, 2022, **61**, e202109068.

276 L. Leiserowitz, *Acta Crystallogr. Sect. B Struct. Crystallogr. Cryst. Chem.*, 1976, **32**, 775–802.

277 O. Ivasenko and D. F. Perepichka, *Chem. Soc. Rev.*, 2011, **40**, 191–206.

278 T. N. Wassermann, C. A. Rice, M. A. Suhm and D. Luckhaus, *J. Chem. Phys.*, 2007, **127**, 234309.

279 Z. Zhang, M. I. Hashim and O. Miljanić, *Chem. Commun.*, 2017, **53**, 10022–10025.

280 M. I. Hashim, H. T. M. Le, T. H. Chen, Y. S. Chen, O. Daugulis, C. W. Hsu, A. J. Jacobson, W. Kaveevivitchai, X. Liang, T. Makarenko, O. Miljanić, I. Popovs, H. V. Tran, X. Wang, C. H. Wu and J. I. Wu, *J. Am. Chem. Soc.*, 2018, **140**, 6014–6026.

281 D. Sen and W. Gilbert, *Nature*, 1998, **334**, 364–366.

282 K. Kobayashi, M. Koyanagi, K. Endo, H. Masuda and Y. Aoyama, *Chem. A Eur. J.*, 1998, **4**, 417–424.

283 X. Z. Luo, X. J. Jia, J. H. Deng, J. L. Zhong, H. J. Liu, K. J. Wang and D. C. Zhong, *J. Am. Chem. Soc.*, 2013, **135**,

11684–11687.

284 X. Ding, Z. Liu, Y. Zhang, G. Ye, J. Jia and J. Chen, *Angew. Chem. Int. Ed.*, 2022, **61**, e202116483.

285 J. A. Swift, A. M. Reynolds and M. D. Ward, *Chem. Mater.*, 1998, **10**, 4159–4168.

286 M. J. Horner, K. T. Holman and M. D. Ward, *J. Am. Chem. Soc.*, 2007, **129**, 14640–14660.

287 Y. Liu, C. Hu, A. Comotti and M. D. Ward, *Science*, 2011, **333**, 436–440.

288 A. Karmakar, R. Illathvalappil, B. Anothumakkool, A. Sen, P. Samanta, A. V. Desai, S. Kurungot and S. K. Ghosh, *Angew. Chem. Int. Ed.*, 2016, **55**, 10667–10671.

289 Y. Li, M. Handke, Y. S. Chen, A. G. Shtukenberg, C. T. Hu and M. D. Ward, *J. Am. Chem. Soc.*, 2018, **140**, 12915–12921.

290 Y. Li, S. Tang, A. Yusov, J. Rose, A. N. Borrfors, C. T. Hu and M. D. Ward, *Nat. Commun.*, 2019, **10**, 4477.

291 D. W. Kang, M. Kang, H. Kim, J. H. Choe, D. W. Kim, J. R. Park, W. R. Lee, D. Moon and C. S. Hong, *Angew. Chem. Int. Ed.*, 2019, **58**, 16152–16155.

292 M. Handke, Y. Wu, Y. Li, C. T. Hu and M. D. Ward, *CrystEngComm*, 2020, **22**, 3749–3752.

293 S. H. Kim, J. H. Park, E. M. Go, W.-S. Kim and S. K. Kwak, *J. Ind. Eng. Chem.*, 2020, **85**, 276–281.

294 Y. Wang, J. Yin, D. Liu, C. Gao, Z. Kang, R. Wang, D. Sun and J. Jiang, *J. Mater. Chem. A*, 2021, **9**, 2683–2688.

295 B. Han, H. Wang, C. Wang, H. Wu, W. Zhou, B. Chen and J. Jiang, *J. Am. Chem. Soc.*, 2019, **141**, 8737–8740.

296 Q. Huang, W. Li, Z. Yang, J. Zhao, Y. Li, Z. Mao, Z. Yang, S. Liu, Y. Zhang and Z. Chi, *CCS Chem.*, 2022, **4**, 1643–1653.

297 H. Wahl, D. A. Haynes and T. Le Roex, *Cryst. Growth Des.*, 2017, **17**, 4377–4383.

298 Y. Luo, X. He, D. Hong, C. Chen, F. Chen, J. Jiao, L. Zhai, L. Guo and B. Sun, *Adv. Funct. Mater.*, 2018, **28**, 1804822.

299 S. Bhattacharya, *J. Mol. Struct.*, 2020, **1220**, 128686.

300 X. Zheng, N. Xiao, Z. Long, L. Wang, F. Ye, J. Fang, L. Shen and X. Xiao, *Synth. Met.*, 2020, **263**, 116365.

301 A. Garai, A. G. Kumar, S. Banerjee and K. Biradha, *Chem. Asian J.*, 2019, **14**, 4389–4394.

302 G. Xing, I. Bassanetti, S. Bracco, M. Negroni, C. Bezuidenhout, T. Ben, P. Sozzani and A. Comotti, *Chem. Sci.*, 2019, **10**, 730–736.

303 L. Negi, S. Kumar, B. Dwivedi and D. Das, *Cryst. Growth Des.*, 2021, **21**, 1428–1433.

304 S. Chand, S. C. Pal, A. Pal, Y. Ye, Q. Lin, Z. Zhang, S. Xiang and M. C. Das, *Chem. Eur. J.*, 2019, **25**, 1691–1695.

305 Isostructural crystals - Online Dictionary of Crystallography, https://dictionary.iucr.org/Isostructural_crystals, (last edited on 2019-03-26, accessed 2022-10-10).

306 S. R. Hall and B. McMahon, Eds., *International Tables for Crystallography*, International Union of Crystallography, Chester, England, 2006, vol. G.

307 M. Eddaoudi, J. Kim, N. Rosi, D. Vodak, J. Wachter, M. O'Keeffe and O. M. Yaghi, *Science*, 2002, **295**, 469–472.

308 V. A. Blatov, M. O'Keeffe and D. M. Proserpio, *CrystEngComm*, 2010, **12**, 44–48.

309 RCSR.

310 M. O. Keeffe, M. a Peskov, S. J. Ramsden and O. M. Yaghi, *Acc. Chem. Res.*, 2008, **41**, 1782–1789.

311 Topospro database., https://topospro.com/databases/, (accessed 11 November 2022).

312 V. A. Blatov, A. P. Shevchenko and D. M. Proserpio, *Cryst. Growth Des.*, 2014, **14**, 3576–3586.

313 A. A. Pankova, T. G. Akhmetshina, V. A. Blatov and D. M. Proserpio, *Inorg. Chem.*, 2015, **54**, 6616–6630.

314 R. Hoffmann, A. A. Kabanov, A. A. Golov and D. M. Proserpio, *Angew. Chem. Int. Ed.*, 2016, **55**, 10962–10976.

315 K. Suresh, A. P. Kalenak, A. Sotuyo and A. J. Matzger, *Chemistry*, 2022, **28**, e202200334.

316 A. Ejsmont, J. Andreo, A. Lanza, A. Galarda, L. Macreadie, S. Wuttke, S. Canossa, E. Ploetz and J. Goscianska, *Coord. Chem. Rev.*, 2021, **430**, 213655.

317 D. Kim, X. Liu and M. S. Lah, *Inorg. Chem. Front.*, 2015, **2**, 336–360.

318 C. Serre, F. Millange, C. Thouvenot, M. Noguès, G. Marsolier, D. Louër and G. Férey, *J. Am. Chem. Soc.*, 2002, **124**, 13519–13526.

319 K. Barthelet, K. Adil, F. Millange, C. Serre, D. Riou and G. Férey, *J. Mater. Chem.*, 2003, **13**, 2208–2212.

320 Y. Kamakura, P. Chinapang, S. Masaoka, A. Saeki, K. Ogasawara, S. R. Nishitani, H. Yoshikawa, T. Katayama, N. Tamai, K. Sugimoto and D. Tanaka, *J. Am. Chem. Soc.*, 2020, **142**, 27–32.

321 H. Deng, S. Grunder, K. E. Cordova, C. Valente, H. Furukawa, M. Hmadeh, F. Gándara, A. C. Whalley, Z. Liu, S. Asahina, H. Kazumori, M. O'Keeffe, O. Terasaki, J. F. Stoddart and O. M. Yaghi, *Science*, 2012, **336**, 1018–1023.

322 V. Guillerm, S. Gross, C. Serre, T. Devic, M. Bauer and G. Férey, *Chem. Commun.*, 2010, **46**, 767–769.

323 M. Bosch, S. Yuan, W. Rutledge and H. C. Zhou, *Acc. Chem. Res.*, 2017, **50**, 857–865.

324 S. Krause, J. D. Evans, V. Bon, I. Senkovska, P. Iacomi, F. Kolbe, S. Ehrling, E. Troschke, J. Getzschmann, D. M. Többens, A. Franz, D. Wallacher, P. G. Yot, G. Maurin, E. Brunner, P. L. Llewellyn, F.-X. Coudert and S. Kaskel, *Nat. Commun.*, 2019, **10**, 3632.

325 J. Wang, Y. Zhang, Y. Su, X. Liu, P. Zhang, R.-B. Lin, S. Chen, Q. Deng, Z. Zeng, S. Deng and B. Chen, *Nat. Commun.*, 2022, **13**, 200.

326 X. Chen, Y. Peng, X. Han, Y. Liu, X. Lin and Y. Cui, *Nat. Commun.*, 2017, **8**, 2171.

327 X. Guan, F. Chen, Q. Fang and S. Qiu, *Chem. Soc. Rev.*, 2020, **49**, 1357–1384.

328 H. R. Abuzeid, A. F. M. EL-Mahdy and S. W. Kuo, *Giant*, 2021, **6**, 100054.

329 S. T. Emmerling, R. Schuldt, S. Bette, L. Yao, R. E. Dinnebier, J. Kästner and B. V Lotsch, *J. Am. Chem. Soc.*, 2021, **143**, 15711–15722.

330 Z. Mu, Y. Zhu, B. Li, A. Dong, B. Wang and X. Feng, *J. Am. Chem. Soc.*, 2022, **144**, 5145–5154.

331 K. Wang, X. Kang, C. Yuan, X. Han, Y. Liu and Y. Cui, *Angew. Chem. Int. Ed.*, 2021, **60**, 19466–19476.

332 L. Wang, J. Zhou, Y. Lan, S. Ding, W. Yu and W. Wang, *Angew. Chem. Int. Ed.*, 2019, **131**, 9543–9547.

333 Y.-J. Li, W.-R. Cui, Q.-Q. Jiang, Q. Wu, R.-P. Liang, Q.-X. Luo and J.-D. Qiu, *Nat. Commun.*, 2021, **12**, 4735.

334 X. Han, J. Zhang, J. Huang, X. Wu, D. Yuan, Y. Liu and Y. Cui, *Nat. Commun.*, 2018, **9**, 1294.

335 J. Yang, S. Ghosh, J. Roeser, A. Acharjya, C. Penschke, Y. Tsutsui, J. Rabeah, T. Wang, S. Y. Djoko Tameu, M. Y. Ye, J. Grüneberg, S. Li, C. Li, R. Schomäcker, R. Van De Krol, S. Seki, P. Saalfrank and A. Thomas, *Nat. Commun.*, 2022, **13**, 6317.

336 S. Li, R. Ma, S. Xu, T. Zheng, G. Fu, Y. Wu, Z. Liao, Y. Kuang, Y. Hou, D. Wang, P. S. Petkov, K. Simeonova, X. Feng, L. Z. Wu, X. B. Li and T. Zhang, *J. Am. Chem. Soc.*, 2022, **144**, 13953–13960.

337 P. Cui, D. P. Mcmahon, P. R. Spackman, B. M. Alston, M. A. Little, G. M. Day and A. I. Cooper, *Chem. Sci.*, 2019, **10**, 9988–9997.

338 S. Tothadi, K. Koner, K. Dey, M. Addicoat and R. Banerjee, *ACS Appl. Mater. Interfaces*, 2020, **12**, 15588–15594.

339 S. Nandi, D. Chakraborty and R. Vaidhyanathan, *Chem. Commun.*, 2016, **52**, 7249–7252.

340 W. Yang, J. Wang, H. Wang, Z. Bao, J. C. G. Zhao and B. Chen, *Cryst. Growth Des.*, 2017, **17**, 6132–6137.

341 Y. L. Li, E. V. Alexandrov, Q. Yin, L. Li, Z. Bin Fang, W. Yuan, D. M. Proserpio and T. F. Liu, *J. Am. Chem. Soc.*, 2020, **142**, 7218–7224.

342 T. Li, B. T. Liu, Z. Bin Fang, Q. Yin, R. Wang and T. F. Liu, *J. Mater. Chem. A*, 2021, **9**, 4687–4691.

343 T. U. Yoon, S. Bin Baek, D. Kim, E. J. Kim, W. G. Lee, B. K. Singh, M. S. Lah, Y. S. Bae and K. S. Kim, *Chem. Commun.*, 2018, **54**, 9360–9363.

344 C. A. Zentner, H. W. H. Lai, J. T. Greenfield, R. A. Wiscons, M. Zeller, C. F. Campana, O. Talu, S. A. Fitzgerald and J. L. C. Rowsell, *Chem. Commun.*, 2015, **51**, 11642–11645.

345 H. W. H. Lai, R. A. Wiscons, C. A. Zentner, M. Zeller and J. L. C. Rowsell, *Cryst. Growth Des.*, 2016, **16**, 821–833.

346 W. Yang, W. Zhou and B. Chen, *Cryst. Growth Des.*, 2019, **19**, 5184–5188.

347 R. Liang, J. Samanta, B. Shao, M. Zhang, R. J. Staples, A. D. Chen, M. Tang, Y. Wu, I. Aprahamian and C. Ke, *Angew. Chem. Int. Ed.*, 2021, **60**, 23176–23181.

348 I. Hisaki, N. Q. Emilya Affendy and N. Tohnai, *CrystEngComm*, 2017, **19**, 4892–4898.

349 Q. Ji, K. Takahashi, S. I. Noro, Y. Ishigaki, K. Kokado, T. Nakamura and I. Hisaki, *Cryst. Growth Des.*, 2021, **21**, 4656–4664.

350 H. Kubo, R. Oketani and I. Hisaki, *Chem. Commun.*, 2021, **57**, 8568–8571.

351 N. B. Shustova, B. D. McCarthy and M. Dincă, *J. Am. Chem. Soc.*, 2011, **133**, 20126–20129.

352 T. Hashimoto, R. Oketani, M. Nobuoka, S. Seki and I. Hisaki, *Angew. Chem. Int. Ed.*, 2023, **62**, e202215836.

353 Q. Yin, P. Zhao, R. J. Sa, G. C. Chen, L. Jian, T. F. Liu and R. Cao, *Angew. Chem. Int. Ed.*, 2018, **57**, 7691–7696.

354 B. Wang, X. L. Lv, J. Lv, L. Ma, R. B. Lin, H. Cui, J. Zhang, Z. Zhang, S. Xiang and B. Chen, *Chem. Commun.*, 2019, **56**, 66–69.

355 K. Ma, P. Li, J. H. Xin, Y. Chen, Z. Chen, S. Goswami, X. Liu, S. Kato, H. Chen, X. Zhang, J. Bai, M. C. Wasson, R. R. Maldonado, R. Q. Snurr and O. K. Farha, *Cell Reports Phys. Sci.*, 2020, **1**, 100024.

356 P. Cui, E. Svensson Grape, P. R. Spackman, Y. Wu, R. Clowes, G. M. Day, A. K. Inge, M. A. Little and A. I. Cooper, *J. Am. Chem. Soc.*, 2020, **142**, 12743–12750.

357 Z. Yang, A. Saeki, A. Inoue, R. Oketani, K. Kamiya, S. Nakanishi, T. Nakamura and I. Hisaki, *Cryst. Growth Des.*, 2022, **22**, 4472–4479.

358 Z. Yang, A. Moriyama, R. Oketani, T. Nakamura and I. Hisaki, *Chem. Lett.*, 2021, **50**, 1909–1912.

359 F. Hu, C. Liu, M. Wu, J. Pang, F. Jiang, D. Yuan and M. Hong, *Angew. Chem. Int. Ed.*, 2017, **56**, 2101–2104.

360 B. Wang, R. He, L. H. Xie, Z. J. Lin, X. Zhang, J. Wang, H. Huang, Z. Zhang, K. S. Schanze, J. Zhang, S. Xiang and B. Chen, *J. Am. Chem. Soc.*, 2020, **142**, 12478–12485.

361 T. Takeda, M. Ozawa and T. Akutagawa, *Angew. Chem. Int. Ed.*, 2019, **58**, 10345–10352.

362 I. Bassanetti, S. Bracco, A. Comotti, M. Negroni, C. Bezuidenhout, S. Canossa, P. P. Mazzeo, L. Marchió and P. Sozzani, *J. Mater. Chem. A*, 2018, **6**, 14231–14239.

363 K. Kobayashi, T. Shirasaka, E. Horn and N. Furukawa, *Tetrahedron Lett.*, 2000, **41**, 89–93.

364 X. Zhang, L. Li, J. X. Wang, H. M. Wen, R. Krishna, H. Wu, W. Zhou, Z. N. Chen, B. Li, G. Qian and B. Chen, *J. Am. Chem. Soc.*, 2020, **142**, 633–640.

365 I. Hisaki, S. Nakagawa, N. Ikenaka, Y. Imamura, M. Katouda, M. Tashiro, H. Tsuchida, T. Ogoshi, H. Sato, N. Tohnai

and M. Miyata, *J. Am. Chem. Soc.*, 2016, **138**, 6617–6628.

366 I. Hisaki, N. Ikenaka, S. Tsuzuki and N. Tohnai, *Mater. Chem. Front.*, 2018, **2**, 338–346.

367 E. Gomez, I. Hisaki and A. Douhal, *Int. J. Mol. Sci.*, 2021, **22**, 4803.

368 M. Kobayashi, H. Kubo, R. Oketani and I. Hisaki, *CrystEngComm*, 2022, **24**, 5036–5040.

369 I. Hisaki, S. Nakagawa, N. Tohnai and M. Miyata, *Angew. Chem. Int. Ed.*, 2015, **54**, 3008–3012.

370 I. Hisaki, N. Ikenaka, E. Gomez, B. Cohen, N. Tohnai and A. Douhal, *Chem. Eur. J.*, 2017, **23**, 11611–11619.

371 I. Hisaki, Y. Suzuki, E. Gomez, Q. Ji, N. Tohnai, T. Nakamura and A. Douhal, *J. Am. Chem. Soc.*, 2019, **141**, 2111–2121.

372 I. Hisaki, Q. Ji, K. Takahashi, N. Tohnai and T. Nakamura, *Cryst. Growth Des.*, 2020, **20**, 3190–3198.

373 K. I. Shivakumar, S. I. Noro, Y. Yamaguchi, Y. Ishigaki, A. Saeki, K. Takahashi, T. Nakamura and I. Hisaki, *Chem. Commun.*, 2021, **57**, 1157–1160.

374 A. S. Beni, A. N. Chermahini and H. Sharghi, *J. Korean Chem. Soc.*, 2011, **55**, 392–399.

375 P. Li, P. Li, M. R. Ryder, Z. Liu, C. L. Stern, O. K. Farha and J. F. Stoddart, *Angew. Chem. Int. Ed.*, 2019, **58**, 1664–1669.

376 P. Li, Z. Chen, M. R. Ryder, C. L. Stern, Q. H. Guo, X. Wang, O. K. Farha and J. F. Stoddart, *J. Am. Chem. Soc.*, 2019, **141**, 12998–13002.

377 P. Li, Y. He, J. Guang, L. Weng, J. C. G. Zhao, S. Xiang and B. Chen, *J. Am. Chem. Soc.*, 2014, **136**, 547–549.

378 S. Feng, Y. Shang, Z. Wang, Z. Kang, R. Wang, J. Jiang, L. Fan, W. Fan, Z. Liu, G. Kong, Y. Feng, S. Hu, H. Guo and D. Sun, *Angew. Chem. Int. Ed.*, 2020, **59**, 3840–3845.

379 P. Li, Y. He, H. D. Arman, R. Krishna, H. Wang, L. Weng and B. Chen, *Chem. Commun.*, 2014, **50**, 13081–13084.

380 P. Li, Y. He, Y. Zhao, L. Weng, H. Wang, R. Krishna, H. Wu, W. Zhou, M. O'Keeffe, Y. Han and B. Chen, *Angew. Chem. Int. Ed.*, 2015, **54**, 574–577.

381 H. Wang, B. Li, H. Wu, T. L. Hu, Z. Yao, W. Zhou, S. Xiang and B. Chen, *J. Am. Chem. Soc.*, 2015, **137**, 9963–9970.

382 W. Yang, B. Li, H. Wang, O. Alduhaish, K. Alfooty, M. A. Zayed, P. Li, H. D. Arman and B. Chen, *Cryst. Growth Des.*, 2015, **15**, 2000–2004.

383 W. Yang, F. Yang, T. L. Hu, S. C. King, H. Wang, H. Wu, W. Zhou, J. R. Li, H. D. Arman and B. Chen, *Cryst. Growth Des.*, 2016, **16**, 5831–5835.

384 H. Wang, H. Wu, J. Kan, G. Chang, Z. Yao, B. Li, W. Zhou, S. Xiang, J. Cong-Gui Zhao and B. Chen, *J. Mater. Chem. A*, 2017, **5**, 8292–8296.

385 H. Wang, Z. Bao, H. Wu, R. B. Lin, W. Zhou, T. L. Hu, B. Li, J. C. G. Zhao and B. Chen, *Chem. Commun.*, 2017, **53**, 11150–11153.

386 Y. Wang, D. Liu, J. Yin, Y. Shang, J. Du, Z. Kang, R. Wang, Y. Chen, D. Sun and J. Jiang, *Chem. Commun.*, 2020, **56**, 703–706.

387 M. Mastalerz and I. M. Oppel, *Angew. Chem. Int. Ed.*, 2012, **51**, 5252–5255.

388 A. Pulido, L. Chen, T. Kaczorowski, D. Holden, M. A. Little, S. Y. Chong, B. J. Slater, D. P. McMahon, B. Bonillo, C. J. Stackhouse, A. Stephenson, C. M. Kane, R. Clowes, T. Hasell, A. I. Cooper and G. M. Day, *Nature*, 2017, **543**, 657–664.

389 T. D. Huan and R. Ramprasad, *J. Phys. Chem. Lett.*, 2020, **11**, 5823–5829.

390 S. L. Price, *Chem. Soc. Rev.*, 2014, **43**, 2098–2111.

391 A. J. Cruz-Cabeza, G. M. Day and W. Jones, *Chem. Eur. J.*, 2009, **15**, 13033–13040.

392 D. H. Case, J. E. Campbell, P. J. Bygrave and G. M. Day, *J. Chem. Theory Comput.*, 2016, **12**, 910–924.

393 M. Morshedi, M. Thomas, A. Tarzia, C. J. Doonan and N. G. White, *Chem. Sci.*, 2017, **8**, 3019–3025.

394 W. Liang, F. Carraro, M. B. Solomon, S. G. Bell, H. Amenitsch, C. J. Sumby, N. G. White, P. Falcaro and C. J. Doonan, *J. Am. Chem. Soc.*, 2019, **141**, 14298–14305.

395 S. A. Boer, M. Morshedi, A. Tarzia, C. J. Doonan and N. G. White, *Chem. Eur. J.*, 2019, **25**, 10006–10012.

396 J. Tang, J. Liu, Q. Zheng, W. Li, J. Sheng, L. Mao and M. Wang, *Angew. Chem. Int. Ed.*, 2021, **60**, 22315–22321.

397 S. A. Boer, L. J. Yu, T. L. Genet, K. Low, D. A. Cullen, M. G. Gardiner, M. L. Coote and N. G. White, *Chem. Eur. J.*, 2021, **27**, 1768–1776.

398 H. Jiang, L. Xie, Z. Duan, K. Lin, Q. He, V. M. Lynch, J. L. Sessler and H. Wang, *Chem. Eur. J.*, 2021, **27**, 15006–15012.

399 P. Muang-Non, H. D. Toop, C. J. Doonan and N. G. White, *Chem. Commun.*, 2022, **58**, 306–309.

400 G. Xing, T. Yan, S. Das, T. Ben and S. Qiu, *Angew. Chem. Int. Ed.*, 2018, **57**, 5345–5349.

401 M. J. Wei, Y. Gao, K. Li, B. Li, J. Q. Fu, H. Y. Zang, K. Z. Shao and Z. M. Su, *CrystEngComm*, 2019, **21**, 4996–5001.

402 Y. Wang, M. Zhang, Q. Yang, J. Yin, D. Liu, Y. Shang, Z. Kang, R. Wang, D. Sun and J. Jiang, *Chem. Commun.*, 2020, **56**, 15529–15532.

403 S. A. Kuznetsova, A. S. Gak, Y. V. Nelyubina, V. A. Larionov, H. Li, M. North, V. P. Zhereb, A. F. Smol'yakov, A. O. Dmitrienko, M. G. Medvedev, I. S. Gerasimov, A. S. Saghyan and Y. N. Belokon, *Beilstein J. Org. Chem.*, 2020, **16**, 1124–1134.

404 X. Q. Xu, L. H. Cao, Y. Yang, F. Zhao, X. T. Bai and S. Q. Zang, *ACS Appl. Mater. Interfaces*, 2021, **13**, 56566–56574.

405 T. Steiner, *Angew. Chem. Int. Ed.*, 2002, **41**, 48.

406 Y. Suzuki, N. Tohnai, A. Saeki and I. Hisaki, *Chem. Commun.*, 2020, **56**, 13369–13372.

Chapter 2. Isostructural construction of HOFs with extended spacer based on shape-fitted docking of hexaazatriphenylene core

2.1 Introduction

Isostructural porous frameworks, whose molecular arrangements and network topology are the same, but with different pore sizes and chemical and physical properties, can provide an important library for a systematic design and optimization of the structure and properties of functional porous materials[1–6]. Therefore, it is a touchstone for reticular chemistry to construct such frameworks[7]. The expansion of the pores may be readily accomplished by elongating the length of ligand molecules or spacer moieties. Indeed, isostructural MOFs and COFs with expanded pores were successfully manufactured with this methodology as described in section 1.8. For example, Yaghi *et al.* reported isostructural MOFs with pore sizes ranging from 1.4 to 9.8 nm constructed from a series of oligophenylene ligands[8]. Isostructural COFs with pores from 4 to 10 nm were also reported[9].

However, it still remains difficult to prepare isostructural frameworks in the case of HOFs[10–15] connected through reversible H-bonds. HOFs have fundamental merits in crystallinity and reusability while the design principle to construct stable HOFs with permanent porosity needs improvement when compared with MOFs and COFs (section 1.7). However, reports of HOFs with permanent porosity have been increasing over the last two decades[16–22]. Homologous building block molecules of HOFs with different lengths of spacers often gave non-isostructural, but diverse frameworks with different molecular arrangements and H-bonded network topologies[17–23]. Only a handful of isostructural HOFs are known so far (section 1.8.4). Cooper, Day, *et al.* employed triptycenetrisbenzimidazolone and its expanded analogue to yield isostructural honeycomb frameworks[24,25]. Farha's, Chao's, and Chen's groups independently reported pyrene-based isostructural HOFs based on pyrene derivatives with different substituents (carboxy, 4-carboxyphenyl, and 6-carboxynaphthalen-2-yl)[26–28]. Miljanić *et al*. also reported a series of quasi-isotropic fluorinated honeycomb HOFs[29,30]. The difficulty to obtain a set of isostructural HOFs clearly originates from weakness of H-bonds. Therefore, a further design principle is necessary to construct isostructural HOFs.

In connection with this, Hisaki's group has recently achieved the fabrication of various isostructural hexagonal networks (HexNets) through predictable H-bonding of C_3-symmetric carboxylic acids with π-conjugated cores, such as triphenylene (Tp) derivatives[31,32], where the most important structural factors are the rigidity of the molecular skeletons and the highly directional and predictable H-bonds (key 1). However, the resultant HexNets stack in different ways to form non-isostructural HOFs. Moreover, they show that two derivatives with even the same Tp core (**Tp** and **BPTp**) with carboxy-phenyl and -biphenyl arms form non-isostructural frameworks (Figure 1a). This is caused by the lack of preferable, unique stacking geometry between the networks. Meanwhile, Hisaki's group has demonstrated that hexaazatriphenylene (HAT) derivatives (**CPHAT**) with carboxy-phenyl groups yielded rigid HOFs[33] (Figure 1b), which displays a single-crystalline porous structure with significant heat resistance up to 339 °C and $S_{A(BET)}$ of 649 $m^2\,g^{-1}$. The crucial structural factor is a twisted conformation of the HAT core that enables

the molecule to stack uniformly through shape-fitted docking in the direction orthogonal to H-bonding (key 2).

Can HAT derivatives with further elongated arms provide another isostructural HOF with larger pores? Herein, the author provides an answer to this question by constructing the multiple generation of isostructural HAT-based HOFs with larger pores. The simple elongation of the arms from phenylene to biphenylene (**BPHAT**) were successful. However, that to terphenylene (**TPHAT**) quickly reached the limit, while the modification of the arms by 1,2-diphenylethyne (tolane) and 4,7-diphenylbenzo-2,1,3-thiadiazole allowed the formation of expanded HOFs (**TolHAT-1** and **ThiaHAT-1**), evidencing the importance of suitable spacer engineering (key 3 in Figure 1c). To the author's knowledge, the present system has so far the largest number of isostructural HOFs with spacer modification. In addition to their structures and properties, including solid-state and solution fluorescence behaviors, structural comparison between the four isostructural HOFs is also described. Interestingly, **ThiaHAT-1** exhibits a large sensitivity to HCl vapors which can be recorded by UV-Vis absorption or emission experiments. Moreover, it is noteworthy that the stability of HOFs can be precisely evaluated by molecular dynamics (MD) simulation, reflecting the importance of considering not only the interaction energy, but also the fluctuation of the molecules. These results give an insight to develop a systematic series of rigid HOFs.

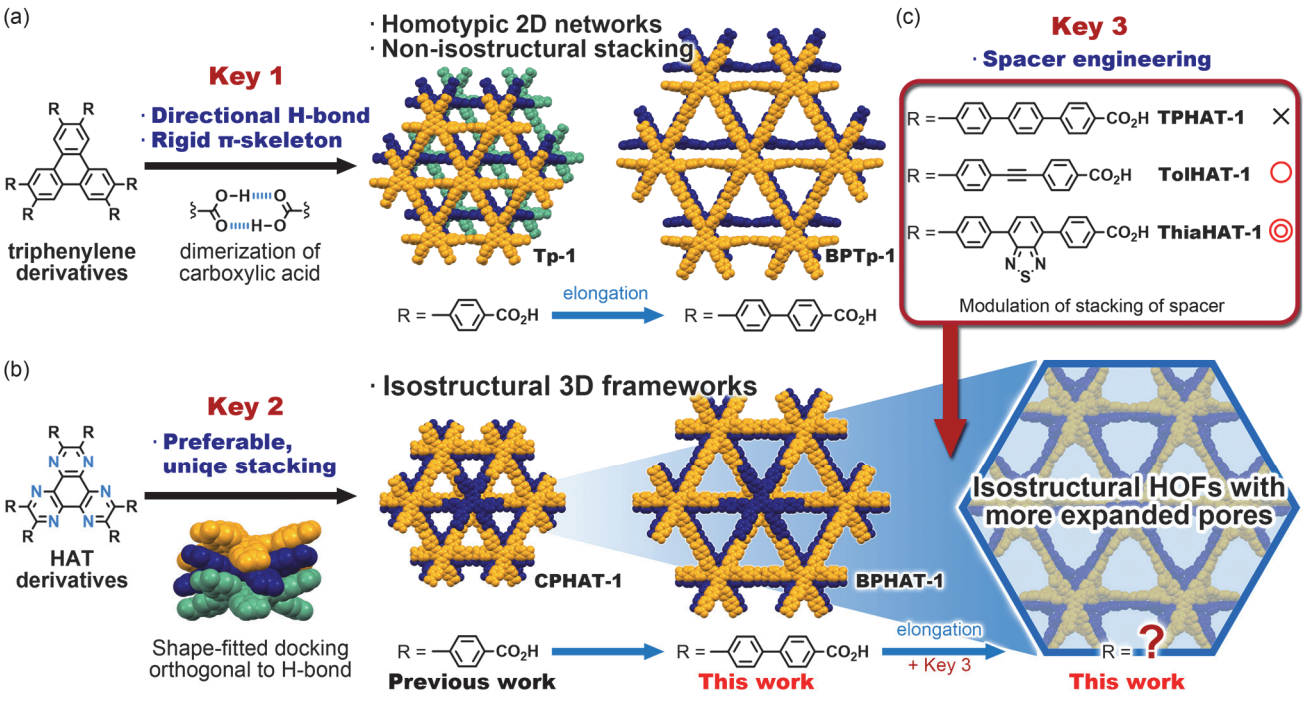

Figure 1. Illustration of keys 1, 2, and 3 to construct isostructural HOFs with different pore sizes. (a) Frameworks formed from triphenylene derivatives. The molecules form isostructural hexagonal network motifs through directional H-bonding of the carboxy group (key 1), while the stacking configurations of the derivatives differ from each other to result in non-isostructural HOFs (**Tp-1** and **BPTp-1**). (b) Frameworks formed from HAT-based molecules. Both molecules with carboxy-phenyl and -biphenyl groups form rigid and stable isostructural HOFs (**CPHAT-1** and **BPHAT-1**) due to the uniform shape-fitted docking of the twisted HAT core (key 2). (c) Construction of isostructural frameworks with larger pores by a systematic engineering of the spacer moieties (key 3).

2.2 Synthesis and crystallization

HAT derivatives, **BPHAT**, **TPHAT**, **TolHAT**, and **ThiaHAT**, were synthesized as shown in Scheme 1. 1,2-Dione derivatives **5a** with biphenyl moieties, **5b** with terphenyl moieties, and **5c** with 4,7-diphenyl-benzo-2,1,3-thiadiazole moieties were synthesized by the Suzuki–Miyaura cross-coupling reaction of 4,4'-(pinacolboryl)benzil derivative **1** with butyl 4-bromophenylcarboxylate (**2**), and hexyl 4'-bromobiphenylcarboxylate derivatives **3** and **4**, respectively. Dione derivative **5d** with a tolane moiety was prepared by the Sonogashira coupling reaction of 4,4'-dibromobenzil (**6**) and hexyl 4-ethynyl-benzoate (**7**). Then hexaaminobenzene (**8**), which was prepared by the reduction of 1,3,5-triamino-2,4,6-trinitrobenzene (**7**)[35], was triply condensed with the corresponding dione derivatives **5a–d** under acidic conditions to afford HAT derivatives with ester groups **9a–d**, respectively. The hydrolysis of **9a–d** gave the building block molecules **BPHAT**, **TolHAT**, **TPHAT**, and **ThiaHAT**, respectively. As a reference compound, **BPTp** with 4'-carboxybiphenyl groups was also synthesized from hydrolysis of precursor **12**, which was prepared SMC reaction of 2,3,6,7,10,11-hexabromotriphenylene (**10**) with pinacolato boron derivative **11**.

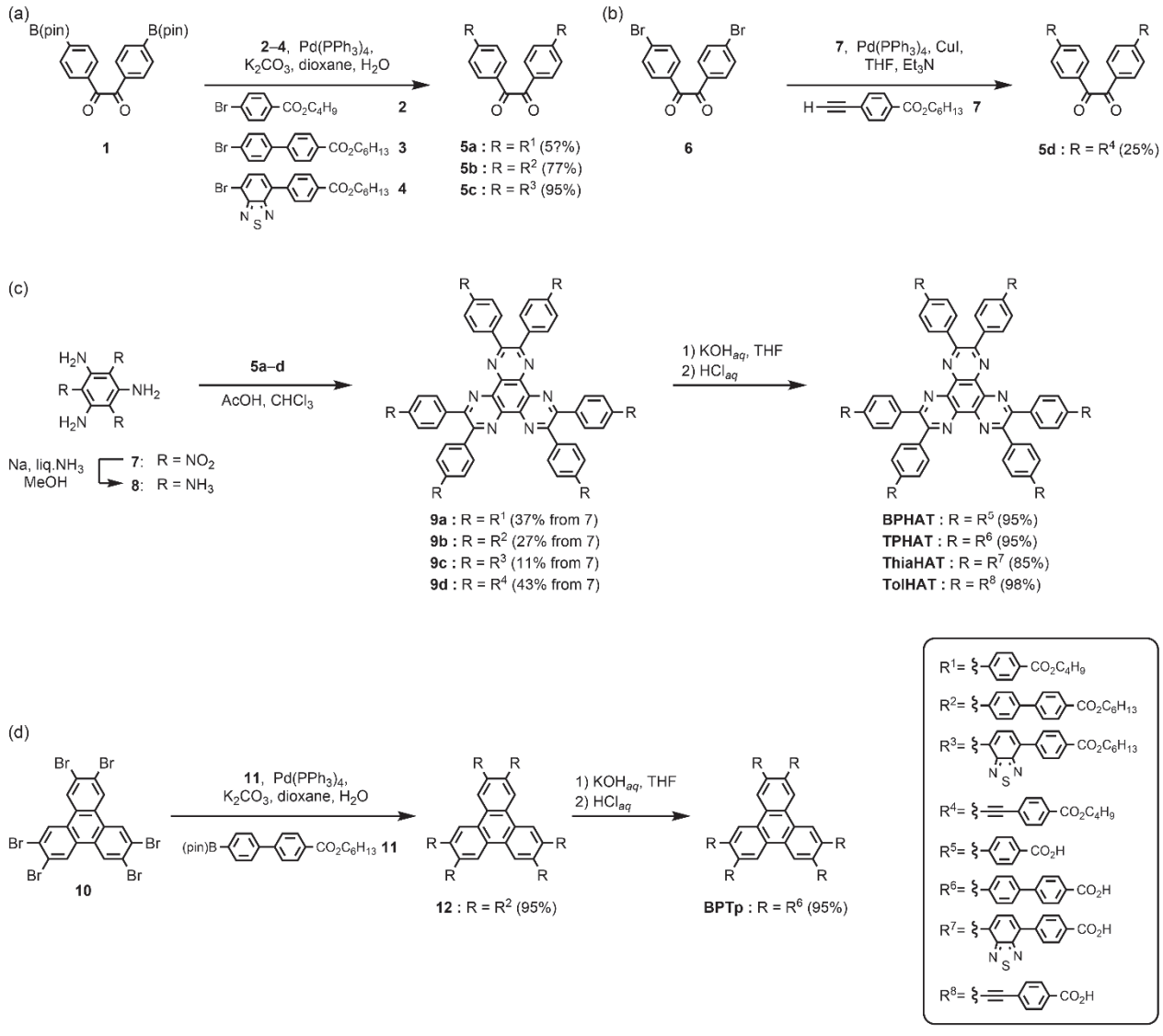

Scheme 1. Synthesis of (a) **5a**, **5b**, **5c** and (b) **5d**, (c) **BPHAT**, **TPHAT**, **ThiaHAT**, and **TolHAT**, and (d) **BPTp.**

To get the HOFs, the synthesized carboxylic acids were recrystallized by slow evaporation from a mixed solution of good solvents [DMF or *N*,*N*-dimethylacetamide (DMA)] and an aromatic solvent [1,2,4-trichlorobenzene (TCB) or 1,2,4-trimethylbenzene (TMB)] at 60 °C for **BPHAT**, **TPHAT**, and **TolHAT**, at 100 °C for **BPTp**, and at 120 °C for **ThiaHAT**.

BPHAT, a mono-phenylene extended derivative from **CPHAT**, yielded pale yellow needle-like single crystals (**BPHAT-1**) with a width of <20 μm (Figure 2a). **TPHAT**, a di-phenylene extended derivative, gave pale green precipitates (**TPHAT-P**) (Figure 2b), which only showed weak and broad peaks in the powder X-ray diffraction (PXRD) pattern (Figure 3). **TolHAT**, on the other hand, gave yellow green needle-like single crystals (**TolHAT-1**) with a width of 5–20 μm and a length of over 100 μm (Figure 2c). Similarly, **ThiaHAT** yielded yellow needle-like microcrystals (**ThiaHAT-1**) with a width of approximately 10 μm and a length of over 100 μm (Figure 2d). **TolHAT-1** and **ThiaHAT-1** were subjected to single-crystalline X-ray diffraction (SCXRD) measurements with synchrotron X-ray radiation to pin-point their crystalline structure.

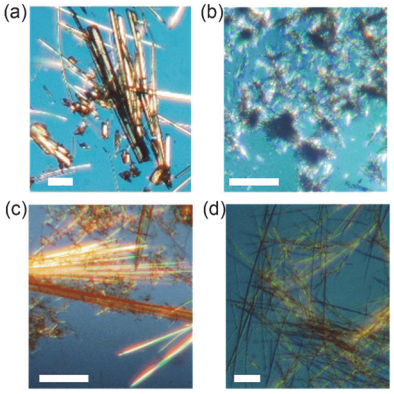

Figure 2. Polarized optical microscopy (POM) images of (a) **BPHAT-1**, (b) **TPHAT-P**, (c) **TolHAT-1**, and (d) **ThiaHAT-1** under daylight. Scale bar: 100 mm.

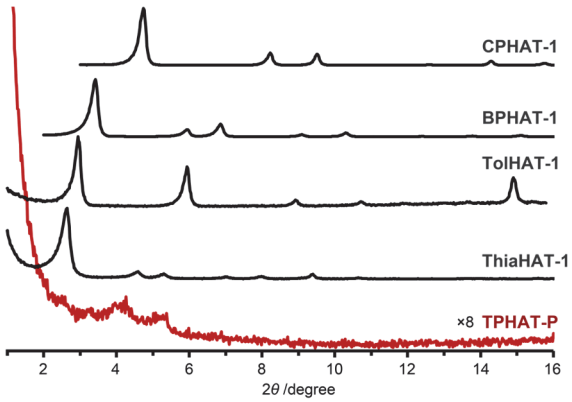

Figure 3. PXRD patterns of **CPHAT-1**, **BPHAT-1**, **TolHAT-1**, **ThiaHAT-1**, and **TPHAT-P**. If **TPHAT-P** is isostructural framework with **ThiaHAT-1**, peaks at around 2θ = 2.68° will be appeared. However, there is no clear peak there, thus **TPHAT-P** is not an isostructure as other HAT derivatives.

2.3 Crystallography

The crystal structure of **BPHAT-1** is shown in Figure 4a, in which **BPHAT** molecules crystallize in the *P*-3 space group to form a porous hexagonal framework. The lattice parameters were $a = b = 29.7532(15)$ Å, $c = 7.1146(6)$ Å, $V = 5454.4(6)$ Å. The carboxy groups form self-complementary H-bonds to give helical strands (Figure 4c). The O1···O3 and O2···O4 distances of the H-bonds are 2.62 and 2.57 Å, respectively. The crystal structure of **BPHAT-1** is isostructural with that of previously reported **CPHAT-1** (Figure 4c). **BPHAT** molecules are one-dimensionally stacked along the b axis with a staggered angle of 60° and intermolecular distances of 3.56 Å (Figure 4d). The **BPHAT** molecule has a twisted conformation due to packing forces; the root mean square deviation (RMSD) of the HAT core from planarity is 0.204, which enables shape-fitted docking between adjacent HAT cores. Owing to this twisted conformation, six peripheral carboxybiphenyl groups are alternately directed up and down (torsion angle between the adjacent biphenyl groups is 22.18°), which results in the construction of a 3D H-bonded network with primitive cubic (***pcu***) topology (Figure 4e). The network is six-fold interpenetrated to give a significantly rigid framework. Threefold helical channels run along the *c* axis and the channels have a triangular shaped cross section with a width of *ca.* 14.5 Å; the solvent-accessible volume was calculated using the PLATON software[36] to be 45% (Figure 4f). The channels accommodate TCB molecules, three of which are located at the three corners of a triangular channel with disorder into two positions (Figure 5), and the others are located in the center of the channel and are completely disordered.

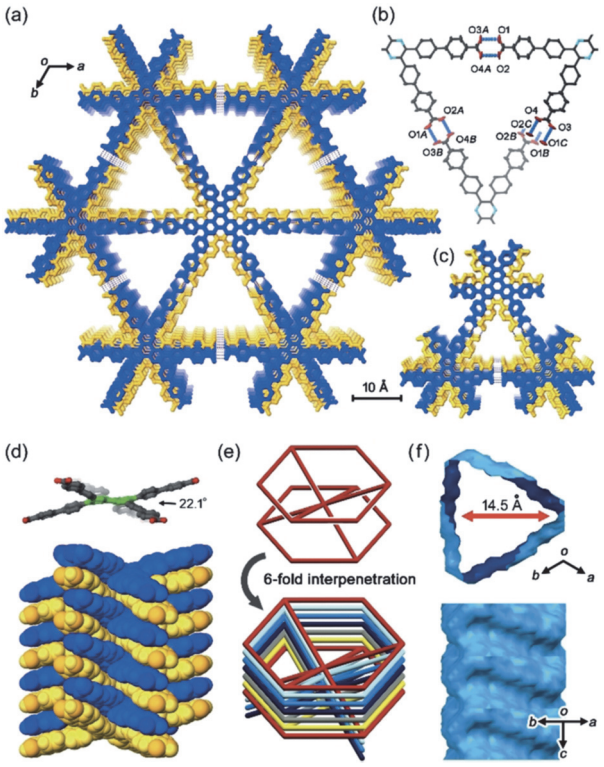

Figure 4. Crystal structure of **BPHAT-1**. Packing diagram of (a) **BPHAT-1** and (c) **CPHAT-1**. Solvent molecules accommodated in the channel are omitted for clarity. (b) H-bonded threefold helical strand. Symmetry code: (A) −x+y, 1−x, 1+z; (B) 1−y, 1+x−y, 2+z; (C) 1−y, 1+x−y, −1+z. (d) Twisted nonplanar conformation of **BPHAT** (top) where the central HAT moiety is colored green; its shape-fitted 1D-stacked column (bottom). (e) Schematic models of single (top) and sixfold (bottom) interpenetrated frameworks with ***pcu*** topology. (f) Visualization of the helical channel surface.

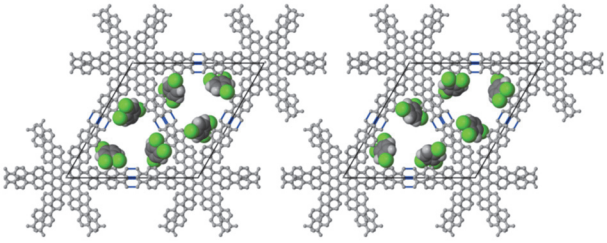

Figure 5. Packing diagram of **BPHAT-1** with solvent (TCB) molecules. TCB molecules at the corners are disordered into two positions as shown left and right, while the other located at around the center were severely disordered, and therefore, were not solved.

TolHAT and **ThiaHAT** crystallized into the space group *R*-3*c* to yield porous frameworks (**TolHAT-1** and **ThiaHAT-1**) (Figure 6). **TolHAT-1** has the cell parameters of $a = b = 59.529(1)$ Å, $c = 6.9637(2)$ Å, and $V = 21371.4(8)$ Å^3 and **ThiaHAT-1** has $a = b =$

65.827(5) Å, *c* = 6.9879(7) Å, and *V* = 26223(4) Å^3. The latter has a slightly elongated framework due to the longer arms of the building block molecule. Both molecules have D_{3h}-symmetry and are stacked *via* shape-fitted docking of the HAT cores with intermolecular distances of 3.49 Å to form 1D columns. The root means square deviations (RMSDs) of the HAT cores of **TolHAT** and **ThiaHAT** in the crystals are 0.215 Å and 0.229 Å, respectively. Their torsion angles between adjacent aryl arms in the *ortho*-positions are 23.5° and 24.5°, respectively. The optimized structures obtained at the B3LYP/6-31G(d) level show more planar conformations (RMSD on the HAT core: 0.111 Å for **TolHAT** and 0.108 Å for **ThiaHAT**; and torsion angles between arms: 17.8° for **TolHAT** and 16.7° for **ThiaHAT** (Figure 8), indicating that packing forces significantly induced the molecular distortion of the HAT moieties in the crystalline states. In **TolHAT-1** and **ThiaHAT-1**, the HAT derivatives form dimers of carboxyl groups through H-bonds to provide 3D networks with a ***pcu***-topology (Figure 6i). The networks are 8-fold interpenetrated to give the whole frameworks possessing large C_3-symmetric 1D pores with a triangular aperture. The height and base of the aperture in **TolHAT-1** are 19.2 Å and 20.4 Å, respectively, and those of **ThiaHAT-1** are 19.0 Å and 19.7 Å, respectively (Figure 6d,h). Although **ThiaHAT** has a longer arm than **TolHAT**, the pores of **ThiaHAT-1** are smaller than

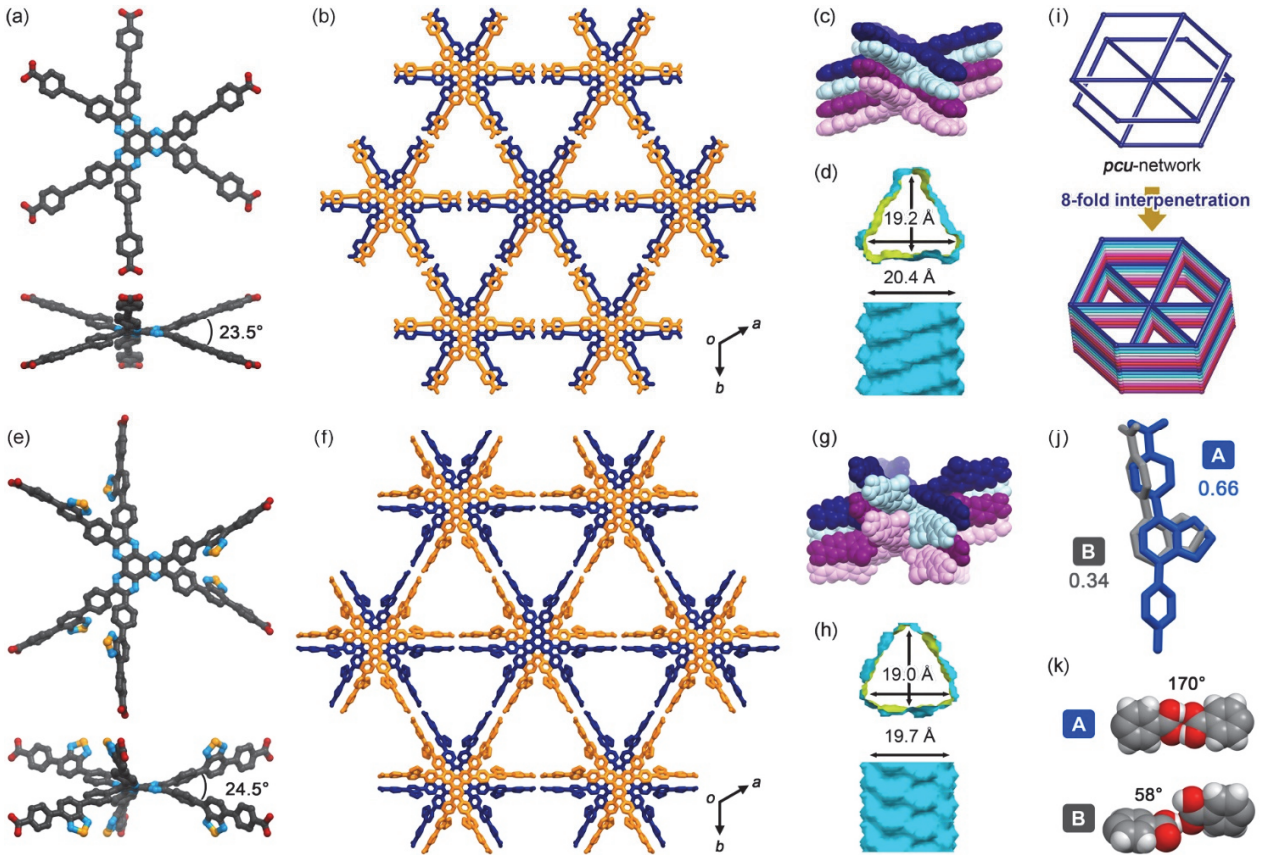

Figure 6. Crystal descriptions of (a–d) **TolHAT-1** and (e–h) **ThiaHAT-1**. (a,e) Twisted nonplanar conformations viewed down the *c* axis (top) and the *ab* planes (bottom). (b,f) Packing diagrams. (c,g) 1D columns formed by shape-fitted docking of the HAT derivatives. (d,h) Visualized void surfaces viewed down the *c* axis (top) and the *ab* planes (bottom) (yellow: inside and cyan: outside). (i) A H-bonded ***pcu***-topological network, which interpenetrates by 8-fold to form the frameworks of **TolHAT-1** and **ThiaHAT-1**. (j) The disordered arms of **ThiaHAT-1** into two positions A and B with an occupancy of 0.662 and 0.338, respectively. (k) H-bonded dimers formed from the arms A (major) and B (minor). A structure in site B is described in Figure 7 and not shown in (e–h).

those of **TolHAT-1** because of the bulky thiadiazol groups of **ThiaHAT**. The void ratios of **ThiaHAT-1** and **TolHAT-1**are 48% and 55%, respectively, which were calculated by using PLATON software with a probe radius of 1.2 Å[36]. It should be noted that the arms of the **ThiaHAT** molecule are disordered in two positions A and B with a site occupancy of 0.662 and 0.338, respectively (Figure 6j). The carboxy group in site A forms a typical complementary H-bonded dimer with an O–H/O distance and an angle of 2.6 Å and 170°, respectively, while the group in site B forms a truncated dimer with an O–H/O distance and a dihedral angle between carboxylate planes of 2.7 Å and 59°, respectively (Figure 6k). In both conformations, the benzothiadiazole groups are inclined into the pore and aligned vertically along the *c* axis (Figures 7 and 9).

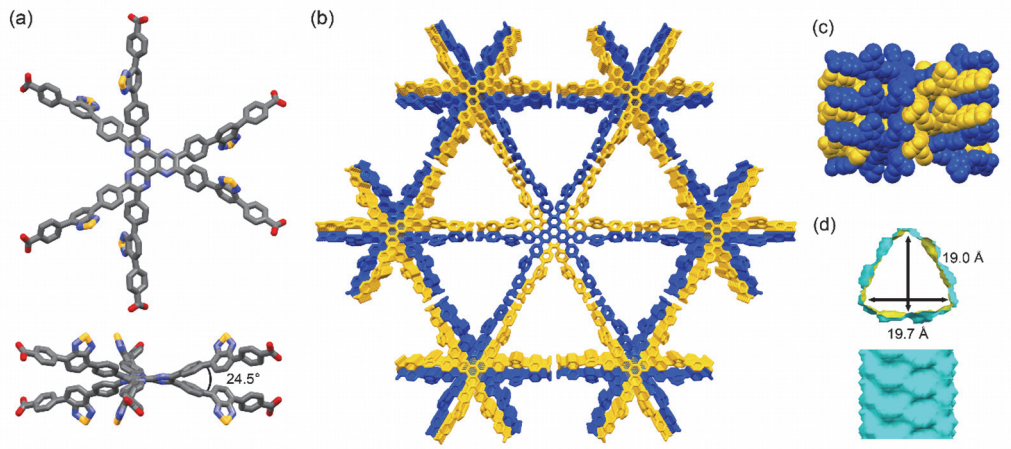

Figure 7. Crystal descriptions about site B of **ThiaHAT-1**. (a) Twisted nonplanar conformations viewed down the *c* axis (top) and the (100) planes (bottom). (b) packing diagrams. (c) 1D columnar structure composed of π-stacked HAT derivatives. (d) visualized void surfaces viewed down along the *c* axis (top) and the *ab* planes (bottom). (yellow: inside, cyan: outside).

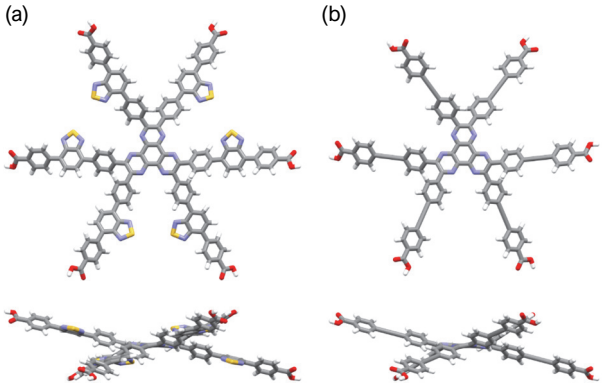

Figure 8. Optimized structure of (a) **TolHAT** and (b) **ThiaHAT** (top) viewed down and (bottom) viewed side.

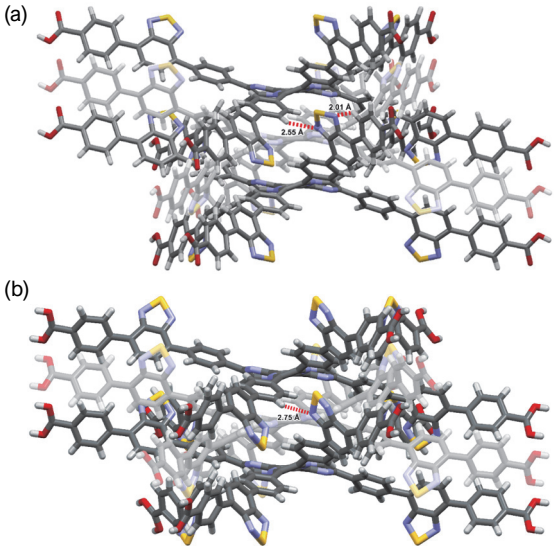

Figure 9. Interlayer and Intralayer H-bonding interaction between N atom and H atom of (a) A-site and (b) B-site structures in **ThiaHAT-1.**

A crystal structure of the obtained crytal **BPTp-1** is shown in Figure 10. **BPTp** forms 2D assembling structure of hexagonal networks (HexNet) motifs through H-bonding. These adjacent HexNet stacked by two edge-to-face stackings (CH-π interactions). One is between hydrogen of the phenylene ring I and π-conjugated plane of the triphenylene ring, and another is between hydrogen of the phenylene ring I and π-conjugated plane of the phenylene ring II (Figure 11a,b). Two of three carboxyphenyl groups in an asymmetric unit are disordered in two position described in Figure 10c,d. In each position, **BPTp** molecules form phenylene triangle motifs through complementary H-bonding. The molecule of TCB in a gap between the biphenyl arms was crystallographically solved (Figure 10a). Other guests are not solved due to severe disorder. Compared with the crystal structure of **Tp-1**[53] (Figure 11), **BPTp** constructs a homotypic HexNet through complimentary H-bonding and, considering only adjacent two layers, an isostructural stacking

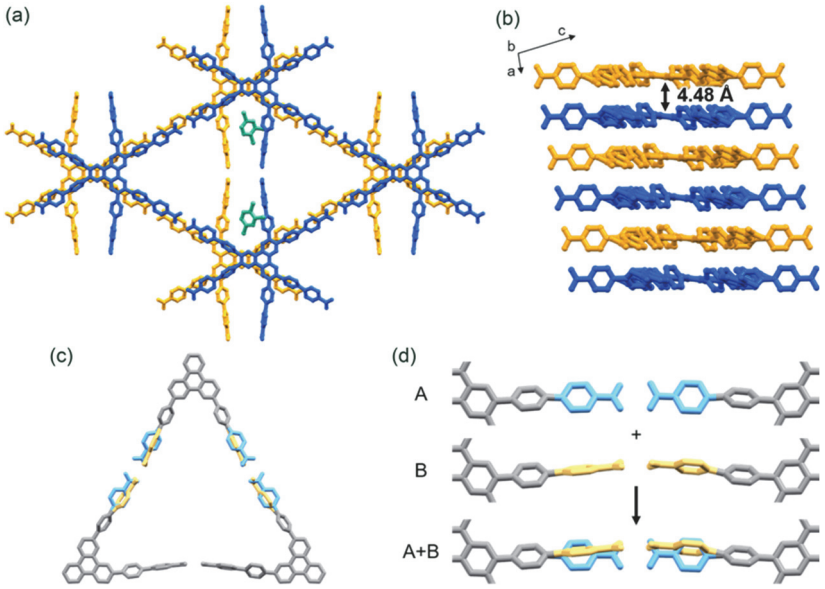

Figure 10. Crystal structure of **BPTp-1**. (a) Packing diagram. Guest molecules (TCB) shows green. (b) Stacking diagram, (c) H-bonding network motif, and (d) disordered conformation of arm in two positions.

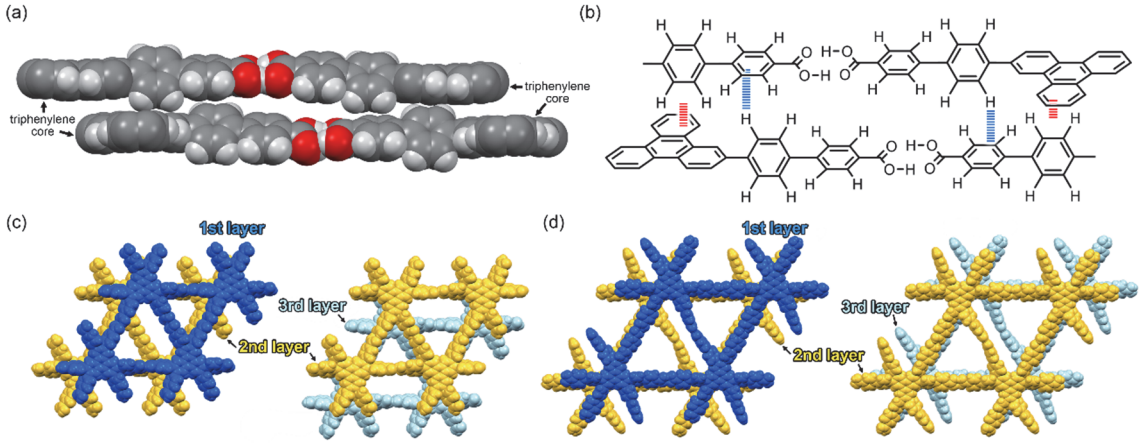

Figure 11. Leading intermolecular interactions of **BPTp-1** observed between the adjacent HexNet sheets drawn as (a) space filling models and (b) chemical structures. The phenylene rings in the order adjacent to the Tp core were named as I and II. Comparison between stacking structures of (c) **Tp-1** and (d) **BPTp-1**.

structure with simply extended arm moieties, whose inter-layer distances are similar as Tp structures of 4.48 Å. On the other hand, these whole structures are different. In **Tp-1**, an orientation of stacking changes every HexNets. While in **BPTp-1**, HexNets stacks in the same orientation. This is caused from a lack of preferable unique stacking geometry between flat Tp cores.

Further structural comparison is conducted focusing on the assembling position of the arm moieties in **BPHAT-1**, **TolHAT-1**, and **ThiaHAT-1**, as well as in previously reported HOF **CPHAT-1** (Figure 12, Table 1). The benzene rings directly bonded to the HAT core are labeled Ar-I. Similarly, the benzene rings adjacent to the terminal carboxyl group are labeled Ar-III in **BPHAT**, **TolHAT**, and **ThiaHAT**. The middle moieties between Ar-I and Ar-III rings are labeled Ar-II in **ThiaHAT**. The dihedral angles of the neighboring aryl groups (*i.e.* the HAT core, Ar-I, Ar-II, and Ar-III) are listed in Table 1. The torsion angles between Ar-I and the core are 23.5° for **CPHAT**, 25.5° for **BPHAT**, 25.6° for **TolHAT**, and 28.2° for **ThiaHAT**. The distortions are similar to each other. Ar-I rings are aligned *via* edge-to-face CH-π interaction with a contact angle of 33.6° (**CPHAT**), 38.1° (**BPHAT**), 37.1° (**TolHAT**), and 46.5° (**ThiaHAT**). The contact angles of all these HOFs follow the same tendency as the distortion described above with the exception of **ThiaHAT** due to the bulky group. In **BPHAT-1**, Ar-I and Ar-III were twisted moderately (−26.7°), and their rotation direction was opposite to the rotation direction between the core and Ar-I. Therefore, the torsion angle between the core and Ar-III was only −16.0°. Adjacent Ar-III moieties were assembled nearly parallel (15.0°) *via* face-to-face π stacking. Similarly, **TolHAT-1** has a small torsion angle (−15.1°) between Ar-I and Ar-III rings because of the less sterically hindered ethynyl moiety, resulting in parallel face-to-face π stacking of the adjacent Ar-III rings. On the other hand, it is difficult for **ThiaHAT-1** to form the same parallel assembly of the arms due to bulky Ar-II rings, *i.e.,* a 2,1,3-benzothiadiazole (Tz) group. The Tz group is twisted by 37.4° and 18.8° against Ar-I and Ar-III, respectively. Adjacent Tz groups interact through face-to-edge CH-π interactions with a contact angle of 58.5°. Every other Tz group is oriented in the same direction and assembled through multiple dipole–dipole interactions[37,38]. There is also an intermolecular H-bonding interaction between Ar-II nitrogen and Ar-I hydrogen atoms of two molecules away (Figure 9). Another disorder structure, site B exhibited a similar trend (Figure 13). Consequently, the introduction of the Tz group forces the arm to have a limited conformation, which combined with shape-fitted docking of the HAT core, induces the **ThiaHAT** molecules to be organized into a crystalline framework. On the basis of the aforementioned results, the author suggests that, in the case of **TPHAT**, the conformations of the terphenyl arm may not be suitable either for attractive face-to-face or for face-to-edge interaction, preventing the formation of crystalline porous frameworks. Additionally, considering the above interpretation, it could be possible to construct isostructural HOFs with further expanded pores by varying the bulkiness of elongated arms. Namely, molecules with no steric hindrance between arm components, such as **TolHAT**, could form HOFs through simply face-to-face π stacking, while those with sterically hindered arm components, such as **ThiaHAT**, could also produce HOFs through edge-to-face interactions among conformationally restricted arm components.

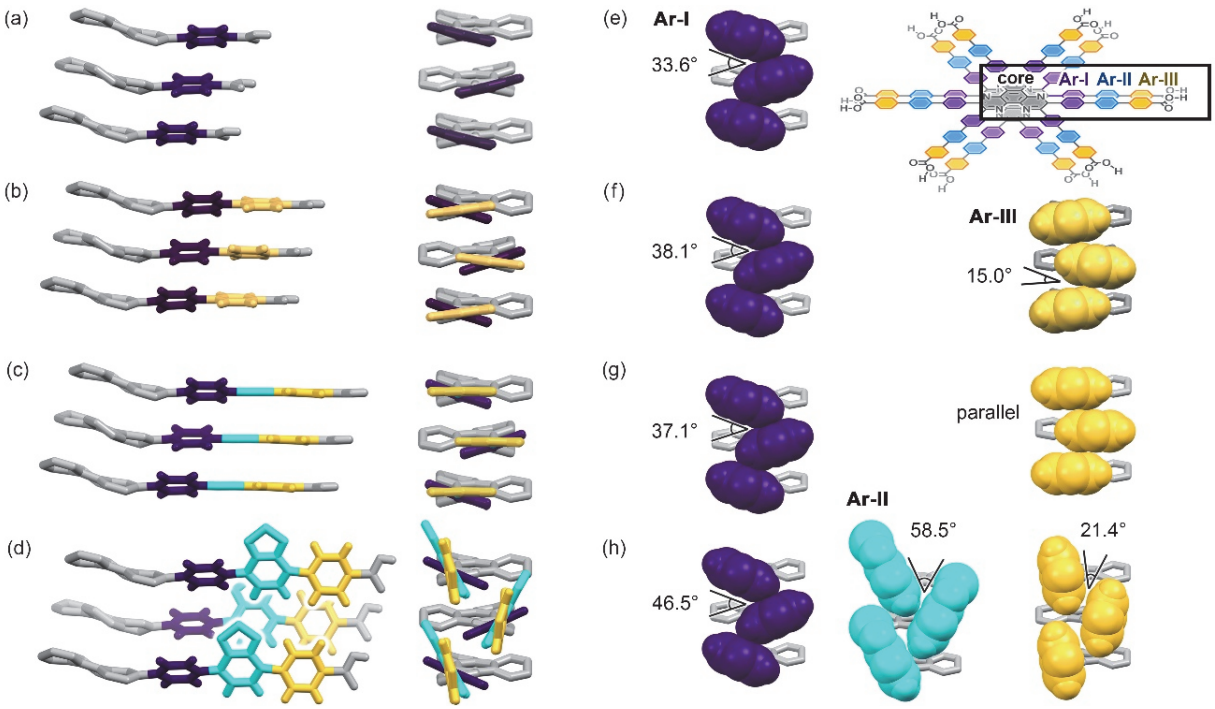

Figure 12. Spacer assembling manners of (a) **CPHAT-1**, (b) **BPHAT-1**, (c) **TolHAT-1**, and (d) major part (site A) of **ThiaHAT-1** from the orthogonal two different views (left and right). (e–h) Contact manners of aryl rings (Left: Ar-I, Center: Ar-II, Right: Ar-III) in **CPHAT-1**, **BPHAT-1**, **TolHAT-1**, and **ThiaHAT-1**, respectively. The aromatic rings in the order adjacent to the HAT core are defined the name and color as I: purple, II: cyan, and III: yellow, respectively. The HAT core is colored gray. (Inset) Chemical structures of stacking HAT derivatives.

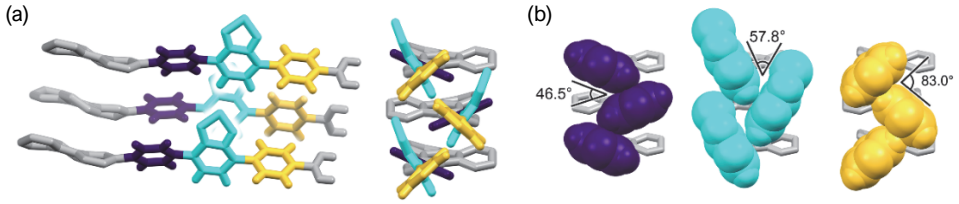

Figure 13. (a) Spacer assembling manners of minor part (site B) of **ThiaHAT-1** from the orthogonal two different views (left and right). (b) Contact manners of aryl rings (Left: Ar-I, Center: Ar-II, Right: Ar-III) in site B of **ThiaHAT-1**. The aromatic rings in the order adjacent to the HAT core are defined the name and color as I: purple, II: cyan, and III: yellow, respectively. The HAT core is colored gray.

Table 1. Dihedral angles among the core and aromatic rings in the spacer moiety.

	CPHAT / °	**BPHAT** / °	**TolHAT** / °	**ThiaHAT** (Major)[a] / °	**ThiaHAT** (Minor)[a] / °
Core-I	23.5	25.5	25.6	28.2	28.2
Core-II	–	–	–	61.6	62.6
Core-III	–	−16.0	−19.1	80.4	41.7
I-II	–	–	–	37.4	38.5
I-III	–	−26.7	−15.1	55.5	65.6
II-III	–	–	–	18.8	76.6

[a] (Major) and (Minor) denote A and B site of disordered spacer moieties of **ThiaHAT-1.**

2.4 Thermal analysis and activation

To investigate their thermal behavior, thermal gravimetric (TG) and variable temperature (VT) PXRD analyses were conducted on the as-formed crystals of HOFs. The TG curve of bulk crystalline **BPHAT-1** reached a plateau at 180 °C *via* multistep 53% weight loss and the plateau was maintained until the compound began to decompose at around 320 °C (Figure 14a). The observed weight loss indicates a host/guest ratio of 1:7, which is also supported by ^{1}H NMR spectroscopy measurements (Figure 15). To obtain structural information during removal of the TCB molecules from the pores by heating, variable-temperature powder X-ray diffraction (VT-PXRD) patterns of bulk crystalline **BPHAT-1** were recorded while heating from room temperature to 360 °C (Figure 14b). The diffraction intensity of the (100) peak was also plotted (Figure 14c). As observed in other previously reported systems[31,33], the peak intensity was poor in the low-temperature region (rt to 100 °C) because of disordered TCB molecules inside the channels. Disordered TCB molecules were removed by heating, so that the peak intensity increased and reached a plateau at 126 °C. It is noteworthy that the observed PXRD pattern, which is in good agreement with that

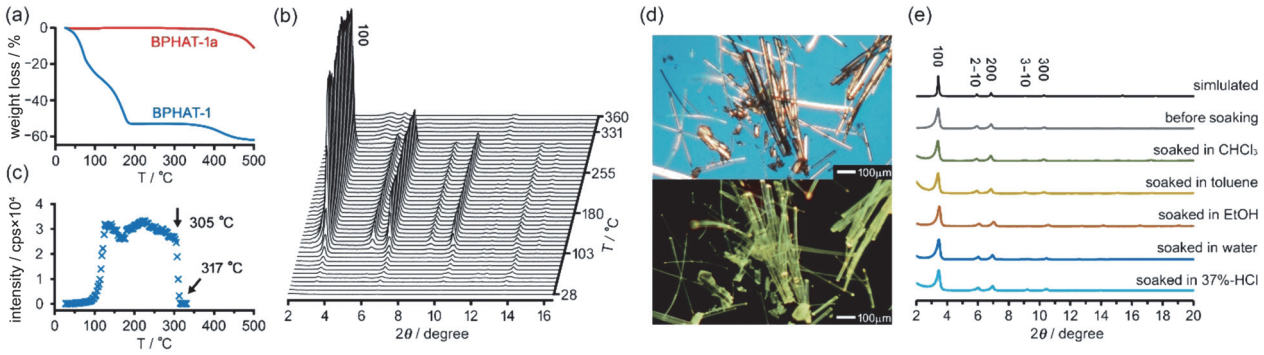

Figure 14. Thermal and chemical durability of crystalline **BPHAT-1a**. (a) TG profiles of **BPHAT-1** (blue) and **BPHAT-1a** (red). (b) VT-PXRD patterns of **BPHAT-1** heated from rt to 360 °C. (c) Changes of the 100 peak intensity of VT-PXRD with temperature. The intensity rapidly decreased at 305–317 °C, which indicated collapse of the framework. (d) POM images of **BPHAT-1a** under (top) ambient light and (bottom) UV light with a wavelength of 365 nm. (e) PXRD patterns of **BPHAT-1a** simulated from SXRD data, before soaking, and after soaking in hot solvents for 7 days: $CHCl_3$ (60 °C), toluene (100 °C), ethanol (60 °C), water (100 °C), and 37% HCl (60 °C).

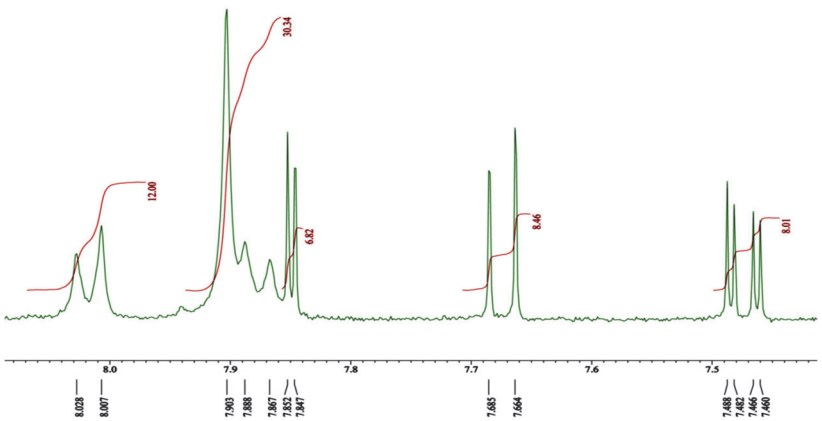

Figure 15. ^{1}H NMR (DMSO-d_6) spectrum of as-formed **BPHAT-1**.

of **BPHAT-1**, was retained up to 305 °C, which indicates that the framework shows no structural changes upon removal of the TCB molecules and that it has significantly high temperature resistance.

The crystalline bulk of **TolHAT-1** was prepared from a mixed solution of DMA and 1,2,4-trimethylbenzene (TMB) instead of DMA and TCB because of its more prominent PXRD pattern, although both of them have the same framework structure (Figure 16). TG analysis of **TolHAT-1** shows a stepwise curve with no clear plateau, indicating that solvent molecules were released from the pore in two steps: up to approximately 80 °C and up to 300 °C (Figure 17)[34]. PXRD patterns were recorded with increasing temperatures to follow the structural changes in the framework induced by guest removal (Figure 18a). The intensity of diffraction peaks such as those at 2θ = 2.96° and 5.94°, ascribable to the (2 −1 0) and (4 −2 0) planes, respectively, slightly increases upon removal of the disordered solvent molecules up to 85.5 °C (red line). Then, the intensity of the original peaks decreases at higher temperatures, and instead, weak peaks at 2θ = 3.60° and 5.06° were recorded, indicating a structural transition. This temperature corresponds to the second stage of guest removal in the TG curve, indicating that the structural transition coincides with the removal of guest molecules from the framework.

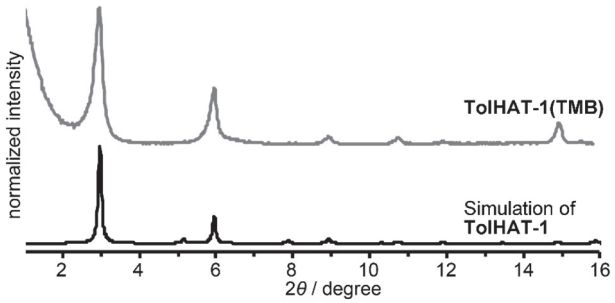

Figure 16. A PXRD pattern of (top) **TolHAT-1** obtained from 1,3,5-trimethylbenzene (TMB) and (bottom) that simulated from X-ray diffraction analysis on a single crystal obtained from 1,2,4-trichlorobenzene (TCB), indicating that both have the same crystal structure.

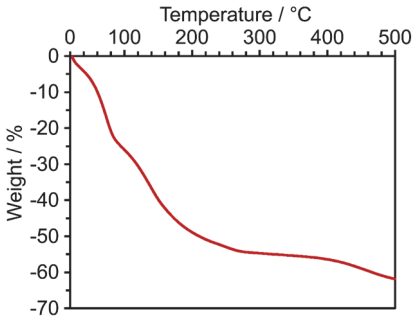

Figure 17. TG profile of **TolHAT-1**.

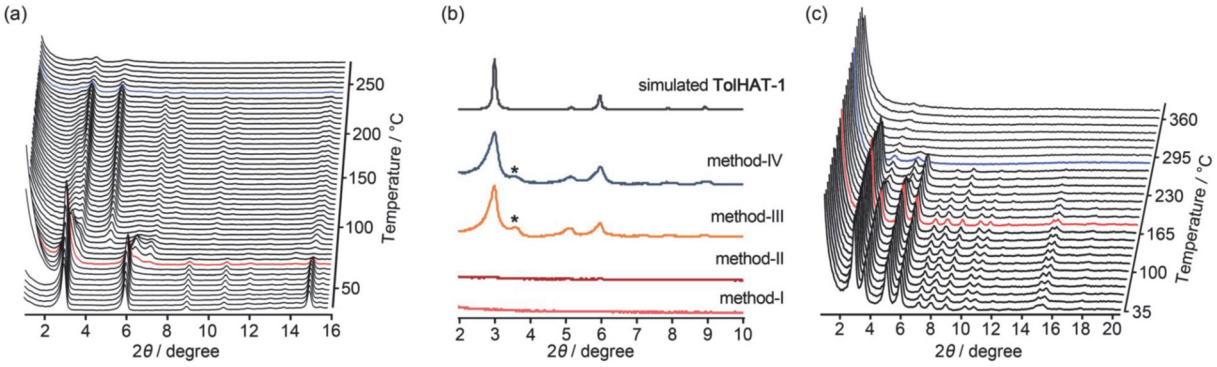

Figure 18. (a) VT-PXRD patterns of as-formed HOF **TolHAT-1**. (b) PXRD patterns of activated HOF **TolHAT-1a*N*** (N =I–IV) with simulation pattern of **TolHAT-1**. (c) VT-PXRD patterns of **TolHAT-1aIV** from rt to 360 °C. Red line indicated the collapse temperature and blue line exhibited the temperature at completely collapsed. An asterisk '*' denotes unknown peak shown in activated **TolHAT** crystals.

In thermal analysis of **ThiaHAT-1**, similar properties to **BPHAT-1** were observed (Figure 19). The TG curve shows two-step release of solvent (TCB) molecules, suggesting that TCB molecules are in two different locations in the voids corresponding to the middle and the corner ones[34]. The curve reaches a plateau at 180 °C, indicating a complete removal of solvent molecules. The HOF was also subjected to VT-PXRD experiments (Figure 19c). The PXRD peaks of the as-formed **ThiaHAT-1** show no shift at different temperatures, while their intensities increase over 100 °C until reaching a plateau at 170 °C due to the removal of severely disordered TCB molecules, which is frequently observed for HOFs[32–34]. The original diffraction peaks are retained up to 305 °C; however, higher temperatures produce a rapid decrease of the intensity of the (100) peak, evidencing the collapse of the framework.

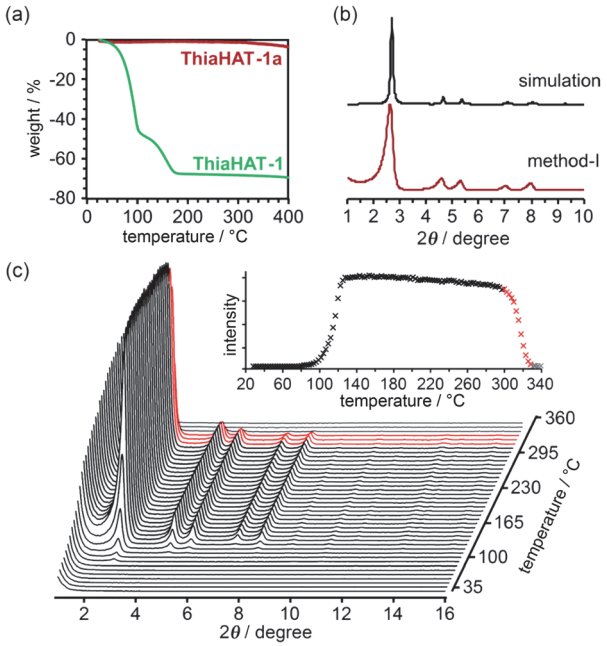

Figure 19. (a) TG profiles of **ThiaHAT-1** (green line) and **ThiaHAT-1a** (red line). (b) PXRD pattern of **ThiaHAT-1a** activated *via* method I with simulation pattern of **ThiaHAT-1**. (c) VT-PXRD patterns of **ThiaHAT-1** heated from rt to 360 °C. (inset) Changes of the (100) peak intensity of **ThiaHAT-1** with temperature. The intensity rapidly decreased at 300–330 °C (red line), which indicated collapse of the framework and no peak appeared at over 330 °C.

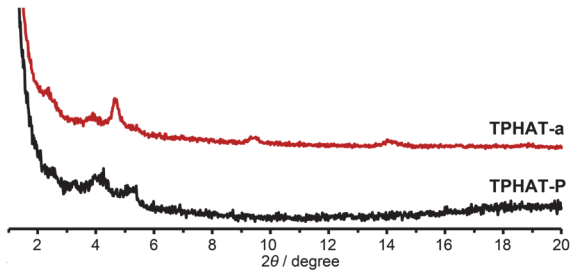

Figure 20. PXRD patterns of **TPHAT-P** and **TPHAT-a**.

The activations (*i.e.,* removal of solvent molecules filling the pores) of **BPHAT-1**, **TPHAT-P**, and **ThiaHAT-1** were accomplished at 150 °C, 120 °C, and 120 °C under vacuum for 24 h to yield the activated crystalline material **BPHAT-1a**, **ThiaHAT-1a**, and **TPHAT-a**, respectively. Keeping this in mind, the activation of **TolHAT-1** was performed by the following four methods: (I) heating at high temperature (120 °C) under vacuum; (II) immersing in benzene to exchange the trapped solvent with benzene molecules followed by heating at relatively low temperature (80 °C) under vacuum; (III) immersing in benzene followed by freeze-drying; (IV) immersing sequentially in dichlorobenzene, chlorobenzene, toluene, and benzene, followed by freeze-drying. PXRD patterns of the materials activated by methods I–IV, termed **TolHAT-1a*N*** (*N* = I–IV), were recorded (Figure 18b). The complete removal of the solvent from the activated materials was confirmed by ^{1}H NMR spectroscopy (Figures 21–24) and TG analysis (Figures 14a and 19a).

TPHAT-a showed the weak pattern, which was similar to **TPHAT-P** (Figure 20). Notably, **BPHAT-1a** retained single crystallinity, as indicated by polarized optical microscopy (POM) observations (Figure 14d), and SXRD analysis of **BPHAT-1a** was successfully accomplished. **BPHAT-1a** has the same framework as **BPHAT-1** (section 2.10.2), although a very slight increase of the *a*, *b*, and *c* axes was observed. The

crystallinity of **TolHAT-1aI** and **TolHAT-1aII** was completely lost. However, **TolHAT-1aIII** retained its crystallinity, while one non-identifiable peak appeared at 3.60°, which may be ascribable to another phase partially formed by the transformation of the original framework. By a more controlled exchange of the solvent molecules, the intensity of the peak became weaker (**TolHAT-1aIV**), but still present, revealing that the framework of **TolHAT-1a** is quite fragile and prone to undergoing phase transition. The obtained **TolHAT-1aIV** was then subjected to VT-PXRD measurements (Figure 18c). The intensity of the peak at 2θ = 2.96° starts to decrease at 190 °C (the pattern colored in red) and vanishes at 298 °C (blue line) (Figures 17b and 18). This behavior is in contrast with that of a HOF based on hexakis[(4-carboxyphenyl)ethynyl]benzene, which is stable at high temperatures up to 300 °C, as reported by Chen *et al*.[23] **ThiaHAT-1a** (Figure 19b) maintained its structure and crystallinity. Other activation methods (methods II and IV) also gave the same activated HOFs (Figure 25). The activation completion was confirmed by the ^{1}H NMR spectrum of the material dissolved in DMSO-d_6 (Figure 24). This **ThiaHAT-1a** was also subjected to VT-PXRD experiments, showing that the crystalline network is stable up to 305 °C (Figure 26).

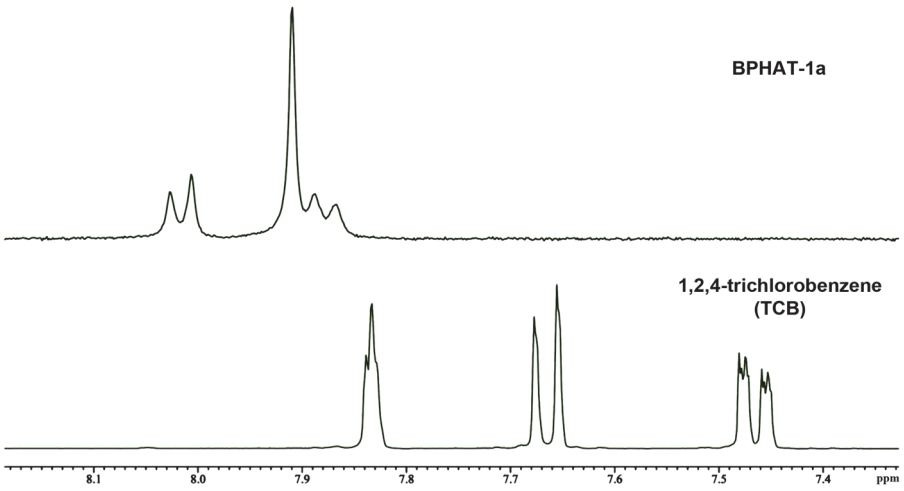

Figure 21. ^{1}H NMR (DMSO-d_6) spectra of (top) **BPHAT-1a** and (bottom) TCB. The spectrum of **BPHAT-1a** shows no peaks ascribable to TCB, indicating that solvent molecules are completely removed by activation process.

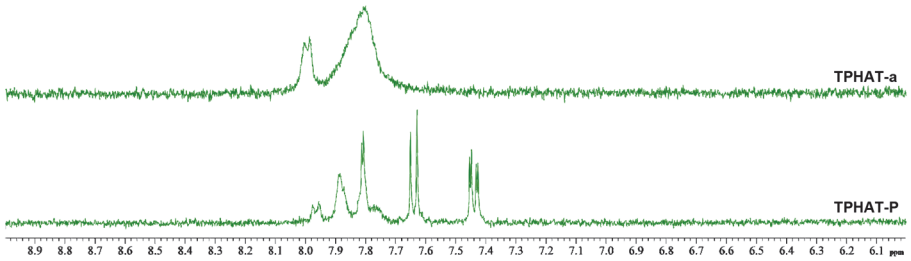

Figure 22. ^{1}H NMR (DMSO-d_6) spectra of (top) **TPHAT-a** and (bottom) **TPHAT-P**. Chemical shift of **TPHAT** changes with concentration due to an aggregation in DMSO solution. **TPHAT-a** was obtained by **TPHAT-P** heating at 120 °C under vacuum for 24 h.

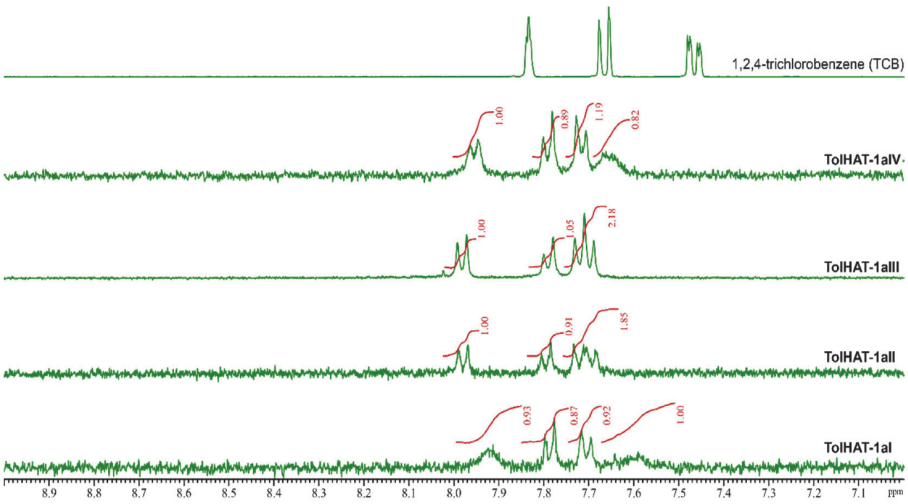

Figure 23. ^{1}H NMR (DMSO-d_6) spectra of the activated HOF **TolHAT-1a*N*** (N = I–IV). Chemical shift of **TolHAT** changes with concentration due to an aggregation in DMSO solution.

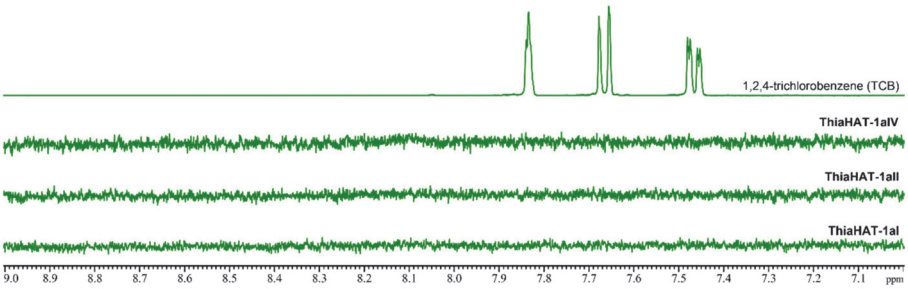

Figure 24. ^{1}H NMR (DMSO-d_6) spectra of the activated HOF **ThiaHAT-1a*N*** (N = I, II, and IV). **ThiaHAT** is almost insoluble to DMSO.

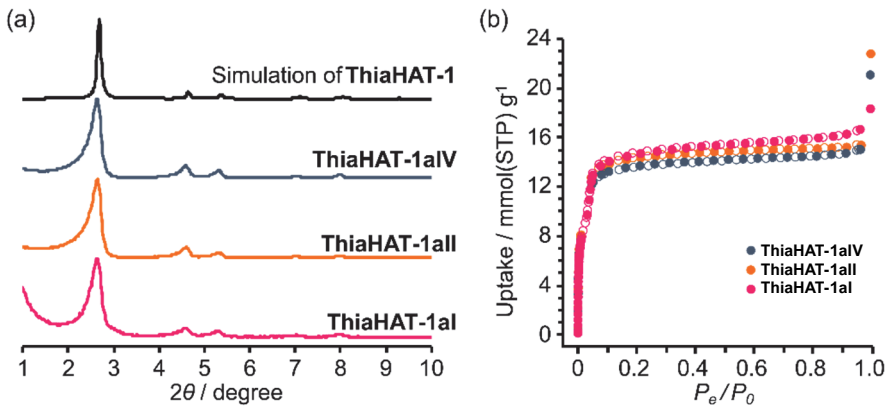

Figure 25. Evaluation of **ThiaHAT-1a*N*** (*N* = I, II, and IV). (a) PXRD patterns and (b) N_2 gas sorption isotherms at 77K. Open symbol: adsorption, solid symbol: desorption.

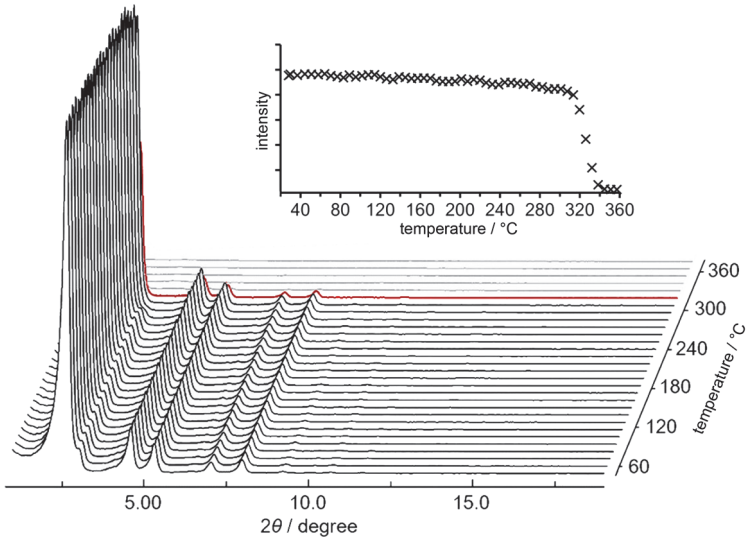

Figure 26. VT-PXRD patterns of **ThiaHAT-1a** heated from rt to 360 °C. (Inset) Changes of the (100) peak intensity with temperature. The intensity rapidly decreased at 306–330 °C, which indicated collapse of the framework.

2.5 Evaluation of the chemical durability

To evaluate the chemical stability, the activated HOFs were immersed in various solvents and solutions and tested through PXRD measurements (Figures 14e and 27). The framework of **BPHAT-1a** resisted solvents, which would typically cleave the H-bonds. For example, **BPHAT-1a** is hardly soluble in dichloromethane, while it is moderately soluble in DMF. The original PXRD profile of **BPHAT-1a** shown in Figure 14e retained after the HOF is soaked in chloroform at 60 °C, toluene at 100 °C, ethanol at 60 °C, water at 100 °C, and 37% HCl at 60 °C for 7 days. For the case of **TolHAT-1aIV** and **ThiaHAT-1a** (Figure 27), they were immersed in *conc.* HCl_{aq}, $NaOH_{aq}$, ethanol, $CHCl_3$, and diethyl ether, at rt for 24 h. The crystallinities of **TolHAT-1aIV** after soaking are lower than that of the original, indicating that the introduction and removal of guest molecules caused a partial collapse of the framework. The PXRD patterns of **ThiaHAT-1a** soaked in, on the other hand, retain the original diffraction profile, indicating its good stability in various solvents. However, the porosity after being immersed in *conc.* HCl_{aq} and $NaOH_{aq}$ became lower than that of pristine **ThiaHAT-1a** (Figure 28, Table 2). However, alkaline aqueous solution, such as aqueous KOH, immediately dissolved the crystalline powder, which is the durability limitation of HOFs connected by dimerization through the carboxy groups.

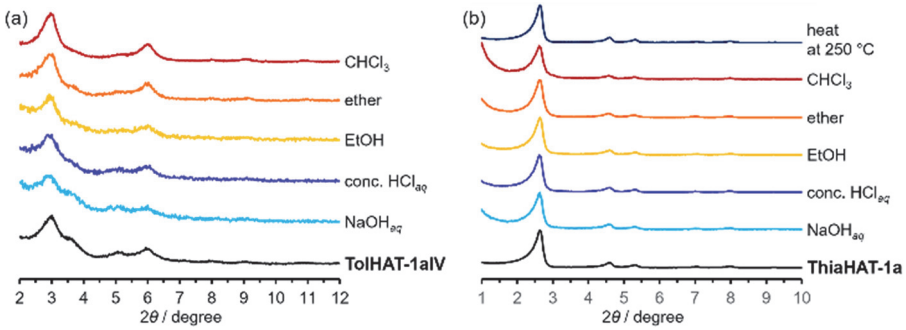

Figure 27. PXRD patterns of (a) **TolHAT-1aIV**, and (b) **ThiaHAT-1a** soaked in various solvents: $CHCl_3$, ether, EtOH, *conc.* HCl_{aq}, and $NaOH_{aq}$ (pH10), at rt for 24 h. The uppermost pattern of **ThiaHAT-1a** was measured from a crystalline balk heated at 250 °C for 24 h.

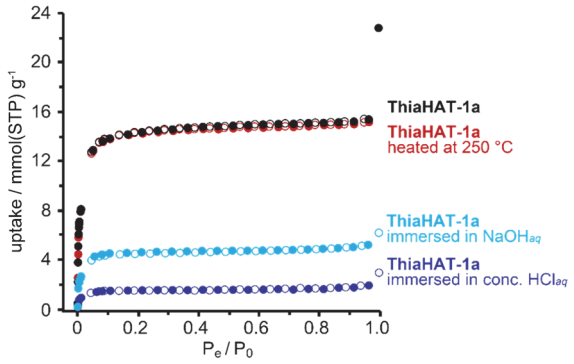

Figure 28. N_2 gas sorption isotherms of different **ThiaHAT-1a** samples at 77K. open symbol: adsorption, solid symbol: desorption.

Table 2. BET surface areas and NLDFT pore diameters of different samples of **ThiaHAT-1a** estimated from N_2 adsorption.

	$S_{A(BET)}$ / $m^2\,g^{-1}$	d_{NLDFT} / Å
ThiaHAT-1a	1394	1.55
After heated at 250 °C	1327	1.02
After immersed in conc. HCl_{aq}	138.5	1.09
After immersed in $NaOH_{aq}$ (pH10)	425.7	1.09

2.6 Evaluation of the porosity

The permanent porosity of the activated frameworks of **BPHAT-1**, **TolHAT-1** and **ThiaHAT-1** (Figures 29 and 30, Table 3), as well as **TPHAT-P** (Figure 31b), was evaluated by gas absorption experiments at 77 K for N_2, O_2, and H_2 and at 195 K for CO_2. **BPHAT-1a** has a type I N_2 sorption isotherm with an uptake of 16.1 mmol(STP) g^{-1} at 101 kPa. The BET specific surface area: $S_{A(BET)}$ and pore size calculated using nonlocal density functional theory (NLDFT) for the N_2 isotherm: d_{NLDFT} were 1288 $m^2\,g^{-1}$ and 1.24 nm, respectively (Figure 29b). The uptake of other gases was as followed [O_2: 18.8, CO_2: 13.4, and H_2: 4.89 mmol(STP) g^{-1}]. For the case of **TolHAT-1a*N*** (*N* = I–IV), the uptake of N_2 gas varied with the activation method (Figure 31a, Table 4) and **TolHAT-1aIV** showed the highest porosity among them ($S_{A(BET)}$: 330 $m^2\,g^{-1}$ and pore width: 1.66 nm) (Figure 30a,b). This demonstrates the importance of a controlled activation. The gas uptakes and BET surface area of **TolHAT-1aIV** are yet lower than those of **BPHAT-1a** ($S_{A(BET)}$: 1288 $m^2\,g^{-1}$, Table 3), suggesting that a large part of the original structure was collapsed or transformed into a less- or nonporous structure. The gas sorption isotherms of **ThiaHAT-1a**, on the other hand, show a significant uptake of gasses [N_2: 18.3, O_2: 21.9, CO_2: 13.8, and H_2: 3.28 mmol(STP) g^{-1}] (Figure 30c,d). The $S_{A(BET)}$ and d_{NLDFT} were calculated to be 1394 $m^2\,g^{-1}$, and 1.58 nm, respectively, which are larger than those of **BPHAT-1a**.

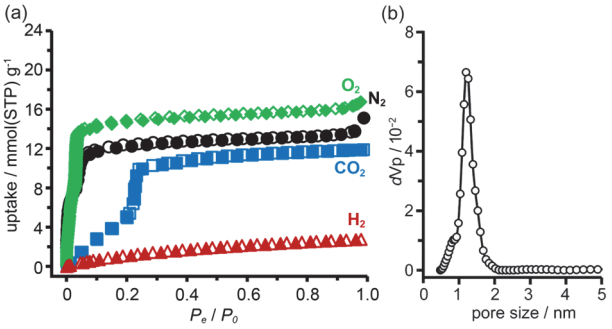

Figure 29. (a) Gas sorption isotherms of **BPHAT-1a**: O_2 (77 K), N_2 (77 K), CO_2 (195 K), H_2 (77 K). Solid and open symbols denote absorption and desorption processes, respectively. (b) Pore size distribution calculated by the NLDFT method.

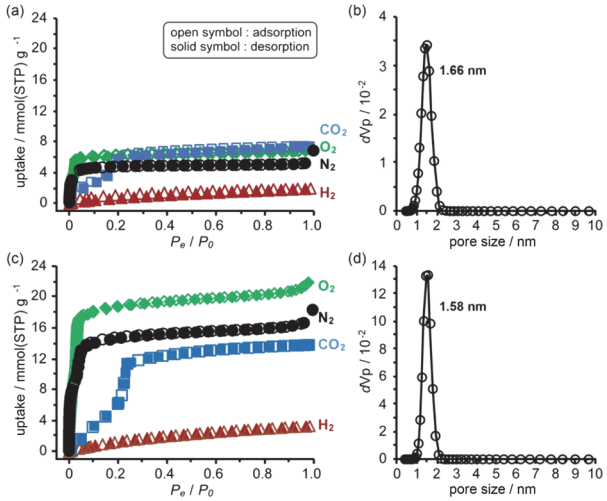

Figure 30. (a,c) Gas sorption isotherms and (b,d) pore distribution of (a,b) **TolHAT-1aIV** and (c,d) **ThiaHAT-1a**. The isotherms were recorded at 77K for N_2, O_2, and H_2 and at 195 K for CO_2. Solid and open symbols denote absorption and desorption processes, respectively.

Table 3. Gas uptakes, BET surface areas ($S_{A(BET)}$), and NLDFT pore diameters (d_{NLDFT}) of **TPHAT-a**, **BPHAT-1a**, **TolHAT-1aIV**, and **ThiaHAT-1a**. $S_{A(BET)}$ and d_{NLDFT} were based on N_2 adsorption.

	TPHAT-a	**BPHAT-1a**	**TolHAT-1aIV**	**ThiaHAT-1a**
N_2 uptake / mmol(STP) g^{-1}	11.2[a]	16.1	6.84	183.
CO_2 uptake / mmol(STP) g^{-1}	3.32	13.4	7.43	13.8
O_2 uptake / mmol(STP) g^{-1}	0.866	18.8	6.96	21.9
H_2 uptake / mmol(STP) g^{-1}	0.132	4.90	1.94	3.28
$S_{A(BET)}$ / m^2 g^{-1}	8.8	1288	330	1394
d_{NLDFT} / nm	—	1.24	1.49	1.55

[a] Due to the large amount of surface sorption in the N_2 isotherm of **TPHAT-a**, the N_2 uptake at P_e/P_0 = 1.0 was larger than **TolHAT-1aIV.**

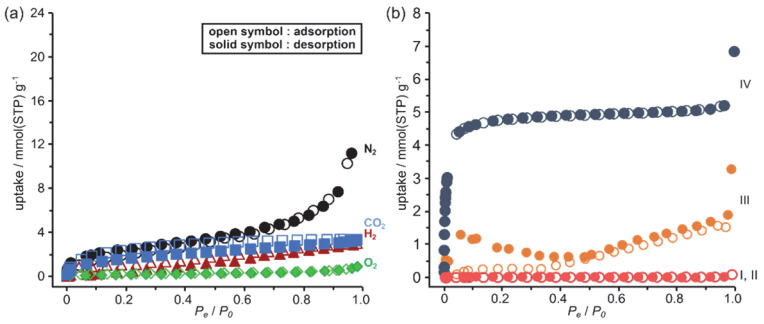

Figure 31. (a) Gas sorption isotherms of **TPHAT-a**, and (b) N_2 gas sorption isotherms of **TolHAT-1a*N*** (*N* = I–IV) at 77 K. Open symbol: adsorption, solid symbol: desorption. **TPHAT-a** dried sample of **TPHAT-P** at 120 °C for 24 h under vacuum) has low gas uptakes [N_2: 11.2, O_2: 0.886, H_2: 0.132, CO_2: 3.32 / mmol(STP) g^{-1}] and the $S_{A(BET)}$ was calculated to be 8.8 m^2 g^{-1} based on a N_2 adsorption isotherm, indicating an almost non-porous structure.

Table 4. N_2 gas uptakes of **TolHAT-1a*N*** (N = I–IV).

TolHAT-1a	N_2 uptake / mmol(STP) g^{-1}
I	0.0241
II	0.188
III	3.27
IV	6.84

2.7 Computational evaluation of stability

To investigate the stability of the HOFs, the intermolecular interactions and extents of structural disorder were calculated. Firstly, complexation energies between two stacked molecules in HOFs were calculated (Figure 32). The stability increases proportionally to the spacer length in the cases of **CPHAT-1** (−38.4 to −58.4 kcal mol^{-1}), **BPHAT-1** (−63.9 to −90.9 kcal mol^{-1}), and **TolHAT-1** (−82.1 to −108.6 kcal mol^{-1}). This result suggests that **TolHAT** supposed to be more stable than **CPHAT-1** and **BPHAT-1**, which is not in agreement with the actual stability. In the case of **ThiaHAT**, the increase of stabilization energy (−74.0 to −112.7 kcal mol^{-1}) becomes slow; particularly the energy calculated at the M062X level is smaller than that of **TolHAT**, which is caused by the face-to-edge contact of the spacer moieties. These results indicate that the stability of the HOFs cannot be evaluated from complexation energies. Secondly, to assess the structural disorders of the HOFs, all atom MD (molecular dynamics) simulations were conducted at 300 K and 1 bar on the frameworks of **CPHAT-1**, **BPHAT-1**, **TolHAT-1**, and **ThiaHAT-1**.

The procedures of MD are described in section 2.10.6 and snapshot configurations of **CPHAT-1** and **TolHAT-1** seen from the *c*-axis are depicted in Figure 32a as representative examples. The structural disorder is more evident in the spacer parts than in the HAT cores, and the disorder of the spacer is larger for **TolHAT-1** than for **CPHAT-1**. The extent of disorder can be quantified in terms of the root-mean-square displacement (RMSD) averaged over all the heavy (non-hydrogen) atoms in the system. In the present work, RMSD was computed for the fluctuations in the *a*- and *b*-directions. A RMSD plot over the time course of MD for 10 ns (Figure 33b) shows that the frameworks

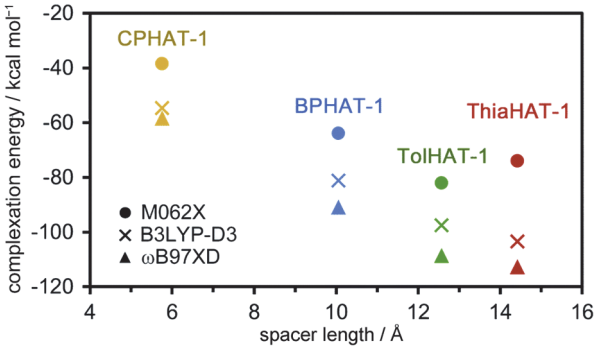

Figure 32. Complexation energy – spacer length plot of **CPHAT-1**, **BPHAT-1**, **TolHAT-1**, and **ThiaHAT-1**, calculated at the B3LYP-D3/6-311G(d,p), M062X/6-311G(d,p) and ωB97XD/6-311(d,p) levels with counterpoise method for BSSE correction.

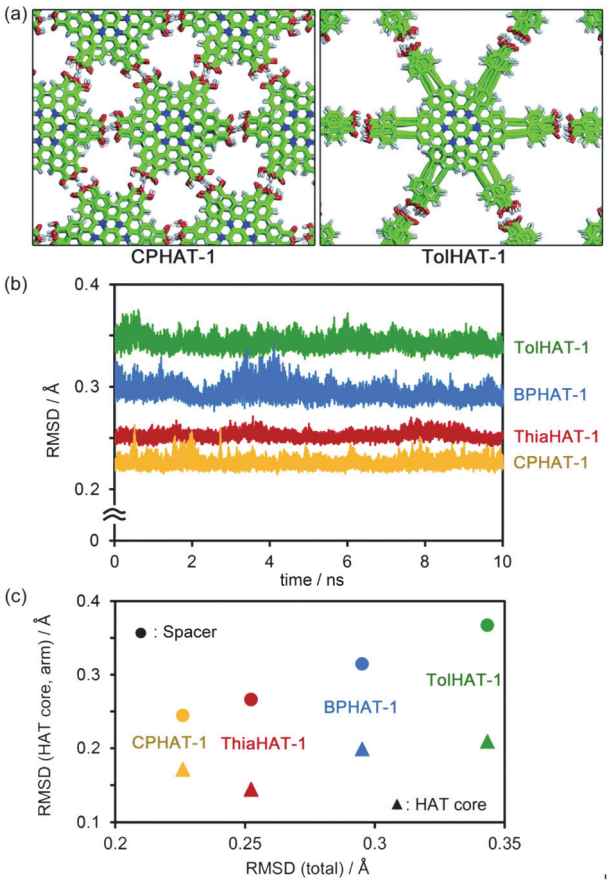

Figure 33. (a) Snapshot configurations of **CPHAT-1** and **TolHAT-1** seen from the *c*-axis. (b) RMSD during the time course of MD. (c) Correlation plots of the total RMSD against the contributions from the HAT core and spacer parts. RMSD was computed for the fluctuations of the heavy (non-hydrogen) atoms in the system along the lateral (*a* and *b*) directions. The (total) RMSD values that are plotted in (b) and refer to the abscissa in (c) were calculated over all the heavy atoms. In (c), the RMSDs averaged over 10 ns are shown.

formed by the H-bonds are stable at 300 K. The disorder of the framework represented by RMSD is larger in the order of **TolHAT-1** > **BPHAT-1** > **ThiaHAT-1** > **CPHAT-1**, and this is in fair correspondence with the experimentally observed decomposition temperatures of the frameworks, which reflects a higher stability of the framework in the order of **CPHAT-1** > **BPHAT-1** ~ **ThiaHAT-1** > **TolHAT-1**. The above correspondence is actually reminiscent of the Lindemann criterion which states that the crystal with a larger RMSD will be "closer" to melting. These RMSD (computed along the lateral directions) can thus describe the crystal stability. RMSD is a quantity readily obtained in MD simulations, and it will be of use for predicting the stability of a HOF. Figure 33c further shows the RMSDs computed separately over the HAT core and spacer parts. The RMSD is smaller for the HAT core than for the spacer. As Figure 33a shows, the structural disorder is more pronounced in the spacer part. The correlation with the total RMSD is seen for the spacer RMSD. The crystal stability is thus governed by the extent of disorder of the spacer part, and therefore, a rule-of-thumb for producing more stable HOFs would be the design of spacers with suppressed fluctuations.

2.8 UV-Vis steady state properties

Since porous molecular crystals are promising materials for photophysical materials[39], the photophysical properties of **BPHAT-1**, **TolHAT-1** and **ThiaHAT-1** were evaluated by a combination of UV-Vis steady-state absorption and emission spectroscopy and time-resolved emission and single crystal fluorescence microscopy.

Bulk **BPHAT-1a** and its butyl ester derivative **9a** show a broad absorption band between 300 and 500 nm, and a green-yellow emission with intensity maxima around 500 nm (Figures 34 and 35). The fluorescence quantum yield of the HOF is 5.7%. Fluorescence confocal microscopy measurements on **BPHAT-1a** single crystals showed highly anisotropic emission behavior (Figure 36a,b). The anisotropy histogram for the crystals oriented perpendicularly to the plane of observation has a value of 0.45, while those crystals rotated by 90° (parallel orientation) give a value of −0.30. Similar anisotropy behavior has been reported for **CPHAT-1a**[33]. This strong dependence of the anisotropy on the crystal orientation indicates an ordered crystalline structure for **BPHAT-1a** with preferential orientation of the molecular dipole moments perpendicular to the long crystal axis with the π–π columnar stacking direction parallel to the length axis of the crystal. The emission spectra of **BPHAT-1a** do not vary much between the different crystals, although they do change depending on the position within each crystal. At the edge (point 3 of inset in Figure 36c), the spectra have emission intensity maxima at *ca.* 475 nm (Figure 36c), while those collected close to the edges shift to longer wavelengths (*ca.* 510 nm) and become broader. This behavior is explained in terms of the presence of structural defects along the edges of the crystals. The emission decays of **BPHAT-1a** single crystals collected in the blue (450–500 nm) and green/red (550–660 nm) region of the spectrum give lifetimes of $\tau_1 \approx 0.4$ ns (94%) and $\tau_2 \approx 1.2$ ns (6%), and $\tau_1 \approx 1.1$ ns (80%) and $\tau_2 \approx 2.7$ ns (20%), respectively (Figure 36d). The lifetimes in the blue and green/red emission ranges are comparable to those reported for **CPHAT-1a**, which suggests that the emitters from both crystals in this spectral region

are very similar in nature. The only notable difference is the decrease in the value of the longest component from 4.5 ns for **CPHAT-1a** to 2.7 ns for **BPHAT-1a**. This component is associated with the interactions between the building units of the crystals and the decrease can be explained in terms of the stronger interactions due to the presence of the additional carboxyphenyl groups in **BPHAT-1a**. Thus, the expansion of the aryl arm in **BPHAT-1a** and the change in the pore size did not significantly alter the optical and photophysical properties of the resultant HOF structure.

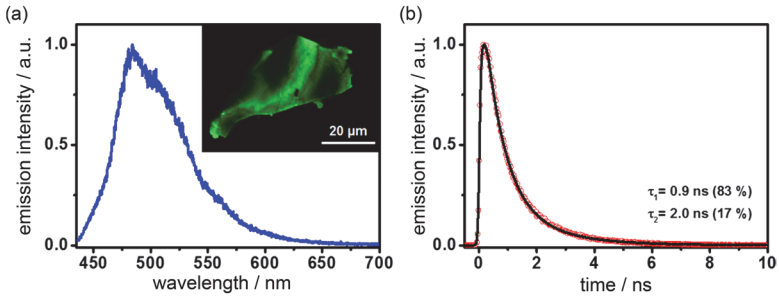

Figure 34. (a) Emission spectra of **9a**. The inset shows an image of **9a**. (b) Fluorescence decay of **9a**. The emission spectrum and also the decay were measured using a HQ430LP filter, Chroma. For the single "crystals" of **9a**, we recorded emission spectra having a maximum at ~ 475 nm, and a shoulder 525 nm. The emission lifetimes are ~ 0.8 ns and ~ 2.1 ns, being their contributions to the emission signal 85% and 15%, respectively.

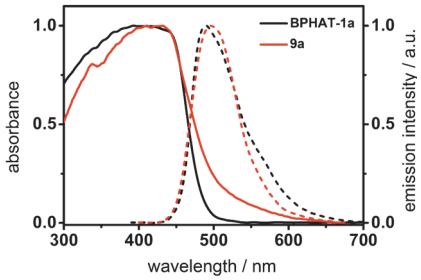

Figure 35. Absorption and emission spectra of bulk of **BPHAT-1a** and its butyl ester precursor **9a**. The excitation wavelength for both emission spectra is 370 nm.

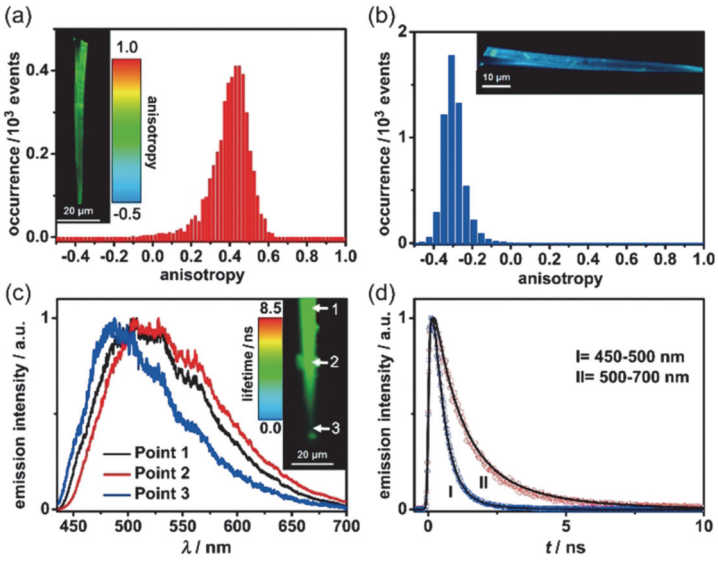

Figure 36. Fluorescence properties of **BPHAT-1a** single crystals. (a,b) Histograms of the emission anisotropy for two positions of a **BPHAT-1a** crystal. The insets show images of the crystals. (c) Emission spectra at different points of a **BPHAT-1a** crystal. The inset shows an image of the crystal and the points of measurement. (d) Fluorescence decay of a **BPHAT-1a** crystal; the I and II decays were measured using FF01-470_28-25 and HQ550LP filters (Chroma).

Unfortunately, during the experiments, **TolHAT-1** was revealed to be unstable under UV light excitation, probably due to the presence of the ethynyl moieties of **TolHAT-1**, which can be a breaking point of the structure upon its excitation with high energies (Figure 37). In contrast, **ThiaHAT-1** exhibits an excellent stability under light irradiation, even under fs-laser excitation conditions. **ThiaHAT-1** crystalline powder displayed a bright yellow emission upon illumination with UV light (365 nm), with an emission quantum yield of 8%. A foreground of the photoproperties of **ThiaHAT-1** is shown in Figure 38.

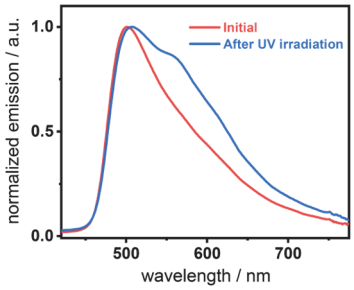

Figure 37. Emission spectra of **TolHAT-1** before and after irradiation with a wavelength of 400 nm. Clearly, after the irradiation, the material is photodegrading and creating new species with different photoproperties.

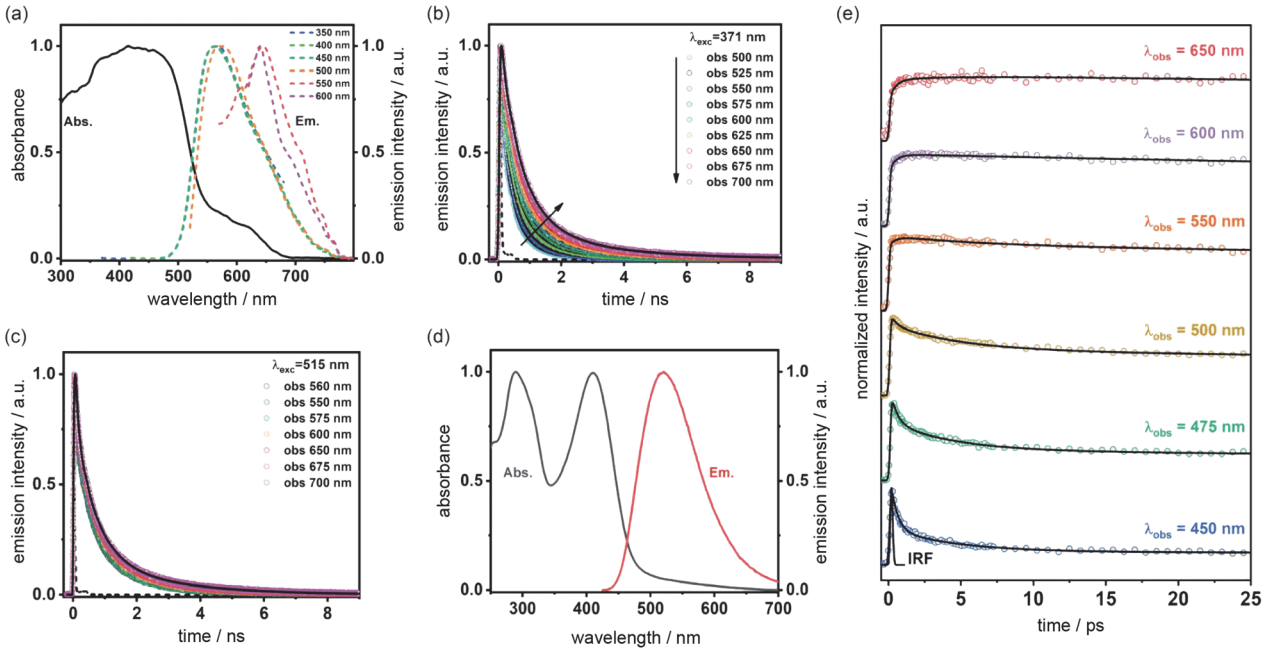

Figure 38. (a) Absorption and emission spectra of **ThiaHAT-1** in the powder form. The excitation wavelengths are indicated in the inset. (b,c) Emission decays of **ThiaHAT-1** in the powder form upon excitation at (b) 371 nm and (c) 515 nm. The solid lines are from the best multiexponential global fit and the recorded wavelengths are indicated in the figure. (d) Absorption and emission spectra of **ThiaHAT-1** in DMF suspension. For emission, the excitation wavelength was 410 nm. (e) fs-Emission decays of **ThiaHAT-1** in DMF suspension. The solid lines are from the best multiexponential global fit and the IRF is the instrumental response function.

The absorption spectrum of **ThiaHAT-1** crystalline powder consists of two broad bands with intensity maxima located at ~435 and 600 nm (Figure 38a). Consequently, the emission spectrum strongly depends on the excitation wavelength. For excitation wavelengths lower than 500 nm, the emission spectrum of **ThiaHAT-1** is a broad band with the maximum intensity centered at 565 nm, while its excitation with wavelengths longer than 500 nm produces a red-shifted emission spectrum, with the intensity maximum showing up at 644 nm (Figure 38a). Both the absorption and emission spectra of **ThiaHAT-1** are red-shifted when compared to its isostructural HOF, **BPHAT-1** (*abs.* 435 nm, *em.* 500 nm)[34,40], reflecting a stronger charge transfer (CT) character. As commented above, **ThiaHAT-1** presents additional absorption (600 nm) and emission (644 nm) bands that are not observed for **BPHAT-1**[34,40]. There exists two plausible explanations: (i) the building blocks of **ThiaHAT-1** are strongly interacting through H bonds, preforming anionic species in the ground state. Similar red-shifted absorption and emission bands owing to anions have been described for other HOFs in the presence of NaOH[40]. (ii) The intrinsic structure of **ThiaHAT-1** induces a higher interaction between crystals, leading to the formation of aggregates, which will absorb and emit less energetic electromagnetic radiation. To shed more light on this and other aspects of the photodynamical properties of **ThiaHAT-1**, its time-resolved photobehavior was investigated by means of a picosecond (ps) time-correlated single photon counting (TCSPC) system.

The photodynamic properties of **ThiaHAT-1** were explored by exciting (ps laser pulses) the sample at 371 and 515 nm and collecting the emission decays at several wavelengths, which were then analyzed using a multiexponential global fit method. The obtained results show a comparable multiexponential photobehavior independently of the excitation wavelength, with time constants of: τ_1 = 160–180 ps, τ_2 = 710–720 ps, and τ_3 = 2.3–2.5 ns (Figure 38b,c and Table 5). The contribution of the shortest component (τ_1) to the signal is higher in the bluest region of the spectrum, while the longest component (τ_3) contributes more to the emission decays recorded at longer wavelengths. Based on that, and following the steady state discussion, the τ_1 component can be attributed to the species initially excited, which deactivate from the first singlet excited state (S_1), while the longest τ_3 component corresponds to the emission of the anionic species. This is further supported by the increase in the total contribution of this component when excited at 515 nm, which may indicate that the red-shifted absorption and emission bands could have originated from the anionic species. On the other hand, as described above, **ThiaHAT-1** also exhibits a strong CT character, and therefore, the intermediate component (τ_2) can be ascribed to the emission of these CT species. The isostructural **BPHAT-1** had also exhibited a multiexponential behavior with time components assigned to species initially excited, others undergoing a CT and anions[34,40].

To unveil the ultrafast dynamics of the proton transfer (PT) and CT reactions, **ThiaHAT-1** crystals dispersed in a DMF solution were investigated by means of an ultrafast femtosecond (fs) upconversion (emission) technique. Prior to the fs-experiments, the steady state properties of **ThiaHAT-1** in DMF were evaluated (Figure 36d). The absorption spectrum is now better defined with narrow bands having their intensity maxima at 208 and 410 nm, while the emission spectrum has its maximum at 510 nm. Subsequently, a suspension of **ThiaHAT-1** in DMF was pumped with a 410-nm fs-laser and its emission was probed at different wavelengths ranging from 450 to 650 nm (Figure 36e). The fs emission decays are

well fitted to a double exponential function with time constants of τ_1 = 450 fs and τ_2 = 4.4 ps and an offset of ~320 ps (Table 6). Both time components decay in the highest energetic regions and rise in the lowest ones, reflecting the occurrence of different photoreactions. However, while the shortest τ_1 component rises from wavelengths longer than 500 nm, the longest τ_2 one only rises in the reddest part (from 650 nm). Based on above explanations, where the anion species fluoresce at the longest wavelengths, it is reasonable to attribute the 4.4 ps component to an excited-state PT reaction. The shortest 450-fs component, which rises from 500 nm, can be therefore associated with an ultrafast CT event, leading to the formation of the species having a CT character, which relax to the ground state within a time of 720 ps as described in the TCSPC part.

Table 5. Values of time Constants (τ_i), normalized (to 100) pre-exponential factors (A_i), and contributions ($c_i = \tau_i \times A_i$) obtained from a global multiexponential fit of the emission decays of **ThiaHAT-1** in solid state upon excitation with wavelengths of 371 and 515 nm, and observation as indicated.

sample	λ_{obs} / nm	τ_1 / fs	A_1	c_1	τ_2 / fs	A_2	c_2	τ_3 / fs	A_3	c_3
	500		77	45		22	49		1	6
	525		69	37		29	52		2	11
	550		61	29		36	53		3	18
	575		53	20		42	54		5	26
ThiaHAT-1	600	180	47	15	710	46	55	2.5	7	30
λ_{exc} = 371 nm	625		42	12		48	52		10	36
	650		38	10		50	50		12	40
	675		36	9		51	48		13	43
	700		34	8		51	46		15	46
	560		48	15		45	55		7	30
	575		48	14		44	55		8	31
	600		46	12		45	52		9	34
ThiaHAT-1	625	160	45	11	720	44	50	2.3	11	39
λ_{exc} = 515 nm	650		45	11		43	47		12	42
	675		45	1		41	44		14	46
	700		46	11		40	40		14	49

Table 6. Values of time constants (τ_i) and normalized (to 100) pre-exponential factors (A_i) and contributions ($c_i = \tau_i \times A_i$) obtained from the best fit of the femtosecond emission decays of **ThiaHAT-1** upon excitation at 410 nm and observation as indicated.

sample	λ_{obs} / nm	τ_1 / fs	A_1	c_1	τ_2 / fs	A_2	c_2	offset / ps
	450	450	70	19	4.4	30	81	310
	475	450	51	9	4.4	49	91	330
ThiaHAT-1/DMF	500	450	31	4	5.0	69	96	320
λ_{exc} = 410 nm	550	450	−100	−100	6.5	100	100	290
	600	450	−100	−100	—	100	100	330
	650	450	−77	−25	4.4	−23	−75	320

The emission properties of **ThiaHAT-1** were also appraised at a single crystal level using a ps time-resolved confocal fluorescence microscope. The emission spectra obtained for different isolated crystals are reminiscent of that obtained for the bulk material (Figure 39). Similarly, the ps-photodynamical behavior provides time constants of 300 ps, 800 ps and 2.7 ns (Figure 40 and Table 7), which are comparable to those observed in the bulk, and therefore, can be attributed to the initially excited species (300 ps), species having CT character (800 ps) and anions (2.7 ns). Interestingly, the emission recorded for the **ThiaHAT-1** single crystals is highly anisotropic, showing a histogram with a value of around 0.45 when the crystals are oriented perpendicularly to the plane of observation, and a value of −0.1 after their rotation by 90° (Figure 41). This fact clearly evidences that **ThiaHAT-1** has a highly ordered structure, where the fundamental units are arranged through π-π stacking interactions along the length axis of the crystal while the dipole moments are oriented perpendicularly.

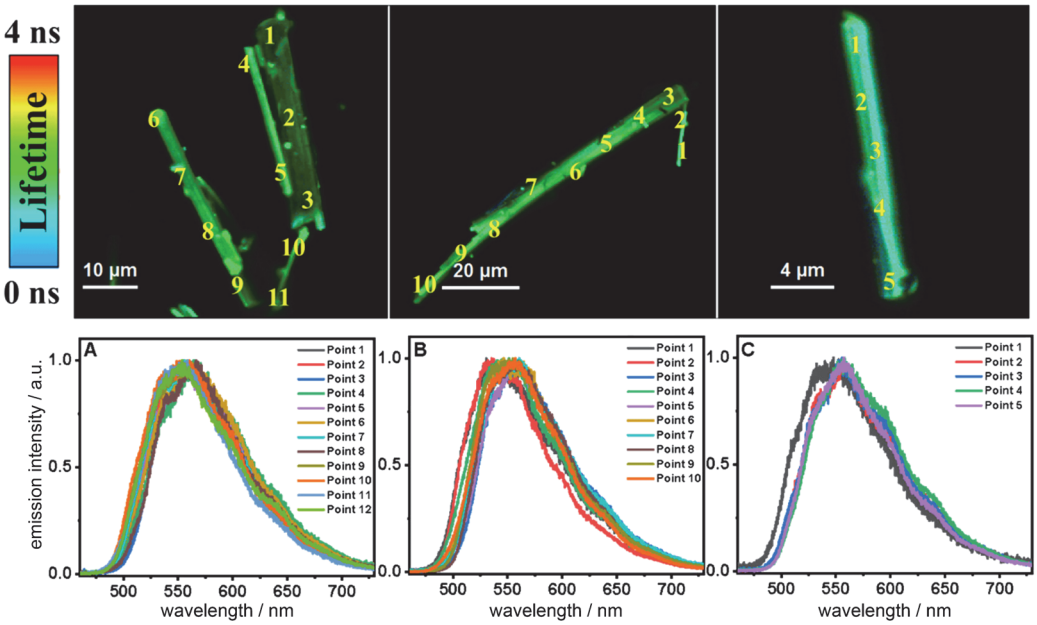

Figure 39. The top figures are FLIM images of different **ThiaHAT-1** isolated crystals. (A–C) Emission spectra collected at different points (indicated in the top images) of the **ThiaHAT-1** crystals. The excitation wavelength was 390 nm.

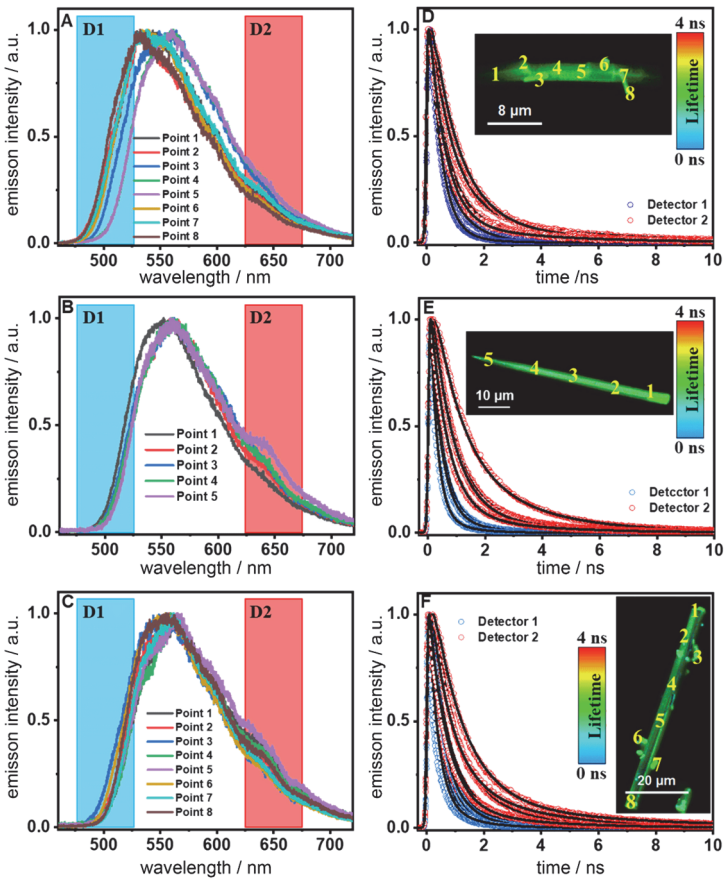

Figure 40. (A-C) Emission spectra and (D-F) emission decays at selected spectral range using two different filters of transmission to gate at blue and red regions (shown in figures A-C as D1 and D2 regions, respectively) at designated points in the **ThiaHAT-1** crystals. The solid lines are from the best-fit using a multiexponential function. The excitation wavelength was 390 nm.

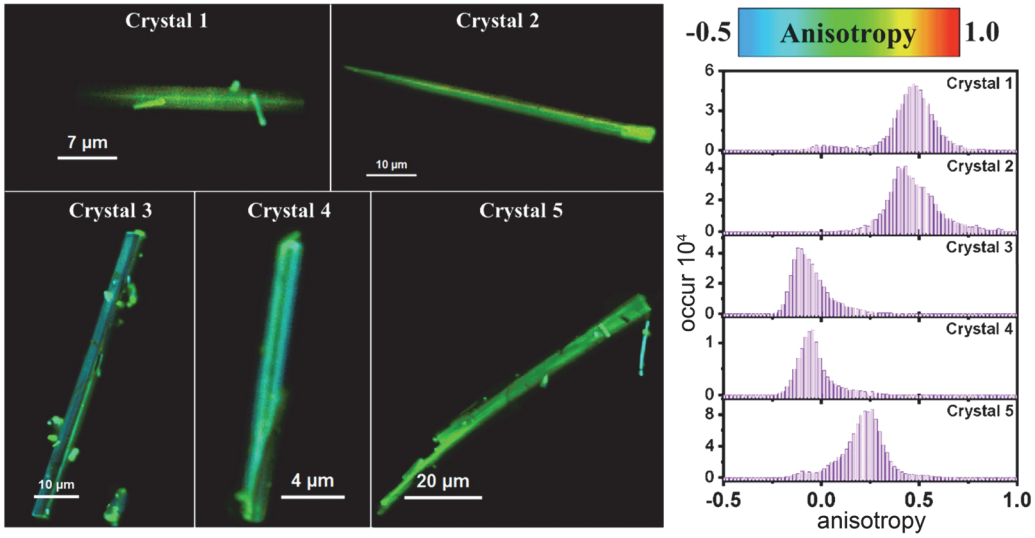

Figure 41. Figures in the left correspond to the FLIM images of **ThiaHAT-1** crystals having different orientation. The figure in the right is a histogram of the emission anisotropy of those crystals.

Table 7. Values of time constants (τ_i) and normalized (to 100) pre-exponential factors (a_i) obtained from the fit of the emission decays collected at different points of the three **ThiaHAT-1** isolated crystals showed in Figure 39. Detector 1 and 2 recorded the signal in the blue and red regions (D1 and D2) represented in Figure 39.

		Crystal 1 (FILM in D)				Crystal 2 (FILM in D)				Crystal 3 (FILM in D)			
point	Detector	τ_1 / fs	a_1	τ_2 / fs	a_2	τ_1 / fs	a_1	τ_2 / fs	a_2	τ_1 / fs	a_1	τ_2 / fs	a_2
1	1	0.3	75	0.7	25	0.3	80	0.8	20	0.3	86	0.8	14
	2	0.6	67	2.5	33	0.8	69	2.7	31	0.7	71	2.7	9
2	1	0.3	85	0.7	15	0.3	66	0.8	34	0.3	82	0.9	18
	2	0.6	73	2.5	27	0.7	87	2.7	13	0.7	89	2.7	11
3	1	0.3	33	0.8	67	0.3	66	0.8	34	0.3	73	0.9	27
	2	0.7	75	2.5	25	0.7	86	2.7	14	0.7	83	2.7	13
4	1	0.2	48	0.5	52	0.3	74	0.8	26	0.3	87	0.9	13
	2	0.9	79	2.5	21	0.7	88	2.7	12	0.7	92	2.7	8
5	1	0.2	40	0.5	60	0.3	90	0.8	10	0.3	86	0.9	14
	2	0.8	77	2.5	23	0.7	90	2.7	10	0.7	92	2.7	8
6	1	0.3	83	0.8	17					0.3	66	0.9	34
	2	0.8	85	2.5	15					0.7	76	2.7	24
7	1	0.3	82	0.8	18					0.3	65	0.9	35
	2	0.6	85	2.5	15					0.7	65	2.7	35
8	1	0.3	87	0.5	13					0.3	80	0.9	20
	2	0.6	88	2.5	12					0.7	90	2.7	10

ThiaHAT-1 has exhibited an outstanding response to the presence of HCl vapors, which can be easily inspected by the naked eye under daylight or UV irradiation. Short time exposure (5 min to 1 h) to HCl vapors induced a strong color change of **ThiaHAT-1** powder from vibrant yellow to dark brown, and disappearance of strong yellow emission was observed upon UV light illumination (Figure 42a). Indeed, the absorption spectrum of **ThiaHAT-1** crystals after being dosed with HCl displays an increase in the intensity of the band at 600 nm (Figure 42b). The emission spectrum of **ThiaHAT-1** suffers from a strong quenching (up to 98% of the initial intensity) upon interaction with HCl vapors (Figure 42c). Additionally, a new band with its intensity maximum located at 700 nm is recorded (Figure 42d). The increase in the intensity of the red-shifted bands reflects a protonation of **ThiaHAT-1**. Apart from the thiadiazol group, this HOF contains several N atoms susceptible to being protonated, so the interaction with a strong acid like HCl will induce the protonation, producing the observed changes. Remarkably, **ThiaHAT-1** retains the dark brown color and quenched emission after its dosing with HCl, making this HOF a promising candidate to fabricate an HCl vapochromic smart sensor. The idea behind this is that if at any time the HOF interacts with HCl, it will retain the information until checked. Additionally, the yellow color and the emission of **ThiaHAT-1** can be partially recovered (up to 55% of the initial emission intensity) by heating the sample at 130 °C for 18 hours (Figure 43). It is noteworthy that acetic acid (AcOH) did not alter the absorption spectrum of **ThiaHAT-1** and just slightly quenched its emission (Figure 44). This can be explained in terms of the weak acidity of acetic acid, which cannot efficiently protonate the HOF.

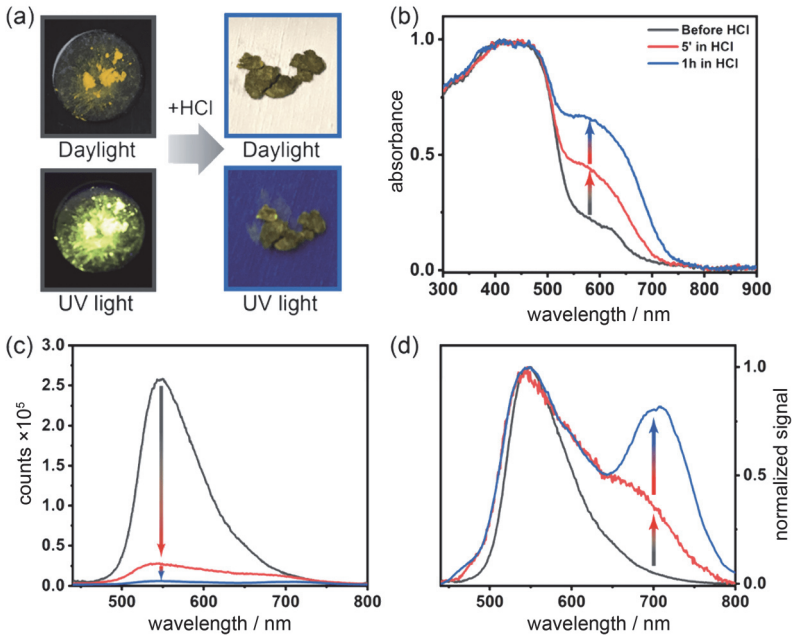

Figure 42. Acid responsiveness of **ThiaHAT-1**. (a) Photographs of the crystalline powder before (left) and after (right) being exposed to HCl under daylight (top) and UV light (365 nm, bottom). (b) Absorption, (c) emission, and (d) normalized emission spectra of **ThiaHAT-1** before and after being exposed to vapors of HCl.

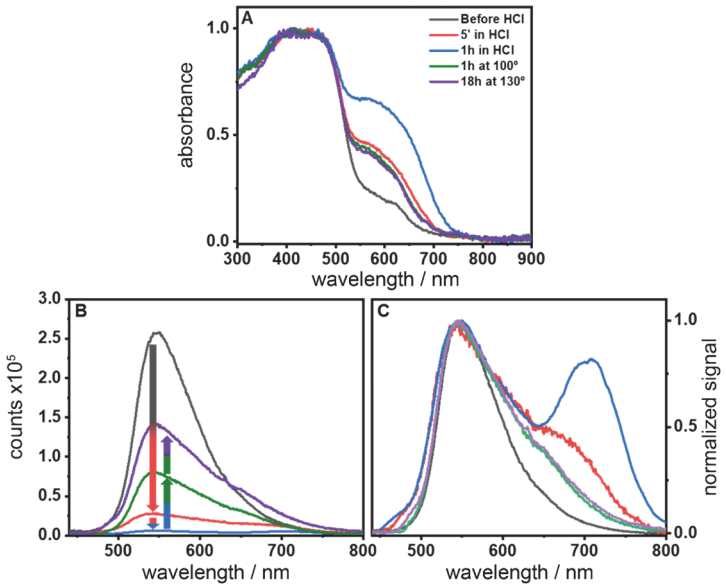

Figure 43. (A) Absorption, (B) emission, and (C) normalized emission spectra of **ThiaHAT-1** before and after being exposed to vapors of HCl, and the subsequent recover of its photoproperties after heating the sample at 100 ºC for 1 h (green line) and 130 ºC for 18h (purple line), respectively.

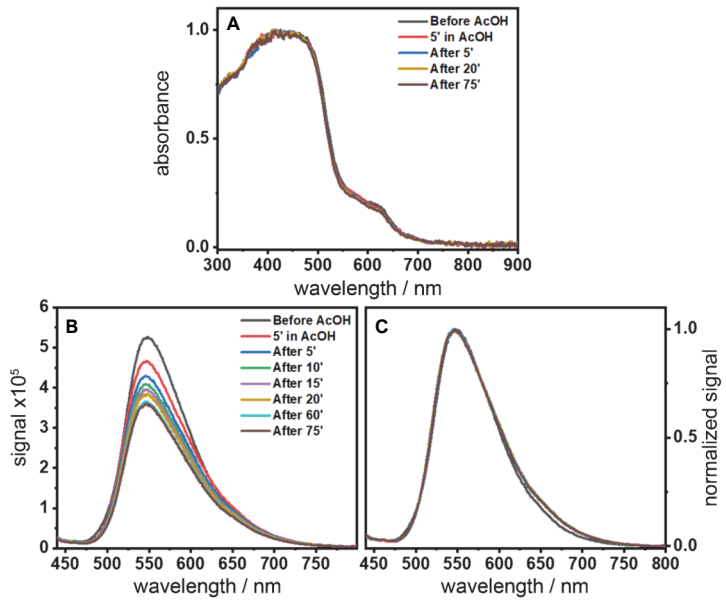

Figure 44. (A) Absorption, (B) emission, and (C) normalized emission spectra of **ThiaHAT-1** before and after being dosed with AcOH for increasing periods of time.

2.9 Conclusion

In this work, the author synthesized four HAT derivatives (**BPHAT**, **TPHAT**, **TolHAT**, and **ThiaHAT**) and explored the construction of isostructural HOFs with larger pores based on shape-fitted docking.

The simple elongation of arms from phenylene to biphenylene were successful to form **BPHAT-1**. However, that to terphenylene quickly reached the limit, while the modification of the spacers with 1,2-diphenylethyne and 4,7-diphenylbenzo-2,1,3-thiadiazole allowed the formation of expanded HOFs (**TolHAT-1** and **ThiaHAT-1**) by shape-fitted docking. The spacers of **TolHAT-1** were oriented co-planar with the HAT, while those of **ThiaHAT-1** were oriented perpendicular, indicating that the spacer accumulation can be modified by its bulkiness. Especially, **BPHAT-1** and **ThiaHAT-1** showed a great stability even at high temperatures (up to 305 °C), a high $S_{A(BET)}$ of 1288 $m^2\,g^{-1}$ and 1394 $m^2\,g^{-1}$, respectively. Moreover, it is noteworthy that the stability of HOFs can be precisely evaluated by MD simulation, reflecting the importance of considering not only the interaction energy, but also the fluctuation of the molecules. The author gave details on the photo behavior of **BPHAT-1** and **ThiaHAT-1** as crystals and in solutions providing information on the dynamics from the fs to the ns regime. Remarkably, **ThiaHAT-1** shows a large sensitivity to HCl vapors which can be followed by either absorption or emission measurements. To summarize, a comparison of the structural, chemical and robustness properties of this series of isostructural HAT HOFs is shown in Table 8. By designing spacers of HOFs based on shape-fitted docking, the author has achieved

Table 8. Summary of the structural features and properties of four isostructural HOFs based on HAT derivatives.

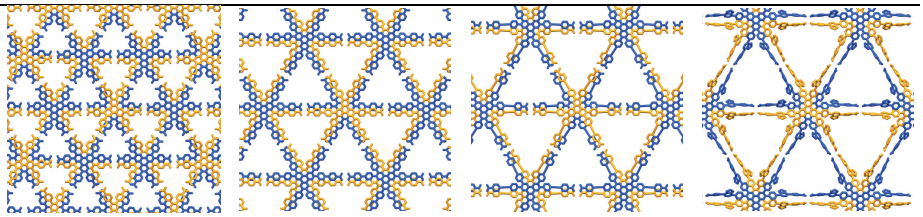

	CPHAT-1	**BPHAT-1**	**TolHAT-1**	**ThiaHAT-1**
Periodicity of framework / Å	21.48	29.75	34.40	38.01
RMSD of HAT core plane / Å	0.267	0.205	0.215	0.229
Stacking distance / Å	3.59	3.57	3.49	3.49
Torsion angle of spacers / °	22.5	22.1	23.5	24.5
Number of interpenetrations	4	6	8	8
height of channel aperture / Å	6.4	14.5	19.2	19.0
Void ratio	0.31	0.45	0.55	0.48
d_{NLDFT} / nm	—[a]	1.24	1.66	1.55
$S_{A(BET)}$ / $m^2\,g^{-1}$	649	1288	440	1394
N_2 uptake / mmol(STP) g^{-1}	0.942	15.9	6.84	18.3
CO_2 uptake / mmol(STP) g^{-1}	6.05	13.4	7.43	13.8
Decomposition temp. / °C	339	307	190	305
Ref.	Ref. 33	This work	This work	This work

[a] Not determined

to construct a series of stable isostructural HOFs with pores that expanded with spacer length, which was difficult to achieve in the past. This design principle gives an insight to develop a systematic series of porous molecular crystalline materials.

2.10 Experimental section

All reagents and solvents were used as received from commercial suppliers. IR spectrum data were obtained from JASCO FT/IR-4200. and ^{13}C NMR spectra were measured on a JEOL 400 YH (400 MHz) spectrometer or Bruker AV400M (400 MHz) spectrometer. Residual proton and carbon of deuterated solvents were used as internal standards for the measurements (for ^{1}H NMR, $CDCl_3$:δ = 7.26 ppm, DMDO-d_6 : δ = 2.50 ppm, NMP-d_9: δ = 5.50 ppm: for ^{13}C NMR, $CDCl_3$: δ = 77.00 ppm, DMSO-d_6 : δ = 39.50 ppm). Mass spectrum data were obtained from a JEOL JMS-700 instrument or autoflex III Bruker. Thermo gravimetric (TG) analysis were performed on Rigaku TG8120 under an N_2 purge (100 mL min^{-1}) at a heating rate of 5 K min^{-1}.

2.10.1 Synthesis of building blocks

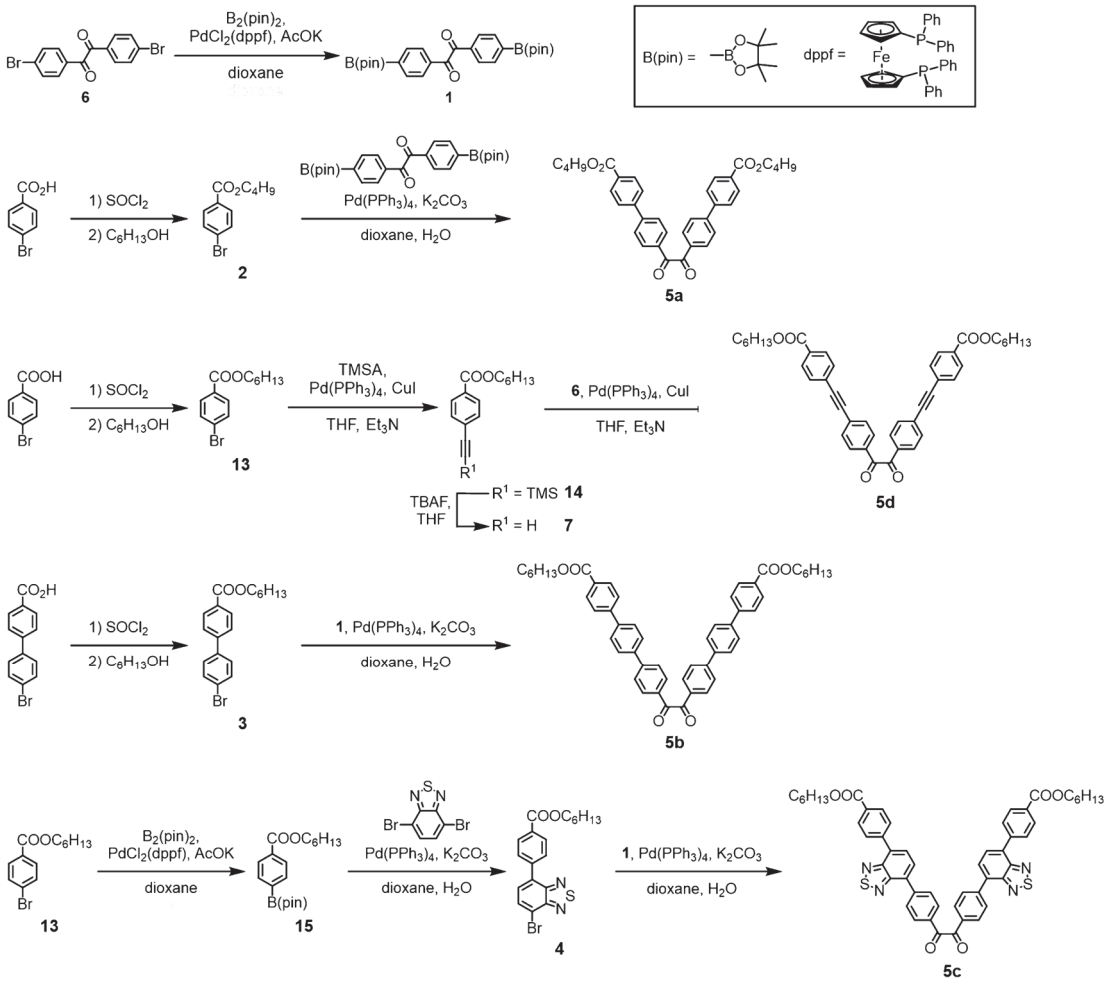

Scheme 2. Synthesis of dione derivatives, **5a, 5b, 5c,** and **5d**.

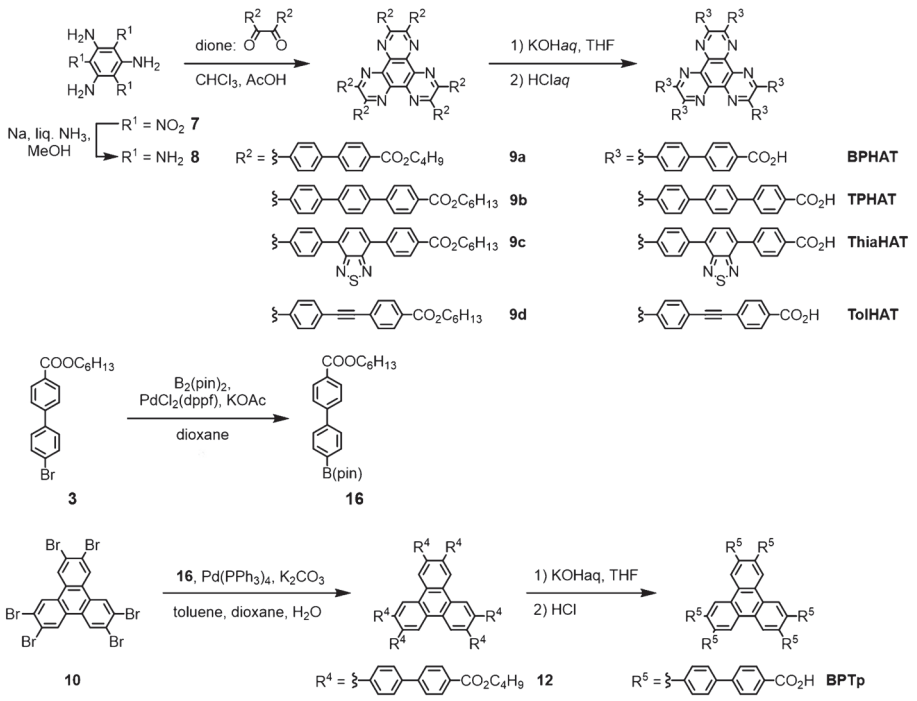

Scheme 3. Synthesis of HAT derivatives, **BPHAT, TPHAT, TolHAT, and ThiaHAT**, and a Tp derivative, **BPTp**.

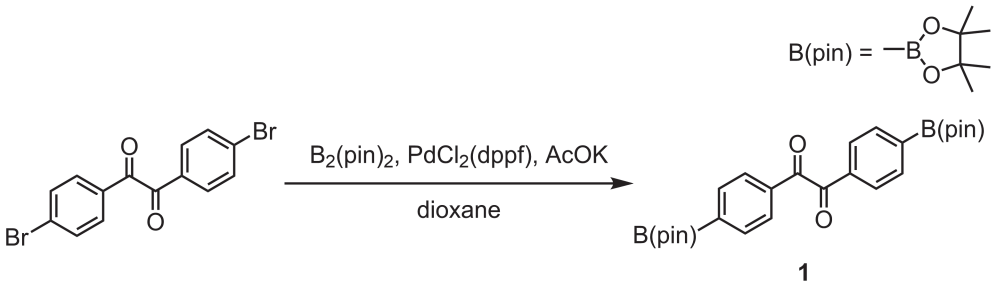

Synthesis of 1. Compound **1** was synthesized from 4,4'-dibromobenzil by following the literature procedure (Scheme 2)[52]. A 200 mL three-necked flask was charged with 4,4'-dibromobenzene (2.04 g, 5.43 mmol), bis(pinacolato)diboron (4.14 g, 16.3 mmol, 3 *eqiv.*), AcOK (4.30 g, 43.8 mmol, 8 eqiv), and $PdCl_2$(dppf) (0.200 g, 0.0273 mmol) under nitrogen. Then degassed dioxane (50 mL) were added and the reaction mixture was refluxed at 80 °C for 17h. After cooling to room temperature, the product was extracted with CH_2Cl_2. The organic phase was combined and washed with water and brine, dried with anhydrous $MgSO_4$, and filtered. The crude product was purified with silica gel column chromatography (MeOH in CH_2Cl_2: 0–5%) to give compound **1** as a pale yellow solid (2.09 g, 4.53 mmol, 70%).

^{1}H NMR (400 MHz, $CDCl_3$) : δ 7.93 (s, 8H) , 1.35 (s, 24H) ppm.

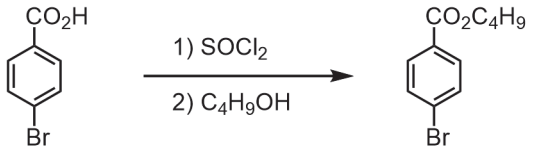

2

Synthesis of 2. A 300 mL three-necked flask was charged with 4-bromobenzoic acid (10.5 g, 52.3 mmol) in dehydrated CH_2Cl_2 (60 mL) under nitrogen. Then $SOCl_2$ (8.5 mL, 105 mmol) were added dropwise at 0 °C and dehydrated DMF (2 drops) at rt. The mixture was refluxed at 45 °C for 4h. After cooling to room temperature, solvent was removed by vacuum and dissolved dehydrated CH_2Cl_2. Then dehydrated n-butanol (9.0 mL) and Et_3N (10 mL) was added and stirred at rt for 18h. The product was extracted with CH_2Cl_2, washed with water and brine, dried with anhydrous $MgSO_4$, and filtered. The crude product was purified with silica gel column chromatography ($CHCl_3$/hexane = 1/5) and cooled at 10 °C, followed removed solid by filtration to give compound **2** as a pale-yellow oil (13.1 g, 50.9 mmol, 97%).

^{1}H NMR (400 MHz, $CDCl_3$) : δ 7.90 (d, 2H, *J* = 8.0 Hz), 7.58 (d, 2H, *J* = 8.4 Hz), 4.32 (t, 2H, *J* = 6.6 Hz) , 1.70–1.82 (m, 2H) , 1.40–1.55 (m, 6H) , 0.982 (t, 3H, *J* = 7.2 Hz) ppm. ^{13}C NMR (100 MHz, $CDCl_3$) : δ 165.8, 131.6, 131.0, 129.4, 127.8, 65.0, 30.7, 19.2, 13.7 ppm.

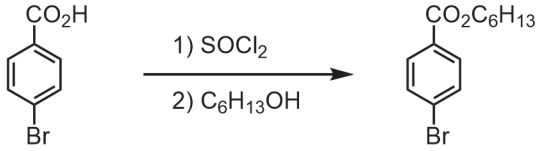

13

Synthesis of 13. A 300 mL three-necked flask was charged with 4-bromobenzoic acid (12.1 g, 60.0 mmol) in dehydrated CH_2Cl_2 (100 mL) under nitrogen. Then $SOCl_2$ (10.0 mL, 124 mmol) were added dropwise at 0 °C and dehydrated DMF (0.5 mL) at rt. The mixture was refluxed at 45 °C for 4h. After cooling to room temperature, solvent was removed by vacuum and dissolved dehydrated CH_2Cl_2. Then dehydrated n-hexanol (11.0 mL) and pyridine (5.0 mL) was added and stirred at rt for 18h. The product was extracted with CH_2Cl_2, washed with water and brine, dried with anhydrous $MgSO_4$, and filtered. The crude product was purified with silica gel column chromatography ($CHCl_3$/hexane = 1/7–1/1) and washed with charcoal to give compound **13** as a pale-yellow oil (16.4 g, 57.8 mmol, 96%).

^{1}H NMR (400 MHz, $CDCl_3$) : δ 7.89 (d, 2H, *J* = 8.4 Hz), 7.57 (d, 2H, *J* = 8.0 Hz), 4.30 (t, 2H, *J* = 6.4 Hz) , 1.70–1.80 (m, 2H) , 1.27–1.50 (m, 6H) , 0.898 (t, 3H, *J* = 7.2 Hz) ppm. ^{13}C NMR (100 MHz, $CDCl_3$) : δ 165.9, 131.6, 131.0, 129.4, 127.8, 65.4, 31.4, 28.6, 25.6, 22.5, 14.0 ppm. HR-MS (EI$^+$): calcd. For $C_{13}H_{17}BrO_2$ $[M]^+$ 284.0412; found: 284.0410.

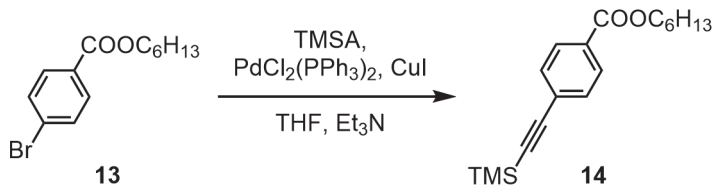

Synthesis of 14. A 100 mL three-necked flask was charged with compound **13** (4.00 g, 14.0 mmol), $PdCl_2(PPh_3)_2$ (0.490 g, 0.700 mmol), CuI (0.266 g, 1.40 mmol) in degassed THF (30 mL) under nitrogen. Then degassed Et_3N (10 mL) and trimethylsilylacetylene, TMSA (4.20 mL, 29.7 mmol) were added and the reaction mixture was heated at 40 °C for 5h. After cooling to room temperature, the solvent was removed under vacuum. The crude product was purified with silica gel column chromatography (CH_2Cl_2/hexane = 1/5) to give compound **14** as a pale yellow oil (3.53 g, 11.7 mmol, 83%).

^{1}H NMR (400 MHz, $CDCl_3$) : δ 7.97 (d, 2H, *J* = 8.8 Hz) , 7.51 (d, 2H, *J* = 8.4 Hz), 4.30 (t, 2H, *J* = 7.2 Hz), 1.70–1.80 (m, 2H), 1.25–1.52 (m, 6H), 0.901 (s, 3H), 0.261 (s, 9H) ppm. ^{13}C NMR (100 MHz, $CDCl_3$) : δ 166.1, 131.8, 130.1, 129.3, 127.6, 104.1, 97.5, 65.3, 31.4, 28.6, 25.7, 22.5, 14.0, −0.17 ppm. HR-MS (FAB+): calcd. For $C_{18}H_{27}O_2Si$ $[M+H]^+$ 303.1780; found: 303.1779

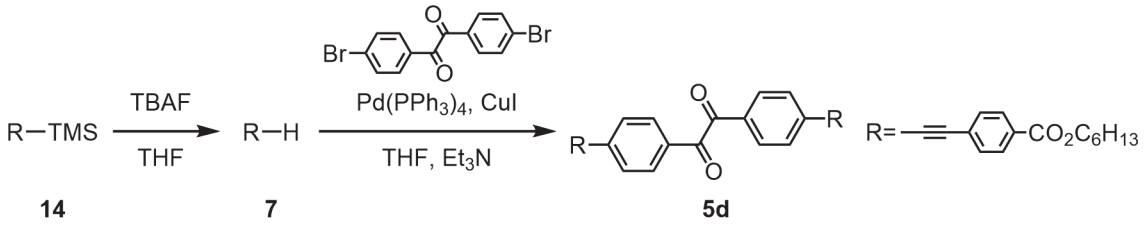

Synthesis of 5d. A 100 mL three-necked flask was charged with compound **14** (4.00 g, 14.0 mmol) in degassed THF (5 mL) under nitrogen. Then 1M tetrabutylammonium fluoride THF solution (5.5 mL, 5.5 mmol) was added dropwise at 0 °C and the reaction mixture was stirred for 15min. After removing solvent under vacuum, the product was extracted with CH_2Cl_2. The organic phase was combined and washed with water and brine, dried with anhydrous $MgSO_4$, and filtered, to give crude compound **7** as a brown solid (1.30 g), which was immediately used in the following reaction without further purification.

A 100 mL three-necked flask was charged with crude compound **7** (1.30 g), 4,4'-dibromobenzil (0.456 g, 1.24 mmol), $Pd(PPh_3)_4$ (0.106 g, 0.0924 mmol), CuI (0.0180 g, 0.0945 mmol) in degassed THF (30 mL) and degassed Et_3N (5 mL) under nitrogen. Then the reaction mixture was heated at 30 °C for 14h. After cooling to room temperature, the solvent was removed under vacuum. The crude product was well washed acetone to give compound **5a** as a pale blown solid (0.410 g, 0.615 mmol, 25% from compound **14** in 2 steps).

M.p. 178.5 °C. ^{1}H NMR (400 MHz, $CDCl_3$) : δ 8.05 (d, 2H, *J* = 8.8 Hz), 7.99 (d, 2H, *J* = 8.4 Hz), 7.68 (d, 4H, *J* = 8.8 Hz), 7.61 (d, 4H, *J* = 8.4 Hz), 4.33 (t, 4H, *J* = 6.8 Hz), 1.73–1.83 (m, 4H), 1.27–1.50 (m, 12H), 0.909 (t, 6H, *J* = 7.2 Hz) ppm. ^{13}C NMR (100 MHz, $CDCl_3$) : δ 193.0, 166.0, 132.23, 132.21, 131.72, 130.6, 129.9, 129.60, 129.57, 126.8, 93.2, 90.9, 65.5, 31.4, 28.6, 25.7, 22.5, 14.0 ppm. HR-MS (FAB+): calcd. For $C_{44}H_{43}O_6$ $[M+H]^+$ 667.3060; found: 667.3073.

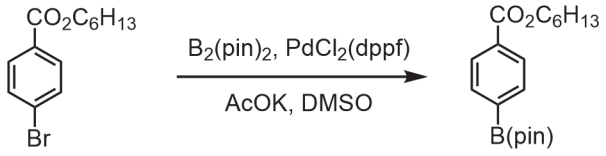

13 15

Synthesis of 15. A 100 mL three-necked flask was charged with compound **13** (6.09 g, 21.4 mmol), $(Bpin)_2$ (5.67 g, 22.5 mmol), AcOK (5.89 g, 60.0 mmol), and $PdCl_2(dppf)$ (0.521 g, 0.641 mmol) under nitrogen. Then degassed DMSO (20 mL) were added and at vacuumed at rt for 15 min. The reaction mixture was stirred at 80 °C for 17h. After cooled to room temperature, the reaction mixture was poured into water. The participate was extracted with AcOEt. The organic phase were combined and washed with water, dried with anhydrous $MgSO_4$, and filtered. The crude product was purified with silica gel column chromatography (AcOEt/hexane = 1/7) to give compound **15** as a pale yellow oil (5.58 g, 16.8 mmol, 79%).

^{1}H NMR (400 MHz, $CDCl_3$) : δ 8.02 (d, 2H, *J* = 8.0 Hz), 7.86 (d, 2H, *J* = 8.0 Hz), 4.32 (t, 2H, *J* = 6.6 Hz) , 1.72–1.82 (m, 2H), 1.30–1.52 (m, 18H), 0.900 (t, 3H, *J* = 5.6 Hz) ppm. ^{13}C NMR (100 MHz, $CDCl_3$) : δ 166.7, 134.6, 132.7, 130.1, 131.7, 128.5, 127.2, 84.13, 65.20, 31.44, 28.66, 25.68, 24.68, 22.52, 13.96 ppm. HR-MS (EI$^+$): calcd. For $C_{19}H_{29}O_4B$ $[M]^+$ 332.2159; found: 332.2153

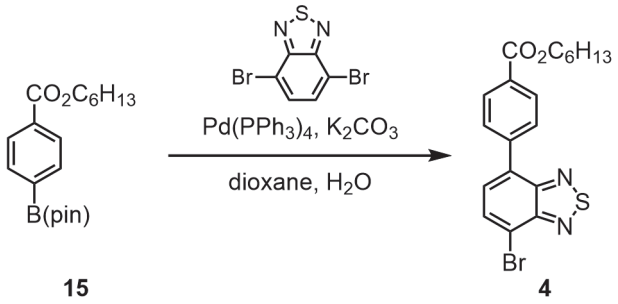

15 4

Synthesis of 4. A 200 mL three-necked flask was charged with 4,7-dibromo-2,1,3-thiadiazol (8.24 g, 28.0 mmol), compound **15** (4.66 g, 14.0 mmol), K_2CO_3 (3.80 g, 28.1 mmol) in degassed dioxane (45 mL) under nitrogen and heated at 80 °C. Then $Pd(PPh_3)_4$ (0.880 g, 0.762 mmol) was added and stirred for 8 h. Due to the reaction was not completed, degassed water (10 mL) and $Pd(PPh_3)_4$ (0.220 g, 0.190 mmol) were added, stirred at 80 °C for 80 h, and refluxed at 110 °C for 8 h. After solvent removal under vacuum, the participate was rinsed with $CHCl_3$ three times. Then the crude product was purified with silica gel column chromatography ($CHCl_3$/hexane = 1/1→1/2) to give compound **4** as a pale yellow solid (3.99 g, 9.51 mmol, 68%).

M.p. 68.1 °C. ^{1}H NMR (400 MHz, $CDCl_3$) : δ 8.20 (d, 2H, *J* = 8.0 Hz), 7.92–8.00 (m, 3H), 7.57–7.69 (m, 1H), 4.36 (t, 2H, *J* = 6.8 Hz), 1.74–1.84 (m, 2H), 1.30–1.52 (m, 6H), 0.916 (t, 3H, *J* = 6.8 Hz) ppm. ^{13}C NMR (100 MHz, $CDCl_3$) : δ 166.3, 153.9, 152.9, 140.8, 132.9, 132.2, 130.5, 130.0, 129.1, 129.7, 114.2, 65.3, 31.5, 28.7, 25.7, 22.6, 14.0 ppm. HR-MS (FAB+): calcd. For $C_{19}H_{20}N_2O_2SBr$ $[M+H]^+$ 419.0429; found: 419.0423.

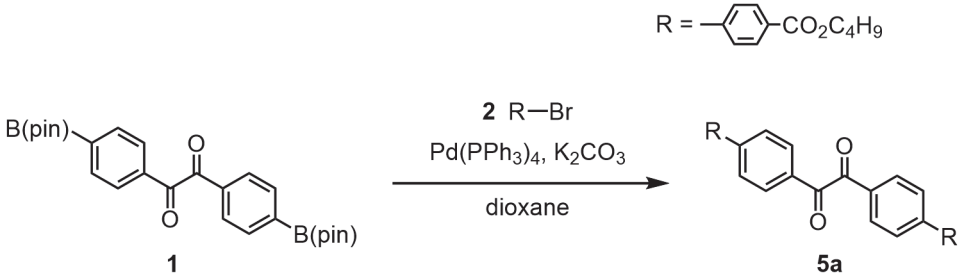

Synthesis of 5a. A 200 mL three-necked flask was charged with compound **1** (3.75 g, 8.10 mmol), compound **2** (4.21 g, 16.4 mmol), K_2CO_3 (4.73 g, 40.0 mmol), and $Pd(PPh_3)_4$ (1.00 g, 0.865 mmol) in degassed dioxane (100 mL) under nitrogen. Then the reaction mixture was refluxed for 14h. After solvent removal under vacuum, the participate was washed with $CHCl_3$, and removed insoluble by filtration. The filtrate was washed with water and brine, dried with anhydrous $MgSO_4$, and filtered. The crude product was purified with short silica gel column chromatography ($CHCl_3$), following well wash by hexane to give compound **5a** as a pale-yellow solid (4.02 g, 7.14 mmol, 88%).

M.p. 167 °C. ^{1}H NMR (400 MHz, $CDCl_3$) : δ 8.15 (d, 2H, *J* = 8.4 Hz) , 8.10 (d, 2H, *J* = 8.4 Hz) , 7.78 (d, 2H, *J* = 8.4 Hz) , 7.70 (d, 2H, *J* = 8.4 Hz) , 4.36 (t, 2H, *J* = 6.8 Hz) , 1.74–1.81 (m,2H) , 1.45–1.55 (m, 2H) , 1.00 (t, 3H, *J* = 7.6 Hz) ppm. ^{13}C NMR (100 MHz, $CDCl_3$) : δ 193.7, 166.2, 146.4, 143.6, 132.3, 130.6, 130.5, 130.3, 127.9, 127.3, 65.0, 30.8, 19.3, 13.8 ppm. HR-MS (FAB+) calcd. for $C_{36}H_{35}O_6$ $[M]^+$ 563.2355 ; found 563.2426.

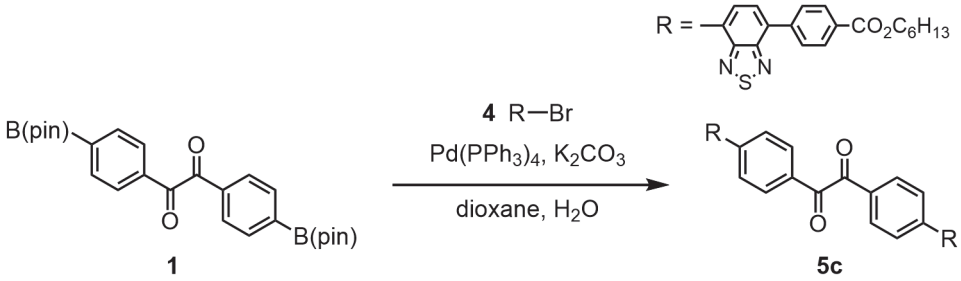

Synthesis of 5c. A 200 mL three-necked flask was charged with crude compound **1** (1.62 g, 3.50 mmol), compound **4** (3.00 g, 7.15 mmol), K_2CO_3 (2.03 g, 15.0 mmol), and $Pd(PPh_3)_4$ (0.406 g, 0.398 mmol) in degassed dioxane (30 mL) and degassed water (5 mL) under nitrogen. Then the reaction mixture was refluxed at 110 °C for 17h. After cooling to room temperature, water (70 mL) was added and the participate was collected by filtration, rinsed with water (50 mL) and acetone (100 mL). The crude product was well washed acetone and AcOEt to give compound **5c** as a green solid (2.96 g, 3.33 mmol, 95%).

M.p. 226.1 °C. ^{1}H NMR (400 MHz, $CDCl_3$) : δ 8.16–8.25 (m, 12H), 8.07 (d, 4H, *J* = 8.0 Hz), 7.88–7.93 (m, 4H), 4.37 (t, 4H *J* = 6.8 Hz), 1.76–1.86 (m, 4H), 1.30–1.52 (m, 12H), 0.923 (s, 6H) ppm. ^{13}C NMR (100 MHz, $CDCl_3$) : δ 194.00, 166.37, 153.85, 153.70, 143.57, 141.27, 133.62, 132.53, 132.37, 130.49, 130.29, 129.88, 128.83, 128.41, 65.31, 31.48, 28.73, 25.73, 22.57, 14.03 ppm. HR-MS (FAB+): calcd. For $C_{52}H_{47}N_4O_6S_2$ $[M+H]^+$ 887.2937; found: 887.2926

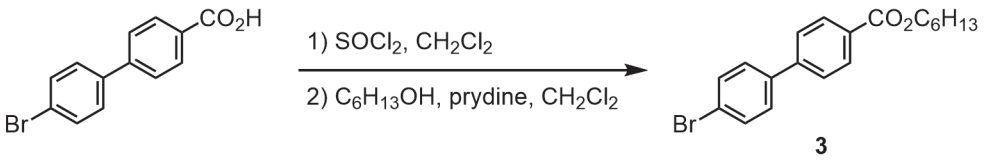

3

Synthesis of 3. A 200 mL three-necked flask was charged with 4'-bromo-4-biphenylcarboxylic acid (3.00 g, 10.8 mmol) in dehydrated CH_2Cl_2 (80 mL) under nitrogen. Then $SOCl_2$ (1.70 mL, 21.0 mmol) were added dropwise at 0 °C. The mixture was refluxed at 50 °C for 4h. After cooling to room temperature, solvent was removed under vacuum and dissolved dehydrated CH_2Cl_2. Then dehydrated n-hexanol (5.0 mL) and triethylamine (6.0 mL) were added and stirred at rt for 16 h. The organic phase was diluted with CH_2Cl_2 (40 mL) and washed with 1M HCl_{aq}, water and brine, dried with anhydrous $MgSO_4$, and filtered. The crude product was purified with silica gel column chromatography ($CHCl_3$/hexane = 1/2–1/0) to give compound **3** (3.40 g, 9.41 mmol, 87%) as a white solid.

M.p. 47.0 °C. ^{1}H NMR (400 MHz, $CDCl_3$) : δ 8.11 (d, 2H, *J* = 8.8 Hz) , 7.58–7.63 (m, 4H) , 4.34 (t, 2H, *J* = 6.8 Hz) , 1.75–1.82 (m, 2H) , 1.30–1.51 (m, 6H) , 0.92 (t, 3H, *J* = 7.2 Hz) ppm. ^{13}C NMR (100 MHz, $CDCl_3$) : δ 166.4, 144.2, 139.0, 132.1, 130.2, 129.7, 128.8, 126.8, 122.5, 65.2, 31.5, 28.7, 25.7, 22.6, 14.0 ppm. HR-MS (FAB+): calcd. For $C_{19}H_{21}O_2Br$ $[M+H]^+$ 361.0803; found: 361.0805.

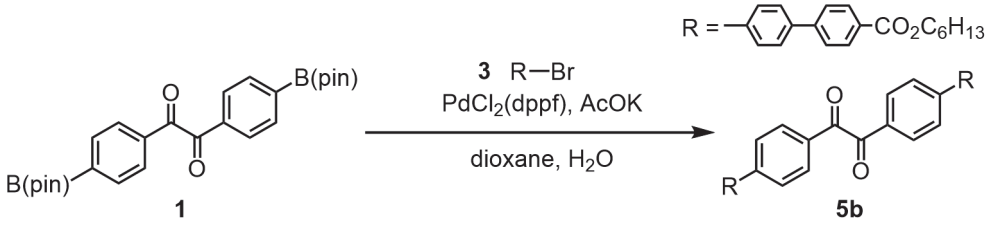

1 5b

Synthesis of 5b. A 200 mL three-necked flask was charged with compound **1** (0.948 g, 2.05 mmol), compound **3** (1.48 mg,4.10 mmol), K_2CO_3 (1.35 g, 10.0 mmol), and $Pd(PPh_3)_4$ (0.474 g, 0.410 mmol) in degassed dioxane (30 mL) and degassed water (5 mL) under nitrogen. Then the reaction mixture was refluxed at 110 °C for 17h. After cooling to room temperature, water (30 mL) was added and the participate was collected by filtration, rinsed with water and acetone. The crude product was well washed acetone and AcOEt to give compound **5b** as a gray solid (1.24 g, 1.58 mmol, 77%).

M.p. 238.1 °C. ^{1}H NMR (400 MHz, $CDCl_3$) : δ 8.13 (m, 8H) , 7.81 (d, 4H, *J* = 8.4 Hz) , 7.75 (s, 8H) , 4.34 (t, 2H, *J* = 6.8 Hz) , 1.75–1.82 (m, 2H) , 1.30–1.51 (m, 6H) , 0.92 (t, 3H, *J* = 7.2 Hz) ppm. ^{13}C NMR (100 MHz, $CDCl_3$) : δ 194.0, 166.6, 146.9, 144.6, 140.4, 139.3, 132.0, 130.7, 128.02, 128.00, 127.7, 127.0, 65.3, 31.6, 28.8, 25.8, 22.7, 14.1 ppm. HR-MS (FAB+): calcd. For $C_{52}H_{50}O_6$ $[M+H]^+$ 770.3613; found: 770.3616.

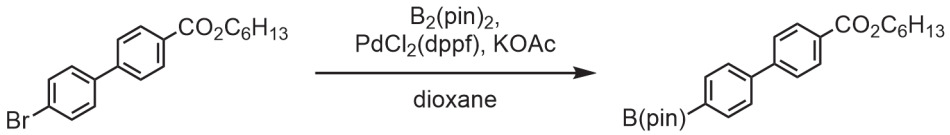

3 **16**

Synthesis of 16 A 100 mL three-necked flask was charged with compound **3** (2.02 g, 5.60 mmol), bis(pinacolato)diboron (1.56 g, 6.10 mmol), AcOK (1.90 g, 19.3 mmol), and $PdCl_2$(dppf) (0.130 g, 0.173 mmol) under nitrogen. Then degassed dioxane (15 mL) were added and the reaction mixture was refluxed at 90 °C overnight. After cooling to room temperature, the product was extracted with AcOEt. The organic phase was combined and washed with water, dried with anhydrous $MgSO_4$, and filtered. The crude product was purified with silica gel column chromatography (AcOEt/hexane = 1/6) to give crude compound **16** as a white solid (3.14 g) which was used in the following reaction without further purification.

^{1}H NMR (400 MHz, $CDCl_3$) : δ 8.13 (d, 2H, *J* = 8.4 Hz) , 7.63–7.75 (m, 6H) , 7.59 (d, 2H, *J* = 8.8 Hz) , 7.51 (d, 2H, *J* = 8.4 Hz), 4.35 (t, 2H, *J* = 6.6 Hz), 1.74–1.84 (m, 2H), 1.30–1.52 (m, 6H), 0.915 (t, 2H, *J* = 7.6 Hz) ppm.

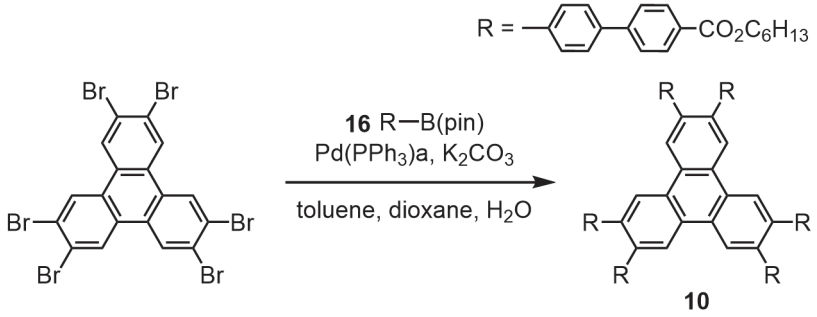

10

Synthesis of 10. A 100 mL three-necked flask was charged with 2,3,6,7,10,11-hexabromotriphenylene (236 mg, 0.336 mmol), crude compound **16** (892 mg, ca. 2.2 mmol), K_2CO_3 (700 mg, 5.19 mmol), and $Pd(PPh_3)_4$ (130 mg, 1.11 mmol) in degassed toluene (10 mL), dioxane (15 mL) and degassed water (5 mL) under nitrogen. Then the reaction mixture was refluxed at 100 °C for 36h. After removing solvent under vacuum, the product was extracted with $CHCl_3$. The organic phase was combined and washed with water and brine, dried with anhydrous $MgSO_4$, and filtered. The crude product was purified with silica gel column chromatography(CH_2Cl_2 in MeOH = 0%–1%) to give compound **10** as a pale yellow solid (388 mg, 0.203 mmol, 60%)

M.p. >300 °C. ^{1}H NMR (400 MHz, $CDCl_3$) : δ 8.11 (d, 2H, *J* = 8.8 Hz) , 7.70 (d, 2H, *J* = 8.0 Hz) , 7.63 (d, 2H, *J* = 7.2 Hz) , 7.50 (d, 2H, *J* = 7.2 Hz), 4.34 (t, 2H, *J* = 6.8 Hz), 1.74–1.84 (m, 2H), 1.30–1.52 (m, 6H), 0.941 (t, 2H, *J* = 7.6 Hz) ppm. ^{13}C NMR (100 MHz, $CDCl_3$) : δ 166.5, 144.8, 141.2, 139.5, 138.6, 130.1, 129.4, 127.1, 126.8, 125.8, 65.2, 31.5, 28.7, 22.6, 14.0 ppm. HR-MS (MALDI): calcd. For $C_{132}H_{132}O_{12}$ $[M]^+$ 1908.9713; found: 1908.9688.

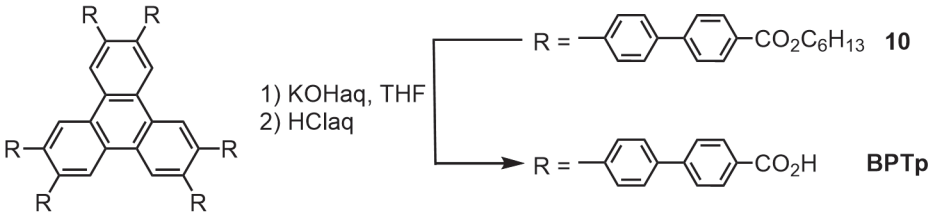

Synthesis of BPTp. A reaction mixture of compound **10** (19 6 mg, 1.02 mmol) in THF (15 mL) and 5%-KOH aqueous solution (10 mL) was stirred for 3 days at 60 °C. After cooled to room temperature, organic phase was removed in vacuo, following addition of 37%-HCl into the reaction mixture until precipitate was not formed anymore. The precipitate was collected by centrifugation, washed with water, and dried in vacuo to yield **BPTp** (131 mg, 0.932 μmol, 91%) as pale brown solid.

M.p. >300 °C. ^{1}H NMR (400 MHz, DMSO-d_6) : δ 9.00 (br, 6H), 7.99 (d, 12H, J = 8.0 Hz), 7.82 (d, 12H, J = 8.0 Hz) , 7.74 (d, 12H, J = 8.4 Hz) , 7.55 (d, 12H, J = 8.4 Hz) ppm. ^{13}C NMR (100 MHz, DMSO-d_6) : δ 167.11, 160.46, 152.93, 143.52, 140.75, 139.19, 137.12, 130.77, 129.96, 128.61, 126.62, 126.59 ppm. HR-MS (MALDI): calcd. For $C_{96}H_{59}O_{12}$ $[M]^+$ 1403.4001; found: 1403.4025.

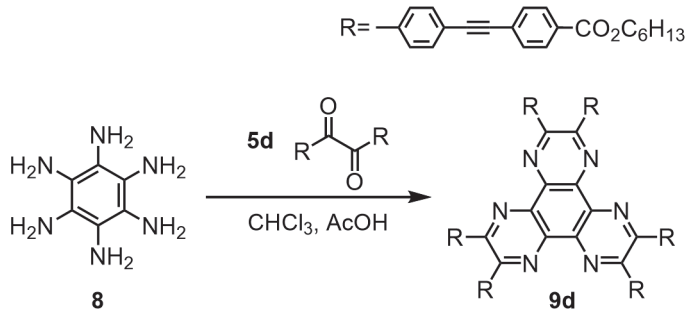

Synthesis of 9d. A 100 mL round bottom flask was charged with compound **5d** (620 mg, 930 μmol) in degassed $CHCl_3$ (13 mL) and degassed AcOH (3 mL), and heated at 70 °C. Then compound **8** dispersed in $CHCl_3$ (50 mg, 297 μmol) and stirred for 24 h at 70 °C. After the reaction solvent was removed in vacuo, the product was extracted with $CHCl_3$. The organic phase was combined and washed with *sat.* $NAHCO_{3aq}$, water and brine, dried with anhydrous $MgSO_4$, and filtered. The crude product was purified by silica gel column chromatography ($CHCl_3$) and preparative HPLC to yield compound **9d** (164 mg, 79.7 μmol, 27%) as green solid.

M.p. 240.0 °C. ^{1}H NMR (400 MHz, $CDCl_3$) : δ 8.05 (d, 2H, J = 8.8 Hz), 7.99 (d, 2H, J = 8.4 Hz), 7.68 (d, 2H, J = 8.8 Hz), 7.61 (d, 2H, J = 8.4 Hz), 4.33 (t, 2H, J = 6.8 Hz), 1.73–1.83 (m, 2H), 1.27–1.50 (m, 6H), 0.909 (t, 2H, J = 7.2 Hz) ppm. ^{13}C NMR (100 MHz, $CDCl_3$) : δ 193.0, 166.0, 132.32, 132.30, 131.7, 130.6, 129.9, 129.60, 129.57, 126.8, 93.2, 90.9, 65.5, 31.4, 28.6, 25.7, 22.5, 14.0 ppm. HR-MS (MALDI): calcd. For $C_{138}H_{126}O_{12}N_6$ $[M]^+$ 2058.9428; found: 2058.9457.

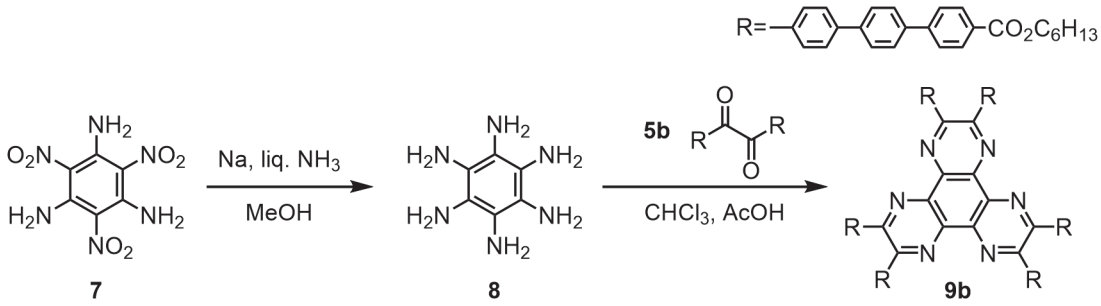

Synthesis of 9b. A 100 mL three-neck flask equipped with magnetic stirrer, gas inlet, and gas condenser was charged with compound **7** (100 mg, 0.387 mmol) and dehydrated methanol (7 mL) and was steeped in a cool bath. Approximately 10 mL of ammonia was condensed into the flask. To a reaction mixture with stirring was added sodium (160 mg, 6.63 mmol) in small pieces to keep mild reflux of ammonia. After reflux for 30 min, the condenser and bath were removed to allow ammonia evaporating and dehydrated methanol was added to the reaction mixture. The precipitate was collected by filtration, washed with degassed ethanol and degassed diethylether to yield compound **8** (*ca.* 45.0 mg) as an off-white solid, which was immediately used in the following reaction without further purification.

A 100 mL round bottom flask was charged with compound **5b** (604 mg, 0.783 mmol) in degassed $CHCl_3$ (30 mL) and degassed AcOH (5 mL), and heated at 60 °C. Then HAB dispersion in $CHCl_3$ and the reaction mixture was stirred for 8 h at 60 °C. After the reaction solvent was removed in vacuo, the crude product was purified by silica gel column chromatography (MeOH in $CHCl_3$ = 0%→1%) to yield compound **9b** (113 mg, 0.0477 mmol, 11% from compound **7** in two steps) as brown solid.

M.p. 251.2 °C. ^{1}H NMR (400 MHz, $CDCl_3$) : δ 8.13 (d, 12H, *J* = 8.0 Hz) , 8.04 (d, 12H, *J* = 8.4 Hz) , 7.67–7.82 (m, 48H) , 4.35 (t, 12H, *J* = 6.4 Hz) , 1.75–1.85 (m, 12H) , 1.30–1.54 (m, 36H) , 0.92 (t, 18H, *J* = 7.2 Hz) ppm. ^{13}C NMR (100 MHz, $CDCl_3$) : δ 166.5, 153.5, 144.7, 141.4, 140.0, 139.6, 139.4, 137.8, 131.0, 130.1, 129.5, 127.7, 127.6, 127.1, 126.9, 65.2, 31.5, 28.7, 22.6, 14.0 ppm. HR-MS (MALDI): calcd. For $C_{162}H_{151}N_6O_{12}$ $[M+H]^+$ 2372.1285; found: 2372.1364.

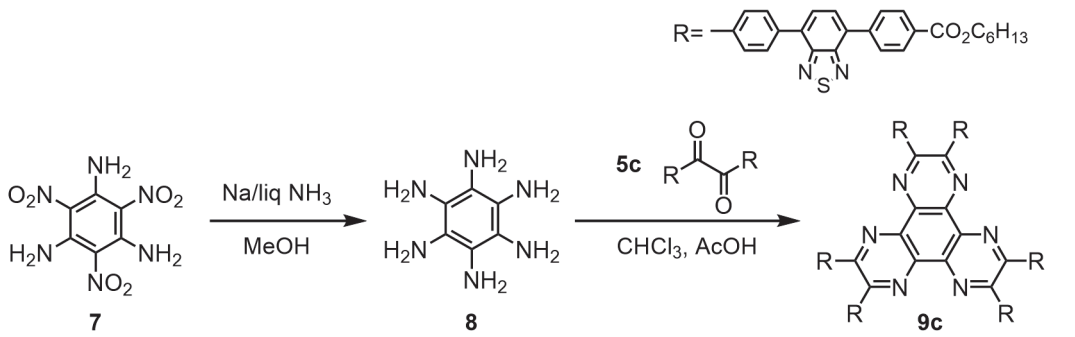

Synthesis of 9c. A 100 mL three-neck flask equipped with magnetic stirrer, gas inlet, and gas condenser was charged with compound **7** (300 mg,1.16 mmol) and dehydrated methanol (10 mL), and was steeped in a cool bath. Approximately 10 mL of ammonia was condensed into the flask. To a reaction mixture with

stirring was added sodium (480 mg, 20.9 mmol) in small pieces to keep mild reflux of ammonia. After reflux for 30 min, the condenser and bath were removed to allow ammonia evaporating and dehydrated methanol was added to the reaction mixture. The precipitate was collected by filtration, washed with degassed ethanol and degassed diethyl ether to yield compound **8** (*ca.*196 mg) as an off-white solid, which was immediately used in the following reaction without further purification.

A 100 mL round bottom flask was charged with compound **5c** (2.66 g, 3.00 mmol) in degassed $CHCl_3$ (50 mL) and degassed AcOH (10 mL), and heated at 70 °C. Then HAB dispersion in $CHCl_3$ and the reaction mixture was stirred for 19 h at 70 °C. After the reaction solvent was removed in vacuo, the crude product was purified by silica gel column chromatography (AcOEt/$CHCl_3$ = 1/25) and preparative HPLC to yield compound **9c** (113 mg, 0.0477 mmol, 43% from compound **7** in 2 steps) as green solid.

M.p. 290.0 °C. ^{1}H NMR (400 MHz, $CDCl_3$) : δ 8.13–8.29 (m, 36H), 8.05 (d, 12H, *J* = 8.0 Hz), 7.92 (d, 6H, *J* = 7.6 Hz), 7.85 (d, 6H, *J* = 8.0 Hz), 4.37 (t, 12H, *J* = 6.8 Hz), 1.74–1.86 (m, 12H), 1.30–1.52 (m, 36 H), 0.922 (s, 18H) ppm. ^{13}C NMR (100 MHz, $CDCl_3$) : δ 166.4, 154.0, 153.9, 153.6, 133.2, 132.6, 13.8, 129.8, 129.5, 129.2, 128.5, 128.2, 65.3, 34.5, 28.7, 25.7, 22.6, 14.0 ppm. HR-MS (MALDI): calcd. For $C_{162}H_{139}N_{18}O_{12}S_6$ $[M+H]^+$ 2719.9139; found: 2719.9183.

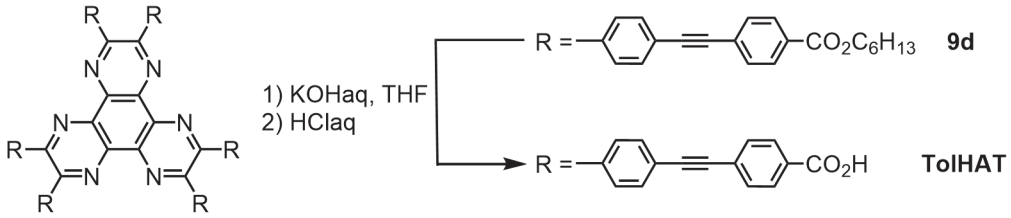

Synthesis of TolHAT. A reaction mixture of compound **9d** (659 mg, 397 μmol) in THF (20 mL) and 5%-KOH aqueous solution (20 mL) was stirred for 48 h at 60 °C. After cooled to room temperature, organic phase was removed in vacuo, following addition of 37%-HCl into the reaction mixture until precipitate was not formed anymore. The precipitate was collected by centrifugation, washed with water, and dried in vacuo to yield **TolHAT** (532 mg, 379 μmol, 95%) as brown solid.

M.p. >300 °C. ^{1}H NMR (400 MHz, DMSO-d_6) : δ 8.37 (d, 12H, *J* = 8.4 Hz), 8.16 (d, 12H, *J* = 8.0 Hz), 8.00–8.15 (m, 24H) ppm. ^{13}C NMR (100 MHz, DMSO-d_6) : δ 166.3, 152.4, 139.3, 138.3, 131.3, 131.2, 130.7, 130.1, 129.3, 126.1, 122.7, 91.3, 90.1 ppm. HR-MS (MALDI): calcd. For $C_{126}H_{67}N_{18}O_{12}S_6$ $[M+H]^+$ 2215.3405; found: 2215.3416.

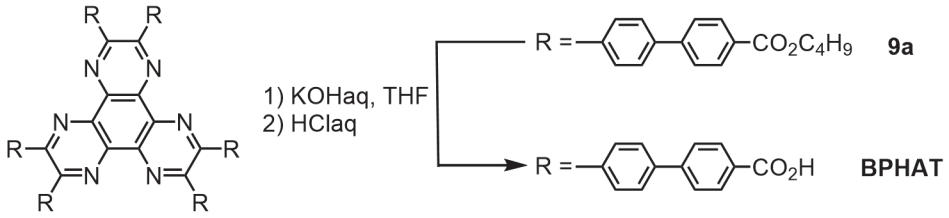

Synthesis of BPHAT. A reaction mixture of compound **9a** (659 mg, 397 μmol) in THF (20 mL) and 5%-KOH aqueous solution (20 mL) was stirred for 2 days at 60 °C. After cooled to room temperature, 37%-HCl was added into the reaction mixture until precipitate was not formed anymore. The precipitate was collected by centrifugation, washed with water, and dried in vacuo to yield **BPHAT** (532 mg, 379 μmol, 95%) as brown solid.

M.p. >300 °C. ^{1}H NMR (400 MHz, DMF-d_7, 0.71 mM): δ 8.16 (d, 12H, J = 8.4 Hz), 8.06 (d, 12H, J = 8.4 Hz), 7.98 (d, 12H, J = 8.4 Hz), 7.96 (d, 12H, J = 8.4 Hz) ppm. ^{13}C NMR (100 MHz, DMF-d_7, 0.71 mM): δ 167.7, 154.0, 144.3, 140.9, 140.8, 139.3, 131.6, 131.0, 130.7, 127.59, 127.56 ppm. HR-MS (MALDI) calc. for $C_{90}H_{55}N_6O_{12}$ $[M+H]^+$ 1411.3872; found 1411.3826.

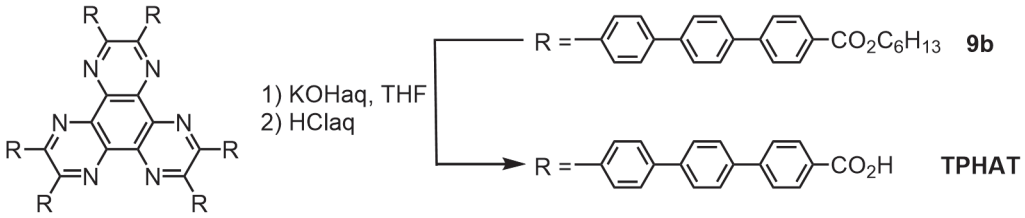

Synthesis of TPHAT. A reaction mixture of compound **9b** (62.5 mg, 26.7 μmol) in THF (30 mL) and 5%-KOH aqueous solution (20 mL) was stirred for 3 days at 60 °C. After cooled to room temperature, organic phase was removed in vacuo, following addition of 37%-HCl into the reaction mixture until precipitate was not formed anymore. The precipitate was collected by centrifugation, washed with water twice, and dried in vacuo. Obtained solid was washed with $CHCl_3$, to yield **TPHAT** (41.6 mg, 22.3 μmol 85%) as yellow solid. M.p. >300 °C. ^{1}H NMR (400 MHz, DMSO-d_6) : δ 8.30 (s), 7.70–8.10 (m) ppm. HR-MS (MALDI) calc. for $C_{126}H_{77}N_6O_{12}$ $[M-H]^-$ 1865.5594 ; found 1865.5572. ^{13}C NMR spectrum was not obtained due to low solubility of **TPHAT**.

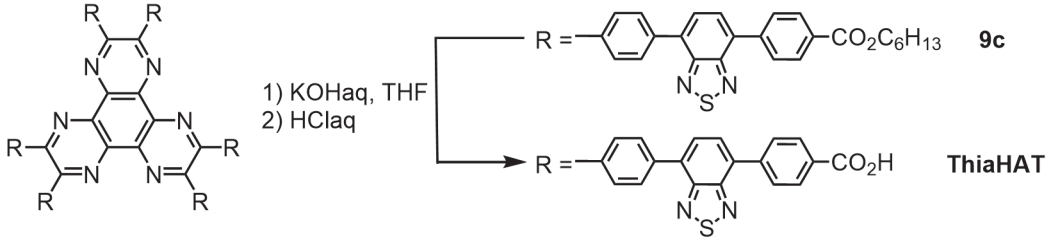

Synthesis of ThiaHAT. A reaction mixture of compound **9c** (81.8 mg, 30.0 μmol) in THF (30 mL) and 5%-

KOH aqueous solution (35 mL) was stirred for 3 days at 60 °C. After cooled to room temperature, organic phase was removed in vacuo. Then 6%-HCl was added into the aqueous reaction mixture until precipitate was not formed anymore and stirred at rt for 1h. The precipitate was collected by centrifugation, washed with water three times, acetone, and THF and dried in vacuo to yield **ThiaHAT** (65.5 mg, 29.6 μmol, 99%) as brown solid.

M.p. >300 °C. ^{1}H NMR (400 MHz, NMP-d_9) : δ 8.30 (s), 7.70–8.10 (m) ppm. HR-MS (MALDI): calcd. For $C_{126}H_{67}N_{18}O_{12}S_6$ $[M+H]^+$ 2215.3505; found: 2215.3461. Elemental analisys: calculated for $[M+3H_2O]$ C:66.60, H:3.20, N:11.10; found C:66.45, H:3.22, N: 10.72. ^{13}C NMR spectrum was not obtained due to low solubility of **ThiaHAT**.

2.10.2 Single crystal X-ray measurement and analysis

Diffraction data of **TolHAT-1** was collected at SPring-8 (BL02B1) with monochromated synchrotron radiation (λ = 0.42112 Å), **ThiaHAT-1** was collected at Spring-8 (BL40XU) with synchrotron radiation (λ = 0.81106 Å), and **BPHAT-1** and **BPTp-TCB** was collected with a two-dimensional X-ray detector (PILATUS 200K/R) equipped on a Rigaku XtaLAB P200 diffractometer by using Cu-Kα radiation monochromated with multilayer mirror (λ=1.54187 Å). Diffraction Data collection, cell refinement, and data reduction were carried out with Crysalis PRO[41]. SHELXT[43] were used for the structure solution of the crystals. These calculations were performed with the observed reflections [I > 2σ(I)] with the program CrystalStructure crystallographic software or OLEX-2 crystallographic software[48–50]. Structural refinement was performed by SHELXL[45]. All non-hydrogen atoms except for highly disordered solvent molecules accommodated in voids were refined with anisotropic displacement parameters, and hydrogen atoms were placed in idealized positions and refined as rigid atoms with the relative isotropic displacement parameters. SQUEEZE function equipped in the PLATON program was used to remove severely disordered solvent molecules in voids[46,51].

Table 9. Crystal data of **BPHAT-1**, **BPHAT-1a**, **TolHAT-1**, **ThiaHAT-1**, and **BPTp-1**.

	BPHAT-1	**BPHAT-1a**	**TolHAT-1**	**ThiaHAT-1**	**BPTp-1**
System	*trigonal*	*trigonal*	*trigonal*	*trigonal*	*Monoclinic*
Space group	*P*-3	*P*-3	*R*-3*c*	*R*-3*c*	*I2/a*
Formula	$(C_{90}H_{54}N_6O_{12})\cdot(C_6H_3Cl_3)$	$C_{90}H_{54}N_6O_{12}$	$C_{17}H_9NO_2$	$C_{21}H_{11}N_3O_2S$	$C_{53}H_{50}O_6Cl_3$
Fw	1955.80	1411.45	1555.584	1802.094	889.327
a / Å	29.7532(15)	29.7810(10)	59.5294(11)	65.827(5)	9.3082(3)
b / Å	29.7532(15)	29.7810(10)	59.5294(11)	65.827(5)	53.6910(12)
c / Å	7.1146(6)	7.1709(3)	6.96369(19)	6.9879(7)	30.7096(6)
α / °	90	90	90	90	90
β / °	90	90	90	90	97.504(2)
γ / °	120	120	120	120	90
V / Å^3	5454.4(6)	5507.9(3)	21371.4(8)	26223(4)	15216.2(7)
Z	2	2	6	6	4
D / g cm^3	1.191	0.851	0.728	0.843	1.337
Crystal size / mm	0.15 × 0.05 × 0.05	0.15 × 0.06 × 0.05	0.05 × 0.008 × 0.008	0.1 × 0.02 × 0.02	0.1 × 0.1 × 0.1
Crystal color	yellow green	yellow green	yellow green	yellow	colorless
R_1 (I > 2.0σ(I))	0.130	0.078	0.1267	0.1688	0.1349
wR_2 (all)	0.385	0.241	0.3874	0.4127	0.3858
Completeness	0.971	0.961	1.00	0.999	0.997
GOF	1.226	1.039	1.265	1.386	1.377
λ / Å	1.54184	1.54184	0.42112 (synchrotron)	0.81106 (synchrotron)	1.54184
T / K	93	93	90	95	93
CCDC no.	1841012	1841011	2081132	2081131	2081133

2.10.3 Variable temperature PXRD (VT-PXRD) measurement

Powder X-ray diffraction (PXRD) data were collected on a Rigaku Ultima-IV (40 kV, 44 mA) using graphite-monochromatized Cu-Kα radiation (λ = 1.54187 Å) at room temperature. A scan rate is 2.0° min^{-1}. VT-PXRD data were collected on same apparatus as PXRD with a temperature control unit. Balk of Crystals placed on an aluminum substrate was subjected to VT-PXRD measurement under the air atmosphere. Temperature of the sample was increased from room temperature to 360 °C with a rate of 0.5° min^{-1} or 1.0° min^{-1}. Each PXRD scan of each measurements has a temperature width of *ca*. 5.1 °C [**TolHAT-1(TMB)**, **TolHAT-1aIV**, and **ThiaHAT-1a**], *ca.* 2.6 °C [**ThiaHAT-1**], and *ca*. 2.5 °C [**BPHAT-1**].

2.10.4 Sorption/desorption experiments

Gas sorption measurements were performed on BELSORP-max (BEL, Japan). The adsorption isotherms of N_2, O_2, CO_2, and H_2 were corrected at 77K, 77 K, 195 K and 77 K, respectively. The activated bulk samples of **BPHAT-1a**, **TPHAT-a**, **TolHAT-1a*N*** (*N* = I–IV), and **ThiaHAT-1a*N*** (N = I, II, and IV) were used. $S_{A(BET)}$ and d_{NLDFT} were based on N_2 absorption isotherms.

2.10.5 Theoretical calculations

Optimized structure of **TolHAT** and **ThiaHAT** were calculated by the DFT method at the B3LYP/6-31G level. These calculations were carried out using Gaussian09W[55]. Atomic coordinates in the crystal structures were adopted except for hydrogen atoms which were optimized were computed at B3LYP-D3/6-311G(d,p) level of theory. The complexation energy was evaluated by the following three methods: B3LYP-D3/6-311G(d,p), M062X/6-311G(d,p), and ωB97XD/6-311G(d,p). The corrections of basis set superposition error (BSSE) are evaluated by means of counterpoise method. These calculations were carried out using Gaussian09W. In Figure 11, the complexation energies for **TolHAT-1**, **ThiaHAT-1**, **CBPHAT-1**, and **CPHAT-1** are plotted against a spacer length. The spacer length means a distance between a C atom of HAT adjacent to arm moiety and that of carboxylic acid.

Table 10. The Spacer lengths of HAT derivatives, and complexation energy of stacking between two HAT derivatives.

	Spacer length / Å	Energy of B3LYP-D3 / kcal mol^{-1}	Energy of M062X / kcal mol^{-1}	Energy of ωB97XD / kcal mol^{-1}
CPHAT	5.757	−54.66	−38.47	−58.39
BPHAT	10.06	−81.16	−63.89	−90.92
TolHAT	12.57	−97.54	−82.12	−108.56
ThiaHAT	14.42	−103.5	−73.97	−112.69

2.10.6 Molecular dynamics simulations

MD (molecular dynamics) simulations were performed at 300 K and 1 bar using GROMACS 2016-4[56]. The initial configuration of each HOF system was constructed by retrieving the unit-cell structure of the crystal in CIF format and replicating it periodically 9, 9, and 12 times along the *a, b*, and *c* directions, respectively. The unit cell of MD was then a parallelepiped, and the periodic boundary condition was employed with minimum image convention. The force field was GAFF (general AMBER force field), and the atomic partial charges were determined with RESP (restrained electrostatic potential)[57,58]. The RESP procedure was carried out after DFT calculations for the monomeric forms at the B3LYP/6-31G(d,p) level with Gaussian09[43]. In DFT, the geometrical optimization was done only for the hydrogen atoms and the non-hydrogen atoms were kept fixed at the coordinates in the CIF file. After the energy minimization with

the steepest descent method for 50000 steps, MD was carried in the *NPT* ensemble over 2 ns for equilibration and over 10 ns for production; see the next paragraph for the procedure of equilibration. The RMSD was computed by referencing the average structure of the crystal obtained from the production run.

In MD, the electrostatic interaction was handled by the smooth particle-mesh Ewald (PME) method with a real-space cutoff of 12 Å, a spline order of 6, a relative tolerance 10^{-5}, and a reciprocal-space mesh size of 48 along each of the *x*, *y*, and *z* directions[59]. The Lennard-Jones (LJ) interaction was truncated at 12 Å with a switching range of 10–12 Å[60], and the long-range correction was not incorporated. The Lorentz-Berthelot rule was employed to combine the LJ interaction between unlike pairs of atoms, and the truncation was applied on atom-atom basis both for the real-space part of PME and for LJ. The leap-frog method was adopted to integrate the equation of motion at a time step of 1 fs[61]. The equilibration consisted of 7 steps. In the 1st, 3rd, and 5th steps, the temperature was elevated linearly against time with a duration of 200 ps from 0 to 100 K, from 100 to 200 K, and from 200 to 300 K, respectively, and in the 2nd, 4th, and 6th, the temperature was fixed at 100, 200, and 300 K respectively, over 300 ps. The 7th step was performed at constant temperature at 300 K over 500 ps. In the 1st to 6th steps, the temperature and pressure were regulated by the velocity rescaling with a time constant of 0.1 ps and the Berendsen barostat with a coupling time of 2 ps, respectively, and in the 7th step, the velocity rescaling with 1 ps and the Parrinello-Rahman barostat at a coupling time of 2 ps were employed[62–64]. In both of the Berendsen and Parrinello-Rahman barostats, the isothermal compressibility was set to 4.5×10^{-6} bar^{-1} and the semi-isotropic coupling was employed for the lateral (a and b) and normal (c) directions. The LINCS algorithm was used for the other molecules to fix the lengths of all the bonds involving a hydrogen atom[65].

2.10.7 Time-resolved spectroscopy

Picosecond emission decays were measured using a time-correlated single photon counting (TCSPC) system[51]. The sample was excited by a 40-ps pulsed diode laser centered at 371 (< 5 mW, 40 MHz repetition rate) and instrument response function (IRF) of ~ 70 ps. The IRF of the system has been measured using a standard LUDOX (Sigma-Aldrich) solution in 1 cm cell. The decays were deconvoluted and fitted to multiexponential function using the FLUOFIT package (PicoQuant) allowing single and global fits. The quality of the fit was estimated by χ^2, which was always below 1.2.

2.10.8 Microscopic fluorescence spectroscopy

The confocal microscopy measurements were performed on a MicroTime 200 confocal microscope (PicoQuant). For excitation, the author used a diode laser with excitation wavelength of 390 nm (40 ps full width at half-maximum of intensity). In brief, it consists of inverse Olympus IX 71 microscope equipped with water immersion objective (x60 NA1.2, Olympus) and 2D piezo scanner (Physik Instrumente). The emitted light is then focused on a pinhole of 50 μm and later collimated to two independent single photon avalanche photodiodes (Micro-Photon-Devices) for time-resolved measurements. The single molecule

emission spectra were collected through Shamrock SR-303i (Andor Technology) imaging spectrograph and detected by Andor Newton EMCCD camera (Andor Technology). For the anisotropy measurements the light was passed through a polarizing beam-splitter that allows for the simultaneous detection of the parallel and perpendicular parts of the emission. A G-factor of 1.2, accounting for differences in the detection sensitivity for both polarizations in the setup, was used in the calculation of the polarization and anisotropy. For each sample between 10 and 15 crystals have been analyzed both in spectral and kinetic modes. The emission signal was collected using a 430 nm long pass filter (Chroma). For the decays measured at discrete wavelengths at the blue and red part of the spectrum the author used a FF01-445/40-25 (445±25 nm) and FF01-540/50-25 (540±25 nm) filters (Semrock).

2.11 References

1. A. G. Slater and A. I. Cooper, *Science*, 2015, **348**, aaa8075.
2. C. S. Diercks, Y. Liu, K. E. Cordova and O. M. Yaghi, *Nat. Mater.*, 2018, **17**, 301–307.
3. M. J. Kalmutzki, N. Hanikel and O. M. Yaghi, *Sci. Adv.*, 2018, **4**, aat9180.
4. C. Gropp, S. Canossa, S. Wuttke, F. G´andara, Q. Li, L. Gagliardi and O. M. Yaghi, *ACS Cent. Sci.*, 2020, **6**, 1255–1273.
5. J. Li, P. M. Bhatt, J. Li, M. Eddaoudi and Y. Liu, *Adv. Mater.*, 2020, **32**, 2002563.
6. W. Xu, B. Tu, Q. Liu, Y. Shu, C. C. Liang, C. S. Diercks, O. M. Yaghi, Y. B. Zhang, H. Deng and Q. Li, *Nat. Rev. Mater.*, 2020, **5**, 764–779.
7. O. M. Yaghi, M. J. Kalmutzki and C. S. Diercks, Introduction to Reticular Chemistry: Metal-Organic Frameworks and Covalent Organic Frameworks, *Wiley*, 2019, ISBN 978-3-527-3450-1.
8. H. Deng, S. Grunder, K. E. Cordova, C. Valente, H. Furukawa, M. Hmadeh, F. Gandara, A. C. Whalley, Z. Liu, S. Asahina, H. Kazumori, M. O'Keeffe, O. Terasaki, J. F. Stoddart and O. M. Yaghi, *Science*, 2012, **336**, 1018–1023.
9. Z. Mu, Y. Zhu, B. Li, A. Dong, B. Wang and X. Feng, *J. Am. Chem. Soc.*, 2022, **144**, 5145–5154.
10. Y. F. Han, Y. X. Yuan and H. B. Wang, *Molecules*, 2017, **22**, 266.
11. J. Luo, J. W. Wang, J. H. Zhang, S. Lai and D. C. Zhong, *CrystEngComm*, 2018, **20**, 5884–5898.
12. R. B. Lin, Y. He, P. Li, H. Wang, W. Zhou and B. Chen, *Chem. Soc. Rev.*, 2019, 48, 1362–1389.
13. I. Hisaki, C. Xin, K. Takahashi and T. Nakamura, *Angew. Chem. Int. Ed.*, 2019, **58**, 11160–11170.
14. I. Hisaki, J. Inclusion Phenom. Macrocyclic *Chem.*, 2020, **96**, 215–231.
15. B. Wang, R.-B. Lin, Z. Zhang, S. Xiang and B. Chen, *J. Am. Chem. Soc.*, 2020, **142**, 14399–14416.
16. F. Hu, C. Liu, M. Wu, J. Pang, F. Jiang, D. Yuan and M. Hong, *Angew. Chem. Int. Ed.*, 2017, **56**, 2101–2104.
17. B. Han, H. Wang, C. Wang, H. Wu, W. Zhou, B. Chen and J. Jiang, *J. Am. Chem. Soc.*, 2019, **141**, 8737–8740.
18. P. Li, Y. He, H. D. Arman, R. Krishna, H. Wang, L. Weng and B. Chen, *Chem. Commun.*, 2014, **50**, 13081–13084.
19. Y. He, S. Xiang and B. Chen, *J. Am. Chem. Soc.*, 2011, **133**, 14570–14573.
20. P. Li, Z. Chen, M. R. Ryder, C. L. Stern, Q. H. Guo, X. Wang, O. K. Farha and J. F. Stoddart, *J. Am. Chem. Soc.*, 2019, **141**, 12998–13002.
21. K. Kobayashi, T. Shirasaka, E. Horn and N. Furukawa, *Tetrahedron Lett.*, 2000, **41**, 89–93.
22. P. Li, P. Li, M. R. Ryder, Z. Liu, C. L. Stern, O. K. Farha and J. F. Stoddart, *Angew. Chem. Int. Ed*., 2019, **58**, 1664–1669.
23. X. Zhang, L. Li, J. X. Wang, H. M. Wen, R. Krishna, H. Wu, W. Zhou, Z. N. Chen, B. Li, G. Qian and B. Chen, *J. Am. Chem. Soc.*, 2020, **142**, 633–640.
24. A. Pulido, L. Chen, T. Kaczorowski, D. Holden, M. A. Little, S. Y. Chong, B. J. Slater, D. P. McMahon, B. Bonillo, C. J. Stackhouse, A. Stephenson, C. M. Kane, R. Clowes, T. Hasell, A. I. Cooper and G. M. Day, *Nature*, 2017, **543**, 657–664.
25. M. Mastalerz and I. M. Oppel, *Angew. Chem. Int. Ed.*, 2012, **51**, 5252–5255.
26. Q. Yin, P. Zhao, R. J. Sa, G. C. Chen, L. Jian, T. F. Liu and R. Cao, *Angew. Chem. Int. Ed.*, 2018, **57**, 7691–7696.
27. K. Ma, P. Li, J. H. Xin, Y. Chen, Z. Chen, S. Goswami, X. Liu, S. Kato, H. Chen, X. Zhang, J. Bai, M. C. Wasson, R. R. Maldonado, R. Q. Snurr and O. K. Farha, *Cell Rep. Phys. Sci.*, 2020, **1**, 100024.
28. B. Wang, X. L. Lv, J. Lv, L. Ma, R. B. Lin, H. Cui, J. Zhang, Z. Zhang, S. Xiang and B. Chen, *Chem. Commun.*, 2019, **56**, 66–69.
29. T.-H. Chen, I. Popov, W. Kaveevivitchai, Y.-C. Chuang, Y.-S. Chen, O. Daugulis, A. J. Jacobson and O. Š. Miljanić, *Nat.*

Commun., 2014, **5**, 5131.

30. M. I. Hashim, H. T. M. Le, T. H. Chen, Y. S. Chen, O. Daugulis, C. W. Hsu, A. J. Jacobson, W. Kaveevivitchai, X. Liang, T. Makarenko, O. Miljanić, I. Popovs, H. V. Tran, X. Wang, C. H. Wu and J. I. Wu, *J. Am. Chem. Soc*., 2018, **140**, 6014–6026.
31. I. Hisaki, S. Nakagawa, N. Ikenaka, Y. Imamura, M. Katouda, M. Tashiro, H. Tsuchida, T. Ogoshi, H. Sato, N. Tohnai and M. Miyata, *J. Am. Chem. Soc.*, 2016, **138**, 6617–6628.
32. I. Hisaki, Y. Suzuki, E. Gomez, Q. Ji, N. Tohnai, T. Nakamura and A. Douhal, *J. Am. Chem. Soc.*, 2019, **141**, 2111–2121.
33. I. Hisaki, N. Ikenaka, E. Gomez, B. Cohen, N. Tohnai and A. Douhal, *Chem. Eur. J.*, 2017, **23**, 11611–11619.
34. I. Hisaki, Y. Suzuki, E. Gomez, B. Cohen, N. Tohnai and A. Douhal, *Angew. Chem. Int. Ed.*, 2018, **57**, 12650–12655.
35. D. Z. Rogers, *J. Org. Chem.*, 1986, **51**, 3904–3905.
36. A. L. Spek, *Acta Crystallogr., Sect. D: Biol. Crystallogr.*, 2009, **65**, 148–155.
37. C. Song, Y. He, B. Li, Y. Ling, H. Wang, Y. Feng, R. Krishna and B. Chen, *Chem. Commun.*, 2014, **50**, 12105–12108.
38. T. Ikeda, T. Iijima, R. Sekiya, O. Takahashi and T. Haino, *J. Org. Chem.*, 2016, **81**, 6832–6837.
39. M. R. Nunzio, I. Hisaki and A. Douhal, *J. Photochem. Photobiol. C: Photochem. Rev.*, 2021, **47**, 100418.
40. E. Gomez, Y. Suzuki, I. Hisaki, M. Moreno and A. Douhal, *J. Mater. Chem. C*, 2019, **7**, 10818–10832.
41. Rigaku Oxford Diffraction (2015), Software CrysAlisPro 1.171.38.41o. Rigaku Corporation, Tokyo, Japan.
42. G. M. Sheldrick, *Acta Crystallogr. Sect. A*, 2008, **64**, 112.
43. G. M. Sheldrick, *Acta Crystallogr. A*, 2015, **71**, 3–8.
44. Rigaku (2015). CrystalStructure. Ver. 4.2. Rigaku Corporation, Tokyo, Japan.
45. G. M. Sheldrick, *Acta Crystallogr. Sect. C*, 2015, **71**, 3.
46. P. v. d. Sluis, A. L. Spek, *Acta Crystallogr. Sect. A*, 1990, 46, 194.
47. J. A. Organero, L. Tormo, A. Douhal, *Chem. Phys. Lett.,* 2002, **363**, 409.
48. Rigaku (2018). CrystalStructure. Version 4.3. Rigaku Corporation, Tokyo, Japan.
49. O. V. Dolomanov, L. J. Bourhis, R. J. Gildea, J. A. K. Howard and H. Puschmann, H. *J. Appl. Cryst.*, 2009, **42**, 339–341.
50. L. J. Bourhis, O. V. Dolomanov, R. J. Gildea, J. A. K. Howard and H. Puschmann, *Acta Crystallogr. Sect. A*, 2015, **71**, 59–75.
51. A. L. Spek, *Acta Crystallogr. Sect. D*, 2009, **65**, 148–155.
52. T.-T.-T. Nguyen, D. Türp, D. Wang, B. Nölscher, F. Laquai and K. Müllen, *J. Am. Chem. Soc.*, 2011, **133**, 11194–11204.
53. I. Hisaki, N. Ikenaka, N. Tohnai and M. Miyata, *Chem. Commun.*, 2016, **52**, 300–303.
54. I. Hisaki, Y. Suzuki, E. Gomez, B. Cohen, N. Tohnai and A. Douhal, *Angew. Chem. Int. Ed*., 2018, **47**, 1143–1146.
55. Gaussian 09, Revision D.01, M. J. Frisch, G. W. Trucks, H. B. Schlegel, G. E. Scuseria, M. A. Robb, J. R. Cheeseman, G. Scalmani, V. Barone, G. A. Petersson, H. Nakatsuji, X. Li, M. Caricato, A. Marenich, J. Bloino, B. G. Janesko, R. Gomperts, B. Mennucci, H. P. Hratchian, J. V. Ortiz, A. F. Izmaylov, J. L. Sonnenberg, D. Williams-Young, F. Ding, F. Lipparini, F. Egidi, J. Goings, B. Peng, A. Petrone, T. Henderson, D. Ranasinghe, V. G. Zakrzewski, J. Gao, N. Rega, G. Zheng, W. Liang, M. Hada, M. Ehara, K. Toyota, R. Fukuda, J. Hasegawa, M. Ishida, T. Nakajima, Y. Honda, O. Kitao, H. Nakai, T. Vreven, K. Throssell, J. A. Montgomery, Jr., J. E. Peralta, F. Ogliaro, M. Bearpark, J. J. Heyd, E. Brothers, K. N. Kudin, V. N. Staroverov, T. Keith, R. Kobayashi, J. Normand, K. Raghavachari, A. Rendell, J. C. Burant, S. S. Iyengar, J. Tomasi, M. Cossi, J. M. Millam, M. Klene, C. Adamo, R. Cammi, J. W. Ochterski, R. L. Martin, K. Morokuma, O. Farkas, J. B.

Foresman, and D. J. Fox, Gaussian, Inc., Wallingford CT, 2016.

56. M. J. Abraham, T. Murtola, R. Schulz, S. P´all, J. C. Smith, B. Hess and E Lindahl, *SoftwareX*, 2015, **1–2**, 19–25.
57. J. Wang, R. M. Wolf, J. W. Caldwell, P. A. Kollman and D. A. Case, *J. Comput. Chem*., 2004, **25**, 1157–1174.
58. C. I. Bayly, P. Cieplak, W. D. Cornell and P. A. Kollman, *J. Phys. Chem*., 1993, **97**, 10269–10280.
59. U. Essmann, L. Perera, M. L. Berkowitz, T. Darden, H. Lee and L. G. Pedersen, *J. Chem. Phys.*, 1995, **103**, 8577–8593.
60. D. van der Spoel and P. J. van Maaren, *J. Chem. Theory Comput*., 2006, **2**, 1–11.
61. R. W. Hockney, S. P. Goel and J. Eastwood. *J. Comp. Phys.*, 1974, **14**, 148–158.
62. G. Bussi, D. Donadio and M. Parrinello, *J. Chem. Phys.*, 2007, **126**, 014**-**101.
63. H. J. C. Berendsen, J. P. M. Postma, W. F. van Gunsteren, A. DiNola and J. R. Haak, *J. Chem. Phys.*, 1984, **81**, 3684–3690.
64. M. Parrinello and A. Rahman, *J. Appl. Phys.*, 1981, **52**, 7182–7190.
65. B. Hess, H. Bekker, H. J. C. Berendsen and J. G. M. Fraaije, *J. Comput. Chem.*, 1997, **18**, 1463–1472.

Chapter 3. HOFs constructed through different assemblies: shape-fitted docking of nonplanar π-conjugated cores and triaxially-woven of non-annulated planar cores

3.1 Introduction

As shown in section 1.7, the assemblies of hydrogen-bonded organic frameworks (HOFs) are crucially affected by less-directional and less-characteristic interactions such as van der Waals interaction. Therefore, it is still difficult to construct a porous HOF as it was designed. Curved, nonplanar, and cyclic π-conjugated molecules have been investigated intensively to date because of their exotic molecular structures and unusual optical and electronic properties[1–3]. These molecules also are attractive as building blocks for solid-state molecular assemblies possessing various functionality[4] because of their features, such as: a bowl-shaped or twisted system that can be stacked, reducing defects[5–7] and achieving high charge carrier conductivity[8]; the ability to make the bulk materials dynamic through structural and electronic changes of the π-system; and greater solubility of the nonplanar π-conjugated molecules in common organic solvents compared with the corresponding planar flat molecules, which allows for the study of different crystallization conditions[9].

These features prompted the construction of porous HOFs with nonplanar π-conjugated building block molecules. The hexaazatriphenylene (HAT) hexacarboxylic acid derivatives, which have a twisted conformation in crystalline states due to the packing force, provided significantly rigid HOFs through shape-fitted docking of the HAT cores (Chapter 2). In addition, a bowl-shaped sumanene derivative gave hydrogen bonded (H-bonded) network structures with undulated single and double layers[10]. In both cases, the nonplanarity of the molecules had a significant effect on the supramolecular structures and dynamic behavior of the resulting HOFs in contrast to the planar systems[11–13].

On the contrary, a 2D network constructed by networking planar building-block molecules (Figure 1a) assembles the low-dimensional network sheet with or without interpenetration. If the sheets stack without interpenetration, the resultant framework has a layered structure (Figure 1b), while the sheets assemble with interpenetration to give an interwoven framework, which in many cases, is a diaxially woven framework (Figure 1c)[14–17]. When a widely π-conjugated planar structure such as pyrene is applied as a core of the building-block molecules, layered frameworks are usually obtained due to favorable face-to-face π-stacking interactions between the cores. However, a small π-conjugated core makes interpenetration manners versatile. The resultant frameworks differ in geometrical and topological aspects, which crucially affect the stability and properties of the resultant crystalline reticular materials. Therefore, understanding and manipulating assemblies are important for the development of reticular chemistry. Although a handful of HOFs is composed of nonplanar π-conjugated molecules[18], such HOFs remain unexplored despite their interesting structures and properties.

The present study demonstrates that the twisted polycyclic aromatic hydrocarbon (PAH) dibenzo[*g*,*p*]chrysene (DBC) derivative **CPDBC** forms a porous HOF, in which the π-conjugated moieties

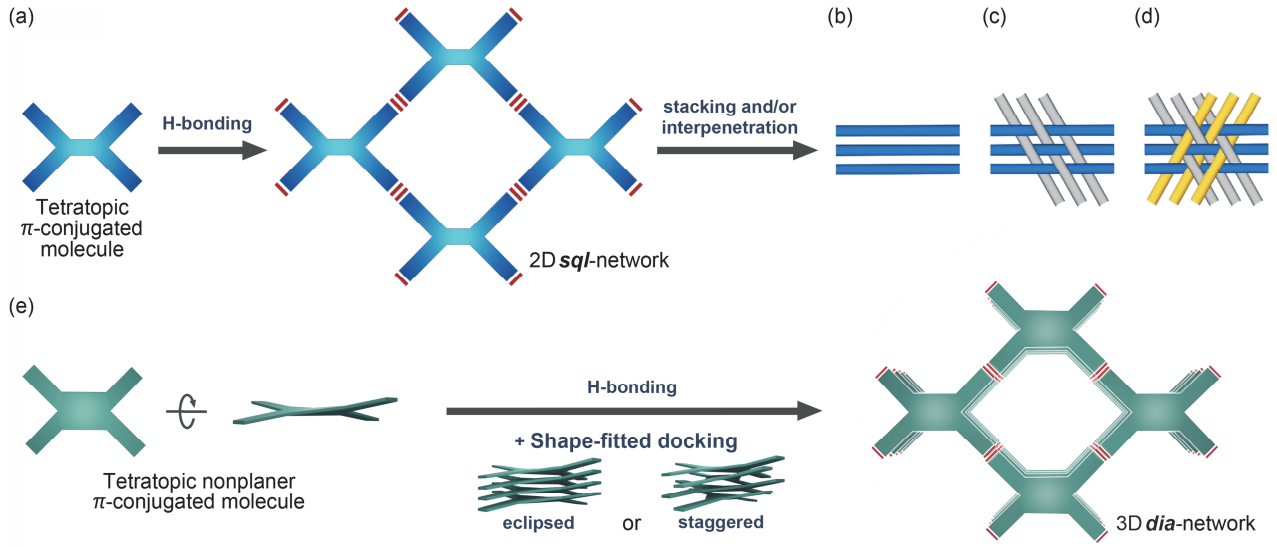

Figure 1. Hierarchical interpretation of the formation of (a) H-bonded 2D ***sql*** network by planar π-conjugated molecules and side views of assembling: (b) non-interpenetrated, (c) diaxially woven, and (d) triaxially-woven frameworks. (e) Hierarchical construction of the formation of 3D ***dia*** network by nonplanar π-conjugated molecules through H-bonding and shape-fitted docking (eclipsed or staggered).

are accumulated through shape-fitted docking. DBC, an annulated molecular structure of tetraphenylethene (TPE), has been applied to ambipolar charge transport in an amorphous solid state[19], and crystalline COF[8]. However, no examples of HOFs based on DBC have been reported. The **CPDBC** gave two types of frameworks (**CPDBC-1** and **CPDBC-2**) with eclipsed and staggered molecular orientations, respectively, although the latter was a ‘‘*disappeared crystal*’’[20].

As a comparison, the HOF construction was performed using **CBPE** with a TPE core, which is a planar, non-annulated molecule exhibiting aggregation-induced emission[21–26]. The HOF, **CBPE-1** formed an unexpected structure, triaxially-woven chicken wires (Figure 1d). This is, to the best of the author’s knowledge, the first example of porous triaxially-woven HOFs, although a handful of triaxially-woven 2D networks (Kagome networks) have been reported[27]. Dincă *et al*. reported that its analogous molecule, tetrakis(4-carboxyphenyl)ethene **CPE**, formed a non-interpenetrated HOF[28]. Based on the comparison with two TPE-based HOFs imply that a conformational disproportion of the outer phenylene rings of **CBPE** is one of the important factors for emergence of the present triaxially-woven framework. Although homotypic chicken wires can be derived based on the crystal engineering approach, their accumulation is expected to be difficult to control due to the lack of a broad π-conjugated plane.

The bulk crystalline **CPDBC-1** was successfully activated to give **CPDBC-1a** with a large BET surface area of 1548 $m^2 g^{-1}$ and moderate thermal stability. The photoconductivity of **CPDBC-1** and **CPDBC-1a** was also evaluated using a flash-photolysis time-resolved microwave conductivity (FP-TRMC) technique[29].

Activated HOF **CBPE-1a** exhibited thermal stability up to 220 °C and moderate permanent porosity with a BET surface area of 555 $m^2 g^{-1}$. From a perspective of solid-state fluorescence, **CBPE** is responsible for removing solvent molecules inside the HOFs and for mechanical stimulus (grinding).

While HOF construction sometimes yields unexpected porous structures, assembling based on shape-fitted docking achieves the structure as designed. The triaxially interwoven system contributed insight into

the development of another new type of functional porous organic material. Furthermore, shape-fitted docking is a well-understood and -controllable assembly and is a promising design principle for constructing a series of isostructural HOFs.

3.2 Synthesis and crystallization

1,1,2,2-Tetrakis(4-bromophenyl)ethylene (**1**) was synthesized from benzophenone, then Suzuki–Miyaura cross-coupling reaction of **1** and boronic acid **2** gave precursor **3**, following hydrolysis in KOH_{aq} to yield **CBPE**. These reactions were conducted according to ref 22. 2,7,10,15-Tetrabromodibenzo[*g*,*p*]chrysene (**4**) was synthesized by bromination of tetraphenylethene, followed by one-electron oxidation cyclization with DDQ, as reported previously[30,31]. SMC reaction of **4** and boronic ester **5** gave tetraphenyl DBC derivative **6**, which was subsequently hydrolyzed by KOH to give **CPDBC** (Scheme 1).

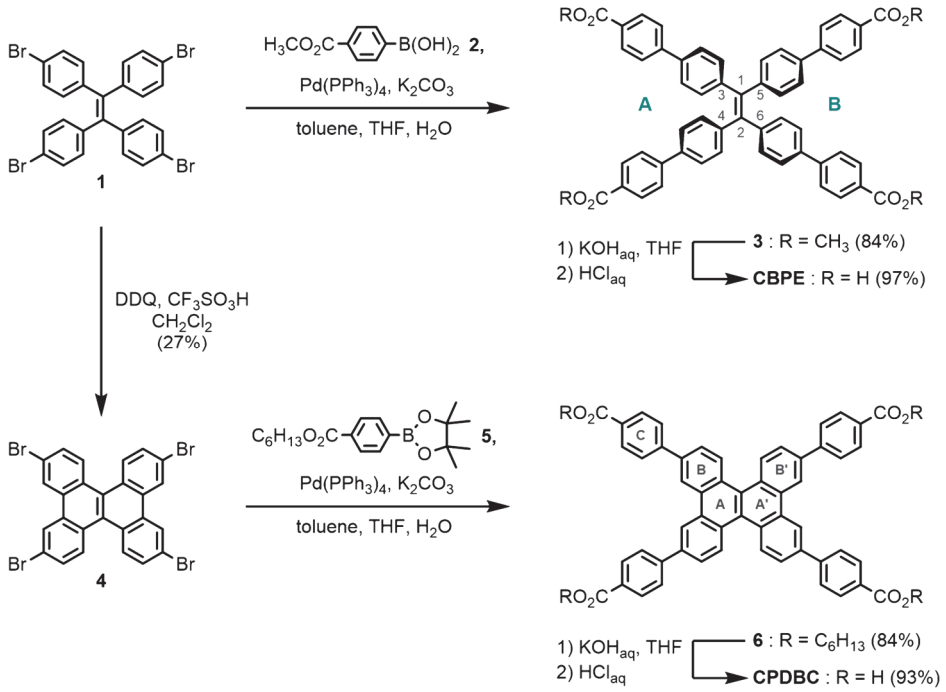

Scheme 1. Synthesis of **CBPE** and **CPDBC**. **CBPE** was synthesized according to literature[22].

Crystallization of **CBPE** and **CPDBC** was conducted by slow evaporation of a mixed solution of DMF and aromatic solvent [methyl benzoate (MeBz) or *N*,*N*-diethylaniline (DEAni), 5-*tert*-butyl-*m*-xylene (tBuXy)] at 80 °C, yielding hexagonal-shaped single crystals, **CBPE-1(MeBz)** and **CBPE-1(DEAni)**, and needle single crystal, **CPDBC-1** (Figure 2a–c). In contrast, only slow evaporation of a mixed solvent of DMF and 3-carene for 2 days at 80 °C gave a prism-shaped crystal, **CPDBC-2** (Figure 2d), in which the molecules were stacked in a different manner from **CPDBC-1**. Note that **CPDBC-2** was obtained only in several batches of viscous

liquid derived from the alteration of 3-carene, one of the terpenoids. Needle crystals **CPDBC-1** were yielded in all cases: crystallization with rapid volatilization at 80 °C before 3-carene altered, that at low temperatures (< 80 °C) where the solvent did not alter, that with solvent that inhibited the formation of H-bond, and that with a viscous polymer. **CPDBC-2** could not be replicated despite great effort. This type of crystal is known as a "*disappearing crystal*" [20], indicating that unknown and undefined factors exist that provide porous molecular crystals.

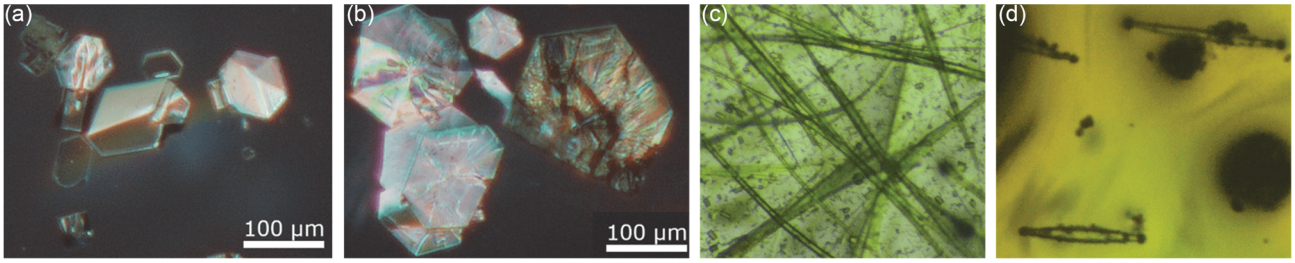

Figure 2. Polarized optical microscopy (POM) images of (a) **CBPE-1(MeBz)**, (b)**CBPE-1(DEAni)**, (c) **CPDBC-1**, and (d) **CPDBC-2** under daylight. Scale bar: 100 mm.

3.3 Crystallography

Although **CBPE-1(MeBz)** and **CBPE-1(DEAni)** crystallize in different space groups (*i.e.*, trigonal *P*321 and orthorhombic *C*222) due to size effects of the solvent molecule, both crystals have the isoreticular hydrogen-bonded framework. Therefore, only the crystal structure of **CBPE-1(MeBz)** is discussed in detail for simplicity, and then that of **CBPE-1(DeAni)** is briefly described.

The crystal structure of **CBPE-1(MeBz)** is shown in Figure 3a. Tetratopic **CBPE** forms an undulated chicken wire with periodicities of 25.2 Å along the *a* axis and 41.9 Å along the *c* axis though complementary hydrogen-bonded dimer formation of the carboxyl groups (Figure 3b). Interestingly, the chicken wires are triaxially-woven to give a porous HOF, which is well-explained by the topological illustration drawn with the ToposPro software (Figure 3c)[32]. **CBPE-1(MeBz)** exhibits voids I and II. Voids I and II are equal from the topological point of view, but the undulated network structure makes voids I form a 1D infinite channel and voids II a discrete small space (Figure 3d). Void I has the largest width of 9.3 Å and bottleneck with diameter of 3.6 Å. Void II, on the other hand, has dimensions of 7.1×8.1 Å. More strictly, voids I can be classed into two kinds of channels I' and I" with closely similar shapes, and in the same way voids II can be classified as II' and II". This complexity is brought about by the fact that three crystallographically independent molecules are contained in the crystal, and one of them solely constructs one chicken wire network, while two of them collectively form another network (Figure 4). The void fraction of the framework was calculated by PLATON[33,34] to be 27%. Solvent molecules are not solved due to sever disorder in the void spaces.

The crystal structure of **CBPE-1(DEAni)** is shown in Figure 5. It is a similar structure to **CBPE-1(MeBz)**, undulated chicken wire with periodicities of 25.2 Å along the *a* axis and 41.5 Å along the *c* axis though

complementary H-bonded dimer formation of the carboxyl groups (Figure 5b). **CBPE-1(DEAni)** exhibits voids I and II. Voids I and II are equal from the topological point of view, but the undulated network structure makes voids I form a 1D infinite channel and voids II a discrete small space (Figure 5c,d). Void I has the largest width of 9.9 Å and bottleneck with diameter of 3.7 Å. Void II, on the other hand, has dimensions of 7.1×8.1 Å. The void fraction of the framework was calculated by PLATON[33,34] to be 27%. Solvent molecules are not solved due to sever disorder in the void spaces.

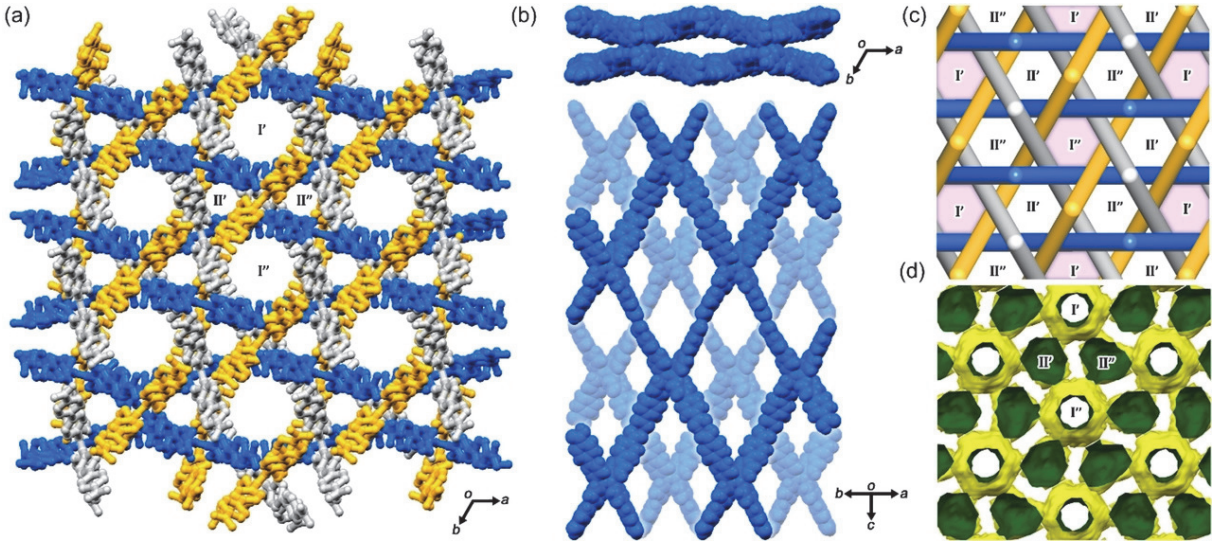

Figure 3. Crystal structure of triaxially-woven **CBPE-1(MeBz)**. (a) Packing diagram, in which layers with different orientation are classified by colors (orange, cyan, and gray). The large voids I and the small voids II are classified as I', I'' and II', II'', respectively, due to decreased crystal symmetry caused by three crystallographically independent molecules. (b) Neighboring 2D structural motifs (hydrogen-bonded chicken wires). (c) Schematic description of the hydrogen-bonded networks with ***wvm***-typed weave. (d) Visualized contact surface of void spaces viewed from the *c* axis (green: inside, yellow: outside).

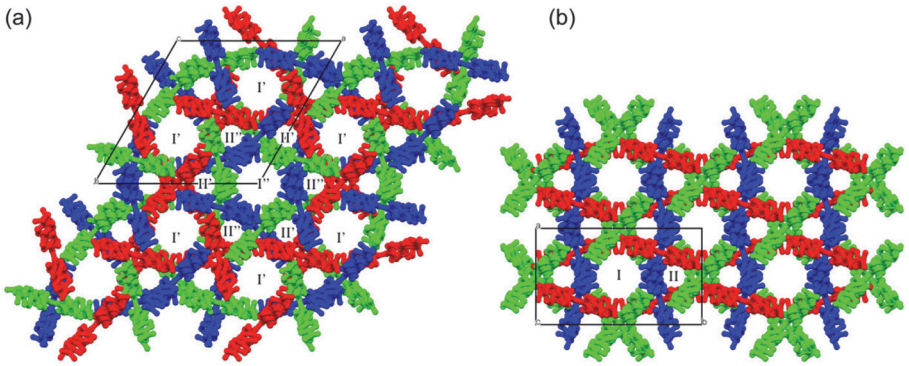

Figure 4. Packing diagrams (2 x 2 cells) of (a) **CBPE-1(MeBz)** and (b) **CBPE-1(DEAni)** with three symmetrically-independent molecules in different colors, where one chicken wire was composed of one identical red molecule, while the other two composed of two molecules (green and blue) in a mixed way.

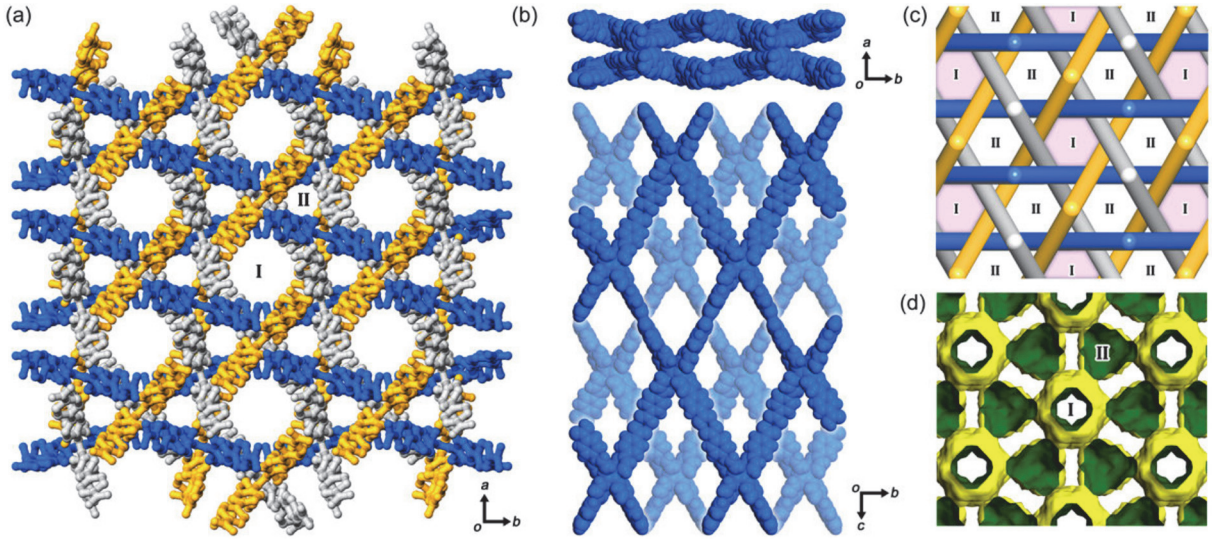

Figure 5. Crystal structure of triaxially-woven **CBPE-1(DEAni)**. (a) Packing diagram, in which layers with different orientation are classified by colors (orange, cyan, and gray). (b) Lower dimensional structural motif (H-bonded chicken wire). (c) Schematic description of the H-bonded networks with ***wvm***-typed weave. (d) Visualized contact surface of void spaces viewed from the *c* axis (green: inside, yellow: outside).

As already reported in the literature, **CPE** gives a non-interpenetrated layered assembly of hydrogen-bonded chicken wires, as shown in Figure 6. However, its expanded analogue **CBPE** was revealed to give a triaxially-woven framework (Figures 3 and 5). To disclose the origin of these differences, the author carefully considers the rotational conformation of the peripheral four phenylene and biphenylene arms in **CPE** and **CBPE**, respectively. Hereby, twist angles ω_{in} and ω_{out} are introduced, where ω_{in} is the dihedral angle between the inner phenylene ring bonded to the ethene moiety and the mean plane consisting of the ethene carbon atoms (C1, C2) and the aromatic carbon atoms (C3, C4, C5, C6) directly bonded to the ethene moiety, and ω_{out} the dihedral angle between the outer phenylene ring bonded to the carboxyl group and the mean plane defined above (Figure 7). The values of the twist angles ω_{in} and ω_{out} are listed in Table 1. These angles are closely related to the shapes of the voids and intercalation of the hydrogen-bonded networks (see below). In Figure 8a–c, partial structures of the molecules constructing barrel-shaped channels (void I') in **CBPE-1(MeBz)** and visualized surfaces of voids and channels are shown. The carboxybiphenyl groups form carboxyl dimers, which incline in the same way by approximately 30° to the *c* axis and surround the barrel-shaped channel in a helical fashion. The ω_{in} values of the biphenyl groups constituting a channel wall in the widest part (A) range from 47.7 to 61.1° (*av*. 54.6°). Similarly, the ω_{in} values of the biphenyl groups constituting a wall of the bottleneck part (B) range from 46.7 to 56.4° (*av*. 50.7°). These ω_{in} values are also closely similar to those in the crystal of **CPE** (46.7–53.4°). The ω_{out} values, on the other hand, are significantly disproportionate between biphenyl groups A and B, and range from 17.0 to 30.9° (*av*. 22.4°) in the case of A, and 67.0 to 81.1° (*av*. 75.6°) in the case of B. This tendency is the same in the case of **CBPE-1(DEAni)** (Table 1 and Figure 9). Therefore, disproportion of the twist angles of the outer phenylene rings plays a role in generating the undulated barrel-shaped channel surface and the present triaxially-woven framework. Additionally, Figure 8d,e shows selected arrangements of the phenylene rings at the widest part and the bottle neck of void I, which is composed of six phenylene rings

arranged with contact angles of 51.0–65.4° and 41.7–62.3°, respectively. Formation of the triaxially-woven framework is affected by crystallization solvents. When solvents with a molecular size larger than MeBz and DEAni, such as 1,3,5-trimethylbenzene, were applied for crystallization, no single crystals suitable for XRD analysis were obtained. Therefore, MeBz and DEAni act as good templates for formation of the triaxially-woven framework.

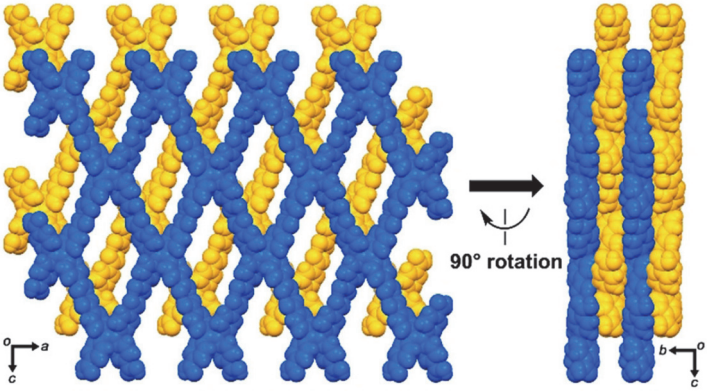

Figure 6. Crystal structure of **CPE** (RefCode: KASRIH) reported by Dincă *et al*[28]. **CPE** gives a non-interpenetrated layered framework. THF molecules in voids are omitted for clarity.

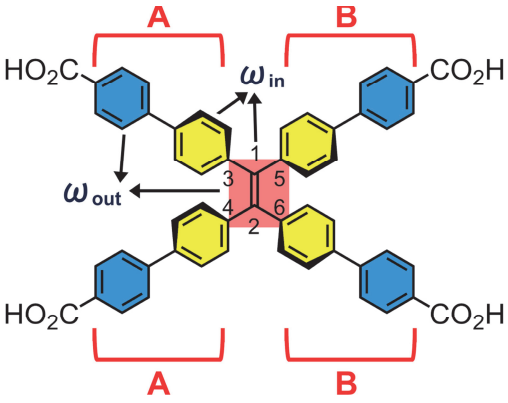

Figure 7. Definition of twisted angles ω_{in} and ω_{out}.

Table 1. Twist angles between peripheral phenylene rings and the central mean plane.

	Molecule	Biphenyl group	ω_{in} / °	ω_{out} / °
CBPE-1(MeBz)[a]	molecule 1	A	50.9, 61.0	17.0, 26.9
		B	53.4, 46.7	72.0, 79.6
	molecule 2	A	57.8, 61.6	25.0, 30.9
		B	47.2, 46.6	73.2, 67.0
	molecule 3	A	47.7, 48.9	17.9, 17.0
		B	56.4, 53.8	80.8, 81.1
	av[b]	A	54.6	22.4
		B	50.7	75.6
CBPE-1(DEAni)[c]	molecule 1	A	-60.45	-26.27
		B	-44.23	-73.83
	molecule 2	A	-49.84	-17.51
		B	-52.00	-79.39
	molecule 3	A	-48.83	-22.58
		B	-56.78	-79.02
	av[b]	A	-53.04	-22.12
		B	-51.00	-77.41
CPE	molecule	A	50.2, 53.4	—
		B	46.7, 49.4	—

[a] **CBPE-1(MeBz)** contains three crystallographically independent molecules. [b] Averaged value of molecules 1–3. [c] Each of three independent molecules has C_2-symmetric axis, and therefore, two arms in A or B are related by the symmetry operation.

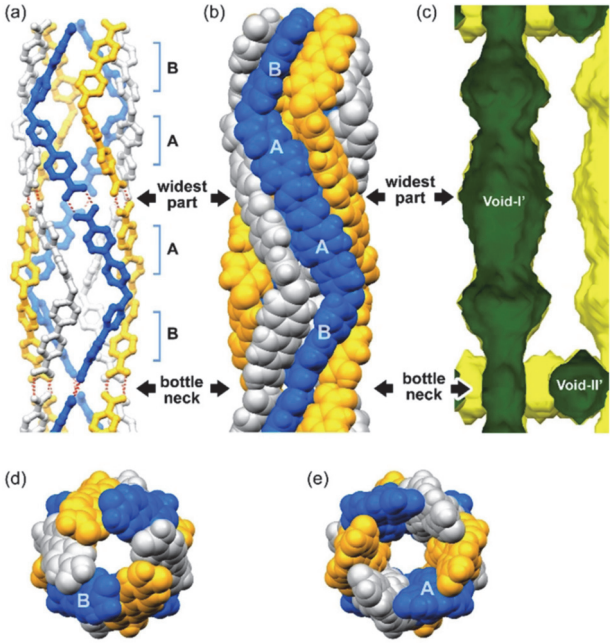

Figure 8. Barrel-shaped cylindrical channel of **CBPE-1(MeBz)** drawn as (a) ball-and-stick and (b) space-filling models, whereby only half parts of the molecules that participate in H-bonding to form the cylinder are shown for clarity. H-bonds between the carboxyl groups are shown with red dashed lines in (a). (c) Cross section of visualized surface of voids I and II viewed from the *a* axis (green: inside, yellow: outside). The widths of the barrel-shaped channels of void I at the widest and narrowest parts are 9.3 Å and 3.8 Å, respectively. Discrete Void-II is located near by the bottle neck part of the channel. Stacking ways of the aryl groups at (d) the narrowest and (e) the widest parts of the barrel-shaped void I.

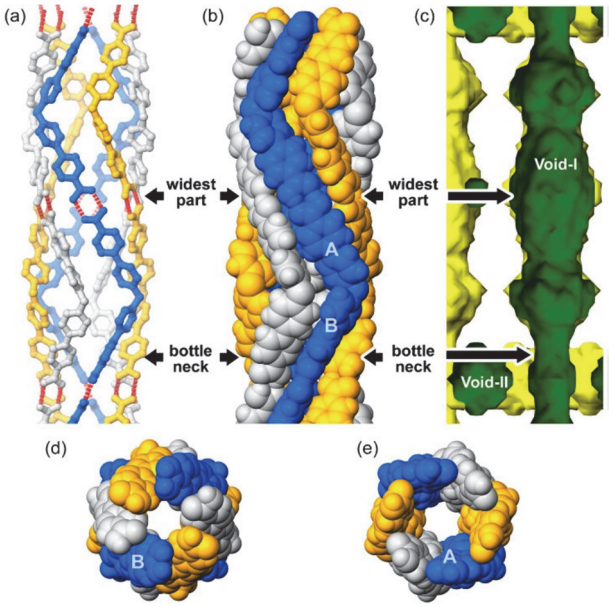

Figure 9. Barrel-shaped cylindrical channel of **CBPE-1(DEAni)** drawn as (a) ball-stick and (b) space-filling models, whereby only half parts of the molecules which participate in H-bonding to form cylinder are shown for clarity. H-bonds between the carboxy groups are shown with red dash lines in (a). (c) Cross section of visualized surface of voids I and II viewed from the *a* axis (green: inside, yellow: outside). The widths of barrel-shaped channel of Void-I at the widest and narrowest parts are 9.9 Å and 3.7 Å, respectively. Discrete Void-II is located near by the bottle neck part of the channel. Stacking ways of the aryl groups at (d) the narrowest and (e) the widest parts of the barrel-shaped void I.

CPDBC-1, belonging to the space group *Pnnn*, has a porous framework possessing one-dimensional (1D) channels (Figure 10a). The molecule has a twisted conformation with D_{2d} symmetry: dihedral angles between benzene rings (B)–(B') and (A)–(A') are 36.52° and 20.76°, respectively. Root mean square deviation (RMSD) of the DBC moiety is 0.680. The observed distortion is smaller than that of the theoretical structure calculated by the DFT method at B3LYP/6-31* level (Figure 11 and Table 2). The DBC cores are stacked in an eclipsed fashion with an intermolecular distance of 3.76 Å (Figure 10b). The peripheral phenylene group (C) is inclined to the ring (B) by 34.40°. The carboxy groups of **CPDBC** form complementary hydrogen-bonded dimers to yield a H-bonded network with ***dia***-topology. The network is interpenetrated 6-fold to give the entire framework (Figure 10d). The channel has a rhombic aperture with dimensions of 29.1 Å × 15.3 Å (Figure 10c). The surface of the channel is very smooth. The void ratio of the channel was 54.6% with a probe radius of 1.2 Å as determined by PLATON. Solvent molecules included in the channel were not solved crystallographically due to severe disorder.

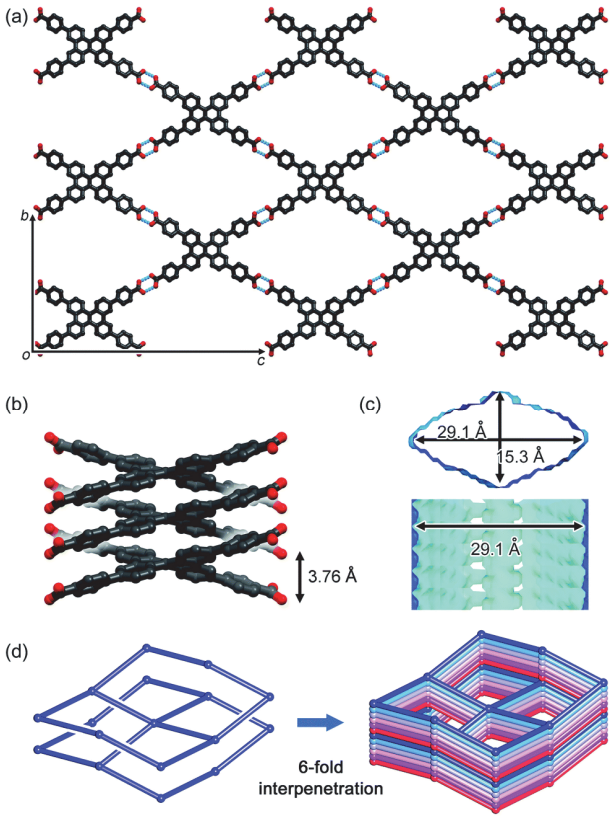

Figure 10. Crystal structure of **CPDBC-1**. (a) Packing diagram, (b) stacking manner, (c) visualized contact surface of the channel, and (d) topological description of the single and interpenetrated frameworks.

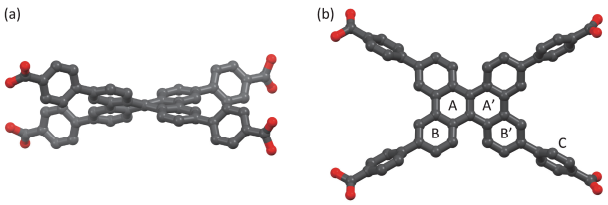

Figure 11. Optimized structure of **CPDBC** by the DFT method at the B3LYP/6-31G* level, viewed along (a) side and (b) top.

Table 2. Selected dihedral angles and RMSD in the optimized **CPDBC**.

Distortion	Dihedral angle / °
(A)-(A')	23.05
(B)-(B')	41.75
(A)-(B)	11.79
(A)-(B')	11.63
(B)-(C)	36.65
RMSD of DBC core	0.7842

The **CPDBC-2**, which belongs to the space group *I*41/*acd*, has a porous framework with 1D-channels (Figure 12a) and a square aperture with dimensions of 16.8 Å × 16.8 Å (Figure 12c). The DBC cores are stacked in a 90°-staggered fashion with an intermolecular distance of 3.71 Å (Figure 12b). The DBC molecules has a twisted conformation with D_{2d} symmetry: dihedral angles between benzene rings (B)–(B') and (A)–(A') are 35.96° and 21.78°, respectively, and the RMSD of the DBC moiety is 0.696. The distortion is also smaller than theoretical one but larger than that of **CPDBC-1**. The carboxy groups form a truncated dimer due to a frustrated geometric requirement of the framework. The open-ended hydroxyl groups presumably interact with solvent molecules through hydrogen bonds, although the solvent molecules could not be solved by crystallography. The H-bonded networks with ***dia***-topology are interpenetrated 6-fold to yield the entire framework (Figure 12d). The channel surface is relatively undulated compared to that of **CPDBC-1** (Figure 12c). The void ratio of the channel was determined by PLATON to be 48.0%, which is smaller than that of **CPDBC-1** because channel undulation creates inaccessible spaces for molecules.

Both of **CPDBC-1** and **CPDBC-2** are the HOFs through shape-fitted docking and their constituents stack in different way, eclipsed and staggered fashion, respectively. The above results indicated that it is possible to construct HOFs as designed through stacking the 3D networks of nonplanar π-conjugated molecules.

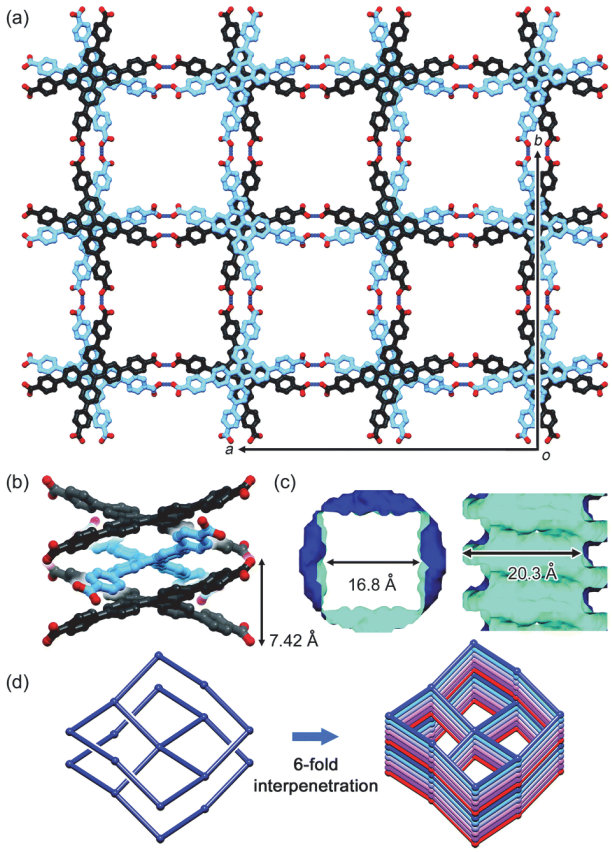

Figure 12. Crystal structure of **CPDBC-2**. (a) Packing diagram, (b) stacking manner, (c) visualized contact surface of the channel, and (d) topological description of the single and interpenetrated frameworks.

3.4 Thermal behaviors and durability

Thermogravimetric (TG) analysis of the as-formed crystalline bulk of **CBPE-1(MeBz)**, **CBPE-1(DEAni)**, and **CPDBC-1** were measured to investigate host/guest ratio. To conduct an evaluation of the material properties, easy-to-handle crystalline bulk of **CPDBC-1** was prepared successfully by slow evaporation of a mixed solution of DMF and methyl benzoate (MeBz) at 80 °C for 2 days (Figure 13). However, an adequate amount of pure **CPDBC-2** was not obtained. Therefore, only **CPDBC-1** was subjected to further evaluation. TG analysis of **CBPE-1(MeBz)** showed 20% weight loss below 200 °C (Figure 14), indicated that MeBz is included in the void with an approximate host/guest molar ratio of 1:1.5. ^{1}H NMR spectroscopy on the bulk material dissolved in DMSO-d_6 also supports this result (Figure 15). TGA of **CBPE-1(DEAni)** reached plateau at 260 °C with a 16% weight loss, which implies an approximate host/guest molar ratio of 1:1. These guest molecules occupy the pores about 70% and 65%, respectively, which are reasonable values (Figure 16).

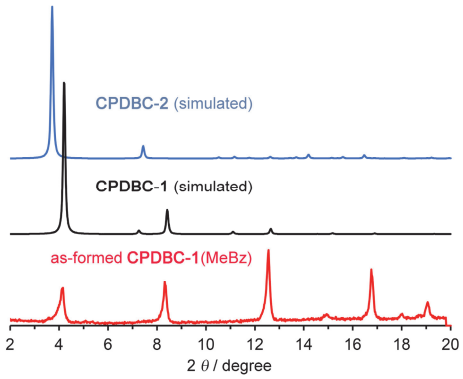

Figure 13. PXRD pattern of crystalline bulk of **CPDBC-1(MeBz)** obtained from a mixed solution of methyl benzoate and DMF, and the simulated patterns of **CPDBC-1** and **CPDBC-2** based on single crystalline X-ray diffraction data. The pattern of **CPDBC-1(MeBz)** is in good agreement with the simulated pattern of **CPDBC-1** obtained from a mixed solution of 5-*tert*-butyl-*m*-xylene and DMF.

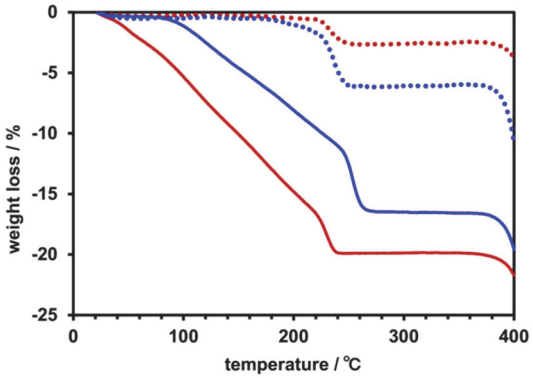

Figure 14. TG profiles of **CBPE-1(MeBz)** (red solid line), **CBPE-1(DEAni)** (blue solid line) and their activated forms (dash line with the corresponding colors).

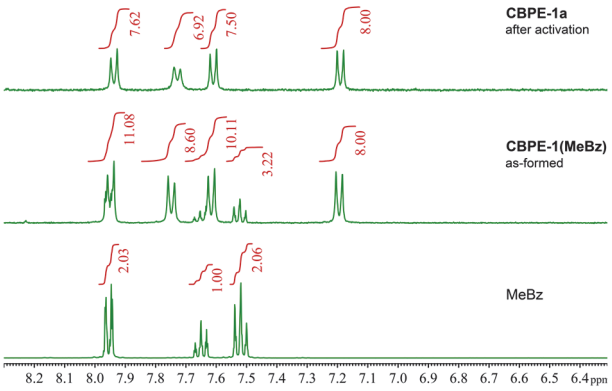

Figure 15. ^{1}H NMR (DMSO-d_6) spectra of MeBz, **CBPE-1(MeBz)**, and its activated forms.

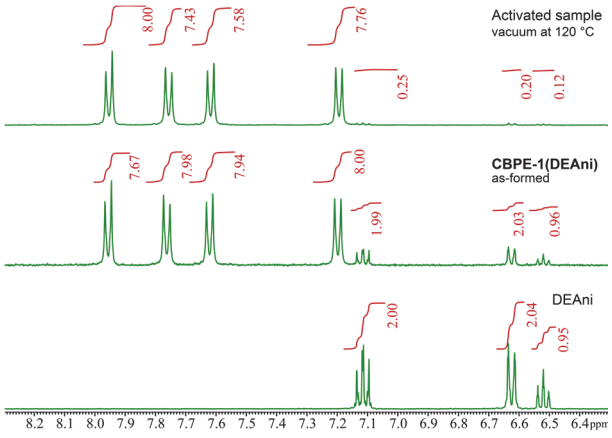

Figure 16. ^{1}H NMR (DMSO-d_6) spectra of DEAni, **CBPE-1(DEAni)**, and its activated samples dried under vacuum at 120 °C. The peaks of activated samples ascribable to the solvent molecules remain in the pores.

The crystalline bulk of as-formed **CPDBC-1** showed a two-step weight loss attributed to release of solvent molecules from the channel (Figure 17) in TG analysis. The first weight loss of 20% was observed up to approximately 70 °C, while the second, an additional 31%, was observed up to 160 °C. The total weight loss corresponds to a host/guest (CPDBC/MeBz) ratio of 1/6, which agrees well with the results from ^{1}H NMR spectroscopy (Figure 18). The first and second weight losses likely correspond to the release of MeBz molecules located in the middle of the channels and on the surface of the channels, respectively[36].

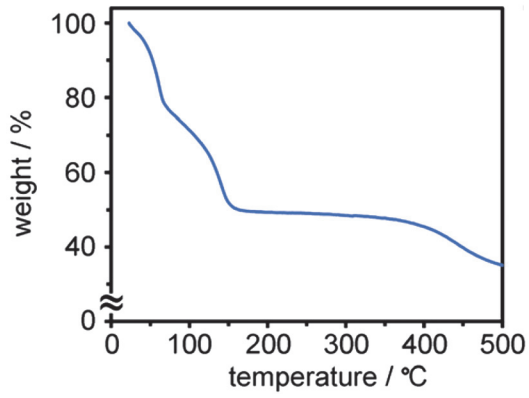

Figure 17. TG profile of **CPDBC-1**.

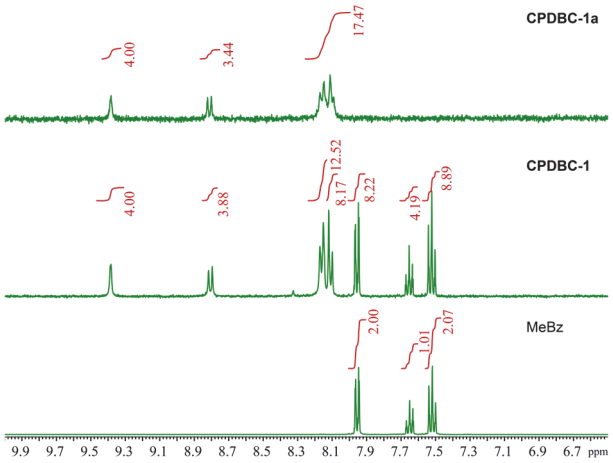

Figure 18. ^{1}H NMR (DMSO-d_6) spectra of MeBz, **CPDBC-1**, and its activated HOF **CPDBC-1a**.

Activation of **CBPE-1(MeBz)** was first attempted by heating the crystalline bulk at 120 °C under vacuum, which resulted in incomplete removal of the MeBz in the crystal. Consequently, activation of the HOF was accomplished by immersing it in diethyl ether at room temperature, followed by heating the resultant ether-included crystalline bulk at 60 °C under vacuum to give activated **CBPE-1a**. The complete removal of MeBz was confirmed by ^{1}H NMR spectroscopy (Figure 16). Retention of the original reticular framework was confirmed by PXRD analysis (Figure 19). TGA of **CBPE-1a**, activated crystalline bulk of **CBPE-1(MeBz)**, showed weight loss of approximately 2% around 200 °C, which is probably attributable to removal of water molecules encapsulated in discrete voids II with a 1:1 host/guest ratio. In the case of **CBPE-1(DEAni)**, activation failed due to the structural change of the framework (Figure 20), probably because the DEAni molecule is too large to pass through the bottleneck of the channel without collapse of the framework.

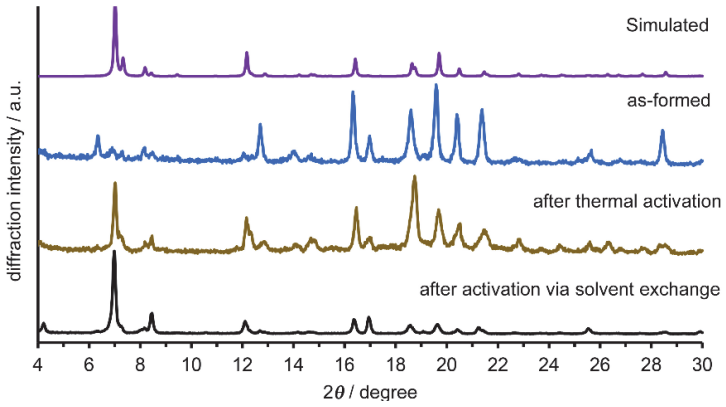

Figure 19. PXRD patterns of **CBPE-1(MeBz)** bulk crystals after attempting activation *via* simple heating under the vacuum condition and solvent exchanging followed by heating under the vacuum condition.

To evaluate the thermal stability of the activated HOF, **CBPE-1a** was subjected to VT-PXRD experiments (Figure 21). The original pattern was retained up to 220 °C, at which characteristic diffraction peaks such as that at 2θ = 6.98° suddenly disappeared. This result, combined with that of TGA, indicates that collapse of the framework and release of water molecules occurred simultaneously at this temperature. At temperatures higher than 220 °C, weak PXRD peaks appear in the wide-angle region, indicating that a crystalline phase still remains, although the precise structure was not explored.

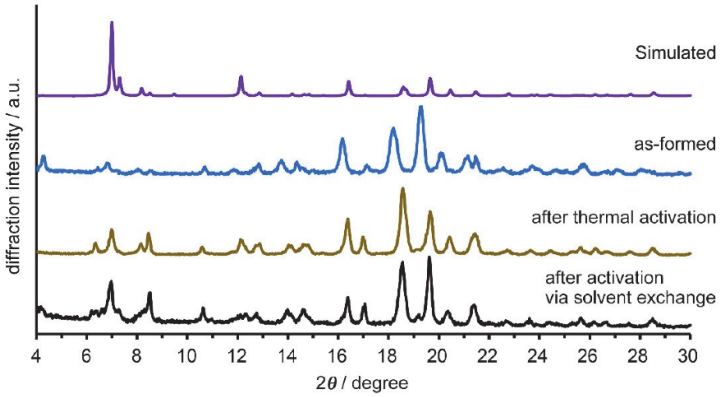

Figure 20. PXRD patterns of **CBPE-1(DEAni)** bulk crystals after attempting activation *via* simple heating under the vacuum condition and solvent exchanging followed by heating under the vacuum condition.

The activation of **CPDBC-1** was conducted by following methods: one is heating at 120 °C under vacuum (TV method) and another is immersing it in diethyl ether at room temperature, followed by heating the resultant ether-included crystalline bulk at 60 °C under vacuum (EV method). The activation of TV method succeeded in maintaining high crystallinity, but that of EV method resulted in less crystalline bulk (Figure 22). Hereafter, **CPDBC-1a** refers to a crystalline bulk activated by the TV method.

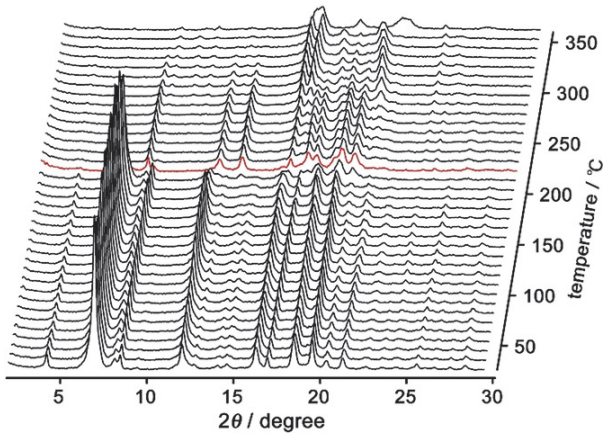

Figure 21. VT-PXRD patterns of **CBPE-1a** heated from room temperature to 360 °C. The red line shows a PXRD pattern of the collapsed structure at 220 °C.

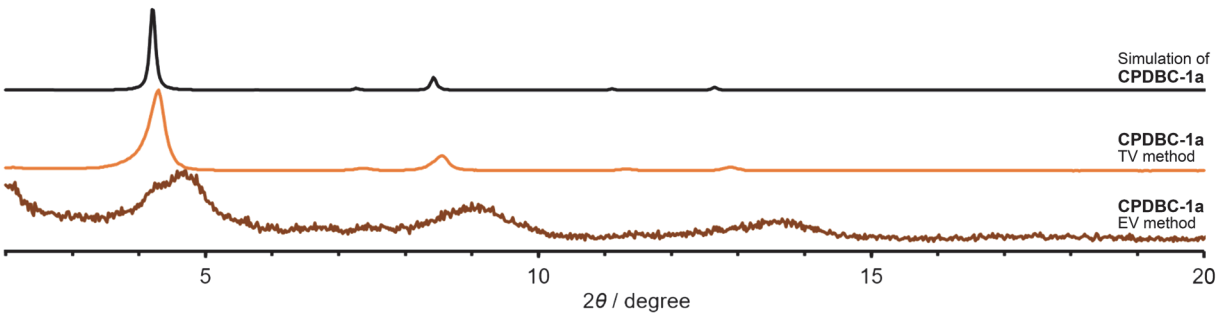

Figure 22. PXRD patterns of balk crystalline **CPDBC-1** activated by TV or EV methods.

To explore the structural changes of the framework upon release of the MeBz molecules from the pore, crystalline bulk of **CPDBC-1** was subjected to varied temperature (VT) PXRD experiments from room temperature to 360 °C under ambient atmosphere (Figure 23). Upon heating, the diffraction intensity increased due to vaporization of the solvent on the crystal surface and within the channel, which has been observed frequently for other HOFs[35,36]. The diffraction peaks of the as-formed **CPDBC-1** at 4.14°, 8.34°, 12.54°, and 16.74° corresponding to the (011), (022), (033), and (044) planes, respectively, shift into the wider angle region (4.48°, 9.02°, 13.56°, and 18.06°, respectively) at temperatures of 60 °C to 90 °C, and then back to positions similar to those of the as-formed framework at 115 °C. This wide-angle shift of the diffraction peaks occurred at the temperature corresponding to the first weight loss in the TG curve, indicating that the framework shrunk along the [011] direction, when solvent molecules with fewer interactions begin to be released from the pores in which the solvent molecules are densely packed (Figure 23 inset). Further release of the solvent resulted in recovery of the original framework to give activated HOF **CPDBC-1a**. Diffraction peak intensity remained in the range of 120 to 230 °C, then gradually decreased up to 280 °C, and decayed rapidly at higher temperatures (Figure 24).

Chemical stability of **CPDBC-1a** was also evaluated by immersing into *conc.* HCl_{aq} or $NaOH_{aq}$ with pH10, revealing that the HOF underwent structural transformation into unknown crystalline phase (Figure 25).

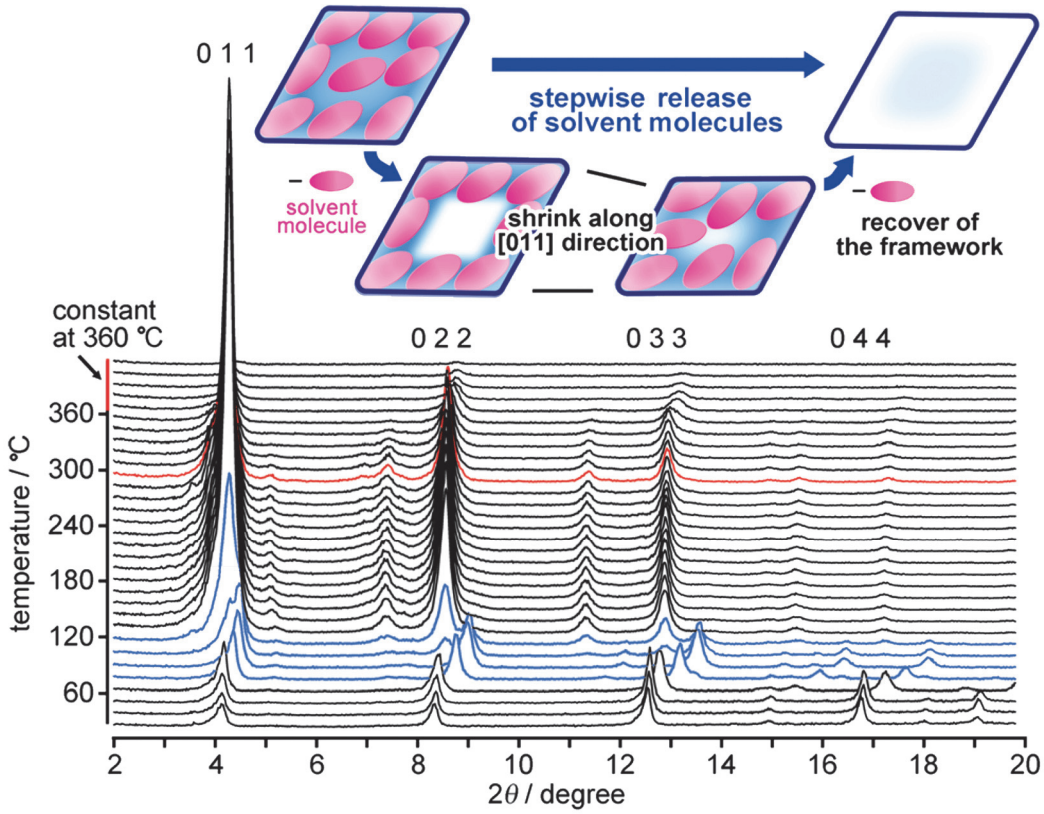

Figure 23. VT-PXRD patterns of **CPDBC-1**. (inset) Schematic representation of transient shrinkage of the framework along the [001] direction during release of solvent molecules from the pore.

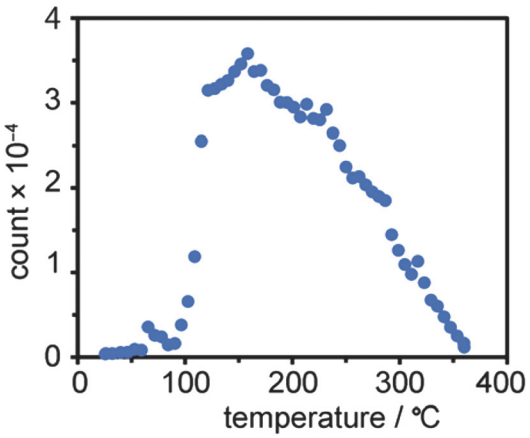

Figure 24. Changes in diffraction intensity of VT-PXRD in Figure 23 at 2θ = 4.14° corresponding to the (011) plane.

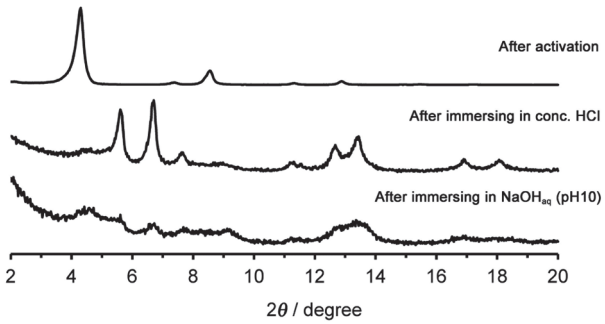

Figure 25. Chemical stability of **CPDBC-1a**. PXRD patterns of **CPDBC-1a** were recorded after immersing in *conc*. HCl and aqueous solution of NaOH (pH10) at rt for 24 h and then drying at 100 °C under vacuum condition. The resultant patterns are clearly different from the original ones, indicating structural transformation.

3.5 Solid state fluorescence behaviors

CPDBC-1 did not fluoresce in the solid state, but triaxially-woven structure with TPE core **CBPE-1** showed. Solid-state fluorescence and excitation spectra and quantum yields (Φ_F) of **CBPE-1(MeBz)**, **CBPE-1a**, and other related solid materials are shown in Figure 26 and Table 3. Upon activation, fluorescence band of **CBPE-1(MeBz)** at 485 nm was slightly blue-shifted by 8 nm (λ_{max} = 477 nm for **CBPE-1a**), and simultaneously, Φ_F was enlarged from 16.5% to 21.6%. The lowest energy band in the excitation spectrum was also blue-shifted by activation. Since the crystal structure of the framework was not changed upon activation judging from the PXRD patterns (Figure 27), the observed changes in fluorescence caused from disappearance of intermolecular interaction between the framework and solvent molecules (*i.e.,* MeBz). It should be mentioned that Omary and Zhou demonstrated that incorporation of the **CBPE** ligand into Zr-MOF (PCN-94) resulted in significant fluorescence blue shift and enhancement of the Φ_F value from 30.0% to 99.9%[22]. This observation, combined with the results, indicates that **CBPE** in the lattice of HOF **CBPE-1a** is not strictly rigidified but rather connected gently through H-bonding. A yellow amorphous solid **CBPE-amorph**, which was

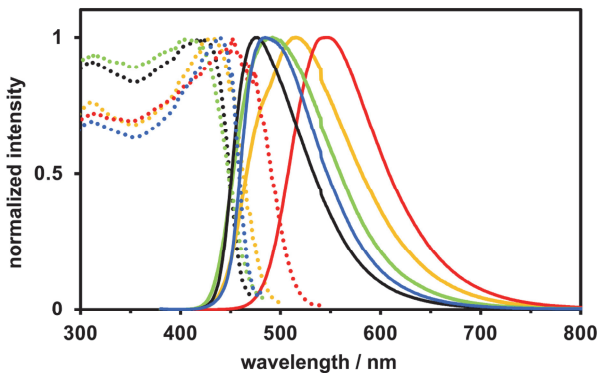

Figure 26. Solid state fluorescence (solid line) and excitation (dash line) spectra of (a) **CBPE-1(MeBz)** (light blue), **CBPE-1a** (black), **CBPE-amorph** (red), **CBPE-1ra(ether)** (yellow), and **CBPE-1ra(MeBz)** (light green).

formed by well-grinding of crystalline bulk of **CBPE-1a** with a mortal and muddler, exhibits fluorescence band at 547 nm, which is redshifted by 70 nm compared with **CBPE-1a**, and the enhanced Φ_F value of 55.5% (excited at 316 nm). These results are provided by loss of rotational flexibility of the aryl groups by denser packing of molecules due to collapse of the low-density porous framework. **CBPE-amorph** powder was then immersed in ether for 18 h at room temperature and in MeBz at 100 °C for 18 h, followed by reactivated with the same condition to get **CBPE-1a**, yielding regenerated empty HOFs **CBPE-1ra(ether)** and **CBPE-1ra(MeBz)**, respectively, with the same crystal structure as the original one. **CBPE-1ra(ether)** shows moderate crystallinity and exhibits fluorescence band at 516 nm and Φ_F of 34.3% (excited at 311 nm,). **CBPE-1ra(MeBz)** is relatively highly-crystalline and shows fluorescence band at 492 nm and Φ_F of 24.5% (excited at 314 nm). Although these values are not completely in agreement with those of the original **CBPE-1a** probably due to remaining amorphous phase, it is revealed that the framework can partly regenerate *via* immersing in solvents instead of recrystallization from a solution.

Table 3. Fluorescence property of **CBPE** in solid states.

	λ_{max} / nm	Φ_F [a]
CBPE-1(MeBz)	485	0.16 (313 nm)
CBPE-1a	477	0.21 (313 nm)
CBPE-amorph	547	0.55 (315 nm)
CBPE-1ra(ether)	516	0.34 (311 nm)
CBPE-1ra(MeBz)	492	0.24 (314 nm)

[a] Excitation wavelength in parentheses.

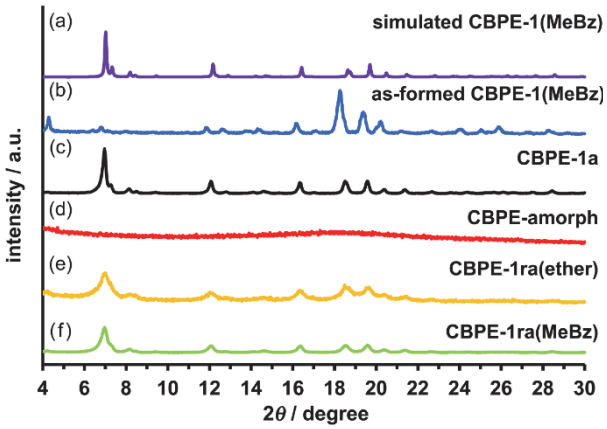

Figure 27. (a) Simulated and (b) experimantal PXRD patterns of **CBPE-1(MeBz)**, and (c–f) experiment patterns of **CBPE-1a**, **CBPE-amorph**, **CBPE-1ra(ether)**, and **CBPE-1ra(MeBz)**.

3.6 Photo-conductivity of **CPDBC-1**

The DBC is known as a structure that exhibits ambipolar charge transport property[8,19]. Crystalline powder of as-formed **CPDBC-1** and **CPDBC-1a** were subjected to flash-photolysis time-resolved microwave conductivity (FP-TRMC) measurements with excitation at 355 nm (Figure 28). The **CPDBC-1** showed a prompt rise within the time resolution upon photo-excitation, which was followed by a slow decay. **CPDBC-1a** exhibited a smaller signal than **CPDBC-1**, while the kinetics appeared very similar. The maximum values of $\varphi\Sigma\mu$ are 7.0×10^{-9} and 3.4×10^{-9} m^2 V^{-1} s^{-1}, for **CPDBC-1** and **CPDBC-1a**, respectively, where φ and $\Sigma\mu$ denote the yield of photogenerated charge carriers (quantum efficiency) and the sum of mobilities for negative and positive carriers, respectively. The observation of photoconductivity suggests a carrier transport path in the DBC-based HOF.

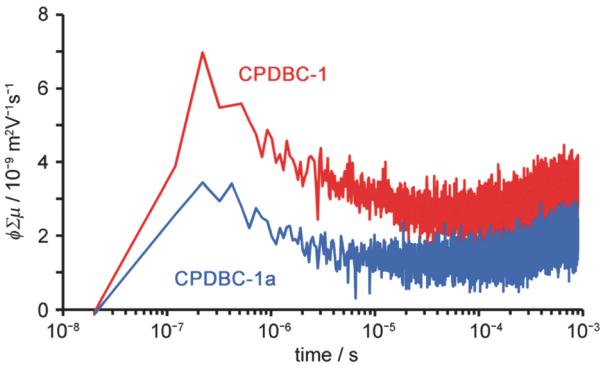

Figure 28. Photo-conductivity ($\varphi\Sigma\mu$) of as-formed **CPDBC-1** (red) and activated **CPDBC-1a** (blue) measured by FP-TRMC experiments.

3.7 Evaluation of porosity

Permanent porosity of **CBPE-1a**, **CBPE-amorph**, and **CBPE-1ra(ether)** was evaluated by CO_2 and N_2 sorption experiments at 195 K and 77 K, respectively (Figure 29 and Table 4). **CBPE-1a** showed type-I sorption isotherms for CO_2 and N_2 with both 5.73 mmol(STP) g^{-1} of uptakes, at $p_e/p_0 = 1$, indicating existence of micropore in the HOF. Hysteric behavior observed only in N_2 sorption can be explained by the fact that the bottle neck width of the channel (3.6 Å) is larger than kinetic diameter of CO_2 (3.30 Å), while comparable with that of N_2 (3.64 Å). Pore sizes were calculated by the non-local density functional theory (NLDFT) on the N_2 sorption isotherm at 77 K to be 6.8 Å for **CBPE-1a** and 6.4 Å for **CBPE-1ra(ether)**. BET specific surface area: $S_{A(BET)}$ of **CBPE-1a** was calculated to be 555 m^2 g^{-1} based on the CO_2 sorption experiment. In the case of **CBPE-amorph**, no N_2 uptake was observed, while CO_2 was absorbed up to 3.19 mmol(STP) g^{-1} with a hysteric profile. This observation indicates that the low-density framework was collapsed in the amorphous phase remaining only small irregular voids, in which CO_2 gas was absorbed due to electrostatic affinity of **CBPE** molecules toward a CO_2 molecule originated from its quadruple polar nature. In the case of partially recovered HOF **CBPE-1ra(ether)**, $S_{A(BET)}$ became smaller compared with **CBPE-1a**, which is consistent with fluorescence behaviors described above. After gas sorption experiments, crystallinity of the framework became lower (Figure 30).

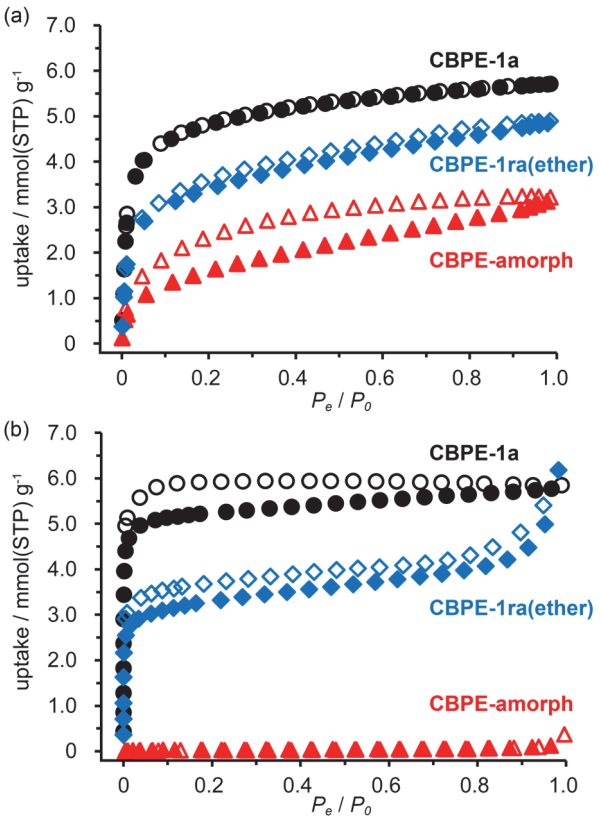

Figure 29. (a) CO_2 and (b) N_2 sorption isotherms of **CBPE** crystalline bulks (**CBPE-1a**, **CBPE-1ra(ether)**, and **CBPE-amorph**) at 195 K and 77K, respectively. Solid symbol: adsorption. Open symbol: desorption.

Table 4. Gas uptake and $S_{A(BET)}$ of **CBPE-1a**, **CBPE-amorph**, and **CBPE-1ra(ether)**.

	CBPE-1a	CBPE -amorph	CBPE -1ra(ether)
CO_2 uptake / mmol(STP) g^{-1}	5.73	3.19	4.89
N_2 uptake / mmol(STP) g^{-1}	5.73	0.0831 [b]	4.07 [b]
$S_{A(BET)}$ (CO_2) [a] / $m^2\,g^{-1}$	555	179	378
S_{ABET} (N_2) [a] / $m^2\,g^{-1}$	475	— [c]	284

[a] $S_{A(BET)}$ are based on CO_2 and N_2 sorption, respectively. [b] Gas uptake before beginning a surface sorption. [c] $S_{A(BET)}$ of **CBPE-amorph** was not able to calculate due to no N_2 adsorption.

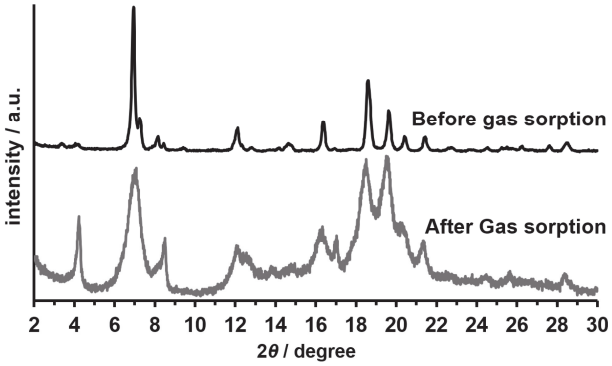

Figure 30. PXRD patterns of **CBPE-1a** before and after gas sorption experiments.

The activated HOF **CPDBC-1a** was subjected to N_2, O_2, CO_2, and H_2 gas sorption experiments at low temperature (77 K, 77 K, 195K, and 77 K, respectively) to evaluate its permanent porosity (Figure 31a). The $S_{A(BET)}$ (1548 $m^2\,g^{-1}$) was calculated based on N_2 sorption. A pore width of 1.34 nm was determined using the non-local density functional theory (NLDFT) (Figure 31b), which agrees well with that estimated from the crystal structure.

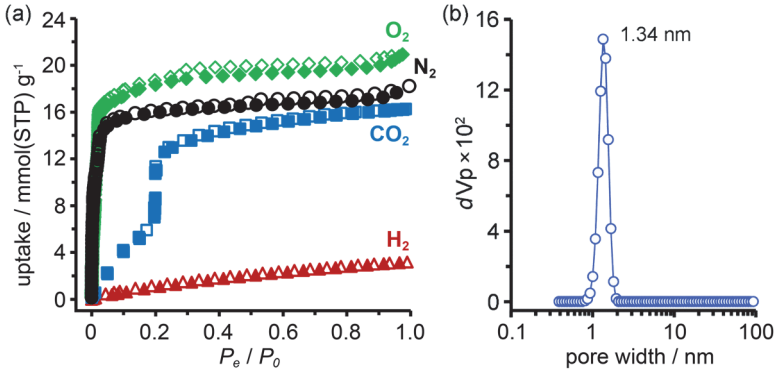

Figure 31. (a) Gas sorption isotherms and (b) NLDFT plot of **CPDBC-1a**. The isotherms were recorded at 77 K for N_2, O_2, and H_2 and at 195 K for CO_2. Solid and open symbols denote absorption and desorption processes, respectively.

3.8 Conclusion

In this study, the author demonstrates that tetratopic carboxylic acid with nonplanar π-conjugated core, dibenzo[*g*,*p*]chrysene (DBC) derivative **CPDBC**, and the one without π-conjugated core, tetraphenylethene derivative **CBPE** construct porous HOFs through different interactions.

The X-shaped tetratopic carboxylic acid, tetrakis(carboxybiphenyl)ethene derivative **CBPE** provides a porous HOF with ***wvm***-like topology constructed by triaxially-woven chicken wires, which is the first example to the author's best knowledge, in contrast to non-interpenetrated layered framework composed of tetrakis(carboxyphenyl)ethene **CPE**. The author thoroughly investigated rotational conformation of the peripheral phenylene rings and revealed that the present exotic frameworks are provided by disproportionate conformation of outer four phenylene rings in the peripheral biphenyl arms. The activated form **CBPE-1a** exhibits thermal stability up to 220 °C and the $S_{A(BET)}$ of 555 $m^2\ g^{-1}$. Moreover, the HOF shows mechanochromic behavior in terms of fluorescence color and quantum efficiency. CBPE in the framework shows a fluorescence band at 477 nm and quantum yield of 0.21, while that in amorphous solid show the band at 547 nm and the quantum yield of 0.55, indicating that **CBPE** in the lattice of HOF **CBPE-1a** is not strictly rigidified but rather connected gently through H-bonding.

Contrary, based on the shape-fitted docking strategy, hydrogen-bonded organic frameworks (HOFs) of a twisted polycyclic aromatic hydrocarbon, DBC derivative **CPDBC**, were constructed. The HOF **CPDBC-1**, in which molecules have eclipsed stacking, was activated successfully to give porous **CPDBC-1a** possessing moderate thermal stability up to 280 °C and a larger $S_{A(BET)}$ of 1548 $m^2\ g^{-1}$. An alternate framework **CPDBC-2**, in which molecules have staggered stacking, also was obtained, although this crystalline form is so-called a ''*disappeared crystal*''. Furthermore, **CPDBC-1** and **CPDBC-1a** showed photoconductivity, although the current was very small.

The derivative **CBPE** with TPE core gave triaxially-woven structure, which is not isostructural with the layered-assemble structure of **CPE**, a smaller analog. This is an example of the structural diversity of HOF. The achievement of ***wvm*** topological HOFs can provide an insight to vary and control the interpenetration manners and to construct a new, diverse type of functional porous organic materials with interwoven network structures.

Non-planar π-conjugated molecules, dibenzo[g,p]chrysene, formed a shape-fitted docking HOF. This assembled structure is promising to be developed into a new optoelectronic HOFs and a platform for isostructural construction of HOFs as well as HAT derivatives in Chapter 2.

3.9 Experimental section

All reagents and solvents were used as received from commercial suppliers. ^{1}H NMR spectra were measured by JEOL 400 YH (400 MHz) spectrometer. ^{13}C NMR spectra were measured by Bruker Avance III-400 spectrometers. Residual proton and carbon of deuterated solvents were used as internal standards for the measurements (for ^{1}H NMR, $CDCl_3$, δ = 7.26 ppm; DMSO-d_6, δ = 2.75 ppm: for ^{13}C NMR, $CDCl_3$, δ = 77.00 ppm; DMSO-d_6, δ = 29.76 ppm). Thermal gravimetric (TG) analysis was performed on Rigaku TG8120 under an N_2 purge (100 mL min^{-1}) at a heating rate of 5 °C min^{-1}.

3.9.1 Synthesis of **CPDBC**

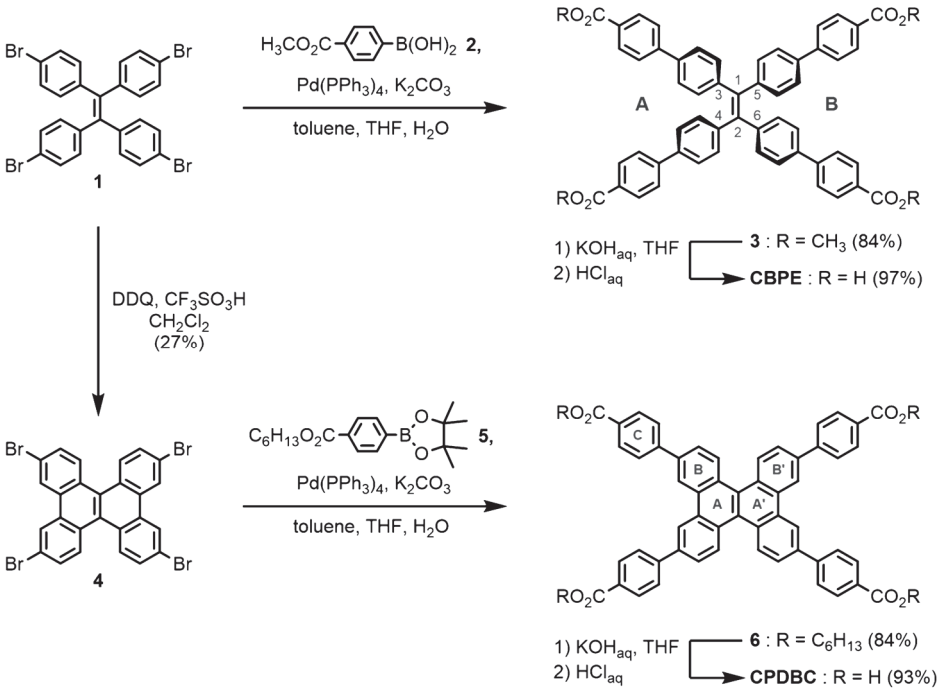

CBPE was synthesized according to literature[22]. 2,7,10,15-Tetrabromodibenzo[*g*,*p*]chrysene (**4**) was synthesized by bromination of tetraphenylethene, followed by the one-electron oxidation cyclization with DDQ, as reported in literature[30,31].

Synthesis of ester precursor 6. A suspension of tetrabromochrysene **4** (1.47 g, 2.29 mmol), boronic acid pinacol ester **5**, K_2CO_3 (3.00 g, 21.7 mmol), and $Pd(PPh_3)_4$ (0.577 g, 0.500 mmol) in a deoxygenated toluene (30 mL), dioxane (70 mL), and H_2O (8 mL) was stirred for 48 h at 110 °C. The solvent was removed in vacuum. To the residual reaction mixture methanol (50 mL) and water (50 mL) were added, followed by being sonicated. The precipitate was filtered by a filter paper and carefully rinsed with water and methanol. The product was purified by reprecipitation with $CHCl_3$ and acetone, followed by passing through a bet of silica gel with $CHCl_3$ to give **3** (917 mg, 0.801 mmol) in 35% yield as yellow solid.

M.p. 179 °C. ^{1}H NMR (400 MHz, $CDCl_3$) : δ 8.11 (d, 2H, J = 8.8 Hz) , 7.70 (d, 2H, J = 8.0 Hz) , 7.63 (d, 2H, J = 7.2 Hz) , 7.50 (d, 2H, J = 7.2 Hz), 4.34 (t, 2H, J = 6.8 Hz), 1.74–1.84 (m, 2H), 1.30– 1.52 (m, 6H), 0.941 (t,

2H, *J* = 7.6 Hz) ppm. ^{13}C NMR (100 MHz, $CDCl_3$): *δ* 166.27, 144.43, 137.45, 130.60, 130.10, 129.50, 128.86, 128.30, 127.02, 126.82, 125.28, 121.59, 65.20, 31.49, 28.73, 25.70, 22.56, 14.00 ppm. HR-MS (FAB+): calcd. For $C_{78}H_{80}O_8$ $[M]^+$ 1144.5853; found: 1144.5847.

Hydrolysis of 6. Hexyl ester derivative **6** (340 mg, 297 μmol) in THF (25 mL) and 5% aqueous solution of KOH (30 mL) was stirred for 48 h at 80 °C. After removing THF in *vaccuo*, 3M-HCl was added till further precipitate did not form. The precipitate was collected by centrifuge and washed with water, methanol, and acetone, and dried to give **CPDBC** (248 mg, 283 μmol) in 95% yield as a yellow solid.
M.p: >300 °C. ^{1}H NMR (400 MHz, DMSO-*d*$_6$) : *δ* 9.02 (s, 4H), 8.23 (d, 4H, *J* = 8.4 Hz) , 8.04 (d, 8H, *J* = 8.4 Hz) , 7.94 (d, 8H, *J* = 8.4 Hz) , 7.73 (d, 4H, *J* = 8.4 Hz) ppm. ^{13}C NMR (100 MHz, DMSO-*d*$_6$): *δ* 167.18, 143.71, 137.11, 130.52, 129.81, 129.76, 128.62, 127.68, 127.25, 126.45, 125.55, 122.07 ppm. HR-MS (FD^+): *calcd.* For $C_{54}H_{32}O_8$ $[M]^+$ 808.2097; found: 808.2092

3.9.2 X-ray diffraction measurements

Powder X-ray diffraction (PXRD) data were collected on a Rigaku Ultima-IV (40 kV, 44 mA) using graphite-monochromatized Cu-Kα radiation (λ = 1.54187 Å) at room temperature. A scan rate is 2.0° min^{-1} .

Single crystal Xray measurement and analysis. Diffraction data of **CBPE-1(MeBz)** was collected on a two-dimensional X-ray detectors (PILATUS 200K/R) equipped in Rigaku XtaLAB P200 diffractometer using multi-layer mirror monochromated Cu-Kα radiation (λ = 1.54187 Å). Diffraction data of **CPDBC-1** and **CBPE-1(DEAni)** was collected at SPring-8 (BL02B1) with monochromated synchrotron radiation (λ = 0.42860 Å) and **CPDBC-2** was collected at SPring-8 (BL40XU) with synchrotron radiation (λ = 0.81106 Å). The cell refinements were performed with software RapidAuto or CrysAlisPro. SHELXT[37] were used for the structure solution of the crystals. All calculations were performed with the observed reflections [I > 2σ(I)] with the program CrystalStructure[38] or OLEX2 crystallographic software[39,40]. Structural refinement was performed by SHELXL[41]. All non-hydrogen atoms except for highly disordered solvent molecules accommodated in voids were refined with anisotropic displacement parameters, and hydrogen atoms were placed in idealized positions and refined as rigid atoms with the relative isotropic displacement parameters. SQUEEZE function equipped in the PLATON program was used to remove severely disordered solvent molecules in voids[34,35].

Table 5. Crystal data of **CBPE-1(MeBz)**, **CBPE-1(DEAni)**, **CPDBC-1**, and **CPDBC-2**.

	CBPE-1(MeBz)	**CBPE-1(DEAni)**	**CPDBC-1**	**CPDBC-2**
System	*trigonal*	*orthogonal*	*orthogonal*	*orthogonal*
Space group	*P*321	*C*222	*Pnnn*	*I*41/*acd*
Formula	$C_{114}H_{108}O_{24}$	$C_{114}H_{108}O_{24}$	$C_{54}H_{32}O_8$	$C_{54}H_{32}O_8$
Formula weight	1802.094	1802.094	808.80	808.80
a / Å	25.1707(5)	14.610(7)	3.7618(5)	45.5006(10)
b / Å	25.1707(5)	25.205(13)	24.323(3)	45.5006(10)
c / Å	41.8989(7)	41.523(10)	42.416(6)	7.4170(2)
α / °	90	90	90	90
β / °	90	90	90	90
γ / °	120	90	90	90
V / Å^3	22989.2(10)	15291(12)	3789.5(9)	3789.5(9)
Z	18	12	2	8
D / g cm^{-3}	1.057	1.059	0.709	0.661
Crystal size / mm	0.1 × 0.1 × 0.1	0.07 × 0.04 × 0.02	0.5 × 0.03 × 0.03	0.1 × 0.02 × 0.02
Crystal color	yellow	yellow	yellow	yellow
R_1 (I > 2.0σ(*I*))	0.1431	0.1017	0.0763	0.0917
wR_2 (all)	0.3679	0.2841	0.2556	0.2920
Completeness	0.999	1.000	0.999	0.950
Goodness of fit	1.174	1.047	1.010	1.053
λ / Å	1.54187 (Cu-*Kα*)	0.42860 (synchrotron)	0.42860 (synchrotron)	0.81106 (synchrotron)
T / K	93	93	93	93
CCDC nos.	2005567	2005568	2027309	2027310

3.9.3 VT-PXRD measurement

Crystalline bulk of **CPDBC-1** and **CBPE-1(MeBz)** placed on an aluminium substrate was subjected to VT-PXRD measurement under the air atmosphere. PXRD data were collected on a Rigaku Ultima-IV using graphite-monochromatized Cu-*Kα* radiation with a temperature control unit. Temperature of the sample was increased from room temperature to 633 °C with a rate of 1.0 °C min^{-1}. During temperature increasing, XRD patterns ranged from 2° to 19.8° for **CPDBC-1** and 2.0° to 29.5° for **CBPE-1(MeBz)** was repeatedly recorded with a scan rate of 3° min^{-1}. Therefore, each PXRD scan has a temperature width of ca. 6.0 °C and 9.3 °C, respectively.

3.9.4 Flash-photolysis time-resolved microwave conductivity (FP-TRMC)

TRMC was performed for the powder samples placed on an adhesive tape on a quartz substrate. The microwave frequency and its power were ~9 GHz and ~3 mW, respectively. The third harmonic generation (355 nm) of a Nd:YAG laser (Continuum Inc., Surelite II, 5–8 ns pulse duration, 10 Hz) was used for the excitation (incident photon density I_0 = 9.1 × 10^{15} photons cm^{-2} $pulse^{-1}$). The photoconductivity ($\Delta\sigma = A^{-1}$ ΔP_r $P_r{}^{-1}$ where A is the sensitivity factor, P_r is the reflected microwave power, and ΔP_r is the change in *P*r upon exposure to light) was converted into the product of the quantum yield (φ) and sum of the charge carrier mobilities $\Sigma\mu$ ($= \mu_+ + \mu_-$) using the relationship $\varphi\Sigma\mu = \Delta\sigma(eI_0F_{light})^{-1}$, where *e* and F_{Light} are the electron charge and correction (or filling) factor, respectively. The experiments were performed at room temperature in the air.

3.9.5 Solid state fluorescence behaviors

Fluorescence and excitation spectra were measured on JASCO FP-8500 spectrofluorometer. Fluorescence quantum yields were determined on the spectrofluorometer equipping ISF-834 integrating sphere. **CBPE-1a** grinded uniformly in a mortar for several minutes to yield **CBPE-amorph**. After immersing **CBPE-amorph** in ether at rt for 24h, and in methyl benzoate at 100 °C for 24 h, the guest replaced with ether and then removed under vacuum at 60 °C to obtain **CBPE-1ra(ether)** and **CBPE-1ra(MeBz)**, respectively.

3.9.6 Sorption/desorption experiments

Gas sorption measurements of **CBPE-1a**, **CBPE-amorph**, and **CBPE-1ra(ether)** were performed on BELSORP-max (BEL, Japan). The adsorption isotherms of N_2 and CO_2 were corrected at 77K and 195 K, respectively. That on activated HOF **CPDBC-1a** were performed for N_2, O_2, CO_2, and H_2, which were corrected at 77K, 77 K, 195 K and 77 K, respectively. NLDFT was conducted based on N_2 isotherms (Figures 31b and 32). The $S_{A(BET)}$ were calculated based on N_2 isotherms (Figures 33 and 34).

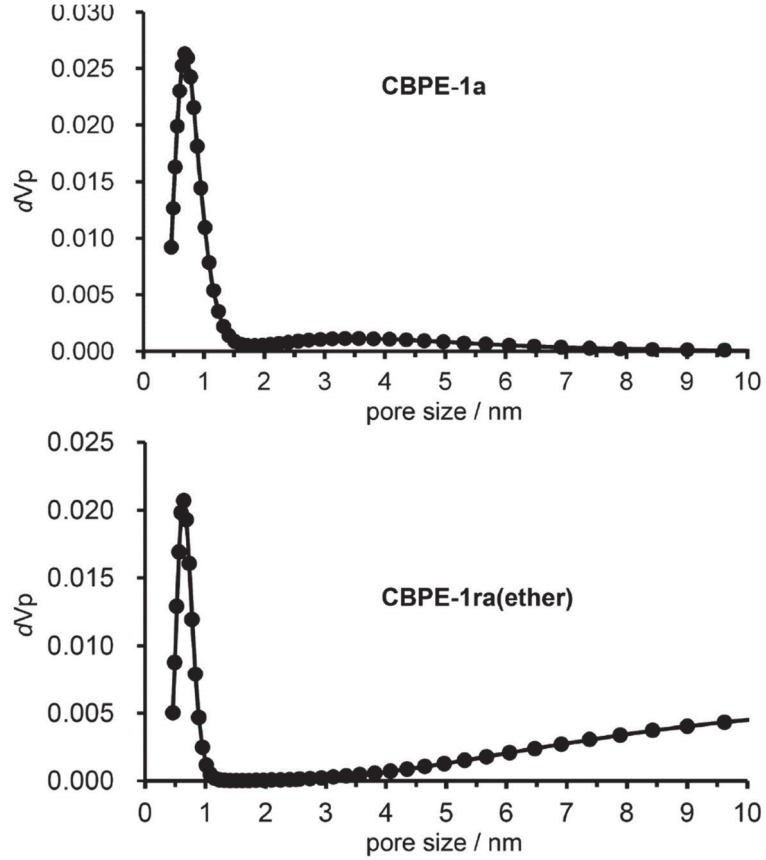

Figure 32. Pore size distribution **CBPE-1a** and **CBEP-1ra(ether)** from NLDFT.

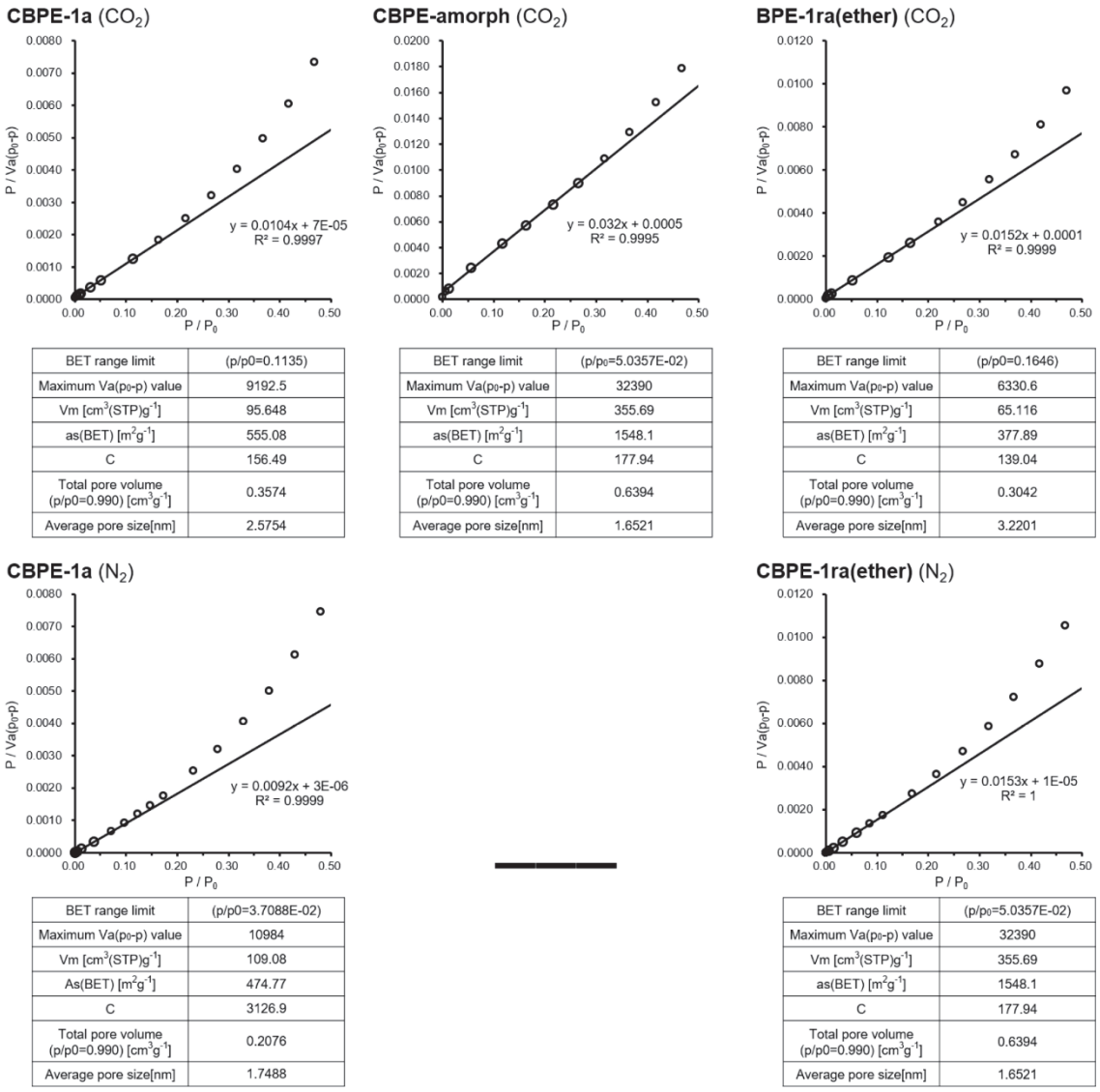

BET range limit	(p/p0=0.1135)
Maximum Va(p_0-p) value	9192.5
Vm [$cm^3(STP)g^{-1}$]	95.648
as(BET) [m^2g^{-1}]	555.08
C	156.49
Total pore volume (p/p0=0.990) [cm^3g^{-1}]	0.3574
Average pore size[nm]	2.5754

BET range limit	(p/p_0=5.0357E-02)
Maximum Va(p_0-p) value	32390
Vm [$cm^3(STP)g^{-1}$]	355.69
as(BET) [m^2g^{-1}]	1548.1
C	177.94
Total pore volume (p/p0=0.990) [cm^3g^{-1}]	0.6394
Average pore size[nm]	1.6521

BET range limit	(p/p0=0.1646)
Maximum Va(p_0-p) value	6330.6
Vm [$cm^3(STP)g^{-1}$]	65.116
as(BET) [m^2g^{-1}]	377.89
C	139.04
Total pore volume (p/p0=0.990) [cm^3g^{-1}]	0.3042
Average pore size[nm]	3.2201

BET range limit	(p/p0=3.7088E-02)
Maximum Va(p_0-p) value	10984
Vm [$cm^3(STP)g^{-1}$]	109.08
As(BET) [m^2g^{-1}]	474.77
C	3126.9
Total pore volume (p/p0=0.990) [cm^3g^{-1}]	0.2076
Average pore size[nm]	1.7488

BET range limit	(p/p_0=5.0357E-02)
Maximum Va(p_0-p) value	32390
Vm [$cm^3(STP)g^{-1}$]	355.69
as(BET) [m^2g^{-1}]	1548.1
C	177.94
Total pore volume (p/p0=0.990) [cm^3g^{-1}]	0.6394
Average pore size[nm]	1.6521

Figure 33. BET surface area analysis of **CBPE-1a**, **CBPE-amorph**, and **CBEP-1ra(ether)**.

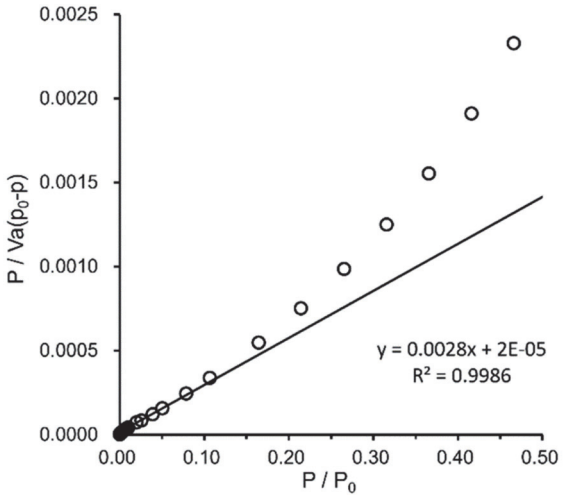

BET range limit	(p/p_0=5.0357E-02)
Maximum Va(p_0-p) value	32390
Vm [$cm^3(STP)g^{-1}$]	355.69
as(BET) [m^2g^{-1}]	1548.1
C	177.94
Total pore volume (p/p0=0.990) [cm^3g^{-1}]	0.6394
Average pore size [nm]	1.6521

Figure 34. BET surface area analysis of **CPDBC-1a**.

3.10 References

1. M. Saito, H. Shinokubo and H. Sakurai, *Mater. Chem. Front.*, 2018, **2**, 635–661.
2. Y. Segawa, D. R. Levine and K. Itami, *Acc. Chem. Res.*, 2019, **52**, 2760–2767.
3. R. Kumar, H. Aggarwal and A. Srivastava, *Chem. Eur. J*., 2020, **26**, 10653–10675.
4. J. B. Lin, E. R. Darzi, R. Jasti, I. Yavuz and K. N. Kouk, *J. Am. Chem. Soc.*, 2019, **141**, 952–960.
5. T. Amaya, S. Seki, T. Moriuhi, K. Nakamoto, T. Nakata, H. Sakane, A. Saeki, S. Tagawa and T. Hirao, *J. Am. Chem. Soc*., 2009, **131**, 408–409.
6. A. Wakamiya, H. Nishimura, T. Fukushima, F. Suzuki, A. Saeki, S. Seki, I. Osaka, T. Sasamori, M. Murata, Y. Murata and H. Kaji, *Angew. Chem. Int. Ed.*, 2014, **53**, 5800–5804.
7. Chaolumen, M. Murata, A. Wakamiya and Y. Murata, *Angew. Chem. Int. Ed.*, 2017, **56**, 5082–5086.
8. N. Keller, T. Sick, N. N. Bach, A. Koszalkowski, J. M. Rotter, D. D. Medina and T. Bein, *Nanoscale*, 2019, **11**, 23338–23345.
9. K. Kawasumi, Q. Zhang, Y. Segawa, L. T. Scott and K. Itami, *Nat. Chem.*, 2013, **5**, 739–744.
10. I. Hisaki, H. Toda, H. Sato, N. Tohnai and H. Sakurai, *Angew. Chem. Int. Ed.*, 2017, **56**, 15294–15298.
11. I. Hisaki, S. Nakagawa, N. Ikenaka, Y. Imamura, M. Katouda, M. Tashiro, H. Tsuchida, T. Ogoshi, H. Sato, N. Tohnai and M. Miyata, *J. Am. Chem. Soc.*, 2016, **138**, 6617–6628.
12. I. Hisaki, N. Ikenaka, N. Tohnai and M. Miyata, *Chem. Commun.*, 2016, **52**, 300–303.
13. I. Hisaki, Y. Suzuki, E. Gomez, Q. Ji, N. Tohnai, T. Nakamura and A. Douhal, *J. Am. Chem. Soc.*, 2019, **141**, 2111–2121.
14. J. Lu, C. Perez-Krap, F. Trousselet, Y. Yan, N. H. Alsmail, B. Karadeniz, N. M. Jacques, W. Lewis, A. J. Blake, F. X. Coudert, R. Cao and M. Schroder, *Cryst. Growth Des*., 2018, **18**, 2555–2562.
15. A. Bajpai, P. Venugopalan and J. N. Moorthy, *CrystEngComm*, 2014, **16**, 4853–4860.
16. D. J. Duchamp and R. E. Marsh, *Acta. Crystallogra. B,* 1969, **25**, 5–19.
17. Y. L. Li, E. V. Alexandrov, Q. Yin, L. Li, Z. B. Fang, W. Yuan, D. M. Proserpio and T. F. Liu, *J. Am. Chem. Soc.,* 2020, **142**, 7218–7224.
18. T. Takeda, M. Ozawa and T. Akutagawa, *Angew. Chem. Int. Ed.*, 2019, **58**, 10345–10352.
19. Y. Ueda, H. Tsuji, H. Tanaka and E. Nakamura, *Chem. Asian J.*, 2014, **9**, 1623–1628.
20. J. Bernstein, Polymorphism in Molecular Crystals, Oxford Science Publications, 2nd edn, 2020.
21. Z. Zhao, J. W. Y. Lam and B. Z. Tang, *Mater. Chem*., 2012, **22**, 23726–23740.
22. Z. Wei, Z. Y. Gu, R. K. Arvapally, Y. P. Chen, R. N. McDougald, Jr., J. F. Ivy, A. A. Yakovenko, D. Feng, M. A. Omary and H. C. Zhou, *J. Am. Chem. Soc.,* 2014, **136**, 8269–8276.
23. Q. Zhang, J. Su, D. Feng, Z. Wei, X. Zou and H.-C. Zhou, *J. Am. Chem. Soc*., 2015, **137**, 100064–10067.
24. J. Dong, X. Li, S. B. Peh, Y. D. Yuan, Y. Wang, D. Ji, S. Peng, G. Liu, S. Ying, D. Yuan, J. Jiang, S. Ramakrishna and D. Zhao, *Chem. mater*., 2019, **31**, 146–160.
25. S. Y. Jiang, S. X. Gan, X. Zhang, H. Li, Q. Y. Qi, F. Z. Cui, J. Lu and X. Zhao, *J. Am. Chem. Soc*., 2019, **141**, 14981–14986.
26. Q. Huang, W. Li, Z. Mao, L. Qu, Y. Li, H. Zhang, T. Yu, Z. Yang, J. Zhao, Y. Zhang, M. P. Aldred and Z. Chi, *Nat. Commun*., **2019**, *10*, 3074.
27. U. Lewandowska, W. Zajaczkowski, S. Corra, J. Tanabe, R. Borrmann, E. M. Benetti, S. Stappert, K. Watanabe, N. A. K.

Ochs, R. Schaeublin, C. Li, E. Yashima, W. Pisula and Klaus M. H. Wennemers, *Nat. Chem.,* 2017, **9**, 1068–1072.

28. N. B. Shustova, B. D. McCarthy and M. Dincă, *J. Am. Chem. Soc.,* 2011, **133**, 20126–20129.
29. A. Saeki, Y. Koizumi, T. Aida and S. Seki, *Acc. Chem. Res.*, 2012, **45**, 1193–1202.
30. Y. Xu, D. Chang, S. Feng, C. Zhang and J. X. Jiang, *New J. Chem.*, 2016, **40**, 9414–9423.
31. T. S. Navale, K. Thakur and R. Rathore, *Org. Lett.*, 2011, **13**, 1634–1637.
32. V. A. Blatov, A. P. Shevchenko and D. M. Proserpio, *Cryst. Growth Des.,* 2014, **14**, 3576–3586.
33. P. v. d. Sluis and A. L. Spek, *Acta Crystallogr. Sect. A,* 1990, **46**, 194.
34. A. L. Spek, *Acta Crystallogr. Sect. D,* 2009, **65**, 148.
35. I. Hisaki, N. Ikenaka, E. Gomez, B. Cohen, N. Tohnai and A. Douhal, *Chem. Eur. J.*, 2017, **23**, 11611–11619.
36. I. Hisaki, Y. Suzuki, E. Gomez, B. Cohen, N. Tohnai and A. Douhal, *Angew. Chem. Int. Ed.*, 2018, **57**, 12650–12655.
37. G. M. Sheldrick, *Acta Crystallogr. A,* 2015, **71**, 3-8.
38. Rigaku (2018). CrystalStructure. Version 4.3. Rigaku Corporation, Tokyo, Japan.
39. O. V. Dolomanov, L. J. Bourhis, R. J. Gildea, J. A. K. Howard and H. Puschmann, *J. Appl. Cryst.*, 2009, **42**, 339–341.
40. L. J. Bourhis, O. V. Dolomanov, R. J. Gildea, J. A. K. Howard and H. Puschmann, *Acta Crystallogr. Sect. A*, 2015, **71**, 59–75.
41. G. M. Sheldrick, *Acta Crystallogr. C* **2015**, *71*, 3-8.

Chapter 4. Isomeric effect of naphthyl spacers on structures and properties of isostructural HOFs

4.1 Introduction

Many interesting porous structures based on organic molecules have been explored through reticular chemistry[1–4]. Metal–organic frameworks (MOFs) and covalent–organic frameworks (COFs) are representative crystalline organic materials with permanent porosity, and the resulting diverse structures have been applied to a wide range of functional materials[5–9]. To obtain frameworks with a finely tuned structure and properties, various isostructural or isoreticular[10] frameworks have been constructed by designing network topology[11–14] and an assembling of the network (*i.e.*, interpenetration, stacking)[15–19]. Porous organic frameworks constructed by self-assembly of molecules through hydrogen bonds (H-bonds) are often called hydrogen-bonded organic frameworks (HOFs)[20–24]. Because of reversible, non-covalent bonds forming the framework, HOFs can be obtained as highly crystalline materials with a large domain by facile methods such as recrystallization and mechanochemistry[25]. They can be also re-used and re-generated by solution processes *via* re-solubilization. In contrast, the weakness of the bonds results in fragile frameworks compared with other porous frameworks such as COFs. Furthermore, the resulting framework is not always the same as the one originally designed, and an unexpected structure sometimes forms. Recently, these shortcomings have been overcome by networking through charge-assisted H-

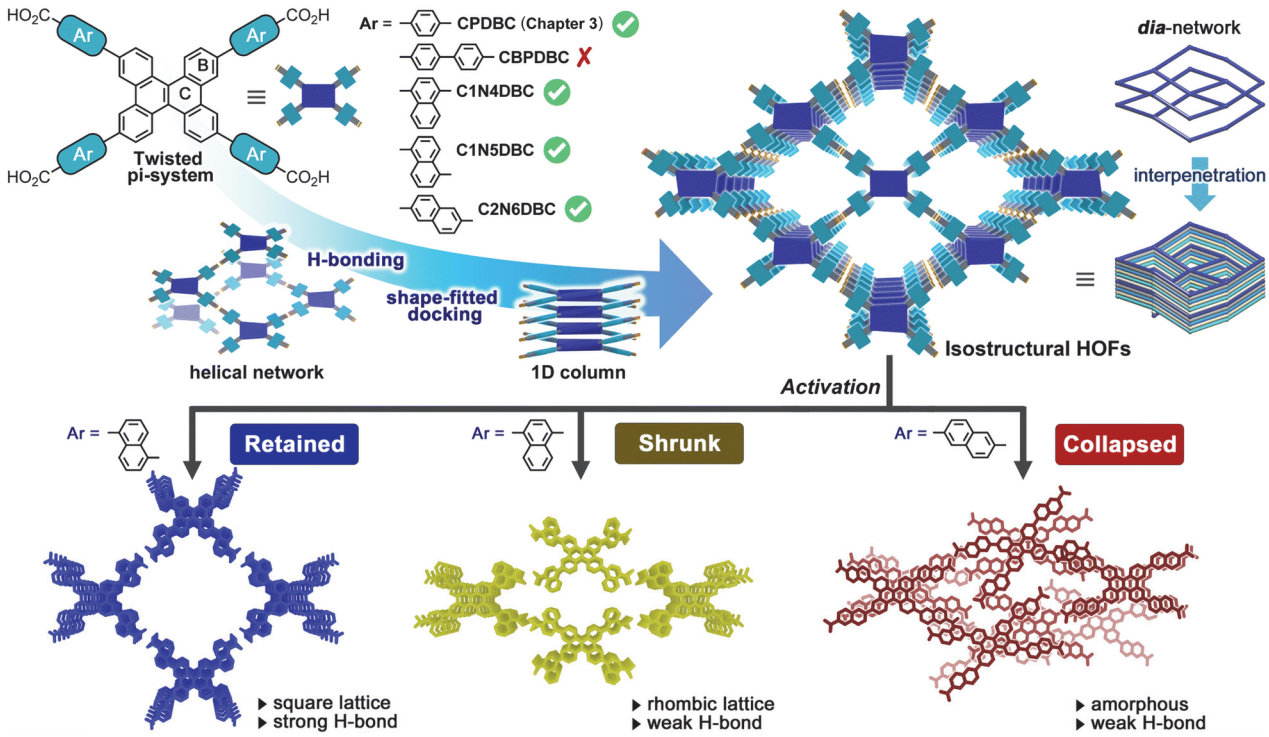

Figure 1. Construction of isostructural HOFs through shape-fitted docking of a dibenzo[*g*,*p*]chrysene (DBC) core and isomeric effects of the naphthyl spaces on the structures and properties. (top) Molecular structures of DBC derivatives: **CPDBC**, **C1N4DBC**, **C1N5DBC**, and **C2N6DBC** that form isostructural HOFs *via* H-bonded helical networking and shape-fitted docking of a DBC core. (bottom) Three activated isostructural HOFs with different substituted naphthyl groups. An isomeric effect led to differences in structural transition behavior during solvent desorption and re-adsorption.

bonding[20,26] and assembling *via* π–π stacking[27–35] to give stable HOFs.

However, systematically constructing a series of isostructural HOFs with different pore sizes is challenging because even molecules with the same geometry and H-bonding groups do not always give isostructural HOFs[36–39]. Several isostructural HOFs were constructed successfully from dihydroimidazolone-annelated triptycene derivatives[40,41], pyrene-based tetratopic carboxylic acids[28,31], fluorinated trispyrazole derivatives[27,32], and tetrathiafulvalene-based tetratopic carboxylic acids[29,30]. In these systems, the following three structural factors play a critical role in forming the isostructural frameworks: (1) well-defined supramolecular synthons formed through directional H-bonds, (2) a core skeleton with robust second interactions working orthogonally to the H-bonding, and (3) a suitable peripheral spacer bonded to the core.

As shown in Chapter 2, Hexaazatriphenylene (HAT) derivatives were also shown to form as many as four isostructural HOFs, in which robust shape-fitted docking among the twisted HAT cores significantly contributed to formation of the isostructural HOFs[33–35]. However, isostructural construction *via* tuning peripheral spacers to change the dynamic properties has not been investigated, although this approach can provide a library of diverse porous functional materials. The present study demonstrates, for the first time, that three dibenzo[*g*,*p*]chrysene (DBC)-based isostructural HOFs exhibit different dynamic behaviors depending on the substitution positions of the isomeric naphthyl spacers during solvent desorption and re-adsorption (Figure 1). DBC forms a twisted conformation due to steric hindrance at the fjord hydrogen atoms[42]. As shown in Chapter 3, its derivative possessing a carboxyphenyl group, **CPDBC**, yielded a HOF with permanent porosity through a H-bonded ***dia*** network and the shape-fitted docking of DBC cores (Figure 1). Based on this information, an attempt was made to introduce larger peripheral groups, a biphenyl group and naphthyl groups with different substitution positions, into the DBC system to investigate the isostructural construction of HOFs and the effects on their properties. A derivative with a carboxybiphenyl group, **CBPDBC**, underwent aggregation and had poor solubility, and produced only low crystalline structures. This is an example of the limitations of simple phenylene elongation of the peripheral group as in the previous HAT example[35]. The DBC derivatives with 1,4-, 1,5-, and 2,6-substituted naphthyl groups (**C1N4DBC**, **C1N5DBC**, and **C2N6DBC**), however, yielded isostructural HOFs (**C1N4DBC-1**, **C1N5DBC-1**, and **C2N6DBC-1**, respectively), comparable to **CPDBC**. Importantly, during the activation processes, **C1N5DBC-1** maintained its porous structure, while **C1N4DBC-1** showed reversible changes in aperture size upon guest desorption and adsorption, and **C2N6DBC-1** experienced shrinkage of the pores followed by collapse to the amorphous phase. These structures were determined precisely by single crystal X-ray diffraction (SCXRD), single crystal electron diffraction (ED), or powder X-ray diffraction (PXRD). These different behaviors resulted from differences in pore geometry and the H-bonding manner of the isostructural HOFs. Their physical properties are affected significantly by the isomeric effect[50,51] of the peripheral groups, while DBC cores are useful for isostructural construction by shape-fitted docking. These results suggest the importance of peripheral groups and provide molecular design insights for the systematic construction of porous molecular crystalline materials.

4.2 Synthesis and crystallization

The DBC tetracarboxylic acids, **CBPDBC**, **C1N4DBC**, **C1N5DBC**, and **C2N6DBC**, were synthesized as shown in Scheme 1. Biphenyl and 2,6-naphthyl-substituted precursors **3a** and **3b** were obtained by Suzuki–Miyaura cross-coupling reaction with 2,7,10,15-tetrabromodibenzo[*g*,*p*]chrysene (**1**) and pinacol boronates with butyl 4'-bromobiphenyl-4-carboxylate and butyl 6-bromo-2-naphthoate moieties, respectively. 1,4- and 1,5-Naphthyl-substituted precursors **3c** and **3d** were also synthesized by the coupling reaction of 2,7,10,15-tetra(pinacolboryl)dibenzo[*g*,*p*]chrysene (**2**), which was synthesized by Miyaura borylation from **1**, and the corresponding aryl bromides; butyl 4-bromo-1-naphthoate and butyl 5-bromo-1-naphthoate, respectively. Precursors **3a–d** were hydrolyzed by KOH in a mixed solution of THF, methanol, and water to afford the building block molecules **CBPDBC**, **C2N6DBC**, **C1N4DBC**, and **C1N5DBC**, respectively.

The synthesized DBC derivatives were dissolved in a mixture of a polar solvent (DMF or 1,4-dioxane) and an aromatic guest solvent (*o*-xylene: Xy, mesitylene: Mes, methyl benzoate: MeBz, 1,2,4-trichlorobenzene: TCB, or 5-*tert*-butyl-*m*-xylene: tBuXy), followed by recrystallization. For **C1N4DBC**, a vapor diffusion method was applied using a DMF/Xy solvent system. For the others, a solvent volatilization method was applied (Table 1, Figure 2).

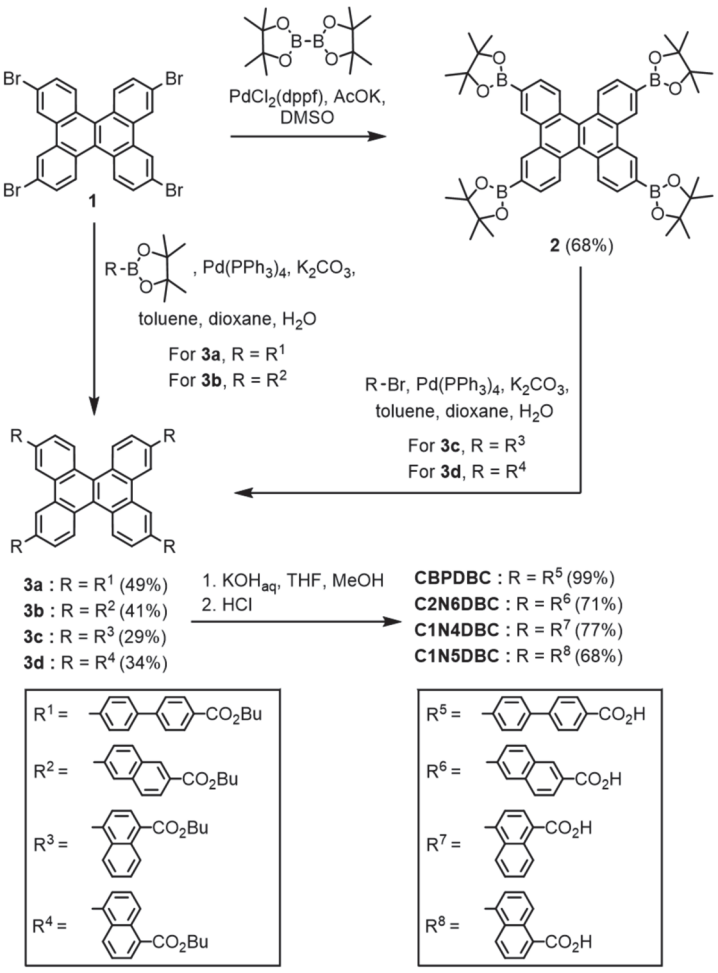

Scheme 1. Synthesis of DBC derivatives **CBPDBC**, **C1N4DBC**, **C1N5DBC**, and **C2N6DBC**.

Table 1. Crystallization conditions (polar solvent, guest solvent, and method) and resultant frameworks.

Compound name	Polar solvent [a]	Guest solvent [a]	Method	Framework
CBPDBC	DMF	TCB	volatilization	**CBPDBC-1**
C1N4DBC	DMF	Xy	vapor diffusion	**C1N4DBC-1**
	dioxane	Xy	volatilization	**C1N4DBC-1**
	DMF	Mes	volatilization	**C1N4DBC-1**
	dioxane	Mes	volatilization	**C1N4DBC-1**
C1N5DBC	DMF	tBuXy	volatilization	**C1N5DBC-1**
C2N6DBC	DMF	tBuXy	Volatilization	**C2N6DBC-1**
	DMF	MeBz	Volatilization	**C2N6DBC-2**

[a] Abbreviations in polar solvent and guest solvent defined in the above description.

As a result, **CBPDBC** yielded microcrystals **CBPDBC-1** from a DMF/TCB system. **C1N4DBC** also obtained microcrystals **C1N4DBC-1** from four system: DMF/Xy, dioxane/Xy, DMF/Mes, and dioxane/Mes, which possessed the same structures from PXRD experiments (Figure 3). Contrary, **C1N5DBC** and **C2N6DBC** yielded needle crystals **C1N5DBC-1** and **C2N6DBC-1**, respectively (Figure 2).

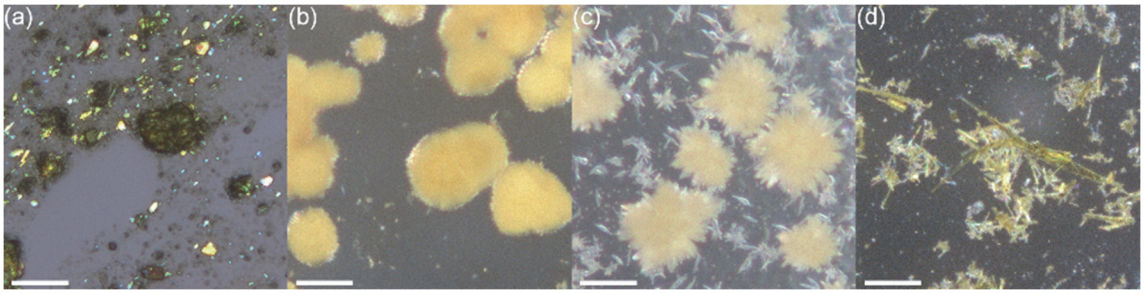

Figure 2. Polarized optical microscopy (POM) images of (a) **CBPDBC-1**, (b) **C1N4DBC-1**, (c) **C1N5DBC-1** and (d) **C2N6DBC-1** under daylight. Scale bar: 200 μm.

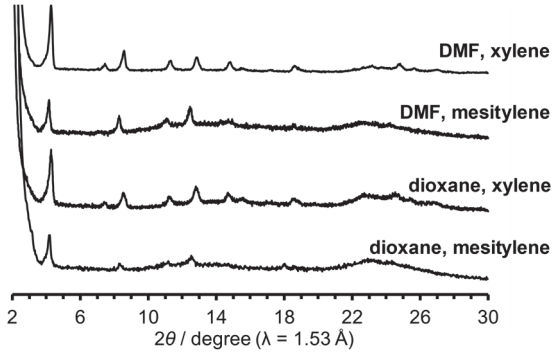

Figure 3. PXRD patterns of as-formed crystalline bulks of **C1N4DBC-1** crystalized from each mixed solution.

4.3 Crystallography

To examine the crystals obtained, preliminary PXRD patterns were recorded on as-formed crystalline precipitates and compared with those of the previously reported HOF **CPDBC-1** as shown in Figure 4. The **CBPDBC-1** showed weak diffraction peaks at 2θ = 1.54°, 3.08°, 4.74°, and 6.28°, which correspond to the (001), (002), (003), and (004) planes, respectively (Table 2), of the estimated framework of **CBPDBC**, assuming that **CBPDBC** would form an isostructural network with **CPDBC-1** (for details in Chapter 3) This indicates that **CBPDBC-1** formed a larger isostructural network than did **CPDBC-1**. However, its low crystallinity precluded further investigation. The microcrystalline **C1N4DBC-1** showed sharp diffraction peaks at 2θ = 4.30°, 7.45°, 8.55°, 11.34°, 12.89°, and 14.78°, which are similar to those of **CPDBC-1** at 2θ = 4.21°, 7.27°, 8.43°, 11.11°, 12.67°, and 14.55°. This similarity is reasonable because **CPDBC** is a substructure of **C1N4DBC** and, therefore, periodicity of the resultant crystals is nearly the same as that

of the isostructural HOF construction. The diffraction peaks of **C1N4DBC-1** corresponded to the (011) (020), (022), (031), (033), and (040) of **CPDBC-1** (Table 3), suggesting that **C1N4DBC-1** also is isostructural with **CPDBC-1**. The **C1N5DBC-1** and **C2N6DBC-1** had diffraction profiles similar to that of **CPDBC-1**, although they shifted slightly into a smaller angle region.

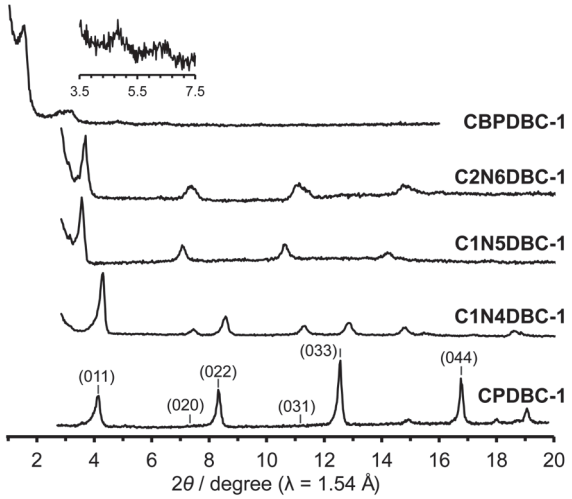

Figure 4. PXRD patterns of as-formed crystalline bulks of **CBPDBC-1**, **C2N6DBC-1**, **C1N5DBC-1**, and **C1N4DBC-1**, along with **CPDBC-1** as the reference[43]. (inset) PXRD pattern of **CBPDBC-1** from 3.5° to 7.5°.

Table 2. Peak parameters of **CBPDBC-1** and lattice spacing of predicted frameworks.

h	k	l	$2\theta_{obs.}$ / °	$d_{obs.}$ / Å	$2\theta_{calc.}$ / °	$d_{calc.}$ / Å
0	0	1	1.54	57.37	1.583	55.8
0	0	2	3.08	28.68	3.167	27.9
0	0	3	4.74	18.64	4.751	18.6
0	0	4	6.28	14.07	6.336	13.95

Table 3. Peak parameters of simulation of **CPDBC-1** and observed **C1N4DBC-1**.

h	*k*	*l*	$2\theta_{CPDBC\text{-}1\ obs.}$ / °	$d_{CPDBC\text{-}1\ obs.}$ / Å	$2\theta_{C1N4DBC\text{-}1\ calc.}$ / °	$d_{C1N4DBC\text{-}1\ calc.}$ / Å
0	1	1	4.21	20.988	4.30	20.559
0	2	0	7.27	12.164	7.45	12.164
0	2	2	8.43	10.493	8.55	10.339
0	3	1	11.11	7.9615	11.34	7.8056
0	3	3	12.67	6.9892	12.89	6.8703
0	4	0	14.55	6.0885	14.78	5.9951

The crystal structures of **C1N5DBC-1** and **C2N6DBC-1** were revealed by SCXRD measurements (Figure 5). Both belong to the space group *Pban* and have isostructural porous frameworks with **CPDBC-1** possessing quadrangular 1D channels. The molecules were connected by intermolecular H-bonds between the peripheral carboxy groups to form 3D ***dia***-topological networks. Their peripheral groups were disordered in two parts, resulting in different H-bonding environments. For simplicity, further structural descriptions focus on the major moieties until describing the details (*vide infra*). The networks were interpenetrated 4- and 8-fold to yield HOFs **C1N5DBC-1** and **C2N6DBC-1**, respectively (Figure 5b,c). In both frameworks, the molecules were stacked one dimensionally *via* the shape-fitted docking of the DBC cores. Stacking distances between the DBC cores were 3.86 Å and 3.84 Å and those between the naphthyl

groups were 3.35 Å and 3.54 Å for **C1N5DBC-1** and **C2N6DBC-1**, respectively. The root mean square derivatives (RMSD) of the DBC cores in **C1N5DBC-1** and **C2N6DBC-1** were 0.669 and 0.716, respectively, indicating that the former distorted less and the latter distorted more than **CPDBC-1** (RMSD: 0.680). The observed distortion of the core was smaller than that of theoretical structures optimized by the density functional theory (DFT) method at the B3LYP/6-311G** level: 0.764 for **C1N5DBC** and 0.761 for **C2N6DBC** (for details, see Table 4). The dihedral angle between aromatic rings Ar–B (Figure 1) also were smaller (**C1N5DBC-1**: calc. 56.21, obs. 41.51, **C2N6DBC-1**: calc. 37.81, obs. 31.91). The observed less-distorted conformations were due to shape-fitted docking, and this phenomenon also was observed in the **CPDBC** system[43]. The **C1N5DBC-1** had a rippled square aperture with dimensions of 26.8 Å 23.3 Å, and that of **C2N6DBC-1** had a rhombic aperture with dimensions of 19.8 Å 30.6 Å. The void ratios of **C1N5DBC-1** and **C2N6DBC-1** were calculated to be 58.4% and 58.3%, respectively, by PLATON with a probe radius of 1.2 Å[44,45]. Solvent molecules included in the channel were not solved crystallographically due to severe disorder.

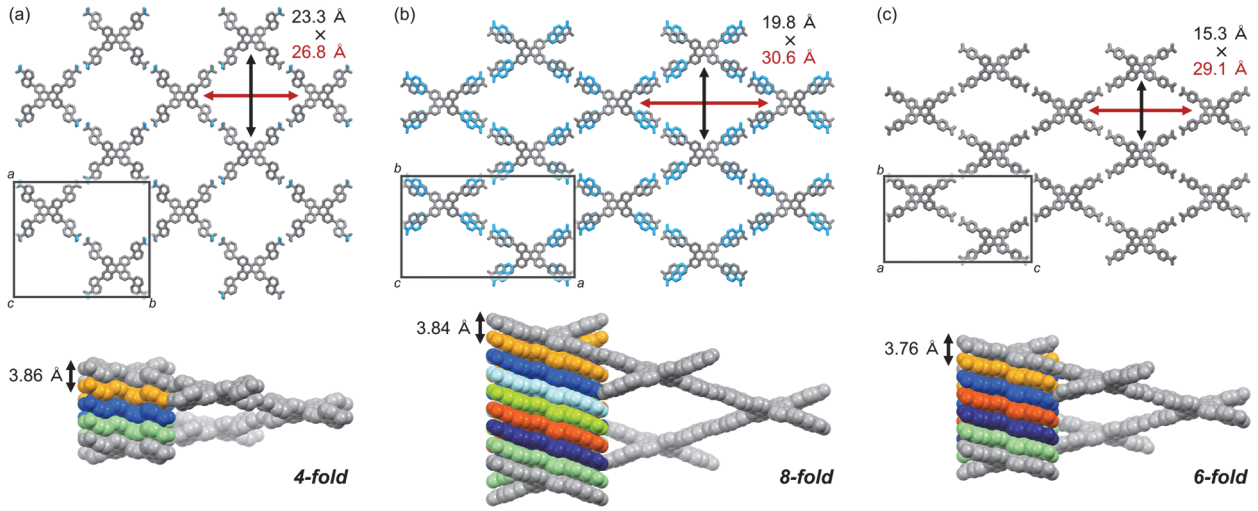

Figure 5. Crystal structures of (a) **C1N5DBC-1**, (b) **C2N6DBC-1**, and (c) **CPDBC-1** as a reference[43]. (top) Packing diagrams. Color code: Gray (major site), cyan (minor site). (bottom) Single ***dia***-network (colored grey) and 1D stacked columnar structures, for which the number of colors in the stacked molecules correspond to the number of the frameworks interpenetrated.

Table 4. Bond angle, dihedral angle, and RMSD of optimized structure of two representative conformations [a].

	C1N4DBC _far apart	C1N4DBC _close together	C1N5DBC _far apart	C1N5DBC _close together	C2N6DBC _far apart	C2N6DBC _close together
Bond angle of Ar-B / °	120.29	120.58	120.25	121.04	120.93	120.98
dihedral angle of Ar-B / °	55.88	55.52	36.94	37.34	57.39	40.97
dihedral angle of B-B' / °	13.65	12.5	14.2	14.3	13.75	4.43
dihedral angle of C-C' / °	41.01	36.3	41	41	41.45	36.82
RMSD of DBC core	0.7500	0.6801	0.7605	0.6596	0.7639	0.6496

[a] The details of "far apart" and "close together" are shown in Figure 7. Atom and plane name are shown in Figure 1.

The terminal carboxy group in **C1N5DBC-1** and the peripheral carboxynaphthyl group in **C2N6DBC-1** are disordered in two positions (Figure 6), which is significant because this is not observed in **CPDBC-1**. Particularly, the two disordered conformations in **C2N6DBC-1** were caused by rotation of the low-symmetry naphthyl groups. One conformer has naphthyl groups far apart, and the other has them close together (Figure 7c,d). In this way, rotation of the less symmetrical naphthyl portion causes the molecular conformation to be drastically different.

In **C1N5DBC-1**, the conformation with naphthyl groups close together was too hindered for shape-fitted docking (Figure 7b) and did not exist in crystalline form. Only the carboxylic acid moiety was disordered at major and minor positions with a site occupancy of 55% and 45%, respectively (Figure 5), and they are tilted from the naphthyl plane by +33.41° and −12.51°, respectively (Figure 8a). The O···O distances in the complementary H-bonded dimer between the same sites (*i.e.*, the major–major and minor–minor) were 2.61 Å and 2.62 Å, respectively. The dimer between the major and minor sites was twisted by 45°, and the O···O distances were 2.68 Å and 2.81 Å (Figures 6a and 8b). However, both conformers of **C2N6DBC-1** could form because their carboxynaphthyl groups did not prevent shape-fitted docking (Figure 7c,d). All of the peripheral groups were disordered in two positions (Figure 6b,d), suggesting that multiple conformations co-existed in the framework. The major and minor sites were occupied with ratios of 0.63 and 0.37, respectively (Figure 6b). This disorder also made the H-bonding more complex (Figure 6d). A truncated H-bond with a length of 2.71 Å existed between major–major and minor–minor, and complementary H-bonds with a length of

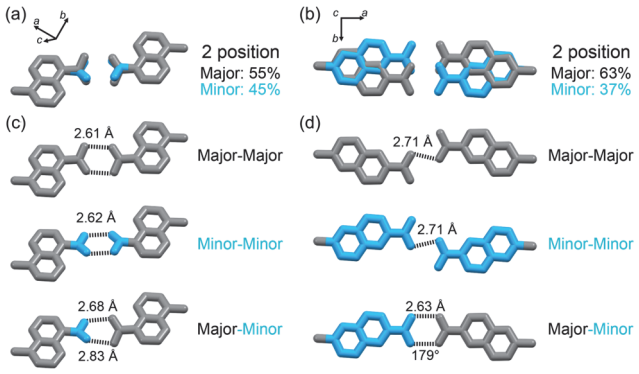

Figure 6. Disordered peripheral structures. (a) Carboxylic acid in **C1N5DBC-1**. Major: 55%, Minor: 45%. (b) 2-Carboxynaphthyl groups in **C2N6DBC-1**. Major: 63%, Minor: 37%. H-bonding networks in (c) **C1N5DBC-1** and (d) **C2N6DBC-1** between major–major, minor–minor, major–minor. Major and minor showed grey and cyan, respectively.

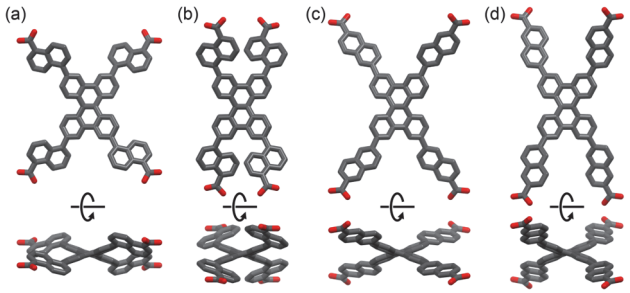

Figure 7. Predicted molecular structures of two representative conformations. **C1N5DBC** with naphthyl groups located (a) far apart and (b) close together. **C2N6DBC** with naphthyl groups located (c) far apart and (d) close together.

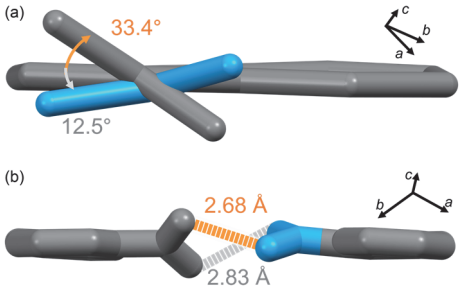

Figure 8. Disordered carboxylic acid of **C1N5DBC-1**. Color code: Gray (major site), cyan (minor site). (a) Dihedral angles of carboxylic acids viewed parallel toward the plane of naphthyl moiety. (b) Distorted complimentary dimer of H-bond between the major and minor sites, which is twisted by 45°.

a 2.64 Å between major–minor, which can exist randomly in the crystal.

Single ***dia***-networks and 1D stacked columnar structures are shown in Figure 9. **C1N4DBC-1** had nearly the same arrangement of carboxylic acid moieties as that of **CPDBC-1**, but due to increasing distortion of the DBC core, the helical pitch increased, and the number of interpenetrations increased to 7-fold from 6-fold. The location of carboxylic acid dimers in **C1N5DBC-1** differed from those in **C1N4DBC-1** and was closer in height to the DBC plane. Therefore, the helical pitch became smaller, resulting in a 4-fold interpenetration. In the HOFs of **C2N6DBC**, the number of interpenetrations increased because the helical pitch was elongated with the longer length of peripheral groups. The number of interpenetrations was 8-fold of **C2N6DBC-1** and 9-fold of **C2N6DBC-2**, which were different due to the distortion of the DBC cores (Table 5).

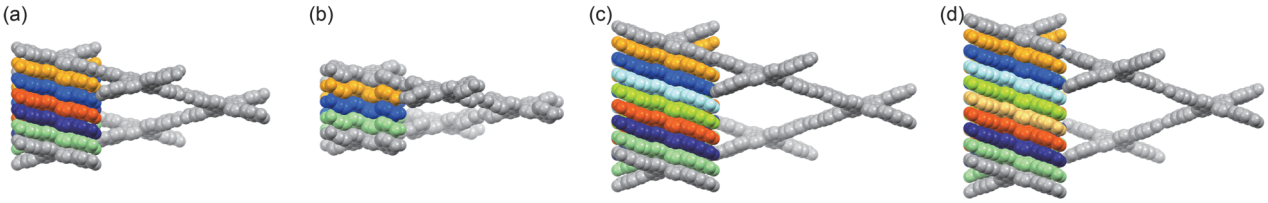

Figure 9. Single ***dia***-network (colored grey) and 1D stacked columnar structures, for which the number of colors in the stacked molecules correspond to the number of the frameworks interpenetrated. (a) **CPDBC-1** as a reference[43,] (b) **C1N5DBC-1**, (c) **C2N6DBC-1**, and (d) **C2N6DBC-2**.

Table 5. Structural data of single crystals (**CPDBC-1**, **C1N4DBC-1x**[a], **C1N5DBC-1, C2N6DBC-1**, and **C2N6DBC-2**).[b]

	CPDBC-1	**C1N4DBC-1x**[a]	**C1N5DBC-1**	**C2N6DBC-1**	**C2N6DBC-2**
RMSD of DBC core	0.680	0.73	0.6689	0.7164	0.7369
Bond angle of peripheral group ω (Ar-B, major) / °	121.48	122	123.72	122.92	125.88
Bond angle of peripheral group ω (Ar-B, minor) / °	—	—	123.72	119.40	114.11
Dihedral angle of B-B' / °	13.10	15	9.04	15.11	16.87
Dihedral angle of C-C' / °	20.74	22	20.46	38.65	39.73
Dihedral angle of Ar-B (major) / °	36.65	36.7	41.48	31.35	29.28
Dihedral angle of Ar-B (minor) / °	—	—	41.48	31.92	28.27
π-π stacking distance between DBC core / Å	3.762	4.0	3.861	3.838	3.797
π-π stacking distance between naphthyl groups / Å	3.422	—	3.345	3.535	3.486
void size (major) / Å×Å	29.1×15.3	9.8×8.4, 4.9×6.4	26.8×23.3	22.7×17.9	31.6×18.0
void size (minor) / Å×Å	—	—	26.8×23.3	30.8×19.8	28.1×17.7
void ratio (major) / %	56.4	32	58.3	58.4	56.4
void ratio (minor) / %	—	—	58.3	59.7	55.2
chemical occupancy (major) / %	—	—	55.0	60.7	57.5
chemical occupancy (minor) / %	—	—	45.0	39.3	42.5

[a] Single crystal structure after activation from the electron diffraction experiment. [b] RMSD denotes "root mean square derivation". "Ar" and "B" means aromatic moieties shown in Figure 1. "Major" or "minor" denote the framework constructed by only molecules with disordered major site or minor site at peripheral groups.

4.4 Thermogravimetric analysis of as-formed HOFs.

To estimate the stoichiometry of the molecules, as-formed crystalline bulks of **C1N4DBC-1**, **C1N5DBC-1**, and **C2N6DBC-1** were subjected to TG analysis (Figure 10a,d,g). The TG curve of **C1N4DBC-1** reached a plateau at *ca.* 180 °C with a weight loss of 32% in two steps, which indicated that the framework contained Xy molecules with a host/guest molar ratio of 1 : 4. The ^{1}H NMR spectrum of the as-formed crystals dissolved in DMSO-d_6 also indicated a ratio of 1 : 3.8 (Figure 11). The **C1N5DBC-1** showed a 55% weight loss in two steps, indicating a host/guest ratio of 1 : 7.6. This agreed well with the ratio of 1 : 7.1 obtained from the ^{1}H NMR analysis (Figure 12). The TG curve of **C2N6DBC-1** did not plateau, but showed a first weight loss of 33% followed by continuous weight loss up to 47%, which was attributed to both release of guest solvent (tBuXy) and partial decomposition of the compound. The first weight loss corresponded to the host/guest ratios of 1 : 3, while the latter cannot be determined due to the unclear boundary between the removal of guest solvent and the decomposition of the carboxylic acid. The host/guest ratio was calculated from ^{1}H NMR to be 1 : 7.4 (Figure 13).

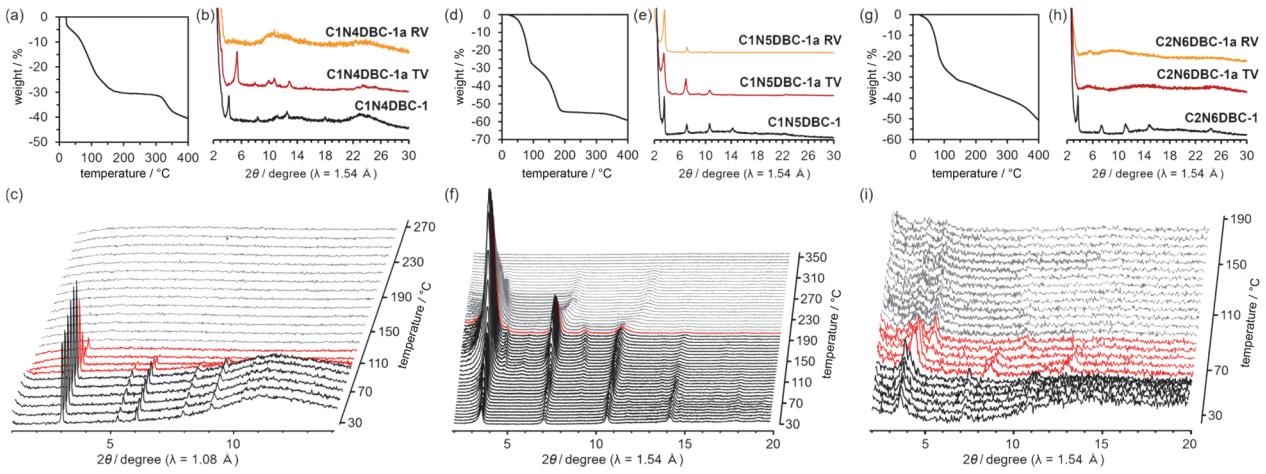

Figure 10. (a,d,g) TG curves, (b,e,h) PXRD patterns after activation, and (c,f,i) VT-PXRD patterns of as-formed HOFs of (a–c) **C1N4DBC-1**, (d–f) **C1N5DBC-1**, and (g–i) **C2N6DBC-1**. Heating rate and radiation of VT-PXRD were 10 °C min^{-1} and synchrotron radiation (λ = 1.0800 Å) for **C1N5DBC-1**, and c.a. 6 °C min^{-1} and Cu-Kα for others. TV and RV in PXRD patterns (b,e,h) indicate activation by thermal vacuum and replace vacuum methods, respectively. TG heating rate was 5 °C min^{-1}.

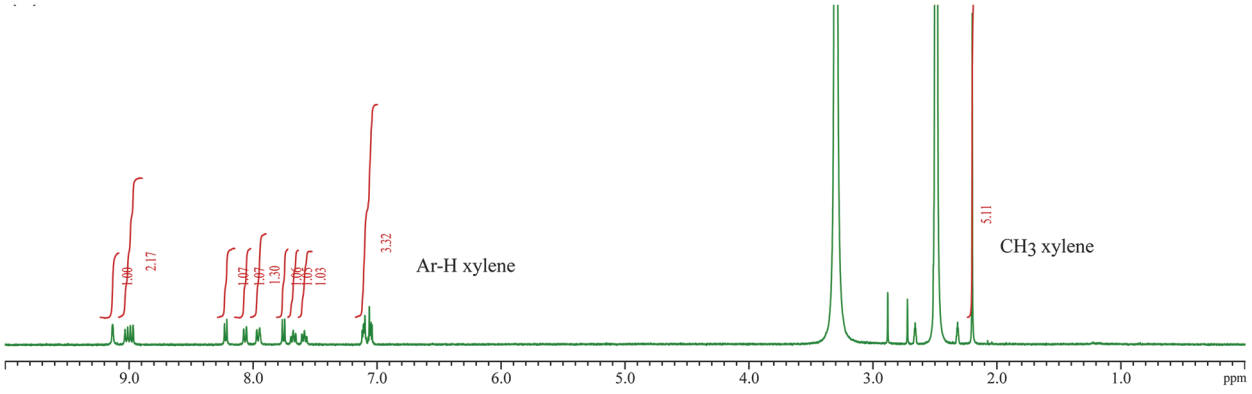

Figure 11. ^{1}H NMR (DMSO-d_6) spectrum of **C1N4DBC-1**, which was crystalized with Xy.

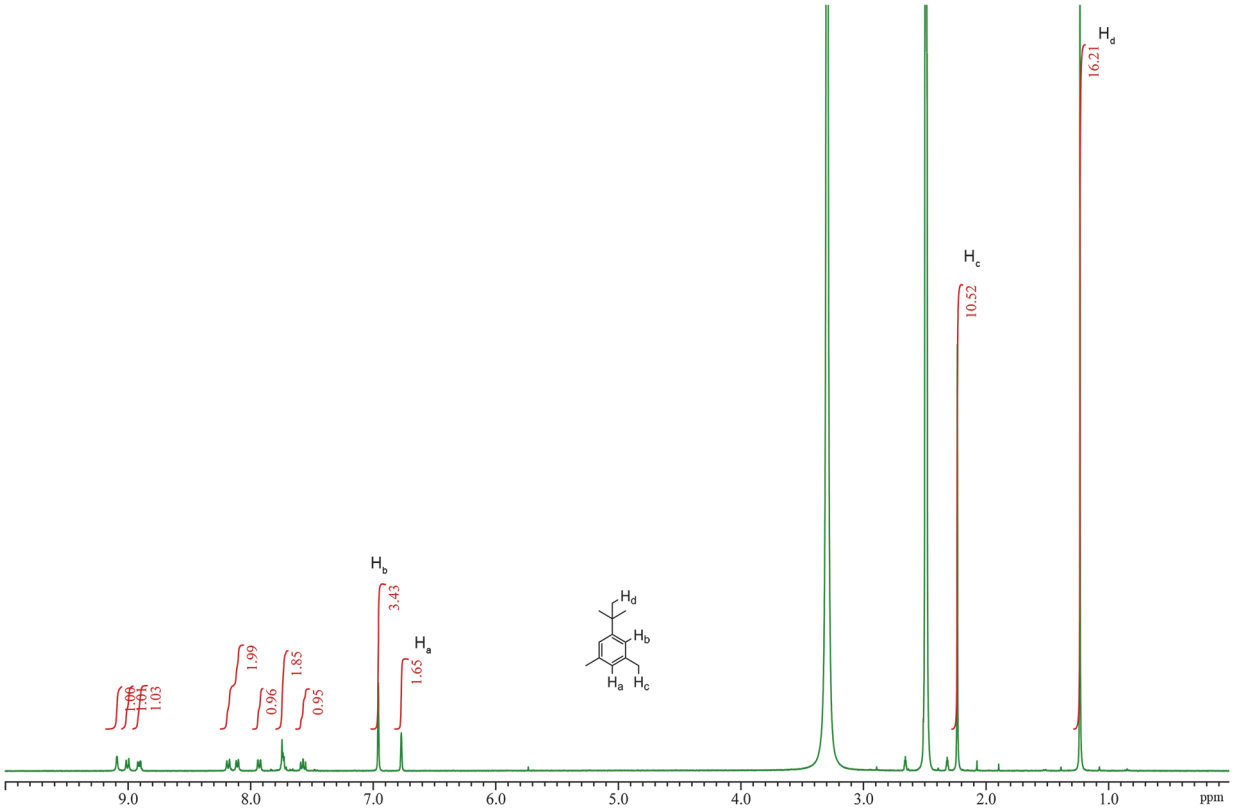

Figure 12. ^{1}H NMR (DMSO-d_6) spectrum of **C1N5DBC-1**.

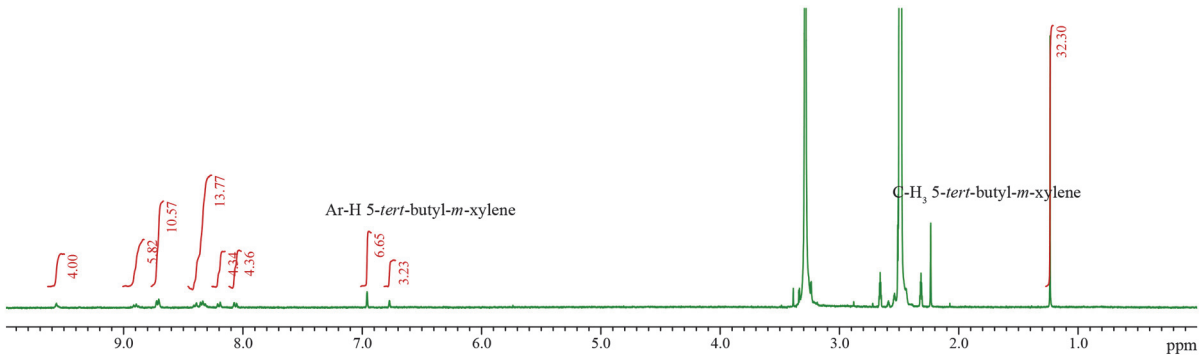

Figure 13. ^{1}H NMR (DMSO-d_6) spectrum of **C2N6DBC-1**.

4.5 VT-PXRD measurements

As-formed crystalline bulks of **C1N4DBC-1**, **C1N5DBC-1**, and **C2N6DBC-1** were subjected to VT-PXRD under ambient atmosphere to investigate their structural transition behavior and thermal stability. Patterns of **C1N4DBC-1** were recorded every 10 °C increase using synchrotron radiation (λ = 1.0800 Å), and those of **C1N5DBC-1** and **C2N6DBC-1** were recorded every *ca.* 6 °C using Cu-Kα radiation (λ = 1.5418 Å) (Figure 10c,f,i). A broad peak around 5–25° in **C1N4DBC-1** was due to an excessive amount of mother liquor that remained and disappeared after the solvent volatilized. The initial phase started to decay at around 100 °C then disappeared entirely at 140 °C. The TG and PXRD results indicated that retaining the original porous structure was difficult after removing half of the guests. **C1N5DBC-1** maintained its initial structure up to 220 °C, where its intensity began to shift. The TG analysis indicated guest removal terminated at 180 °C, showing that this porous structure was stable with no structural transition during guest removal. In contrast, the initial pattern for **C2N6DBC-1** shifted to the lower angle region at 70 °C, and its intensity decayed and disappeared at 100 °C, resulting in an amorphous structure. Thus, the structure collapses before the first step of guest removal. These results indicate that frameworks **C1N4DBC-1** and **C2N6DBC-1** readily underwent a structural transition, and, therefore, should need attention when activation is conducted.

4.6 Activation condition

Based on the results of VT-PXRD measurements, activation (*i.e.*, removing guest molecules from the pores) of the as-formed crystals, **C1N4DBC-1**, **C1N5DBC-1**, and **C2N6DBC-1**, was attempted using the following two methods. The first was a thermal vacuum (TV) method, in which as-formed crystalline powder was heated at 90, 120, 180 °C, respectively, under vacuum. The other was a replaced vacuum (RV) method, in which asformed crystalline powder was immersed in benzene to replace the included solvent with benzene, followed by heating at 60, 60, 100 °C, respectively, under vacuum to remove benzene under milder conditions. The complete removal of the solvent was confirmed by ^{1}H NMR (Figures 15–17), and the crystallinity was determined by PXRD (Figure 10b,e,h).

Although VT-PXRD indicated collapse of the framework by heating under ambient atmosphere, **C1N4DBC-1** showed a good PXRD profile after activation by the TV method, but very low crystallinity by the RV method. Neither pattern after activation matched the initial one, indicating a structural transition occurred to provide the activated framework of **C1N4DBC-1a**. Therefore, **C1N4DBC-1** is a flexible HOF. The **C1N5DBC-1** showed no peak shift upon activation by either method, resulting in the structure-retained, activated framework of **C1N5DBC-1a**. This activated framework had chemical durability against several solvents (Figure 14). Therefore, **C1N5DBC-1** is a stable HOF. The **C2N6DBC-1** lost crystallinity after activation by both the TV and RV methods and became amorphous **C2N6DBC-1a**. Therefore, **C2N6DBC-1** is a fragile HOF.

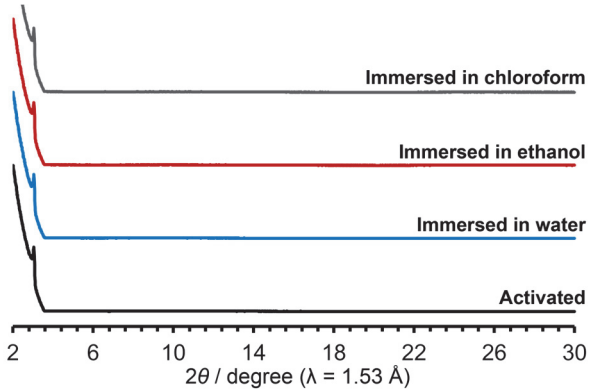

Figure 14. PXRD patterns of **C1N5DBC-1a**. (black) Activated bulk crystal and bulk ones immersed in (blue) water, (red) ethanol, and (gray) chloroform.

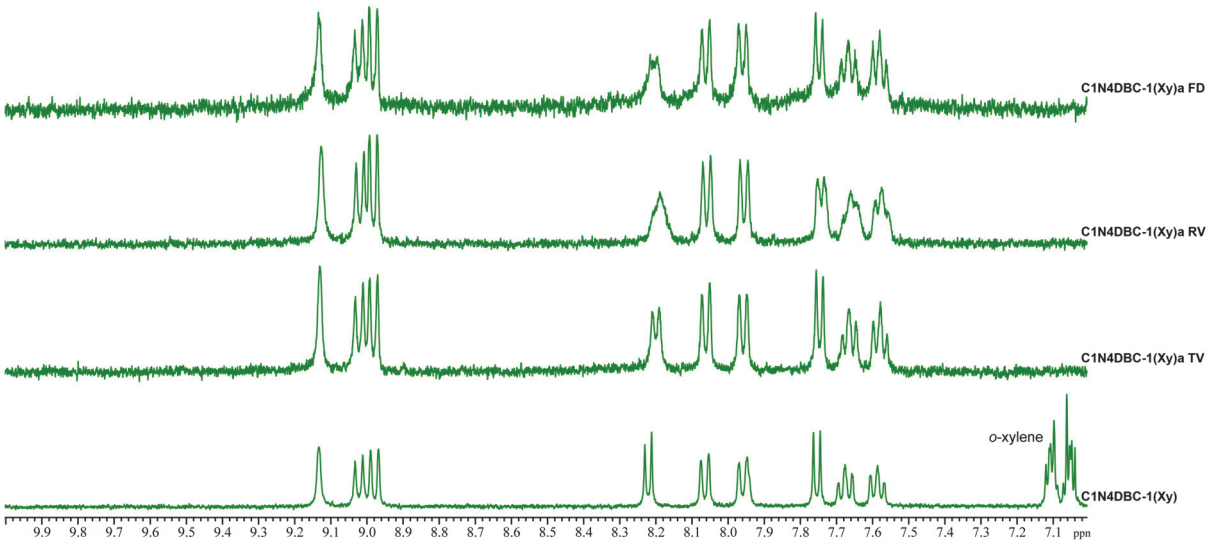

Figure 15. ^{1}H NMR (DMSO-d_6) spectra of as-formed and activated HOFs of **C1N4DBC-1**.

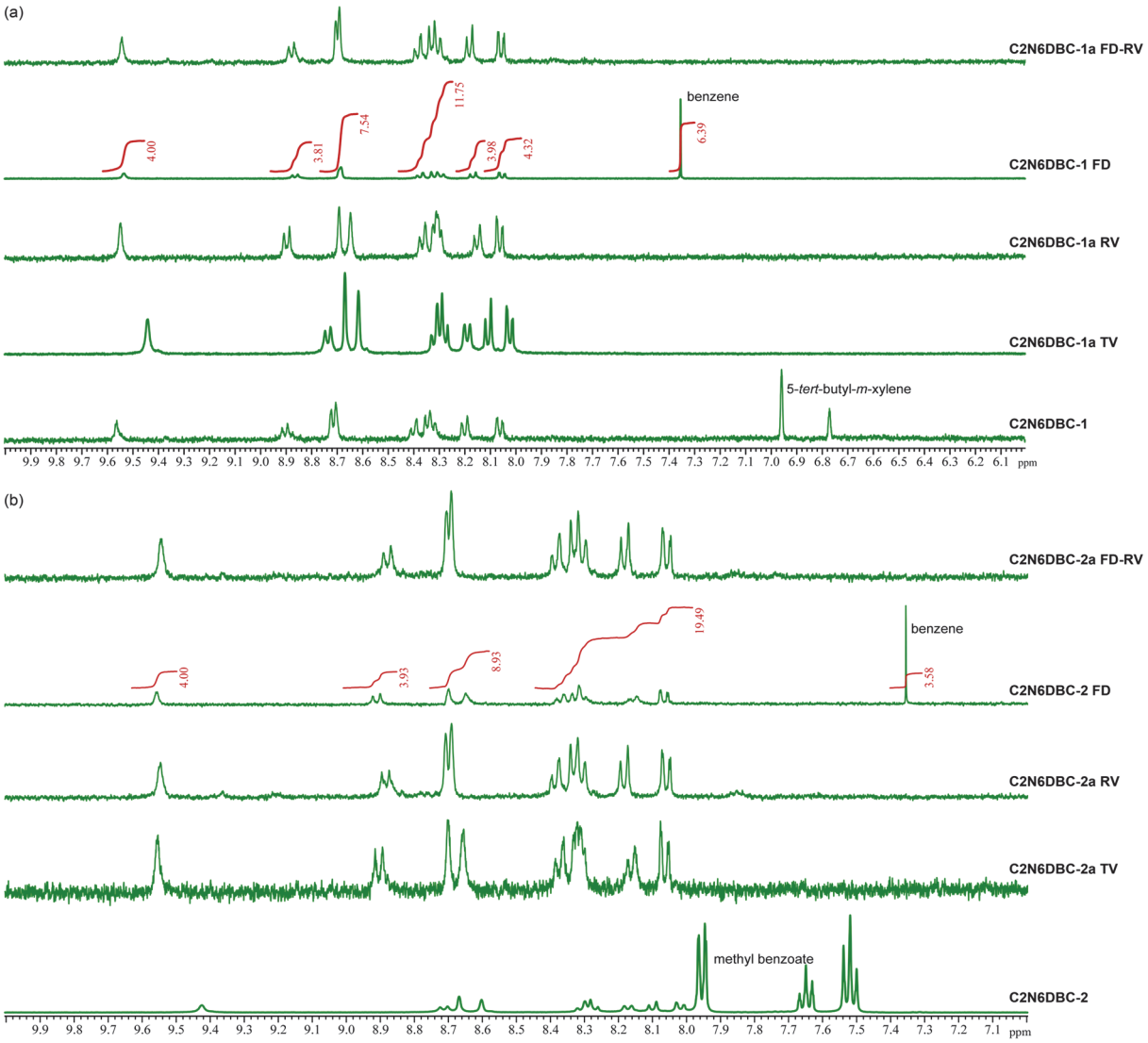

Figure 16. ^{1}H NMR (DMSO-d_6) spectra of as-formed and activated HOFs of (a) **C2N6DBC-1** and (b) **C2N6DBC-2**.

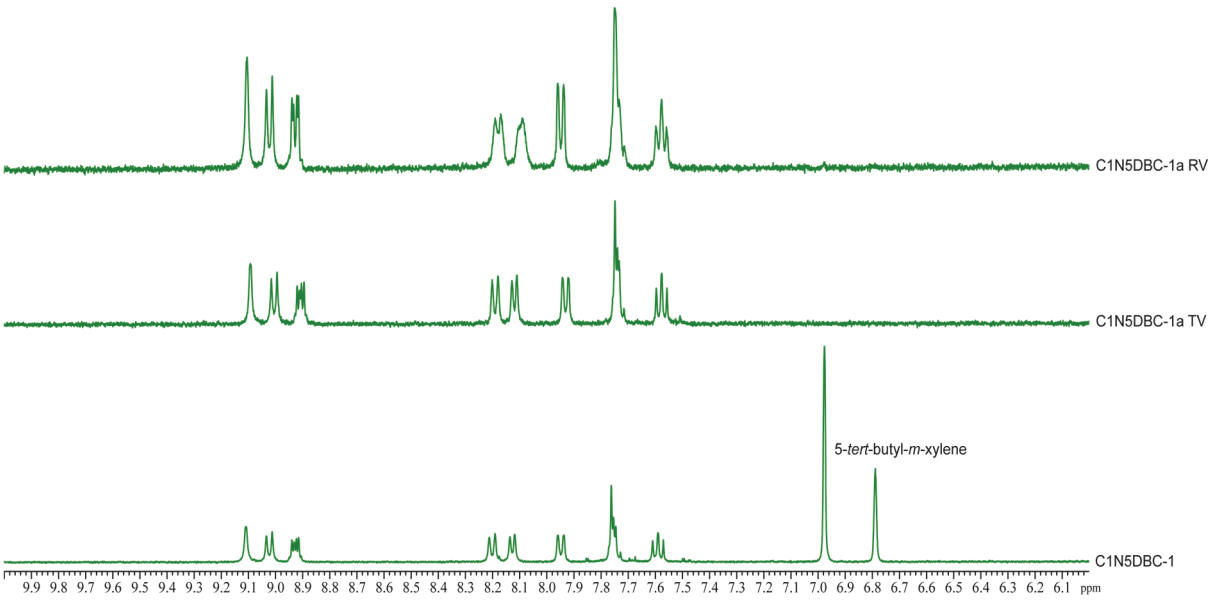

Figure 17. ^{1}H NMR (DMSO-d_6) spectra of as-formed and activated HOFs of **C1N5DBC-1**.

4.7 Structure of activated framework of **C1N4DBC-1**

Results showed that microcrystals of **C1N4DBC-1** obtained from a Mes solution retained their single-crystallinity after heating under vacuum (for details, see 4.13.7). The microcrystals were subjected to ED analysis, which produced a preliminary structure for **C1N4DBC-1x** (Figure 18a–c). The constituent molecule exhibited a conformation with the naphthyl groups far apart (Figure 7c) and stacked through shape-fitted docking of the DBC cores. The network created by intermolecular H-bonds among the carboxy groups gave an isostructural framework possessing 1D channels (Figure 18a). Additionally, the analysis implied that some molecules of Mes remained.

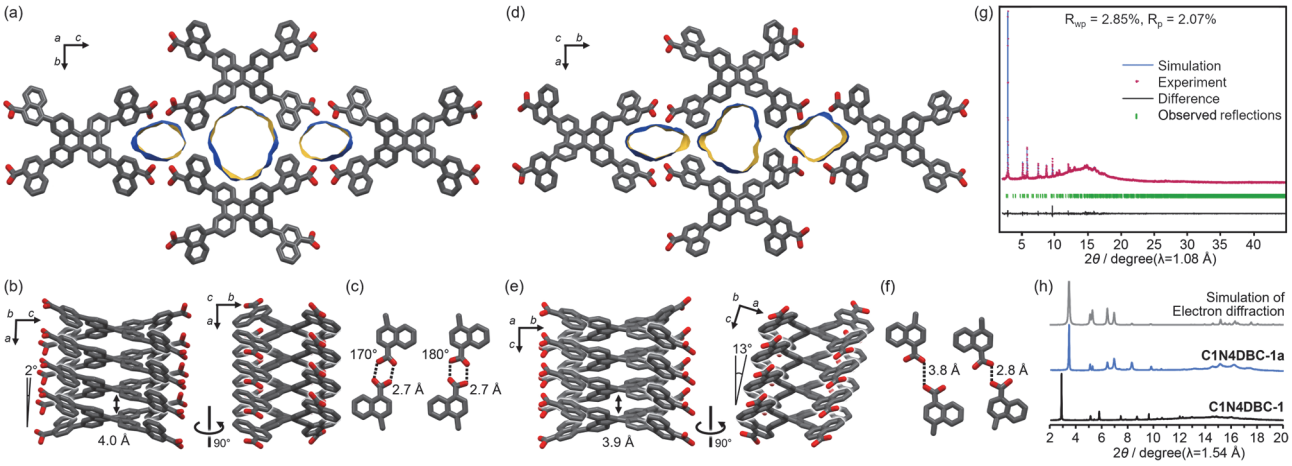

Figure 18. (a) Crystal structure of **C1N4DBC-1x** obtained from electron diffraction analysis. Void surfaces were visualized with blue (outside) and yellow (inside). (b) 1D columnar structure formed in **C1N4DBC-1x** through shape-fitted docking of the DBC core. (c) Complementary H-bonded dimers with a distorted manner. (d) Crystal structure of **C1N4DBC-1a** obtained from powder structure analysis. (e) 1D columns formed by shape-fitted docking of the DBC derivatives with a tilted angle of 13°. (f) Two different dimers with truncated H-bonding manner. (g) Rietveld refinement of **C1N4DBC-1a**. (h) PXRD pattern comparison among crystalline bulk of (bottom) **C1N4DBC-1**, (middle) **-1a**, and (top) simulation of the electron diffraction structure.

Notably, compared with **CPDBC-1** (Figure 5c), the framework of **C1N4DBC-1x** shrank in the direction of the *b* axis, and the facing naphthyl groups divided the pores into three parts. This framework structure was affected by distortion caused by both the molecular conformation and H-bonding manner. The bond angle of the peripheral groups Ar–B (Figure. 1) in **C1N4DBC-1x** was 10°, which is larger than that of the optimized structure (0.3°) (Table 4). The complementary H-bonded dimer also was distorted (Figure 18c).

The crystal structure of the completely activated HOF **C1N4DBC-1a** (Figure 18d), was obtained by Rietveld refinement using synchrotron PXRD patterns (Figure 18g), where the molecular structure was constructed by optimization of the preliminary structure obtained in the ED while maintaining the molecular conformation. Crystal data are also listed in section 4.13.2. Although **C1N4DBC-1a** shows the very similar diffraction profile with **C1N4DBC-1x** (Figure 18h), two structural differences between them were found. The first was the H-bonding manner. The molecules in **C1N4DBC-1a** were networked by truncated H-bonds with an O···O distance of 2.77 Å and 3.76 Å, instead of distorted complementary H-bonds (Figure 18c,f). The second was the stacking direction. The molecules were stacked with an inclination of 13° (Figure

18b,e). A 1D channel along the c axis was divided into three parts by the naphthyl group, with a larger central part (9.07 Å × 8.74 Å) and smaller parts on the left and right (4.53 Å × 9.07 Å, and 5.83 Å × 8.42 Å, respectively).

4.8 Gas sorption measurements

To evaluate porosity of the activated frameworks of DBC derivatives, N_2 and CO_2 absorption experiments were performed at 77 K and 195 K, respectively. The **C1N4DBC-1a** showed almost no adsorption of N_2 in the low-pressure region, but showed type-I CO_2 adsorption isotherms with an uptake of 3.60 mmol(STP) g^{-1} at a relative pressure of 0.99 and 195 K (Figure 19a). These results indicate the existence of micropores. The **C2N6DBC-1a** showed similar CO_2 sorption behavior with an uptake of 3.22 mmol(STP) g^{-1} , although the isotherm exhibited larger hysteresis (Figure 19c). The BET specific surface area: $S_{A(BET)}$ was calculated to be 281 m^2 g^{-1} for **C1N4DBC-1a** and 113 m^2 g^{-1} for **C2N6DBC-1a**. The smaller value of the latter system probably was due to the amorphous nature of **C2N6DBC-1a** without clear channels. The stable **C1N5DBC-1a** exhibited excellent porosity. Both N_2 and CO_2 were adsorbed, with type IV and type V adsorption isotherms, respectively, suggesting the presence of mesopores (Figure 19b). Uptake was 16.8 mmol(STP) g^{-1} for N_2 and 27.5 mmol(STP) g^{-1} for CO_2. The $S_{A(BET)}$ was calculated from the N_2 adsorption isotherm to be 1300 m^2 g^{-1}, indicating that large pores were present. In the adsorption of CO_2, a sharp rise was observed at a relative pressure of approximately 1.0. In contrast, desorption did not show a sharp change but hysteresis with a gradual decrease to the plateau until a relative pressure of 0.7, due to CO_2 aggregation in the pores.

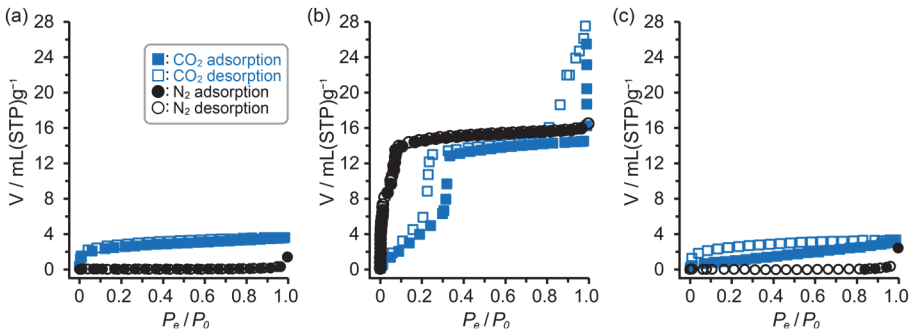

Figure 19. CO_2 (blue) and N_2 (black) absorption isotherms of (a) **C1N4DBC-1a**, (b) **C1N5DBC-1a**, and (c) **C2N6DBC-1a**. Solid and open symbols correspond to adsorption and desorption processes, respectively.

4.9 *In situ* PXRD measurements with loaded molecules

In situ measurements were performed to investigate the structural changes during activation. As a preliminary experiment, the author measured the structural transition behavior of **C1N4DBC-1a** and **C2N6DBC-1a** by the introduction of aromatic molecules into the pores. The guest solvent used for crystallization, and benzene were added to the crystals, and the resulting structural changes were traced by PXRD (Figure 20). To obtain benzene-loaded HOFs denoted as **C1N5DBC-1(benzene), C2N6DBC-1(benzene)**, and **C1N4DBC-1(benzene)**, activated samples were placed in saturated benzene vapor for 24 hours. Activation of benzene-loaded HOFs was performed in heating under vacuum at 70 °C (for **C1N4DBC** and **C1N5DBC**) or 100 °C (for **C2N6DBC**) to yield re-activated HOFs, named as **C1N5DBC-1(benzene)-a, C2N6DBC-1(benzene)-a, and C1N4DBC-1(benzene)-a**. The respective guest solvents used in crystallization were introduced by immersing the activated HOF for 24 hours to yield the immersed HOFs, denoted as **C2N6DBC-1(tBuXy) and C1N4DBC-1(Xy)**.

No changes were observed in **C1N5DBC-1**, which always showed the original structure (Figure 20a). Immersion in the guest solvent restored a similar pattern to that of **C1N4DBC-1** and **C2N6DBC-1** (the patterns at the top of each figure 20b and c). The guest-loaded samples **C2N6DBC-1(tBuXy)** and **C1N4DBC-1(Xy)** yielded patterns in almost the same positions as the as-formed crystals, suggesting structural restoration. **C2N6DBC-1(benzene)** exhibited a pattern with the lowest peak being between **C2N6DBC-1** and **C2N6DBC-1a** (Figure 20b). **C1N4DBC-1(benzene)** showed a broad pattern (4–5°), which is located wider than the lowest pattern of **C1N4DBC-1** (Figure 20c). These behaviors indicated that partial restoration occurred in response to benzene. After re-activation, the emerging patterns disappeared. It is expected that benzene-loaded samples did not show the same restoration behavior as the guest-loaded samples because the PXRD measurements under open conditions show a decrease in the number of molecules in the vacancies due to benzene volatilization.

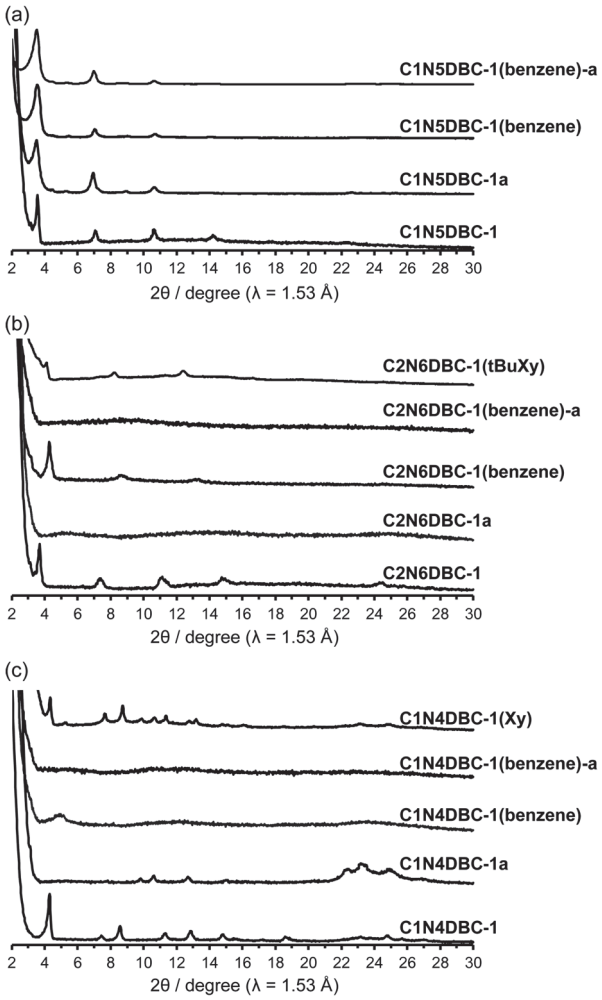

Figure 20. PXRD patterns of activated, benzene-loaded, benzene-removed, and guest-loaded HOFs of (a) **C1N5DBC-1**, (b) **C2N6DBC-1**, and (c) **C1N4DBC-1**.

The **C1N4DBC-1a** that underwent a structural transition upon activation was expected to undergo a structural change induced by loading guest molecules. Rigid HOF **C1N5DBC-1a** showed no structural changes upon adsorption of benzene vapor (Figure 20a). However, **C1N4DBC-1a** showed obvious structural changes that were confirmed by in situ PXRD experiments during adsorption and desorption of benzene vapor (Figure 21). The patterns were recorded under a benzene atmosphere from 0 kPa to 10 kPa with 1 kPa steps at 298 K, followed by a decrease to 0 kPa. The structural transition began at 2 kPa, where the characteristic peak of the initial structure at 2θ = 3.48° (d = 16.5 Å) decayed and a new peak appeared at 2θ = 2.91° (d = 19.7 Å). At 5 kPa, the initial structural pattern completely disappeared and was replaced by that of the benzene-filled HOF **C1N4DBC-1(benzene)**. During the desorption process, the structural transition began between 3 and 0 kPa. At 0 kPa, the pattern of **C1N4DBC-1a** was recovered accompanied by a broad pattern. The broad peak at around 2θ = 3.0–3.3° was attributed to an intermediate state of the activated structure, in which the number of benzenes in the pores decreased. It was also observed in **C1N4DBC-1(benzene)** (Figure 20c). Heating at 60 °C under vacuum finally gave a pure phase of **C1N4DBC-1a**. The **C1N4DBC-1a** also was subjected to the *in situ* experiment using N_2 and CO_2 at 298 K, but no transition occurred (Figure 22).

Contrary, **C2N6DBC-1a** exhibits insensitive behavior against benzene (Figure 23). Continued exposure to benzene vapor at 10 kPa resulted in a post-transition structure with benzene, which collapsed after guest removal under vacuum at 60 °C.

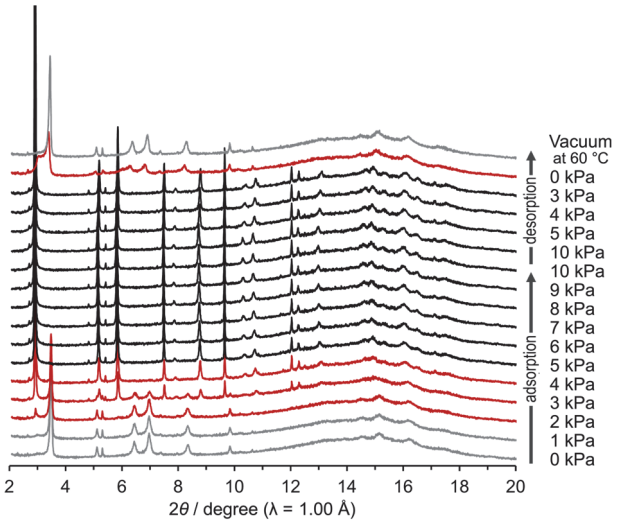

Figure 21. *In situ* PXRD patterns of **C1N4DBC-1a** upon loading and removal of benzene vapor.

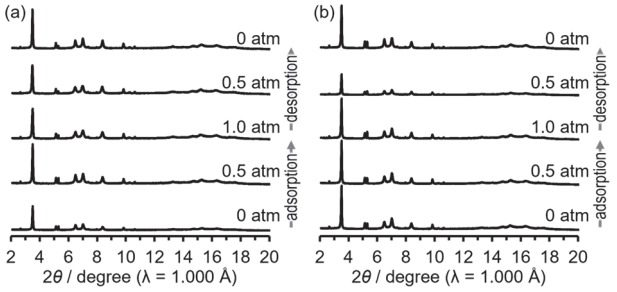

Figure 22. *In situ* PXRD patterns of **C1N4DBC-1a** upon loading and removal of (a) N_2 and (b) CO_2.

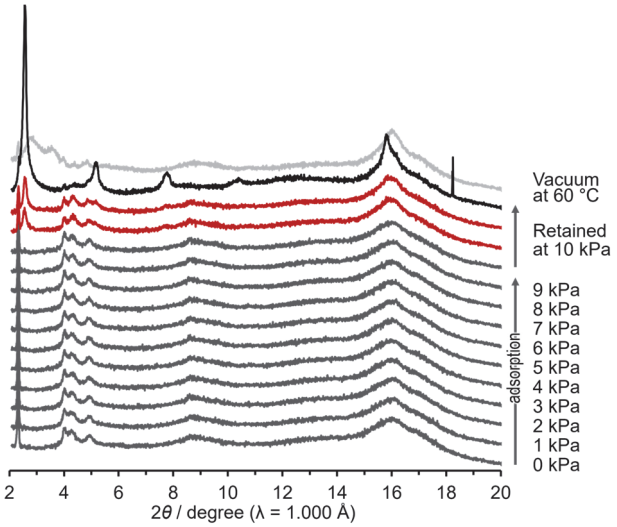

Figure 23. *In situ* PXRD patterns of **C2N6DBC-1a** upon loading and removal of benzene vapor.

4.10 Proposed lattice change in **C1N4DBC-1**

Since the PXRD patterns of **C1N4DBC-1** maintained a good signal/noise ratio during the *in situ* experiment, the mechanism of the structural changes could be proposed based on PXRD patterns. The patterns of **C1N4DBC-1**, **C1N4DBC-1(benzene)**, and **C1N4DBC-1a** are shown in Figure 24c. The broad signals around 10–20° was a background from a glass capillary. Cell parameters and space group were determined using the patterns (Figures 24b and 25); **C1N4DBC-1** belongs to the orthorhombic space group *Pnnn*, while **C1N4DBC-1a** and **C1N4DBC-1(benzene)** belong to the less symmetric monoclinic space group *Pn* (Table 6). The lattices and proposed changes are shown in Figure 24a. The **C1N4DBC-1** lattice was similar to the single crystal structure of **CPDBC-1**. The *a*, *b*, and *c* axes of **C1N4DBC-1** reflect the width and height of the aperture and stacking distance of the rhombic framework, respectively. Axes lengths were −1.04 Å, +0.343 Å, and +0.337 Å compared with the corresponding axes of **CPDBC-1**. Therefore, it formed a slightly wider H-bonding network, and the stacking distance was longer due to the bulky naphthyl groups. Upon activation to **C1N4DBC-1a**, a significant shrinkage by 5.47 Å was observed along the *a* axis direction. Simultaneously, the *b* axis extended by 0.6 Å to form three divided pores. The cell volume decreased by *ca.* 900 Å^3 from **C1N4DBC-1** (3985.5 Å^3). This anisotropic shrinkage was expected to be accompanied by a decrease in the number of guest molecules.

Removal of guest molecules from the pores of HOFs results in pore shrinkage and/or structural transitions of the framework associated with recombination or dissociation[46–49]. The molecular conformation, stacking manner, and H-bonds of **C1N4DBC-1** were perturbed, resulting in shrinkage of the pore aperture along the shorter direction. However, structurally hindered 1-naphthyl spacers as well as the shape-fitted docking of DBC cores prevented a drastic transition that would have led to collapse of the framework into an amorphous state.

Upon loading benzene to **C1N4DBC-1a**, the divided channel was restored and **C1N4DBC-1(benzene)** was formed. The *a* axis elongated by 4.5 Å and the *b* axis contracted by 1.2 Å compared to the activated structure, indicating that the rhombic channel opened along the height direction. This HOF was not identical to **C1N4DBC-1** but had a similar structure with all peaks shifted slightly to the wide angle, and large values of the *c* axis (4.68 Å) and bond angle (95.9°). The cell volume increased by *ca.* 1316 Å^3 from **C1N4DBC-1a** (3080.1 Å^3). Thus, results showed that **C1N4DBC-1** exhibits breathing behavior in which the loading/removal of the guests causes expansion and shrinkage of the pores.

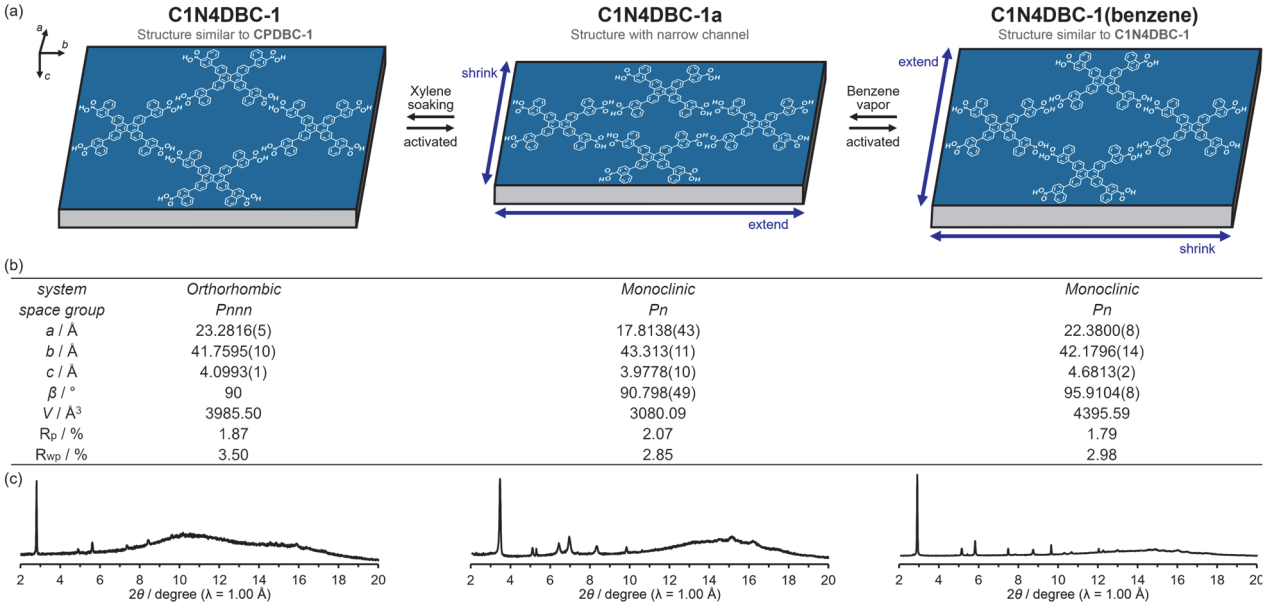

system	*Orthorhombic*	*Monoclinic*	*Monoclinic*
space group	*Pnnn*	*Pn*	*Pn*
a / Å	23.2816(5)	17.8138(43)	22.3800(8)
b / Å	41.7595(10)	43.313(11)	42.1796(14)
c / Å	4.0993(1)	3.9778(10)	4.6813(2)
β / °	90	90.798(49)	95.9104(8)
V / Å^3	3985.50	3080.09	4395.59
R_p / %	1.87	2.07	1.79
R_{wp} / %	3.50	2.85	2.98

Figure 24. (a) Proposed lattice changes in **C1N4DBC-1**, (b) table of the predicted crystalline lattice, and (c) PXRD patterns of **C1N4DBC-1**, **C1N4DBC-1a**, and **C1N4DBC-1(benzene)**.

Table 6. Lattice parameters estimated from PXRD patterns of **C1N4DBC-1**, **-1(benzene)**, and **-1a**.

Name	**C1N4DBC-1**	**C1N4DBC-1(benzene)**	**C1N4DBC-1a**
System	*Orthorhombic*	*Monoclinic*	*Monoclinic*
Space group	*Pnnn*	*Pn*	*Pn*
a / Å	23.2816(5)	22.3800(8)	17.8138(43)
b / Å	41.7595(10)	42.1796(14)	43.313(11)
c / Å	4.09925(8)	4.6813(2)	3.9778(10)
α / °	90	90	90
β / °	90	95.9104(8)	90.798(49)
γ / °	90	90	90
V / Å^3	3985.50	4395.59	3080.09
R_{wp} / %	3.50	2.95	2.85
R_p / %	1.87	1.79	2.07
Temperature / K	298	298	298

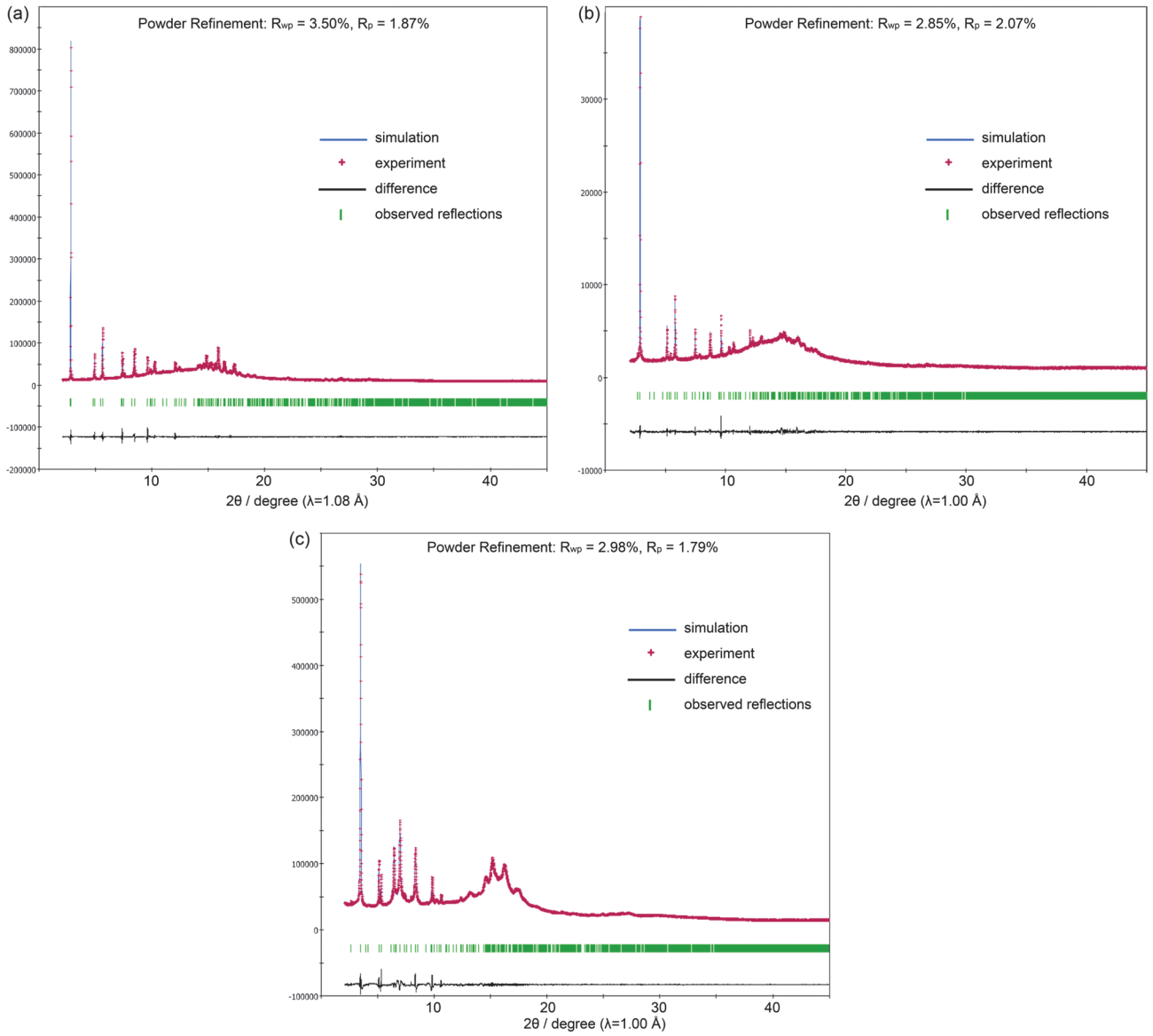

Figure 25. Pawley refinements of (a) **C1N4DBC-1**, (b) **C1N4DBC-1a**, and (c) **C1N4DBC-1(benzene)**: simulation (blue), experimental (red), difference (black, experimental minus refined profiles), and observed reflections (green).

4.11 Computational evaluation of stability

DFT calculations of the intermolecular interactions between two peripheral group molecules were done to investigate the stability of the HOFs. Dispersion-corrected complexation energies were calculated for each stack of carboxynaphthyl groups (major–major, major–minor, minor–minor stacking, Figure 26) and each type of H-bond (major–major, major–minor, minor–minor bonding, Figure 6) (Table 7).

No significant differences were observed in the complexation energy of stacking. The energy ranged from 7.40 kcal mol^{-1} to 8.31 kcal mol^{-1}. The complexation energy of H-bonding was significantly different depending on whether the H-bonding was dimeric or monomeric. The major–major and minor–minor bonds of **C2N6DBC**, which were truncated monomers, show small stabilization values of 9.42 kcal mol^{-1} and 3.14 kcal mol^{-1}, respectively. In addition, the self-complementary dimer, **C1N5DBC**, and the major–minor bond of **C2N6DBC** were strongly stabilized at approximately 20 kcal mol^{-1}. The **C1N5DBC-1** with square pores did not experience an anisotropic shrinkage as **C1N4DBC-1**, and the strong complementary dimers appeared to successfully maintain the initial structure. In **C2N6DBC-1**, while the dissociation of fragile bonds was more likely to occur, it was less likely to occur with strong bonds. While complementary H-bonded dimers firmly networked in **C1N5DBC-1**, **C2N6DBC-1** consisted of a mixture of less stabilized monomers and stable dimers. This coexistence of H-bonds resulted in disorderly structural collapse, leading to crystalline-to-amorphous transition.

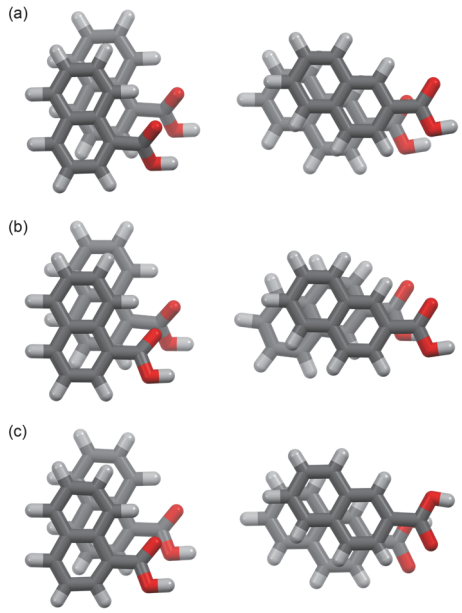

Figure 26. Optimized structures of stacking carboxynaphthyl groups between (a) major–major, (b) major–minor, and (c) minor–minor of (left) **C1N5DBC-1** and (right) **C2N6DBC-1**.

Table 7. Complexation energy (kcal mol^{-1}) of stacked dimers (stacking) and H-bonded dimers (H-bonding) of naphthoic acid groups in **C1N5DBC-1** and **C2N6DBC-1**.

Framework	**C1N5DBC-1**		**C2N6DBC-1**	
interactions	Stacking	H-bonding	Stacking	H-bonding
Major-Major	−7.24	−25.29 [b]	−7.42	−9.42 [a]
Minor-minor	−6.35	−19.88 [b]	−7.48	−21.88 [b]
Major-minor	−8.31	−22.57 [b]	−7.10	−3.14 [a]

[a] truncated H-bonding monomer. [b] Self-complementary H-bonding dimer

4.12 Conclusion

The isomeric effect of the peripheral groups in DBC-based building block molecules on structures and properties of isostructural HOFs were investigated. The HOFs were composed of DBC derivatives with 4-carboxybiphenyl, 1-carboxy-4-naphthyl, 1-carboxy-5-naphthyl, and 2-carboxy-6-naphthyl substituents (**CBPDBC**, **C1N4DBC**, **C1N5DBC**, and **C2N6DBC**, respectively). Results indicated that **CBPDBC** formed a homomorphic network with previously reported **CPDBC**, but only a low crystalline precipitate was obtained. In contrast, HOFs composed of naphthyl-substituted DBC derivatives successfully gave three isostructural HOFs that exhibited different transition behaviors depending on the naphthyl substituents (Table 8). The **C1N5DBC-1** formed a square pore through the complementary H-bonded dimer, which resulted in a stable HOF without a structural transition during guest removal. The activated HOF, **C1N5DBC-1a**, retained large pores with a $S_{A(BET)}$ of 1300 $m^2\ g^{-1}$ and was stable up to 220 °C. The **C1N4DBC-1**, which is a HOF with a structure similar to that of **CPDBC-1**, showed pore shrinkage along the *b* axis during guest removal, giving activated HOF, **C1N4DBC-1a**, with $S_{A(BET)}$ of 281 $m^2\ g^{-1}$. In situ PXRD measurements revealed that **C1N4DBC-1a** underwent reversible crystal-to-crystal structural transition upon loading and removal of benzene. These dynamic behaviors were due to the shape-fitted docking and hindered 1-naphthyl groups: *i.e.*, they prevented structural collapse against activation, and alternately, provided the framework with shrunk and divided channels. The **C2N6DBC-1** showed a crystalline-to-amorphous structural change because of large rhombic pores and the coexistence of weak and strong H-bonds caused by disordering of the peripheral groups. The results implied that the DBC core is fundamental to isostructural constructed HOFs, but that the isomeric effect at the peripheral groups significantly affected structural properties, ranging from stable to flexible to fragile. The behaviors observed were attributed to differences in pore geometry and H-bonding manner, due to the peripheral structure or its disorder. Investigation of the molecular design must include the study of peripheral groups as well, which is needed to control the systematic construction of HOFs with the desired structure and function.

Table 8. Summary of structural features and properties of isostructural HOFs based on DBC core.[a]

	CPDBC-1	**C1N4DBC-1x**[b]	**C1N5DBC-1**	**C2N6DBC-1**
RMSD of the DBC core plane	0.680	0.73	0.669	0.716
Bond angle of peripheral groups Ar-B / °	121.5	122	123.7	122.9
Dihedral angle of peripheral groups Ar-B / °	36.7	29	41.5	31.4
Stacking distance between DBC cores / Å	3.76	4.0	3.86	3.84
Void size / Å × Å	29.1×15.3	9.8×8.4, 4.9×6.4	26.8×23.3	22.7×17.9
Void ratio / %	56.4	32	58.3	58.4
Structure after guest removal	Retained the framework	Shrunk the pore	Retained the framework	Collapsed into an amorphous solid
BET surface area / $m^2\ g^{-1}$	1548	281	1300	113
	Ref. 43 (Chapter 3)	this work	this work	this work

[a] "Ar" and "B" means aromatic moieties shown in Figure 1. This table focused on the major moieties of the disorder for simplicity.
[b] Single crystal structure after activation form the electron diffraction experiment.

4.13 Experimental section

All reagents and solvents were used as received from commercial suppliers. Gel permeation chromatography (GPC) was performed on JAIGEL-1H and -2H with $CHCl_3$ as a solvent. ^{1}H and ^{13}C NMR spectra were measured on a JEOL 400 YH (400 MHz) spectrometer or Bruker AV400M (400 MHz) spectrometer. Residual proton and carbon of deuterated solvents were used as internal standards for the measurements: δ = 7.26 ppm ($CDCl_3$) and δ = 2.49 ppm (DMSO-d_6) for ^{1}H NMR, δ = 77.00 ppm ($CDCl_3$) and δ = 39.50 ppm (DMSO-d_6) for ^{13}C NMR. HR-MS analyses were conducted on a JEOL JMS-700 instrument or autoflex III Bruker. Thermo gravimetric Scheme(TG) analyses were performed on Rigaku Thermo plus EVO2 (TG-DTA8122) under an N_2 purge (300 mL/min) at a heating rate of 5 °C min^{-1}. Crystal structures were drawn using mercury[52] or VESTA[53] software.

4.13.1 Synthesis of building blocks

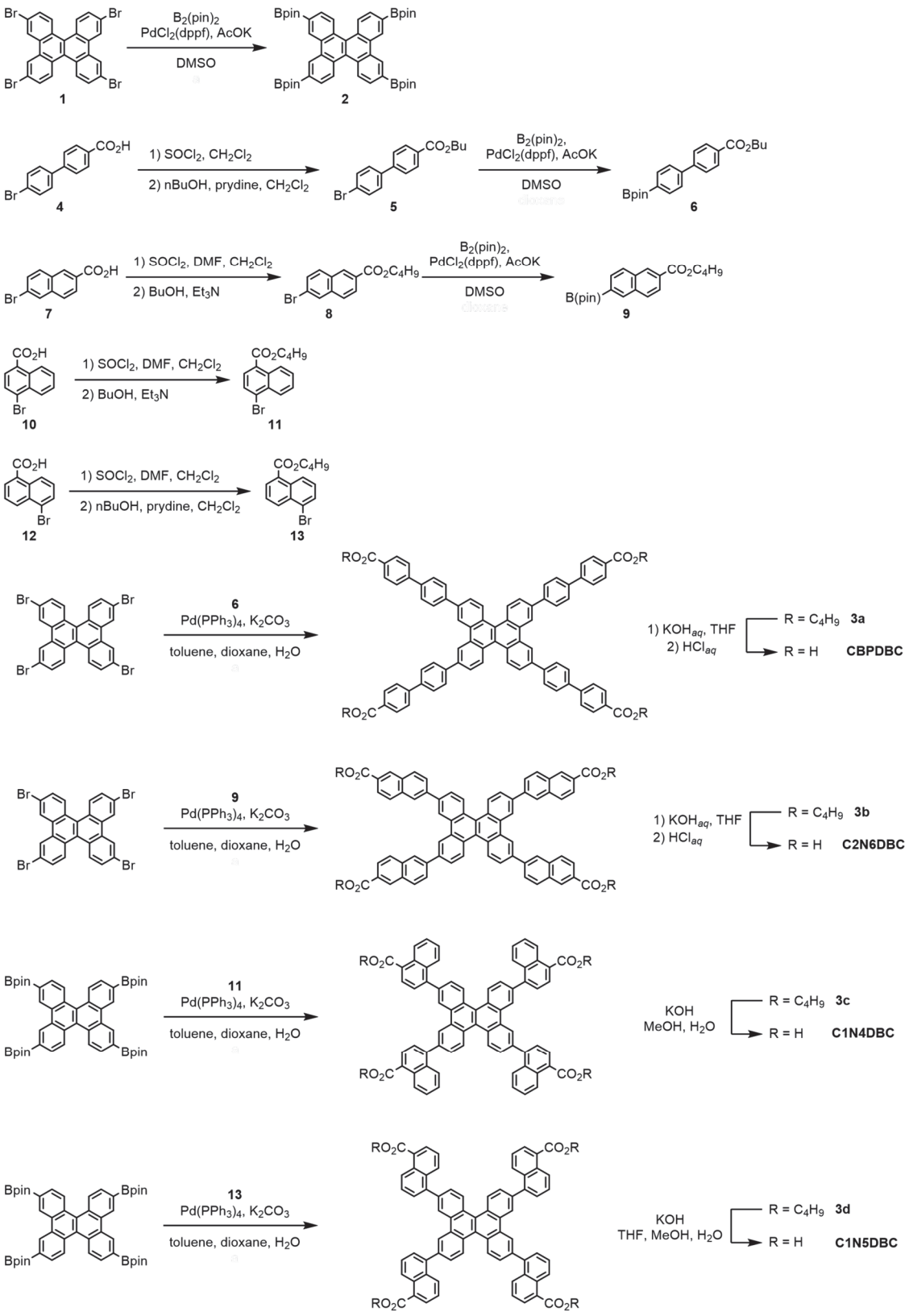

Scheme 2. Synthesis of DBC derivatives. Compound **1**, **5**, and **6** was synthesized by a reported procedure[73,74].

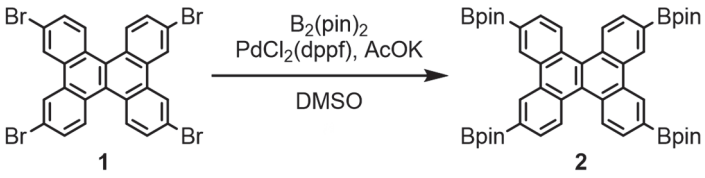

Synthesis of 2. A 100 mL three-necked flask was charged with compound **1** (1.10 g, 1.71 mmol), B_2pin_2 (2.16 g, 8.50 mmol), AcOK (1.47 g, 15.0 mmol), and $PdCl_2(dppf)$ (0.279 g, 0.341 mmol) under nitrogen. Then degassed DMSO (35 mL) were added and at vacuumed at rt for 15 min. The reaction mixture was stirred at 90 °C for 24 h. After cooled to room temperature, the reaction mixture was poured into water (300 mL). was collected by filtration and washed well with water. The dried crude product was purified with short column chromatography (silica gel, $CHCl_3$), following wash with hexane to give compound **2** as a pale-yellow solid (0.959 g, 68%).

M.p. 289 °C. ^{1}H NMR (400 MHz, $CDCl_3$): δ 9.27 (s, 4H), 8.65 (d, 4H, *J* = 8.0 Hz), 8.03 (d, 4H, *J* = 8.4 Hz), 1.46 (s, 48H) ppm. ^{13}C NMR (100 MHz, $CDCl_3$): δ 132.23, 131.25, 130.78, 130.45, 129.04, 128.04, 84.08, 24.97 ppm.

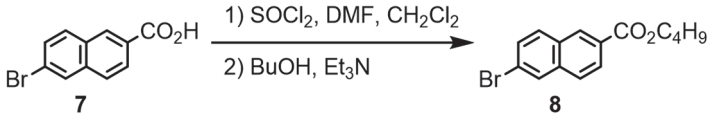

Synthesis of 8.

A 300 mL three-necked flask was charged with 6-bromo-2-naphthoic acid (1.55 g, 6.17 mmol) in dehydrated CH_2Cl_2 (20 mL) under nitrogen. Then $SOCl_2$ (0.45 mL, 6.05 mmol) and DMF (1 drop) were added dropwise at rt. The mixture was refluxed at 45 °C for 6 h. After cooling to room temperature, solvent was removed under vacuum and dissolved dehydrated CH_2Cl_2. Then dehydrated n-butanol (1.5 mL) and triethylamine (5.0 mL) were added and stirred at rt for 18 h. The organic phase was diluted with CH_2Cl_2 (40 mL) and washed with HCl_{aq}, water and brine, dried with anhydrous $MgSO_4$, and filtered. The crude product was purified with short column chromatography (silica gel, AcOEt/hexane = 1/2) to give compound **8** (1.41 g, 92%) as a colourless oil.

^{1}H NMR (400 MHz, $CDCl_3$): δ 8.56 (s, 1H), 8.14–8.04 (m, 2H), 7.86–7.76 (m, 2H), 7.60–7.50 (m, 1H), 4.39 (t, 2H, *J* = 6.8 Hz) , 1.85–1.75 (m, 2H) , 1.51–1.30 (m, 6H) , 1.01 (t, 3H, *J* = 7.4 Hz) ppm. ^{13}C NMR (100 MHz, $CDCl_3$): δ 166.44, 136.37, 130.94, 130.83, 130.75, 130.11, 129.90, 128.26, 127.16, 126.40, 122.51, 65.12, 30.83, 19.30, 13.76 ppm. HR-MS (EI^+): calcd. For $C_{15}H_{15}O_2Br$ $[M]^+$ 306.0255; found: 306.0255.

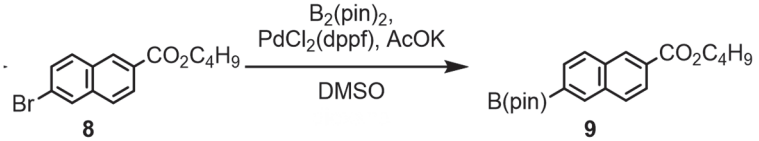

Synthesis of 9. A 100 mL three-necked flask was charged with compound **8** (4.00 g, 13.0 mmol), B_2pin_2

(3.34 g, 13.2 mmol), AcOK (3.14 g, 32.0 mmol), and $PdCl_2$(dppf) (0.503 g, 0.783 mmol) under nitrogen. Then degassed dioxane (25 mL) were added and the mixture was stirred at 100 °C for 18 h. After removing solvent under vacuum, the product was extracted with $CHCl_3$. The organic phase was combined and washed with water, dried with anhydrous $MgSO_4$, and filtered. The crude product was purified with column chromatography (silica gel, AcOEt / hexane = 1 / 2) to give compound **9** (3.73 g, 81%) as a white solid.
M.p. 57 °C. ^{1}H NMR (400 MHz, $CDCl_3$): δ 8.58 (d, 1H, *J* = 1.2 Hz), 8.39 (s, 1H), 4.32 (dd, 1H, *J* = 8.8, 1.6 Hz), 8.00–7.90 (m, 3H), 4.39 (t, 2H, *J* = 6.6 Hz), 1.84–1.77 (m, 2H), 1.55–1.48 (m, 2H), 1.40 (s, 12H), 1.01 (t, 3H, *J* = 7.4 Hz) ppm. ^{13}C NMR (100 MHz, $CDCl_3$): δ 166.7, 135.8, 134.7, 134.0, 131.1, 128.8, 128.7, 128.3, 125.2, 84.09, 83.44, 63.97, 30.82, 24.99, 19.29, 13.74 ppm.

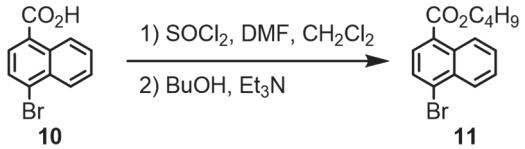

10 **11**

Synthesis of 11. A 300 mL three-necked flask was charged with 4-bromo-1-naphthoic acid (2.00 g, 7.97 mmol) in dehydrated CH_2Cl_2 (20 mL) under nitrogen. Then $SOCl_2$ (0.65 mL, 9.00 mmol) and DMF (1 drop) were added dropwise at rt. The mixture was refluxed at 50 °C for 2 h. After cooling to room temperature, solvent was removed under vacuum and dissolved dehydrated CH_2Cl_2. Then dehydrated n-butanol (2.0 mL) and pyridine (4.0 mL) were added and stirred at rt for 18 h. The organic phase was diluted with CH_2Cl_2 (40 mL) and washed with 3M-HCl_{aq}, water and brine, dried with anhydrous $MgSO_4$, and filtered. The crude product was purified with short column chromatography (silica gel, CH_2Cl_2) to give compound **11** (2.00 g, 82%) as a colorless oil.
^{1}H NMR (400 MHz, $CDCl_3$): δ 9.00–8.90 (m, 1H), 8.40–8.30 (m, 1H), 7.98 (d, 1H, *J* = 7.6 Hz), 7.83 (d, 1H, *J* = 7.6 Hz), 7.70–7.60 (m, 2H), 4.42 (t, 2H, *J* = 6.8 Hz), 1.87–1.75 (m, 2H), 1.57–1.45 (m, 2H), 1.01 (t, 3H, *J* = 7.4 Hz) ppm. ^{13}C NMR (100 MHz, $CDCl_3$): δ 166.78, 132.27, 131.99, 129.75, 128.70, 128.18, 127.45, 127.35, 127.22, 126.15, 64.97, 30.66, 19.23, 13.65 ppm. HR-MS (EI$^+$): calcd. For $C_{15}H_{15}O_2Br$ $[M]^+$ 306.0255; found: 306.0240.

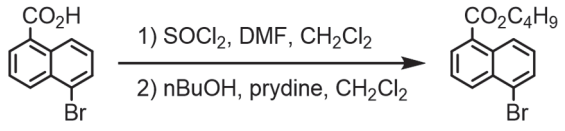

12 **13**

Synthesis of 13. In a 100 mL three necked flask was stirred a mixture of 5-bromo-1-naphthoic acid (1.00 g, 3.98 mmol), H_2SO_4 (0.050 mL) in ^{n}BuOH (15 mL). The mixture was stirred at reflux (100 °C) for 18 h, and then cooled to ambient temperature. The solution was poured into sat. $NaHCO_{3aq}$ and extracted with CH_2Cl_2. The organic phase was combined and washed with water, sat. $NaHCO_{3aq}$, and brine, dried with anhydrous $MgSO_4$, and filtered. The crude product was purified with column chromatography (silica gel, CH_2Cl_2) to give compound **13** (2.09 g, 70%) as a pale-yellow oil.

^{1}H NMR (400 MHz, $CDCl_3$): δ 8.89 (dt, 1H, *J* = 8.8, 1.0 Hz), 8.45 (dt, 1H, *J* = 8.8, 1.0 Hz), 8.20 (dd, 1H, *J* = 7.2, 1.2 Hz), 7.85 (dt, 1H, *J* = 8.0, 0.8 Hz), 7.61 (dd, 1H, *J* = 8.6, 7.4 Hz), 7.44 (dt, 1H, *J* = 8.8, 7.2 Hz), 4.43 (t, 2H, *J* = 6.8 Hz) , 1.87–1.77 (m, 2H), 1.58–1.48 (m, 2H), 1.01 (t, 3H, *J* = 7.8 Hz) ppm. ^{13}C NMR (100 MHz, $CDCl_3$): δ 16629, 132.67, 132.26, 132.07, 130.54, 130.48, 128.24, 127.77, 125.90, 125.77, 123.27, 65.22, 30.81, 19.35, 13.75 ppm. HR-MS (EI^+): calcd. For $C_{15}H_{15}O_2Br$ $[M]^+$ 306.0255; found: 306.0254.

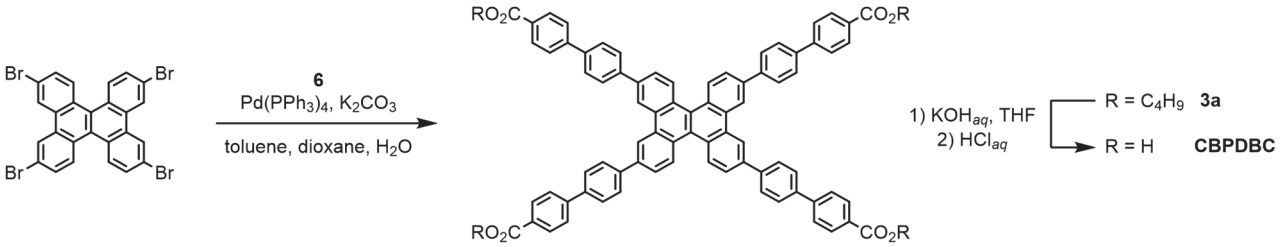

Synthesis of 3a. A 300 mL three-neck flask was charged with compound **1** (0.501 g, 0.778 mmol), compound **6** (1.42 g, 3.72 mmol), K_2CO_3 (1.10 g, 7.96 mmol), and $Pd(PPh_3)_4$ (0.201 g, 0.174 mmol) in degassed toluene (10 mL), dioxane (25 mL), and H_2O (3 mL) under nitrogen. Then the reaction mixture was stirred at 110 °C for 48 h. The solution was blue on the surface due to fluorescence and yellow inside. After removing solvent under vacuum, the product was extracted with $CHCl_3$, washed with water, dried with anhydrous $MgSO_4$, and filtered to give a yellow-brown solid. The crude product was purified by preparative HPLC to give compound **3a** (0.509 g, 49%) as a yellow solid.

M.p. 272 °C. ^{1}H NMR (400 MHz, $CDCl_3$): δ 8.97 (s, 4H), 8.79 (d, 4H), 8.16 (d, 4H), 7,94 (d, 8H), 7.79 (m, 14H), 4.38 (t, 8H), 1.80 (m, 8H), 1.01 (t, 12H) ppm. ^{13}C NMR (100 MHz, $CDCl_3$): δ 166.45, 144.68, 140.43, 139.06, 138.03, 130.96, 130.19, 129.51, 129.20, 128.40, 127.20, 126.87, 126.19, 125.37, 121.61, 64.92, 30.85, 19.32, 13.79 ppm. HR-MS (MALDI): calcd. For $C_{94}H_{80}O_8$ $[M]^+$ 1336.5848; found: 1336.5866.

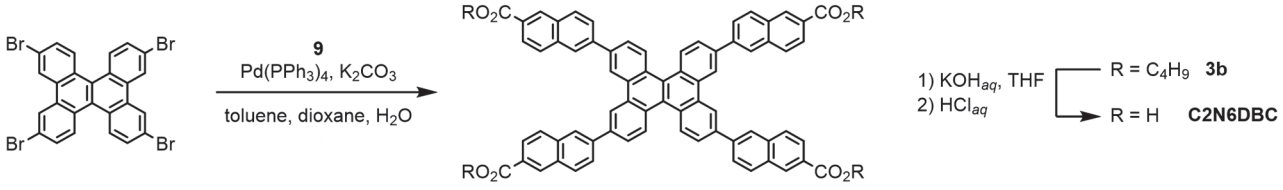

Synthesis of 3b. A 100 mL three-necked flask was charged with compound **9** (705 mg, 3.10 mmol), compound **1** (250 mg, 0.388 mmol), $Pd(PPh_3)_4$ (98.7 mg, 0.0852 mmol), and K_2CO_3 (414 mg, 3.01 mmol) in degassed toluene (10 mL), dioxane (15 mL) and degassed water (5 mL) under nitrogen. Then the reaction mixture was refluxed at 110 °C for 48h. After removing solvent under vacuum, the product was extracted with $CHCl_3$. The organic phase was combined and washed with water, dried with anhydrous $MgSO_4$, and filtered. The crude product was purified with column chromatography (silica gel, $CHCl_3$/hexane = 1/2→1/1) and preparative HPLC to give compound **3b** (68.6 mg, 41%) as a yellow solid.

M.p. 246 °C. ^{1}H NMR (400 MHz, $CDCl_3$): δ 8.45 (s, 4H), 8.24 (s, 4H), 7.94 (d, 4H, *J* = 8.4 Hz), 7.77 (s, 4H), 7.74 (d, 4H, *J* = 8.4 Hz), 7.61 (d, 4H, *J* = 8.8 Hz), 7.55 (d, 4H, *J* = 8.0 Hz), 7.33 (d, 4H, *J* = 8.4 Hz), 4.44 (t, 8H, *J* = 6.6 Hz), 1.93–1.77 (m, 8H), 1.67–1.50 (m, 8H), 1.08 (d, 12H, *J* = 7.4 Hz) ppm. ^{13}C NMR (100 MHz, $CDCl_3$): δ 166.63, 140.09, 138.18, 135.67, 131.71, 130.60, 130.00, 129.16, 128.37, 128.33, 127.98, 126.12, 125.88, 125.68, 125.62, 121.95, 65.09, 30.91, 19.38, 13.85 ppm. HR-MS (MALDI): calcd. For $C_{86}H_{72}O_8$ $[M]^+$ 1232.5222; found: 1232.5221.

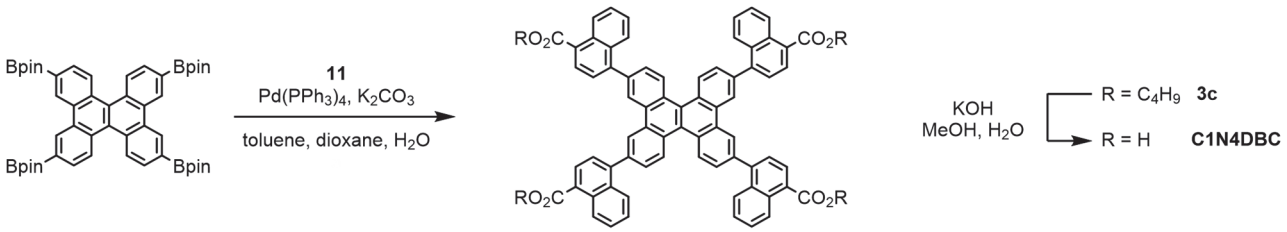

Synthesis of 3c. A 100 mL schulenk tube was charged with compound **2** (0.740 g, 0.889 mmol), compound **11** (1.23 g, 4.00 mmol), $Pd(PPh_3)_4$ (0.231 mg, 0.200 mmol), and K_2CO_3 (1.42 mg, 10.3 mmol) in degassed toluene (15 mL), dioxane (5.0 mL) and degassed water (3.0 mL) under nitrogen. Then the reaction mixture was refluxed at 110 °C for 24 h. After removing solvent under vacuum, the product was extracted with $CHCl_3$. The organic phase was combined and washed with water, dried with anhydrous $MgSO_4$, and filtered. The crude product was purified with column chromatography (silica gel, $CHCl_3$/hexane = 1/1→1/0) and preparative HPLC to give compound **3c** (314 mg, 29%) as a yellow green solid.

M.p. 172 °C. ^{1}H NMR (400 MHz, $CDCl_3$): δ 9.02 (d, 8H, *J* = 8.4 Hz), 9.85 (d, 4H, *J* = 1.6 Hz), 8.26 (d, 4H, *J* = 7.6 Hz), 8.09 (d, 4H, *J* = 8.4 Hz), 7.88 (d, 4H, *J* = 1.6 Hz), 7.70–7.58 (m, 4H), 4.46 (t, 8H, *J* = 6.6 Hz), 1.80–1.70 (m, 8H), 1.60–1.50 (m, 8H), 1.46 (t, 12H, *J* = 6.6 Hz) ppm. ^{13}C NMR (100 MHz, $CDCl_3$): δ 167.64, 144.74, 138.94, 132.25, 131.87, 130.95, 129.39, 128.97, 128.92, 128.86, 127.87, 127.41, 126.59, 126.51, 126.23, 126.10, 125.12, 65.04, 30.88, 19.40, 13.79 ppm. HR-MS (FAB^+): calcd. For $C_{86}H_{72}O_8$ $[M]^+$ 1232.5222; found: 1232.5230.

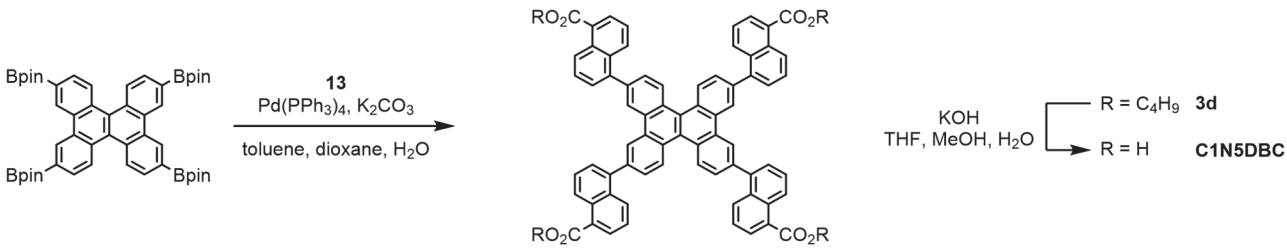

Synthesis of 3d. A 100 mL schulenk tube was charged with compound **2** (740 mg, 0.889 mmol), compound **13** (882 mg, 2.87 mmol), $Pd(PPh_3)_4$ (161 mg, 0.140 mmol), and K_2CO_3 (830 mg, 6.00 mmol) in degassed dioxane (25 mL) and degassed water (3.0 mL) under nitrogen. Then the reaction mixture was refluxed at 100 °C for 24h. After removing solvent under vacuum, the product was extracted with $CHCl_3$. The organic

phase was combined and washed with water, dried with anhydrous $MgSO_4$, and filtered. The crude product was purified by flash purification (Isorera one®, Sfär HC Duo 10g, $CHCl_3$/hexane = 1/2 → 1/1) and preparative HPLC to give compound **3d** (250 mg, 34%) as a yellow green solid.

M.p. 227 °C (decomp.). ^{1}H NMR (400 MHz, $CDCl_3$): δ 9.01 (d, 4H, *J* = 8.4 Hz), 8.96 (d, 4H, *J* = 7.6 Hz), 8.84 (d, 4H, *J* = 0.8 Hz), 8.24 (d, 4H, *J* = 8.4 Hz), 8.17 (d, 4H, *J* = 6.4 Hz), 7.85 (d, 4H, *J* = 8.8 Hz), 7.77–7.60 (m, 8H), 4.46 (t, 8H, *J* = 8.2 Hz), 1.90–1.75 (m, 8H), 1.65–1.50 (m, 8H), 1.02 (d, 12H, *J* = 7.8 Hz) ppm. ^{13}C NMR (100 MHz, $CDCl_3$): δ 167.86, 140.39, 139.32, 132.28, 131.72, 131.01, 130.97, 129.81, 128.91, 128.72, 127.23, 127.68, 127.04, 125.73, 125.27, 124.83, 65.07, 30.87, 19.39, 13.78 ppm. HR-MS (MALDI): calcd. For $C_{86}H_{72}O_8$ $[M]^+$ 1232.5222; found: 1232.5230.

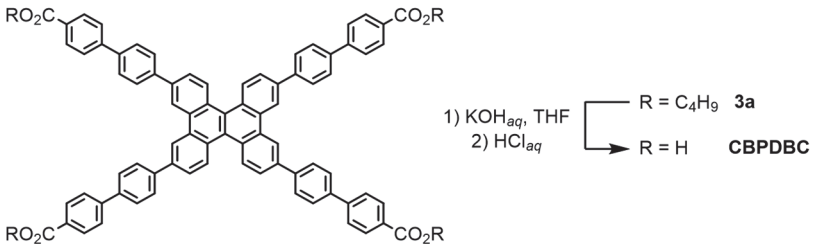

Synthesis of CBPDBC. A 100 mL round-bottomed flask was charged with compound **3a** (143 mg, 106 μmol) and 5%KOH_{aq} (10 mL), and THF (10 mL). Then the suspension was refluxed at 80 °C for 48 h. After removing THF in vacuo, the resultant water suspension was neutralized by 3M-HCl_{aq}. The precipitate was separated by centrifuge, and washed with water three times, methanol once, and acetone once to give **CBPDBC** (119 mg, 99%) as a yellow solid.

M.p. >300 °C. ^{1}H NMR (400 MHz, DMSO-d_6): δ 8.74 (d, 16H, *J* = 2.0 Hz), 8.43 (d, 16H, *J* = 8.8 Hz), 7.76 (q, 12H, *J* = 6.8 Hz) ppm. HR-MS (FAB^+): calcd. For $C_{78}H_{48}O_8$ $[M]^+$ 1112.3343; found: 1112.3349.

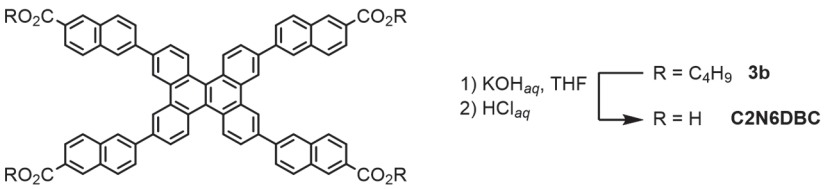

Synthesis of C2N6DBC. A reaction mixture of compound **3b** (134 mg, 0.109 mmol) in THF (40 mL), MeOH (10 mL), and 5%-KOH aqueous solution (40 mL) was stirred for 2 days at 90 °C. After cooled to room temperature, organic phase was removed in vacuo, following addition of 5M-H_2SO_{4aq} into the reaction mixture until precipitate was not formed anymore. The precipitate was collected by filtration, washed well with water, MeOH, $CHCl_3$, and acetone. The filtrate was dried in vacuo to yield **C2N6DBC** (78.7 mg, 71%) as yellow green solid.

M.p. >300 °C. ^{1}H NMR (400 MHz, DMSO-d_6): δ 9.53 (s, 4H), 8.85 (d, 4H, J = 8.8 Hz), 8.70 (s, 8H), 8.45–8.25 (m, 12H), 8.17 (d, 4H, J = 6.0 Hz), 8.05 (d, 4H, J = 9.6 Hz) ppm. ^{13}C NMR (100 MHz, DMSO-d_6, ca. 10 mg/mL): δ 167.37, 139.23, 137.34, 135.15, 133.38, 131.32, 130.46, 130.14, 129.71, 128.47, 128.01, 127.49, 126.33, 126.27, 125.49, 125.26, 121.96 ppm. HR-MS (MALDI): calcd. For $C_{70}H_{40}O_8$ $[M]^+$ 1008.2718; found: 1008.2724.

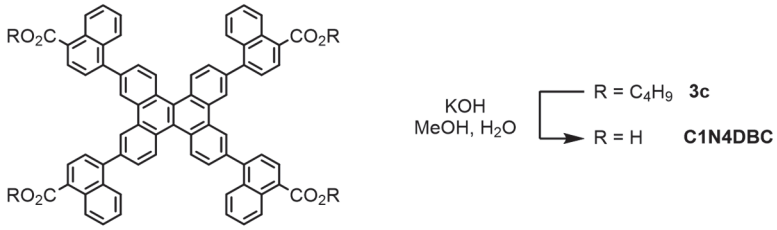

Synthesis of C1N4DBC. A 50 mL round-bottomed flask was charged with compound **3c** (120 mg, 0.0975 μmol) and KOH (800 mg, 14.3 mmol) in MeOH (35 mL) and water (2.0 mL). Then the suspension was refluxed at 90 °C for 3 days. After cooled to room temperature, H_2SO_{4aq} was added into the reaction mixture following stirring over 1h. The precipitate was collected by filtration, washed well with water, MeOH, $CHCl_3$, and acetone. The filtrate was dried in vacuo to yield **C1N4DBC** (75.8 mg, 77%) as yellow green solid.
M.p. >300 °C. ^{1}H NMR (400 MHz, DMSO-d_6): δ 9.13 (s, 4H), 9.02 (d, 4H, J = 9.6 Hz), 8.98 (d, 4H, J = 9.6 Hz), 8.21 (d, 4H, J = 8.0 Hz), 8.06 (d, 4H, J = 8.8 Hz), 7.96 (d, 4H, J = 8.8 Hz), 7.75 (d, 4H, J = 7.6 Hz), 7.66 (t, 4H, J = 7.2 Hz), 7.58 (t, 4H, J = 7.2 Hz) ppm. ^{13}C NMR (100 MHz, DMSO-d_6, ca.10 mg mL^{-1}): δ 167.64, 144.74, 138.94, 132.25, 131.87, 130.95, 129.39, 128.97 128.92, 127.87, 127.56, 127.41, 126.59, 126.51, 126.23, 126.10, 125.12 ppm. HR-MS (MALDI): calcd. For $C_{70}H_{40}O_8$ $[M]^+$ 1008.2718; found: 1008.2719.

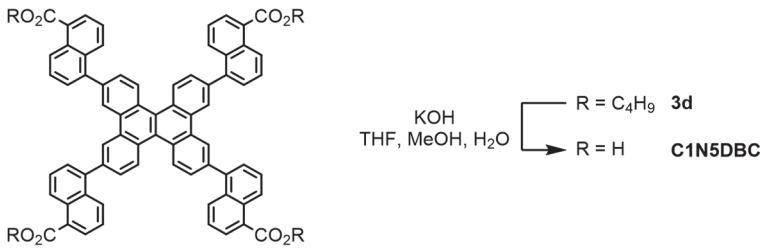

Synthesis of C1N5DBC. A 100 mL shulenck tube was charged with compound **3d** (190 mg, 0.154 mmol) and KOH (505 mg, 9.00 mmol) in THF (12 mL), MeOH (5.0 mL), and water (6.0 mL). Then the suspension was refluxed at 70 °C for 3days. After cooled to room temperature, 4M-HCl_{aq} was added into the reaction mixture until precipitate was not formed anymore. The precipitate was collected by centrifugation, washed well with water, and corrected by filtration. The filtrate was washed well with H_2O, MeOH, and $CHCl_3$, and dried in vacuo. Then this crude solid was dissolved in DMF to remove white insoluble and purified with recrystallization to yield **C1N5DBC** (106 mg, 68%) as light green solid.

M.p. >300 °C. ^{1}H NMR (400 MHz, DMSO-d_6): δ 9.09 (s, 4H), 9.02 (d, 4H, J = 8.8 Hz), 8.96–8.87 (m, 4H), 8.25–8.05 (m, 8H), 7.93 (d, 4H, J = 8.8 Hz), 7.78–7.70 (m, 8H), 7.58 (t, 4H, J = 7.8 Hz) ppm. ^{13}C NMR (100 MHz, DMSO-d_6, ca. 7 mg mL^{-1}): δ 168.84, 139.75, 138.83, 131.51, 130.96, 130.49, 130.11, 129.37, 129.23, 128.71, 128.47, 127.81, 127.75, 126.91, 126.88, 125.40, 125.28 ppm. HR-MS (MALDI): calcd. For $C_{70}H_{40}O_8$ $[M]^+$ 1008.2718; found: 1008.2712.

4.13.2 Single crystal X-ray or electron diffraction measurement and analysis

Diffraction data of **C2N6DBC-1**, **C2N6DBC-2** and **C1N5DBC-1** were collected with synchrotron radiation (λ = 0.81981, 0.81063 and 0.81059 Å, respectively) at BL40XU in SPring-8[62–64]. A Data of **C1N4DBC-1x** was collected with electron radiation (λ = 0.0251 Å) using a Rigaku Synergy-ED equipped with a Rigaku HyPix3000 fast detector (Table 9). Diffraction Data collection, cell refinement, and data reduction were carried out with CrysAlis PRO[54]. SHELXT[55] was used for the structure solution of the crystals. These calculations were performed with the observed reflections [$I > 2\sigma(I)$] with the program OLEX-2 crystallographic software[56–58]. Structural refinement was performed by SHELXL[59]. All non-hydrogen atoms were refined with anisotropic displacement parameters, and hydrogen atoms were placed in idealized positions and refined as rigid atoms with the relative isotropic displacement parameters. SQUEEZE function equipped in the PLATON program was used to treat severely disordered solvent molecules in voids[60,61].

Table 9. Crystal data of **C1N5DBC-1** and **C2N6DBC-1**, **C2N6DBC-2**, and **C1N4DBC-1x**.

	C1N5DBC-1	**C2N6DBC-1**	**C2N6DBC-2**	**C1N4DBC-1x**
Chemical formula	$C_{70}H_{40}O_8$	$C_{70}H_{40}O_8$	$C_{70}H_{40}O_8$	$C_{70}H_{40}O_8$
F_w	1009.02	1009.02	1009.02	1009.02
Crystal system	*Orthorhombic*	*Orthorhombic*	*Orthorhombic*	*Monoclinic*
space group	*Pban*	*Pban*	*Fddd*	*C2/c*
Temperature / K	293	293	293	293
a / Å	38.629 (1)	48.3296 (8)	52.040 (4)	4.0 (5)
b / Å	32.6902 (13)	28.3016 (10)	97.015 (2)	35.6 (15)
c /Å	3.8606 (1)	3.8380 (1)	3.7969 (1)	43.4 (8)
V / Å^3	4875.1 (3)	5249.6 (2)	19169.3 (16)	6249 (869)
Z	2	2	8	4
Radiation type	Synchrotron, λ = 0.81059 Å	Synchrotron, λ = 0.81081 Å	Synchrotron, λ = 0.81063 Å	Transmission electron micro-scope, λ = 0.0251 Å
Crystal size / mm	0.15 × 0.03 × 0.03	0.20 × 0.02 × 0.01	0.20 × 0.05 × 0.002	0.001 × 0.001 × 0.001
No. of measured, Independent, and observed [I > 2σ(I)] reflections	54995, 5966, 4288	43209, 6244, 3155	40772, 5693, 1901	5507, 2631, 1013
R_{int}	0.074	0.088	0.091	0.130
$(\sin\theta/\lambda)_{max}$ / Å^{-1}	0.677	0.676	0.679	0.500
$R_1[F^2 > 2\sigma(F^2)]$, $wR_2(F^2)$, *S*	0.087, 0.292, 1.12	0.104, 0.358, 1.14	0.098, 0.363, 0.94	0.277, 0.664, 1.03
No. of reflections	5966	6244	5693	2631
No. of parameters	205	247	235	306
No. of restraints	199	431	264	546
$\Delta\rho_{max}$, $\Delta\rho_{min}$ / e Å^{-3}	0.45, −0.18	0.28, −0.14	0.28, −0.16	0.34, −0.24
CCDC Nos.	2210180	2210179	2210181	—

4.13.3 Powder X-ray diffraction measurement

Powder X-ray diffraction (PXRD) data were collected on a Rigaku Ultima-IV (40 kV, 44 mA) or PANalytical XPert PRO X'Celerator (45 kV, 40 mA) using Cu-Kα radiation at room temperature and with a scan rate of 2.0° min^{-1}, or 1.2° min^{-1}, respectively. For structural analysis and *in situ* experiment, the powder samples were loaded in a Lindemann glass capillary with 0.5 mm outer diameter (for a measurement with gas or vaper introduction) or a borosilicate glass capillary with 0.5 mm outer diameter (for a measurement under ambient condition or heat). The diffraction data were recorded using a MYTHEN detector with the synchrotron radiation (λ = 1.0000 or 1.0800 Å) at BL02B2 in SPring-8[62–64] with the approval of JASRI (proposal No. 2021A1567). The Pawley PXRD refinement is performed using the Reflex module in the Material Studio ver. 6.0[65], in which a Pseudo-Voigt profile function was used for the profile fitting (background subtracting, peak smoothing, and broadening were taken into account). Then the powder pattern was indexed by the X-cell[66] software, following the Pawley refinement[67] of the cell was performed

(2° < 2θ < 45°) and assigned to each space group. [**C1N4DBC-1**: *Pnnn*, **C1N4DBC-1a**: *Pn*, **C1N4DBC-1(benzene)**: *Pn*]

4.13.4 VT-PXRD measurement

VT-PXRD of **C1N5DBC-1** and **C2N6DBC-1** were collected in a Rigaku Ultima-IV (40 kV, 44 mA) with a temperature control unit. For this VT-PXRD, the HOF powders were placed on an aluminum substrate, and the measurements were conducted in atmospheric conditions. The sample temperature increased from room temperature to 360 °C with a rate of 1.0 °C min^{-1}. PXRD scan of each measurement was collected with a difference in the temperature of ca. 6 °C. A VT-PXRD of **C1N4DBC-1** were conducted at BL02B2 in SPring-8. The powder samples were loaded in a borosilicate glass capillary with 0.5 mm outer diameter. The diffraction data were recorded using a MYTHEN detector with the synchrotron radiation (λ = 1.0800 Å) with 10-°C steps.

4.13.5 *In situ* sorption-PXRD measurements

In situ sorption-PXRD measurements of **C1N4DBC-1a** were performed for N_2, CO_2, and benzene vapor. The crystalline powder of **C1N4DBC-1a** was placed into a borosilicate glass capillary with a diameter of 0.5 mm. The diffraction patterns were recorded using a MYTHEN detector with synchrotron radiation (λ = 1.0000 Å) at beamline BL02B2 of SPring-8. The patterns of gas were recorded at 198 K by increasing the pressure to 0 atm, 0.5 atm, and 1 atm, then decreasing the pressure to 0.5 atm and 0 atm in that order. The patterns of benzene vapor were recorded at 298 K as the vapor was gradually loaded at 0 kPa to 10 kPa with 1-kPa steps and removed to 0 kPa, following activated at 333 K under vacuum to thoroughly remove benzene in the channel.

4.13.6 Powder X-ray diffraction analysis of **C1N4DBC-1a**

The calculation was performed using the Reflex Plus software implemented in Material Studio ver 6.0[65]. The powder pattern was indexed by the X-cell[66] software using 28 reflections, resulting in 5 solutions. A top-ranked solution with relative figures of merit of 0.626*,* the zero-point shift of −0.00667°, and two impurity peaks were refined by the Pawley method (2° < 2θ < 45°) and assigned to space group *Pn* (#7). The Pawley refinement[67] of the cell was again performed (2° < 2θ < 45°). The subsequent crystal structure solution was carried out by using the Monte Carlo/parallel tempering method using the Powder Solve software[68]. Atomic coordinates in the initial structures were adopted by optimizing the single crystal structure of electron diffraction measurement without bonding between the DBC core and naphthyl group by DFT method at B3LYP-D3/6-31G** level. In the Monte Carlo calculation, lengths and angles of covalent bonds between the DBC core and naphthyl groups were refined. A Rietveld refinement[69] (2° < 2θ < 50°) was performed under the following conditions: (1) The pseudo-Voigt function was used for the simulation of the peak shape. (2)

The Bragg-Brentano method was used for line shift refinement. (3) The Berar-Baldinozzi method[70] as used for asymmetric refinement. (4) The background was determined by linear interpolation using 20 terms. (5) The March-Dollas method[70] was applied to correct the effects of preferred orientation. (6) For the refinement of temperature factors, global isotropic temperature factors were used. The molecular conformation was refined by varying the torsion angles around all single bonds. Crystal data for **C1N4DBC-1a**: $C_{70}H_{40}O_8$, *Fw* 1009.082, monoclinic, space group *Pn* (#7), a = 17.8138(43) Å, b = 43.313(11) Å, c = 3.9778(10) Å, β = 90.798(49)°, V = 3068.85 Å^3, Z = 2, d = 1.092 g cm^{-3}, T = 298(2) K, R_p = 0.0501, R_{wp} = 0.0759.

4.13.7 Adsorption/desorption experiments

Gas sorption. The activated bulk samples of **C1N4DBC-1a**, **C1N5DBC-1a**, and **C2N6DBC-1a** were used for gas sorption measurements, which were performed on BELSORP-max (BEL, Japan). The adsorption isotherms of N_2, CO_2 were corrected at 77K and 195 K, respectively. The $S_{A(BET)}$ and d_{NLDFT} were calculated based on N_2 absorption isotherms (Figure 27).

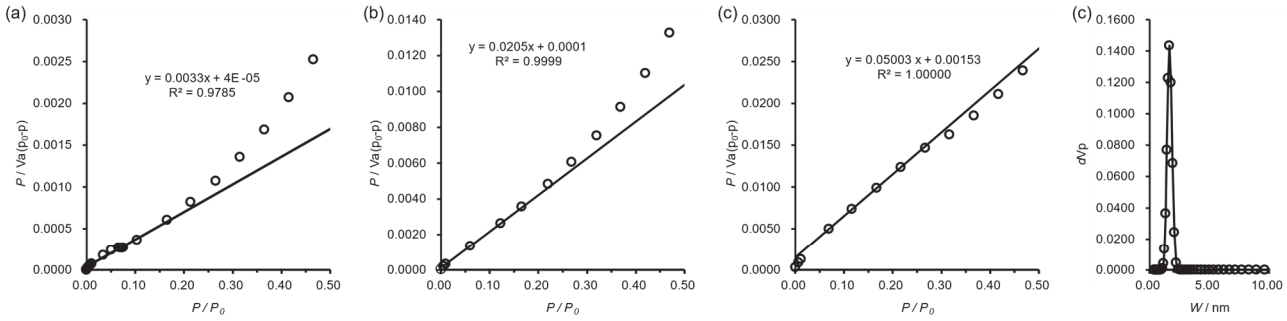

BET range limit	(p/p0=0.1224)
Maxumum Va(p_0-p)	4720.7
Vm [cm^3(STP) g^{-1}]	48.458
as(BET) [m^{2}g^{-1}]	2.81E+02
C	175.62
Total pore volume (p/p0=0.990) [cm^{3}g^{-1}]	0.2236
Average pore size [nm]	3.1806

BET range limit	(p/p0=0.3670)
Maxumum Va(p_0-p)	2.88E+04
Vm [cm^3(STP) g^{-1}]	298.74
as(BET) [m^{2}g^{-1}]	1.30E+03
C	89.592
Total pore volume (p/p0=0.990) [cm^{3}g^{-1}]	0.5798
Average pore size [nm]	1.7837

BET range limit	(p/p0=0.3670)
Maxumum Va(p_0-p)	2008.9
Vm [cm^3(STP) g^{-1}]	19.399
as(BET) [m^{2}g^{-1}]	1.13E+02
C	33.661
Total pore volume (p/p0=0.990) [cm^{3}g^{-1}]	0.1979
Average pore size [nm]	7.0316

N_2 / 77K	C
Gauss	slit
Def. pore size	Solid
ds [nm]	0.34
Vp [cm^{3}g^{-1}]	0.6166
$W_{peak(area)}$ [nm]	1.6705
$W_{peak(vol)}$ [nm]	1.6705

Figure 27. BET plots of (a) **C1N4DBC-1a**, (b) **C1N5DBC-1a** and (c) **C2N6DBC-1a**. (d) NLDFT plot of **C1N5DBC-1a**. The calculations of **C1N4DBC-1a** and **C2N6DBC-1a** were conducted from the CO_2 isotherms. The calculations of **C1N5DBC-1a** were conducted from the N_2 isotherm.

4.13.8 Theoretical calculations

Optimized structures of **C1N4DBC**, **C1N5DBC**, and **C2N6DBC** were calculated by the DFT method at the B3LYP-D3/6-311G** level. These calculations were carried out using Gaussian09W[71].

To estimate the stabilization energy of stacking and H-bonding between two naphthyl groups, atomic coordinates in the crystal structures were adopted except for DBC moieties. Only hydrogen atoms were optimized at B3LYP-D3/6-311G+(d,p) level of theory. The complexation energy of stacking and H-bonding (Figure 6) were evaluated by B3LYP-D3/6-311G+(d,p). The corrections of basis set superposition error

(BSSE) are evaluated by means of counterpoise method. These calculations were carried out using Gaussian09W[71], or Gaussian16[72].

4.14 References

1. M. Yaghi, M. O'Keeffe, N. W. Ockwig, H. K. Chae, M. Eddaoudi and J. Kim, *Nature*, 2003, **423**, 705–14.
2. W. Xu, B. Tu, Q. Liu, Y. Shu, C. C. Liang, C. S. Diercks, O. M. Yaghi, Y. B. Zhang, H. Deng and Q. Li, *Nat. Rev. Mater.*, 2020, **5**, 764–779.
3. E. Ploetz, H. Engelke, U. Lächelt and S. Wuttke, *Adv. Funct. Mater.*, 2020, **30**, 1909062.
4. R. Freund, S. Canossa, S. M. Cohen, W. Yan, H. Deng, V. Guillerm, M. Eddaoudi, D. G. Madden, D. Fairen-Jimenez, H. Lyu, L. K. Macreadie, Z. Ji, Y. Zhang, B. Wang, F. Haase, C. Wöll, O. Zaremba, J. Andreo, S. Wuttke and C. S. Diercks, *Angew. Chem. Int. Ed.,* 2021, **60**, 23946–23974.
5. C. Wang, D. Liu and W. Lin, *J. Am. Chem. Soc.*, 2013, **135**, 13222–13234.
6. S. M. J. Rogge, A. Bavykina, J. Hajek, H. Garcia, A. I. Olivos-Suarez, A. Sepúlveda-Escribano, A. Vimont, G. Clet, P. Bazin, F. Kapteijn, M. Daturi, E. V. Ramos-Fernandez, F. X. I. Llabrés Xamena, V. Van Speybroeck and J. Gascon, *Chem. Soc. Rev.*, 2017, **46**, 3134–3184.
7. M. Wang, H. Guo, R. Xue, Q. Li, H. Liu, N. Wu, W. Yao and W. Yang, *ChemElectroChem*, 2019, **6**, 2984–2997.
8. Z. Li, T. He, Y. Gong and D. Jiang, *Acc. Chem. Res.*, 2020, **53**, 1672–1685.
9. J. Lü and R. Cao, *Angew. Chem. Int. Ed.,* 2016, **55**, 9474–9480.
10. M. Eddaoudi, J. Kim, N. Rosi, D. Vodak, J. Wachter, M. O'Keeffe and O. M. Yaghi, *Science*, 2002, **295**, 469–472.
11. N. Huang, L. Zhai, D. E. Coupry, M. A. Addicoat, K. Okushita, K. Nishimura, T. Heine and D. Jiang, *Nat. Commun.*, 2016, **7**, 12325.
12. W. Lu, Z. Wei, Z. Y. Gu, T. F. Liu, J. Park, J. Park, J. Tian, M. Zhang, Q. Zhang, T. Gentle, M. Bosch and H. C. Zhou, *Chem. Soc. Rev.*, 2014, **43**, 5561–5593.
13. M. J. Kalmutzki, N. Hanikel and O. M. Yaghi, *Sci. Adv.*, 2018, **4**, eaat9180.
14. F. Beuerle and B. Gole, *Angew. Chem. Int. Ed.,* 2018, **57**, 4850–4878.
15. Z. Chen, H. Jiang, M. Li, M. O'Keeffe and M. Eddaoudi, *Chem. Rev.*, 2020, **120**, 8039–8065.
16. A. J. Howarth, P. Li, O. K. Farha and M. O'Keeffe, *Cryst. Growth Des.*, 2018, **18**, 449–455.
17. Z. Chen, K. O. Kirlikovali, P. Li and O. K. Farha, *Acc. Chem. Res.*, 2022, **55**, 579–591.
18. V. Guillerm and D. Maspoch, *J. Am. Chem. Soc.*, 2019, **141**, 16517–16538.
19. S. Y. Ding and W. Wang, *Chem. Soc. Rev.*, 2013, **42**, 548–568.
20. S. Yu, G. Xing, L. Chen, T. Ben and B. Su, *Adv. Mater.*, 2020, **32**, 2003270.
21. R. B. Lin, Y. He, P. Li, H. Wang, W. Zhou and B. Chen, *Chem. Soc. Rev.*, 2019, **48**, 1362–1389.
22. I. Hisaki, C. Xin, K. Takahashi and T. Nakamura, *Angew. Chem. Int. Ed.*, 2019, **58**, 11160–11170.
23. B. Wang, R.-B. Lin, Z. Zhang, S. Xiang and B. Chen, *J. Am. Chem. Soc.*, 2020, **142**, 14399–14416.
24. X. Song, Y. Wang, C. Wang, D. Wang, G. Zhuang, K. O. Kirlikovali, P. Li and O. K. Farha, *J. Am. Chem. Soc.*, 2022, **144**, 10663–10687.
25. W. Qin, D. Si, Q. Yin, X. Gao, Q. Huang, Y. Feng, L. Xie, S. Zhang, X. Huang, T. Liu and R. Cao, *Angew. Chem. Int. Ed.*, 2022, **61**, e202202089.
26. T. Ami, K. Oka, K. Tsuchiya and N. Tohnai, *Angew. Chem. Int. Ed.*, 2022, **61**, e202202597.
27. T.-H. Chen, I. Popov, W. Kaveevivitchai, Y.-C. Chuang, Y.-S. Chen, O. Daugulis, A. J. Jacobson and O. Š. Miljanić, *Nat. Commun.*, 2014, **5**, 5131.

28. Y. Wang, K. Ma, J. Bai, T. Xu, W. Han, C. Wang, Z. Chen, K. O. Kirlikovali, P. Li, J. Xiao and O. K. Farha, *Angew. Chem. Int. Ed.*, 2022, **61**, e202115956.
29. I. Hisaki, N. Q. Emilya Affendy and N. Tohnai, *CrystEngComm*, 2017, **19**, 4892–4898.
30. I. O. Kirlikovali, S. Goswami, M. R. Mian, M. D. Krzyaniak, M. R. Wasielewski, J. T. Hupp, P. Li and O. K. Farha, *ACS Mater. Lett.*, 2022, **4**, 128–135.
31. I. Ma, P. Li, J. H. Xin, Y. Chen, Z. Chen, S. Goswami, X. Liu, S. Kato, H. Chen, X. Zhang, J. Bai, M. C. Wasson, R. R. Maldonado, R. Q. Snurr and O. K. Farha, *Cell Reports Phys. Sci.*, 2020, **1**, 100024.
32. I. I. Hashim, H. T. M. Le, T. H. Chen, Y. S. Chen, O. Daugulis, C. W. Hsu, A. J. Jacobson, W. Kaveevivitchai, X. Liang, T. Makarenko, O. Miljanić, I. Popovs, H. V. Tran, X. Wang, C. H. Wu and J. I. Wu, *J. Am. Chem. Soc.*, 2018, **140**, 6014–6026.
33. I. Hisaki, Y. Suzuki, E. Gomez, B. Cohen, N. Tohnai and A. Douhal, *Angew. Chem. Int. Ed.*, 2018, **57**, 12650–12655.
34. I. Hisaki, N. Ikenaka, E. Gomez, B. Cohen, N. Tohnai and A. Douhal, *Chem. Eur. J.*, 2017, **23**, 11611–11619.
35. Y. Suzuki, M. Gutiérrez, S. Tanaka, E. Gomez, N. Tohnai, N. Yasuda, N. Matubayasi, A. Douhal and I. Hisaki, *Chem. Sci.*, 2021, **12**, 9607–9618.
36. C. A. Zentner, H. W. H. Lai, J. T. Greenfield, R. A. Wiscons, M. Zeller, C. F. Campana, O. Talu, S. A. Fitzgerald and J. L. C. Rowsell, *Chem. Commun.*, 2015, **51**, 11642–11645.
37. H. W. H. Lai, R. A. Wiscons, C. A. Zentner, M. Zeller and J. L. C. Rowsell, *Cryst. Growth Des.*, 2016, **16**, 821–833.
38. W. Yang, W. Zhou and B. Chen, *Cryst. Growth Des.*, 2019, **19**, 5184–5188.
39. Y. L. Li, E. V. Alexandrov, Q. Yin, L. Li, Z. Bin Fang, W. Yuan, D. M. Proserpio and T. F. Liu, *J. Am. Chem. Soc.*, 2020, **142**, 7218–7224.
40. M. Mastalerz and I. M. Oppel, *Angew. Chem. Int. Ed.,* 2012, **51**, 5252–5255.
41. A. Pulido, L. Chen, T. Kaczorowski, D. Holden, M. A. Little, S. Y. Chong, B. J. Slater, D. P. McMahon, B. Bonillo, C. J. Stackhouse, A. Stephenson, C. M. Kane, R. Clowes, T. Hasell, A. I. Cooper and G. M. Day, *Nature*, 2017, **543**, 657–664.
42. Y. Fujii, T. Maruyama, R. Akasaka, K. Sakao, S. Tokai, Y. Taguchi, Y. Matsumoto, S. Kamiguchi, N. Yoshida, T. Iwasawa, *Tetrahedron Lett.*, 2021, **65**, 152758.
43. Y. Suzuki, N. Tohnai, A. Saeki and I. Hisaki, *Chem. Commun.*, 2020, **56**, 13369–13372.
44. P. v. d. Sluis and A. L. Spek, *Acta Crystallogr. Sect. A*, 1990, **46**, 194.
45. A. L. Spek, *Acta Crystallogr. Sect. D*, 2009, **65**, 148–155.
46. X. Y. Gao, Y. L. Li, T. F. Liu, X. S. Huang and R. Cao, *CrystEngComm*, 2021, **23**, 4743–4747.
47. H. Kubo, R. Oketani and I. Hisaki, *Chem. Commun.*, 2021, **57**, 8568–8571.
48. B. Yu, S. Geng, H. Wang, W. Zhou, Z. Zhang, B. Chen and J. Jiang, *Angew. Chem. Int. Ed.,* 2021, **60**, 25942–25948.
49. Q. Ji, K. Takahashi, S. I. Noro, Y. Ishigaki, K. Kokado, T. Nakamura and I. Hisaki, *Cryst. Growth Des.*, 2021, **21**, 4656–4664.
50. Y. Li, L. Guo, Y. Lv, Z. Zhao, Y. Ma, W. Chen, G. Xing, D. Jiang and L. Chen, *Angew. Chem. Int. Ed*., 2021, **60**, 5363–5369.
51. R.-R. Liang, F.-Z. Cui, R.-H. A, Q.-Y. Qi and Xin Zhao, *CCS Chem.*, 2020, **2**, 139–145.
52. C. F. MacRae, I. Sovago, S. J. Cottrell, P. T. A. Galek, P. McCabe, E. Pidcock, M. Platings, G. P. Shields, J. S. Stevens, M. Towler and P. A. Wood, *J. Appl. Crystallogr.*, 2020, **53**, 226–235.

53. K. Momma and F. Izumi, *J. Appl. Crystallogr*., 2011, **44**, 1272–1276.
54. Rigaku Oxford Diffraction (2015), Software CrysAlisPro 1.171.38.41o. Rigaku Corporation, Tokyo, Japan.
55. G. M. Sheldrick, *Acta Crystallogr. Sect. A*, 2015, **71**, 3–8.
56. Rigaku (2018). CrystalStructure. Version 4.3. Rigaku Corporation, Tokyo, Japan.
57. O. V. Dolomanov, L. J. Bourhis, R. J. Gildea, J. A. K. Howard and H. Puschmann, H. *J. Appl. Cryst.*, 2009, **42**, 339–341.
58. L. J. Bourhis, O. V. Dolomanov, R. J. Gildea, J. A. K. Howard and H. Puschmann, *Acta Crystallogr. Sect. A*, 2015, **71**, 59–75.
59. G. M. Sheldrick, *Acta Crystallogr. Sect. C*, 2015, **71**, 3–8.
60. P. v. d. Sluis and A. L. Spek, *Acta Crystallogr. Sect. A*, 1990, **46**, 194.
61. A. L. Spek, *Acta Crystallogr. Sect. D*, 2009, **65**, 148–155.
62. M. Yamakata, S. Goto, T. Uruga, K. Takeshita, T.Ishikawa, *Nucl. Instrum. Methods Phys. Res. A*, 2001, **467–468**, 667.
63. E. Nishibori, M. Takata, K. Kato, M. Sakata, Y. Kubota, S. Aoyagi, Y. Kuroiwa, M. Yamakata, N. Ikeda, *Nucl. Instrum. Methods Phys. Res. A,* 2001, **467–468**, 1045.
64. S. Kawaguchi, M. Takemoto, K. Osaka, E. Nishibori, C. Moriyoshi, Y. Kubota, Y. Kuroiwa, K. Sugimoto, *Rev. Sci. Instrum.*, 2017, **88**, 085111.
65. Material Studio ver 6.0, Accelrys Software Inc.: San Diego, CA, 2011. Neumann, M. A. *J. Appl. Crystallogr.* 2003, **36**, 356–365.
66. G. S. Pawley, *J. Appl. Crystallogr*. 1981, **14**, 357–361.
67. G. E. Engel, S. Wilke, O. König, K. D. M. Harris, F. J. J. Leusen, *J. Appl.Crystallogr*. 1999, **32**, 1169–1179.
68. Rietveld, H. M. *J. Appl. Crystallogr*. 1969, **2**, 65–71.
69. G. Baldinozzi, J.-F. Berar, *J. Appl. Crystallogr.* 1993, **26**, 128–129.
70. W. A. Dollase, *J. Appl. Crystallogr.* 1986, **19**, 267–272.
71. Gaussian 09, Revision D.01, M. J. Frisch, G. W. Trucks, H. B. Schlegel, G. E. Scuseria, M. A. Robb, J. R. Cheeseman, G. Scalmani, V. Barone, B. Mennucci, G. A. Petersson, H. Nakatsuji, M. Caricato, X. Li, H. P. Hratchian, A. F. Izmaylov, J. Bloino, G. Zheng, J. L. Sonnenberg, M. Hada, M. Ehara, K. Toyota, R. Fukuda, J. Hasegawa, M. Ishida, T. Nakajima, Y. Honda, O. Kitao, H. Nakai, T. Vreven, J. A. Montgomery, Jr., J. E. Peralta, F. Ogliaro, M. Bearpark, J. J. Heyd, E. Brothers, K. N. Kudin, V. N. Staroverov, T. Keith, R. Kobayashi, J. Normand, K. Raghavachari, A. Rendell, J. C. Burant, S. S. Iyengar, J. Tomasi, M. Cossi, N. Rega, J. M. Millam, M. Klene, J. E. Knox, J. B. Cross, V. Bakken, C. Adamo, J. Jaramillo, R. Gomperts, R. E. Stratmann, O. Yazyev, A. J. Austin, R. Cammi, C. Pomelli, J. W. Ochterski, R. L. Martin, K. Morokuma, V. G. Zakrzewski, G. A. Voth, P. Salvador, J. J. Dannenberg, S. Dapprich, A. D. Daniels, O. Farkas, J. B. Foresman, J. V. Ortiz, J. Cioslowski, and D. J. Fox, Gaussian, Inc., Wallingford CT, 2013.
72. Gaussian 16, Revision C.01, M. J. Frisch, G. W. Trucks, H. B. Schlegel, G. E. Scuseria, M. A. Robb, J. R. Cheeseman, G. Scalmani, V. Barone, G. A. Petersson, H. Nakatsuji, X. Li, M. Caricato, A. V. Marenich, J. Bloino, B. G. Janesko, R. Gomperts, B. Mennucci, H. P. Hratchian, J. V. Ortiz, A. F. Izmaylov, J. L. Sonnenberg, D. Williams-Young, F. Ding, F. Lipparini, F. Egidi, J. Goings, B. Peng, A. Petrone, T. Henderson, D. Ranasinghe, V. G. Zakrzewski, J. Gao, N. Rega, G. Zheng, W. Liang, M. Hada, M. Ehara, K. Toyota, R. Fukuda, J. Hasegawa, M. Ishida, T. Nakajima, Y. Honda, O. Kitao, H. Nakai, T. Vreven, K. Throssell, J. A. Montgomery, Jr., J. E. Peralta, F. Ogliaro, M. J. Bearpark, J. J. Heyd, E. N. Brothers, K. N. Kudin, V. N. Staroverov, T. A. Keith, R. Kobayashi, J. Normand, K. Raghavachari, A. P. Rendell, J. C. Burant, S. S.

Iyengar, J. Tomasi, M. Cossi, J. M. Millam, M. Klene, C. Adamo, R. Cammi, J. W. Ochterski, R. L. Martin, K. Morokuma, O. Farkas, J. B. Foresman, and D. J. Fox, Gaussian, Inc., Wallingford CT, 2019

73. Y. Suzuki, N. Tohnai, A. Saeki and I. Hisaki, *Chem. Commun.*, 2020, **56**, 13369–13372.
74. X. S. Ke, Y. Hong, P. Tu, Q. He, V. M. Lynch, D. Kim and J. L. Sessler, *J. Am. Chem. Soc.*, 2017, **139**, 15232– 15238.

General conclusion

As described above, the author confirmed the crystal structures of hexatopic and tetratopic carboxylic acids by the single crystalline X-ray diffraction, powder X-ray diffraction, and electron diffraction. They formed complementary dimers of carboxylic acid to yield porous HOFs. It was difficult to control the accumulation of the H-bonded networks with planar molecules, and non-isostructural, diverse frameworks were obtained. On the other hand, the author has shown that nonplanar π-conjugated (*i.e.*, hexaazatriphenylene) core structure can form stable isostructural HOFs through shape-fitted docking, a so-called uniformly stacking. The author has also examined the importance of the peripheral groups of the core for the properties of the resulting HOFs due to the large influence of molecular modifications.

In Chapter 2, the first construction of spacer modified isostructural HOFs with extended pores is described. Based on shape-fitted docking of hexaazatriphenylene, the construction of four isostructural HOFs was constructed, but simple elongation with phenylene was limited. In order to control the accumulation of spacers by manipulating their bulkiness, The author has accomplished isostructural HOF construction with a derivative possessing a long spacer equivalent to a terphenyl. The stability of the HOFs indicates correlation with molecular fluctuations from MD simulations, rather than with stabilization energies from DFT calculations. Among the HOFs obtained, **BPHAT-1** and **ThiaHAT-1** exhibit anisotropic fluorescence behavior as well as fluorescence sensing to HCl vapor.

In Chapter 3, the author described the HOF construction through nonplanar π-conjugated molecules: dibenzo[*g*,*p*]chrysene (DBC), and its planar analog: tetraphenylethene (TPE) as a reference. DBC tetratopic carboxylic acids derivatives construct two different porous HOFs with different shape-fitted docking manner, **CPDBC-1** and **CPDBC-2**. Eclipsed stacking yielded **CPDBC-1**, while staggered stacking with 90° rotation yielded **CPDBC-2**, which is so-called a "*disappeared crystal*." The balk crystalline of **CPDBC-1** exhibit the permanent porosity, stability toward heat (*ca.* 250 °C), and photoconductivity, although the current was very small. On the other hand, by TPE tetratopic carboxylic acid derivative: **CBPE**, unexpected HOF: **CBPE-1** was obtained. **CBPE-1** forms a homotypic ***sql*** network with its small analog: **CPE**, but the assemblies are

quite different. **CPE** is assembled by simple stacking, while **CBPE-1** constructs a triaxially-woven structure, which is the first example to the author's best knowledge. The fluorescence behavior of this HOF was changed by structural transition in response to abrasion and guest removal.

In Chapter 4, Isomeric effect of spacer molecules was observed in the isostructural construction of DBC derivatives. A simple phenylene elongation derivative, **CBPDBC**, failed to construct isostructural HOF due to solubility and aggregation problems. In contrast, HOFs were obtained with three naphthyl DBCs with different substitution sites. Three HOFs, **C1N5DBC-1**, **C1N4DBC-1**, and **C2N6DBC-1** are isostructural but exhibit different structural properties toward guest removal, ranging from stable to flexible to fragile. In situ PXRD measurements showed that **C1N4DBC-1** exhibits a breathing behavior upon the loading and removing of benzene molecules. The behaviors observed were attributed to differences in pore geometry and H-bonding manner, due to the peripheral structure or its disorder.

Through this study, the author clarified the potential utility of shape-fit docking for the systematic construction of isostructural frameworks with persistent porosity in HOFs composed of only weak bonds. Investigation of the molecular design must include the study of not only core but spacer as well what is needed to control the systematic construction of HOFs with the desired structure and function.

List of publication

1. "Docking Strategy to Construct Thermostable, Single-crystalline, Hydrogen-bonded Organic Framework with Large Surface", I. Hisaki, Y. Suzuki, E. Gomez, B. Cohen, N. Tohnai and A. Douhal, *Angew. Chem. Int. Ed.* 2018, **57**, 12650–12655.

2. “Triaxially-woven Hydrogen-bonded Chicken Wires of Tetrakis(carboxybiphenyl)ethene Derivative”, Y. Suzuki, N. Tohnai and I. Hisaki, *Chem. Eur. J.* 2020, **26**, 17056–17062.

3. “Hydrogen-bonded Organic Frameworks of Twisted Polycyclic Aromatic Hydrocarbon”, Y. Suzuki, N. Tohnai, A. Saeki and I. Hisaki, *Chem. Commun*. 2020, **56**, 13369–13372.

4. “Construction of Isostructural Hydrogen-bonded Organic Frameworks: Limitations and Possibilities of Pore Expansion”, Y. Suzuki, M. Gutiérrez, S. Tanaka, E. Gomez, N. Tohnai, N. Yasuda, N. Matubayasi, A. Douhal and I. Hisaki, *Chem. Sci.* 2021, **12**, 9607–9618.

5. “Isomeric Effect of Naphthyl Spacers on Structures and Properties of Isostructural Porous Crystalline Frameworks”, Y. Suzuki, M. Yamaguchi, R. Oketani and I. Hisaki, *Mater. Chem. Front.* 2023, **7**, 106–116.

The following publication is not included in this thesis.

1. "CO_2 Sorption of Layered Hydrogen-bonded Organic Framework Causes Reversible Structural Changes Involving Four Different Crystalline States under Ambient Pressure", I. Hisaki, S. Nakagawa, Y. Suzuki and N. Tohnai, *Chem. Lett.* 2018, **47**, 1143–1146.

2. "Acid Responsive Hydrogen-bonded Organic Frameworks", I. Hisaki, Y. Suzuki, E. Gomez, Q. Ji, N. Tohnai, T. Nakamura and A. Douhal, *J. Am. Chem. Soc.* 2019, **141**, 2111–2121.

3. "Spectroscopy and Dynamics of a HOF and Its Molecular Units: Remarkable Vapor Acid Sensing", E. Gomez, Y. Suzuki, I. Hisaki, M. Moreno and A. Douhal, *J. Mater. Chem. C*, 2019, **7**, 10818–10832.

(Reviews)

1. “HOFs Built from Hexatopic Carboxylic Acids: Structure, Porosity, Stability, and Photophysics”, M. R. Nunzio, Y. Suzuki, I. Hisaki and A. Douhal, *Int. J. Mol. Sci.* 2022, **23**, 1929.

Acknowledgement

The present studies have been carried out at the Division of Advanced Science and Biotechnology, Graduate School of Engineering, Osaka University and the Division of Chemistry, Graduate School of Engineering Science, Osaka University during 2018–2023 under the direction of Professor Ichiro Hisaki.

The author would like to express his sincere gratitude to Professor Ichiro Hisaki for his instructive guidance, invaluable discussion, and encouragement through the course of these studies. He is deeply grateful to Professor Dr. Norimitsu Tohnai and Assistant Professor Ryusei Oketani for helpful suggestion and discussion.

The author wishes to thank to Professor Dr. Norimitsu Tohnai for PXRD and gas sorption experiments, his instructive guidance, helpful advice, and attractive discussion. He also would like to express his gratitude to Professor Dr. Akinori Saeki for FP-TRMC measurement, Professor Dr. Nobuyuki Matsubayasi and Mr. Senri Tanaka for MD calculation, Professor Dr. Abderrazzak Douhal, Associate Professor Dr. Boiko Cohen, and Dr. Eduardo Gomez for Solid state fluorescence microscopy, and Ms. Rika Miyake and Mr. Hiroaki Tanaka for the measurement of NMR and mass spectra.

The author thanks and feels very fortunate to have opportunity to collaborate with Mr. Atsunori Tomimoto, Mr. Kohei Okubo, Mr. Hiroi Sei, and also to all members of Hisaki research group.

The author is deeply grateful to JSPS for the fellowship during 2020–2023.

Finally, the author sincerely thanks his family Mr. Satoru Suzuki, Ms. Yukari Suzuki, and Ms. Kiyoko Suzuki for their constant assistance and encouragement.

March 2023

Yuto Suzuki